Cirrus occurrence and properties determined from ground-based remote sensing

Paolo Dandini

September 2016

Submitted to the University of Hertfordshire in partial fulfilment of the requirements of the degree of PhD

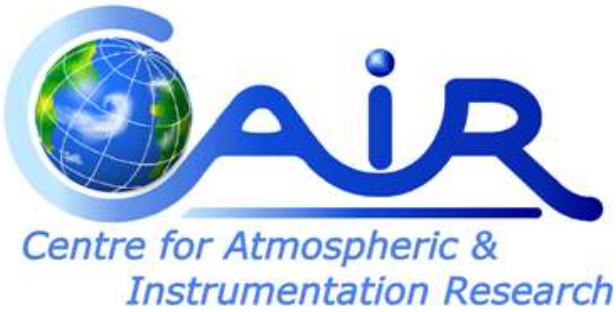

Acknowledgment

Firstly, I would like to express my sincere gratitude to my advisor Prof. Z. J. Ulanowski for the continuous support of my Ph.D study and related research, for his patience, motivation, and immense knowledge. His guidance helped me in all the time of research and writing of this thesis. I could not have imagined having a more experienced advisor and mentor for my Ph.D study.

Besides my advisor, I would like to thank the rest of my thesis committee: Prof. D. Mueller and Dr. A. Baran from Met Office, for their insightful comments and encouragement, but also for the hard questions which incentivized me to widen my research from various perspectives.

My sincere thanks to Prof. P. Kaye, head of CAIR, Prof. H. Jones and Dr. M. Gallaway, who provided me with the opportunity to join their team, and who gave me access to the laboratory and research facilities. Without their precious support it would have not been possible to conduct this research.

I should also thank D. Campbell, principal technical officer, for his continuous and invaluable support, in terms of operation and maintenance of the instrumentation, and for making access to data possible. His contribution has proved to be indispensable.

I want to express my gratitude to Dr. M. Tesche for providing me with processed LIDAR soundings and to Dr. A. Farrow for his kindness and promptness in supporting and helping.

A special thanks to my Research Administrators Mrs. L. Nicholls, Mrs. K. Head and Mrs. E. Thorogood for their constant dedication and commitment.

And lastly I want to thank all my CAIR colleagues who over the years have proved to be supportive, encouraging and fair team players. While working within the CAIR group has been an honour for the excellent skills and professionality of its team members, on a more human level, it has been a unique cultural experience which I will always bring with me and benefit from.

Abstract

The ultimate application of this work is constraining the optical properties of cirrus particles, which are poorly understood, by providing an automatic method, using all-sky cameras and an infrared radiometer, to identify the occurrence of the 22° halo formed by cirrus. This is done by interpreting all sky images in terms of a scattering phase function (SPF), from which the halo ratio (HR) is calculated, and by implementing a cirrus detection algorithm to associate HR measures to ice cloud occurrences. Cirrus reflectivity at solar wavelengths is inversely related to the HR which, being an indirect measure of the regularity of the shape of the ice crystals forming the cloud, relates in turn inversely to the asymmetry parameter *g*. Therefore, the method proposed here to derive statistics of HRs is expected to reduce the uncertainty over the optical and microphysical properties of cirrus.

The light intensity measured by the all sky camera is transformed into a scattering phase function, from which the halo formation is identified. This is done by developing image transformations and corrections needed to interpret all sky images quantitatively in terms of scattering phase function, specifically by transforming the original image from the zenith-centred to the light-source-centred system of coordinates and correcting for the air mass and for vignetting. The SPF is then determined by averaging the image brightness over the azimuth angle and the HR by calculating the ratio of brightness at two scattering angles in the vicinity of the 22^{o} halo peak. The instrument transformation and corrections are performed using a series of Matlab scripts. Given that the HR is an ice cloud characteristic and since the method needs additional temperature information if the halo observation is to be associated with cirrus, a cirrus detection algorithm is necessary to screen out non-ice clouds before deriving reliable HR statistics. Cloud detection is determined by quantifying the temporal fluctuations of sky radiance, expressed as brightness temperature (BT), through De-trended Fluctuation Analysis and setting a clear sky fluctuation threshold. Cloud phase discrimination instead is achieved through first constructing an analytic radiative transfer model to obtain an estimate for average molecular absorption cross-section of water vapour within the spectral window of the radiometer. This is done to model the down-welling clear sky radiance, which is in turn used to correct cirrus emissivity and ultimately determine a dynamic BT threshold for the transition from ice to liquid-containing clouds. In addition to the molecular cross section the screen level air temperature and integrated water vapour are used as input parameters to the model.

The utilisation of the all sky camera for such quantitative measurement was the particularly novel aspect of this work; this has not been done previously to the best of my knowledge. The cirrus detection method proposed is also innovative in that with respect to previous works it does not rely on the use of additional techniques such as LIDAR or microwave radiometry for discriminating cloud phase. Furthermore, the cirrus threshold proposed is not fixed but accounts for the attenuating properties of the atmosphere below the cloud. Once the cirrus detection algorithm is validated and cirrus occurrences determinable, the HR could be extended to estimating the asymmetry parameter and crystal roughness. These are retrievable, for instance, from in-situ observations of single ice crystal 2D scattering patterns from cloud probes of the SID (Small Ice Detector) type. This would be significant for the constraining of the optical and microphysical properties of cirrus.

Outline

Chapter 1

Cloud classification (1.1), a short review of the main atmospheric components, the mechanisms of the radiation-atmosphere interaction (1.2) and the uncertainty associated with clouds over their impact on climate are reviewed. The focus is then on cirrus: the optical phenomena associated to ice clouds (1.3), the microphysics (1.3.2), a review of the in-situ (1.3.3) and satellite observations (1.3.5) of cirrus, the modelling of light scattering (1.3.4) and the role played by ice crystal roughness (1.3.6) with respect to cirrus optical properties. Atmospheric absorption by molecules (1.4), relevant for cloud detection, is then discussed before a brief review of the black body distribution, the down-welling thermal radiation observations and how they apply to the remote sensing of cirrus (1.5).

Chapter 2

The All-Sky cameras' technical specifications (2.3) and the testing of the fish-eye lens projection (2.4.1) are discussed. It follows the method for measuring the SPF through the geometric (2.5), air mass (2.6) and vignetting (2.7) corrections. Image remapping (2.5.1) and interpolation (2.5.2), proposed to implement the geometric correction are compared on four test cases. Two atmospheric models, the plane parallel and radially symmetrical atmospheres, are accounted for quantifying the air mass (2.6) and a comparison of the corresponding results is provided. The causes of vignetting and the method to quantify it, which consists in comparing sky brightness as obtained from two independent measures, one which is affected by vignetting, the imaging, and one which is not, the sun-photometry, are given (2.7). With the working correction for vignetting obtained (2.9) the SPF is ultimately measured on a test case (2.10).

Chapter 3

The instruments used for detecting cirrus are proposed (3.2, 3.3 and 3.4). The selection of clear sky data points via De-trended Fluctuation Analysis is then discussed (3.5). The data set is used to later on test the model of down-welling thermal radiation under clear skies. The model background (3.6) and the deviation of the model from the observed brightness temperature (3.7) follow. The second step of the cirrus detection algorithm, the cirrus threshold method (3.8), is covered before the conclusions (3.9) and the recommended further work to be done to improve the detection algorithm (3.9.1).

Chapter 4

HR time series corresponding to specific test cases are plotted. The cirrus detection method is applied to each test case for cloud discrimination purposes. The sensitivity of the HR to the halo status of cirrus is assessed. A cirrus characterization flow chart (4.6) is finally provided.

Chapter 5

General conclusions about the all sky imaging (5.1) and the cirrus detection algorithm (5.2), future work to undertake (5.3), the application of the investigation and where it could lead in future are set out (5.4).

Appendix 6

Further details about the concept of radiance (6.1), the light scattering by molecules (6.2), and an alternative method for the integration of the black-body distribution over a finite spectral interval (6.3) are discussed. Flow diagrams of some of the main Matlab scripts used are also given (6.4).

Bibliography 7

A list of all the literature consulted is given.

List of Acronyms

AERONET	Aerosol Robotic Network
AM	Air mass
AMC	Air mass correction
AOD	Aerosol optical depth
AT	Air temperature
AVHRR	Advanced very High Resolution Radiometer
BIGF	British Isles continuous GNSS Facility
BM	Background mask
BT	Brightness temperature
CAIR	Centre for Atmospheric and Instrumentation Research
CALIOP	Cloud Aerosol LIDAR with Orthogonal Polarization
CC	Camera plane centre
CGT	Close to ground air temperature
COD	Cloud optical depth
COT	Cloud optical thickness
CN	Condensation nuclei
CP	Camera plane
CSHR	Clear Sky Halo Ratio
DDA	Discrete dipole approximation
DDP	Digital development processing
DFA	De-trended fluctuation analysis
EBCM	Extended boundary conditions method
E-GVAP	EUMETNET GNSS water vapour programme
EPS	Effective particle size
EUMETNET	Network of European Meteorological Services
FASCODE	Fast Atmospheric Signature Code
FC	Fluctuation coefficient
FDTD	Finite-difference time domain
FEL	Fish-eye lens
FITS	Flexible Image Transport System
FOV	Field of view
GC	Geometric correction
GCM	General circulation model
GNSS	Global Navigation Satellite System
HR	Halo Ratio
IWC	Integrated water content
IWP	Integrated water path
IWV	Integrated water vapour
LFA	Lens focal axis
LOWESS	Locally weighted scatter plot smoothing
LOWTRAN	Low Altitude Atmospheric Transmission
LRCBS	LIDAR log of range-corrected backscattered signal
LS	Light source
LWIR	Long wave infrared
MAD	Mean absolute deviation
MET-MT	MET office modelled brightness temperature
MET-T	MET office modelled temperature
MODIS	Moderate Resolution Imaging Spectroradiometer
MODTRAN	Moderate-Resolution Atmospheric Radiance and Transmittance Model

MOSART	Moderate Spectral Atmospheric Radiance and Transmittance Code
MT	Modelled brightness temperature
MWIR	Mid-wave infrared
NRT GNSS	Near real time Global Navigation Satellite System
NWP	Numerical weather predictions
OC	Optical centre
OPTMT	Optimized modelled brightness temperature
PARASOL	Polarization and Anisotropy of Reflectances for Atmospheric Sciences coupled with Observations from a Lidar
PBL	Planetary Boundary Layer
PPM	Principal plane measurement
PSD	Particle size distribution
PSTD	Pseudo-spectral time domain
PWV	Precipitable water vapour
RFO	Radial fall-off
RH	Relative humidity
RMSD	Root Mean Square Deviation
RTDF	Ray Tracing with Diffraction of Facets
SA	Scattering angle
SB	Sky brightness
SBIG	Santa Barbara Instrument Group
SID	Small ice detector
SPF	Scattering phase function
STD	Standard deviation
SWIR	Short wave infrared
VC	Vignetting correction
VIIRS	Visible Infrared Imaging Radiometer Suite
WV	Water vapour
WVP	Water vapour pressure
ZTD	Zenith total delay
ZWD	Zenith wet delay

Table of contents

1 Introduction

In this chapter we will first review cloud classification and the radiation-atmosphere interaction mechanisms to then discuss the optical phenomena associated with cirrus. Cloud microphysics with particular emphasis to the case of ice clouds will follow. In situ observation of cirrus, single ice crystal light scattering modelling, satellite observations, how they are used to investigate cirrus microphysics, the advantages of each technique and their current limitations in retrieving ice crystal morphological data, are then covered. The absorption and emission properties of clouds, atmospheric molecules and particles which we turn next, towards the end of the chapter, will allow us to set out the theoretical basis for the implementation of a cirrus detection algorithm.

1.1 Clouds and classification

Clouds consist of tiny suspended particles of water, ice or both. According to some of the latest classification (1) clouds are divided in ten types as Figure 1-1 shows.

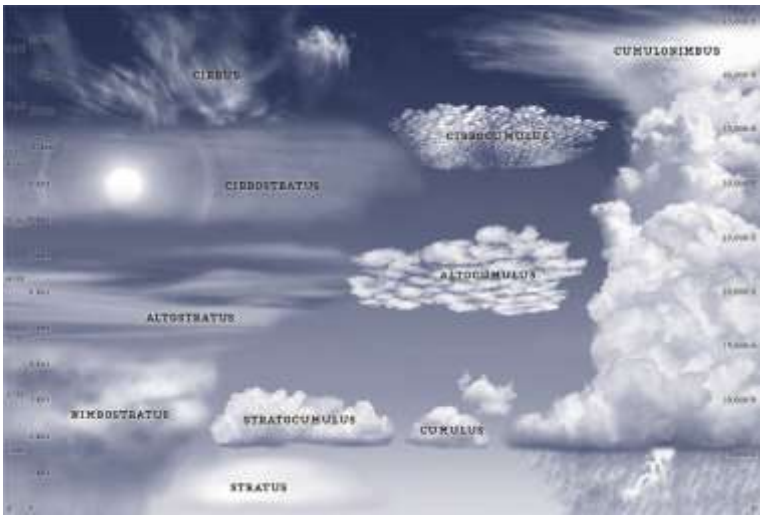

Figure 1-1: The 10 main cloud types (1).

Based on the altitude which they are found at (2) they are generally divided into three categories:

1. **High level clouds: Cirrus, Cirrocumulus and Cirrostratus**
2. **Mid-level clouds: Altocumulus, Altostratus and Nimbostratus**
3. **Low level clouds: Cumulus, Stratocumulus, Stratus and Cumulonimbus**

In addition to the type, clouds can be classified according to the species and variety (see Table 1 (1)).

Genera	Species	Variety
Cirrus	Uncinus, fibratus, spissatus, castellanus	Intortus, radiatus, vertebratus
Cirrostratus	Nubulus, fibratus	-
Cirrocumulus	Castellanus, floccus, lenticularis	Undulatus
Altocumulus	Castellanus, floccus, lenticularis	Translucidus, opacus, undulatus, perlucidus
Altostratus	-	Translucidus, opacus
Nimbostratus	-	-
Stratocumulus	Castellanus, lenticularis	Perlucidus, Translucidus, opacus
Stratus	Fractus, nebulosus	-
Cumulonimbus	Calvus, capillatus	-
Cumulus	Fractus, humilis, mediocris, congestus	-

Table 1: the ten cloud type and their most common species and varieties (1).

While the species relate to the shape and the internal structure of clouds, the variety is linked to their transparency. They may also be classified as ice, water or mixed phase clouds, depending on the particulate phase. When the temperature is very low as it is the case at high altitudes, ice prevails over water. Cirrus and Cirrostratus are composed of ice crystals. However water droplets may be present in Cirrocumulus. Mid level clouds normally contain water droplets but if temperature is sufficiently low ice crystals may also form. Low level clouds instead are composed of water droplets and only occasionally may present a mixed phase content. Cumulonimbus, however, are always mixed (2).

Despite the different origin but with characteristics similar to clouds, contrails should also be accounted for. They are artificially generated clouds. The hot gases released from the aircraft engine exhaust, when in contact with the cold environment may precipitate into water droplets and then into ice crystals if the temperature is low enough. Contrails are the artificial counterpart of cirrus. Like cirrus they are high level clouds, made of ice crystals reflecting solar light back to space and absorbing and emitting thermal radiation. Satellite observations suggest that aviation-generated ice clouds global mean coverage is 0.07% (3). On the other hand space-based measurements show 30% cirrus coverage at any time at mid-latitude and between 60 and 80% at any time at the tropics (4).

Clouds differ not only in terms of their phase, but also microphysical, optical, and radiative properties. Cloud microphysics concerns to the microphysical properties of the cloud constituents such as *size*, *shape*, *roughness*, *particle concentration*, *particle refractive index*, *liquid and ice water content*. Optical properties on the other hand relate to a larger scale. They express how transparent, opaque or absorbing a cloud is. They are obtained as the average over the geometric extent of the cloud, of physical quantities such as the extinction or the absorption coefficients which in turn depend on the microphysics of the cloud. The *optical thickness*, the *extinction* and *absorption coefficients*, the *scattering phase function*, the *asymmetry parameter* are optical properties. Radiative properties are global optical characteristics of clouds such as *reflection* and *transmission functions*. They link global optical properties to microphysical parameters such as particle size and refraction index. In the coming section the main mechanisms of interaction radiation-atmosphere and in particular the role played by the principal atmospheric constituents such as gases and clouds in determining the radiation balance on earth will be briefly reviewed, before focussing on the uncertainty associated with ice clouds.

1.2 Atmosphere and radiation

The main atmospheric constituents are gases, aerosol and clouds. Like matter they all contain discrete electric charges. It is the interaction of solar and earth's radiation with the atmospheric constituents that determines the radiative balance of the atmosphere through the mechanisms of *absorption*, *scattering and emission*. The Earth receives solar radiation mainly in the visible and UV part of the spectrum while it re-radiates mostly between 4 μm and 100 μm by virtue of its temperature. Nearly 90% of the emission is absorbed by the atmosphere then partly re-emitted back to ground (atmospheric emission) and partly into space (see Figure 1-2) together with the remaining 10% which undergoes no absorption. Absorption occurs when the energy of the incident radiation or part of it is absorbed as a consequence of the interaction. Emission which is the inverse process takes place at any temperatures. Clouds emit thermal radiation in varying amounts depending on temperature, optical depth and emissivity. On the other hand the electromagnetic fields travelling through the atmosphere can cause the electric charges to oscillate and as a consequence to radiate electromagnetic waves. Incident radiation from the source excites secondary waves from the scatterer and the superposition of them is what is observed. If the frequency of scattered and incident waves are the same then the scattered field is said to be *elastic*. The interaction mechanism depends on the wavelength and on the size of the particle which in turn relates to its *geometric cross section*. This is the physical quantity that broadly determines the strength of the interaction with the incident radiation. In other terms the type of interaction depends on the ratio of the particle size to the radiation wavelength known as *size parameter x*.

$$x = \frac{2\pi r}{\lambda} \tag{1.1}$$

In Eq. 1.1 *r* is the radius of a sphere which the particle is approximated with. When visible light (0.4 μm < λ < 0.7 μm) interacts with atmospheric molecules it results in $x << 1$. By assuming the interaction mechanism to be elastic, the scattering of light by spherical particles much smaller than the wavelength is well represented by the Rayleigh's theory of scattering. The scattering of light by spherical particles whose size becomes comparable to the wavelength of the radiation has been formalized in the Gustav Mie's theory. When the interaction of light and atmosphere is not elastic it means that the incident radiant flux does not equal the scattered one because some of the energy conveyed by the incident beam has been absorbed as a result of the interaction. Atmospheric particles size varies over a wide range: from the molecular (atmospheric gases) up to the millimetre scale (ice crystal aggregates, rain drops, ash, dust particle). Considering the wide spectrum of wavelengths travelling through the atmosphere the multitude of complex interactions taking place becomes evident.

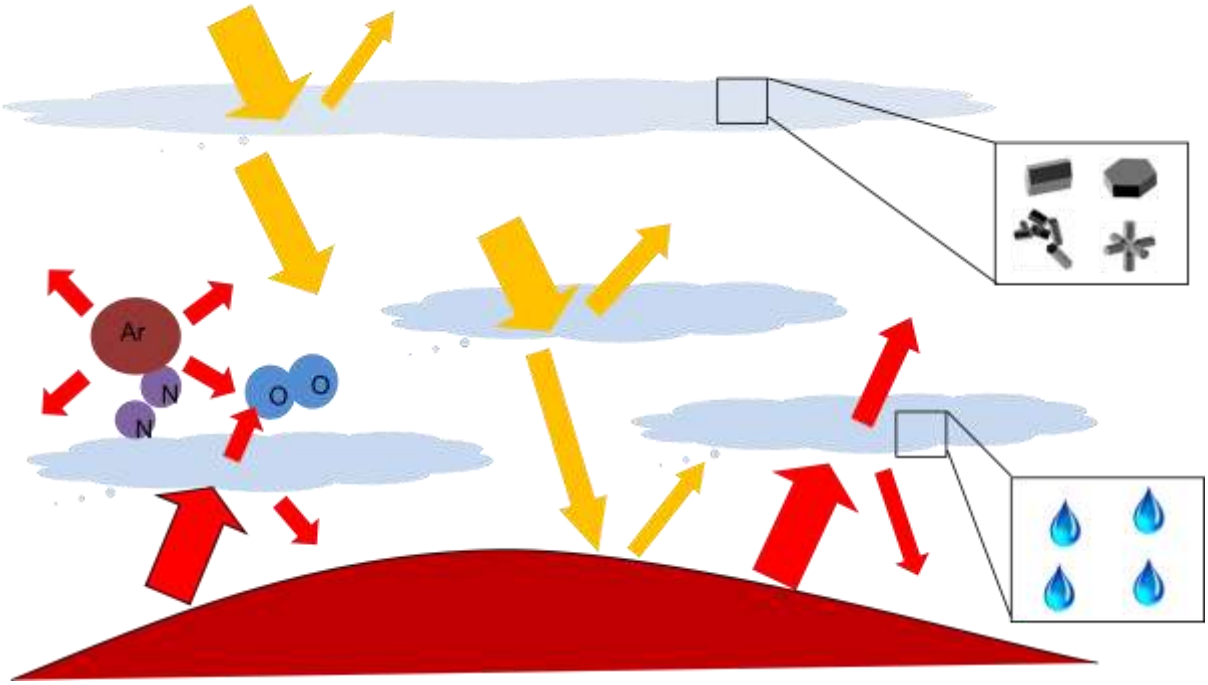

Figure 1-2: Atmospheric constituents and radiative interaction - yellow and red arrows represent visible and thermal radiation respectively.

The UV, visible and infrared portions of the electromagnetic spectrum are the primary components to account for when it comes to determining the net radiative effect. In this respect the complex refractive index of suspended water and ice particles which is responsible for the absorption of solar radiation by clouds depends on the thermodynamic phase, temperature and chemical composition (5). The imaginary component of the refractive index varies by six orders of magnitude between visible (0.4 µm) and near infrared (2 µm) wavelengths - see Figure 1-3. Scattering is generally considered dominant over absorption for visible light whereas when the Earth's thermal emission is accounted for, absorption by cloud particles becomes dominant over scattering.

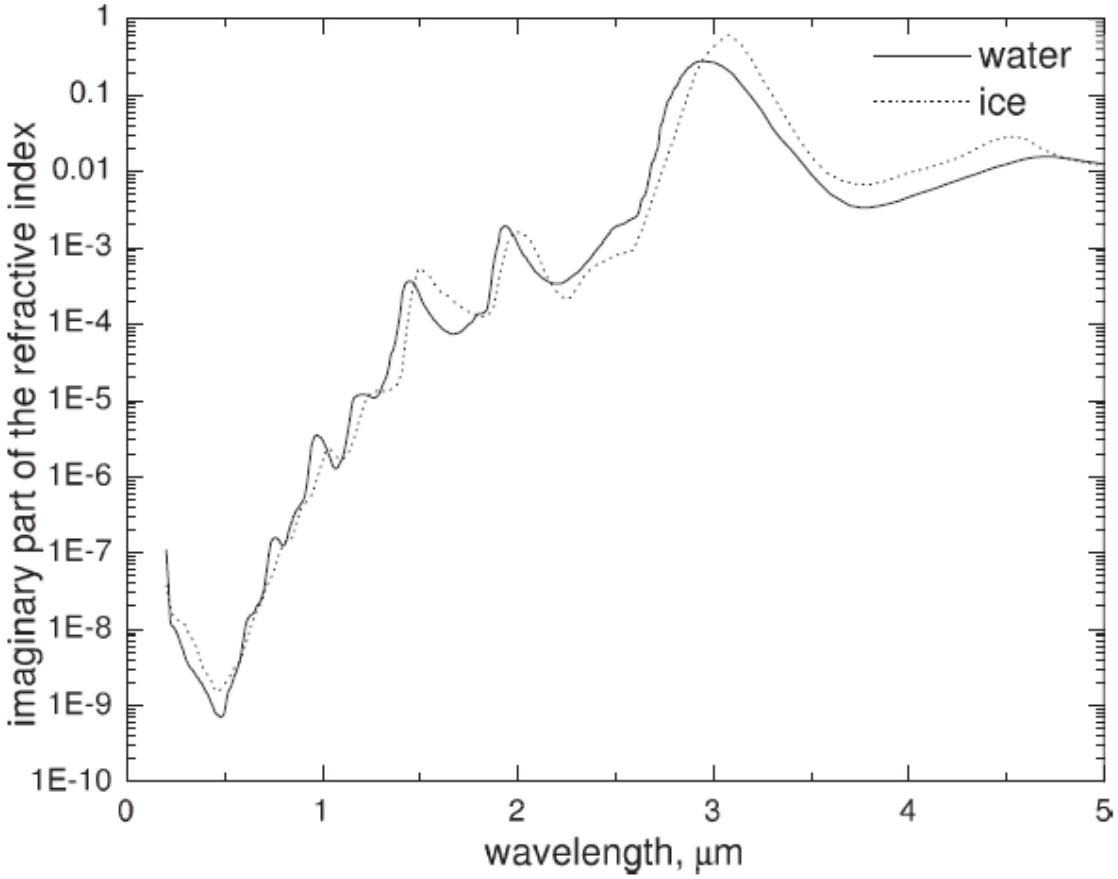

Figure 1-3: Imaginary part of the complex refractive index of ice and water. Copied from (6).

The principal gas species in order of abundance are nitrogen, oxygen and argon. Water vapour, carbon dioxide and ozone are some of the most relevant ones in terms of absorption and emission of radiation. Carbon dioxide is highly absorbing at 15 µm and 4.3 µm, ozone is associated with the absorption band at 9.6 µm while the one at 6.3 µm is due to water vapour. The latter plays a fundamental role in terms of radiation balance at ground level given its diurnal and annual variability. The main parameters that affect the average daily global solar irradiance are: *extraterrestrial radiation*, *solar declination*, *ratio of sunshine duration*, *air temperature*, *earth surface albedo*, *relative humidity*, *cloudiness*, *precipitation*, *evaporation*, *atmospheric composition*, *aerosol optical depth*, *geographical location* and *soil temperature* (1). Among these parameters the one which introduces the largest uncertainty in estimating the daily global solar irradiance is cloudiness because even if predictable, its spatial and temporal variability gives rise to large discrepancies between observations and predictions. Scientists are interested in determining clouds feedback in terms of solar and thermal radiation or in other words how they regulate radiation fluxes at the surface. Cloud contribution to the total radiative flux remains the largest source of uncertainty in climate models. In particular, large uncertainties still remain concerning the net radiative effect of cirrus which is determined by the difference between transmitted and reflected radiation over the visible and infrared spectrum on global scale. Cirrus clouds are found above 6 km and are mainly composed of non-spherical ice crystals whose high morphological complexity makes it highly challenging to predict the way these clouds scatter light and ultimately how they regulate the radiation budget of the Earth-atmosphere system. As opposed to water clouds, our understanding of cirrus clouds in terms of optical and radiative properties is relatively low. The urgent questions that science has to answer are:

1. **What are the microphysical properties of ice crystals?**
2. **What atmospheric conditions determine the properties of ice crystals?**
3. **How do these properties determine the scattering of light, the radiative properties of cirrus and ultimately their net radiative effect?**

For answering these questions the combined effort of different techniques of investigation such as, in situ and remote sensing observations, modelling of light scattering and lab measures are needed.

1.3 Optical phenomena: halos, sun dogs, Parry arc

Cirrus clouds are found typically above 6 km, are mainly composed of non-spherical ice crystals, and interact with both solar radiation and thermal infrared emission from the lower atmosphere and ground. At any time they cover 30% and 70% of the mid-latitudes and tropics respectively. They are often associated to spectacular optical phenomena known as halos such as the 22° halo, the so called "sundogs", the parhelic circle, the upper and lower tangent arcs and the circumzenithal arc. The 22° halo, visible all over the world and throughout the year, forms when cirrus is mainly composed of randomly oriented ice columns and light rays pass through facets inclined 60° to each other (see Figure 1-4 (7)). The light rays may deviate through angles from 22° to 50° but the majority are close to minimum deviation. This occurs when the internally refracted ray travels parallel to one facet of the column. Sundogs instead are visible when light passes through the side (prismatic) facets of hexagonal plates having their basal facets nearly horizontal (see Figure 1-5 (7)). Analogously to the 22° halo, of all rays those which actually make the sundogs visible are the ones passing through two side facets inclined 60° to each other and undergoing the minimum deviation of 22°. In this respect it should be noted that in situ observations (8) of halo forming cirrus clouds prove that halos are not necessarily associated to idealized geometries such as hexagonal columns and plates. Cavities and higher complexity are, in fact, observed. Geometric optic ray tracing techniques reveal that, by assuming more complex shapes for representing the optical properties of ice crystals found in natural occurring cirrus such as hollow columns and bullet-rosettes, halo features are still preserved although a diminished back-scattering and an enhanced side-scattering (for the bullet-rosette case) are predicted. It is the scattering phase function (SPF), obtained by averaging the light scattered over the azimuth angle for each individual scattering direction, that specifies the angular redistribution of light (see Figure 1-6). When impinging on a non absorbing (at visible wavelength) single scatterer, visible light is redistributed over all directions individuated by the radii of the sphere centred around the particle. SPF is a strongly dependent function of the microphysics of ice crystals.

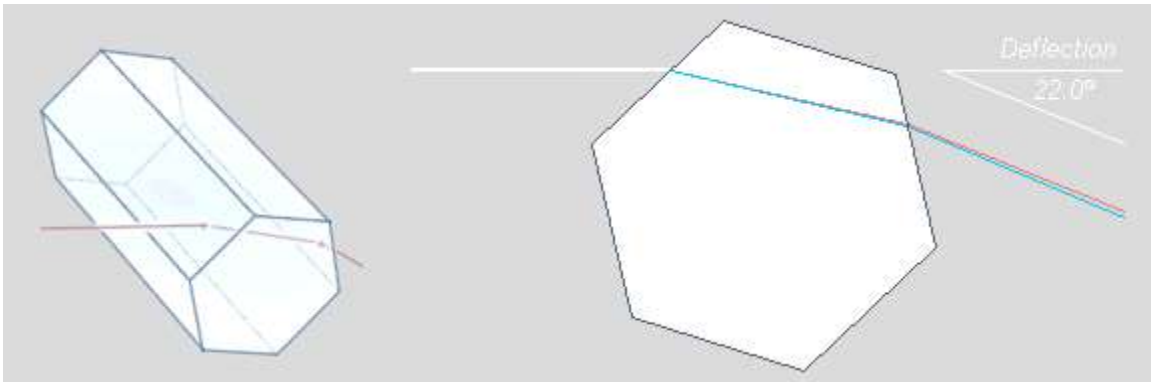

Figure 1-4: Hexagonal column randomly oriented (7).

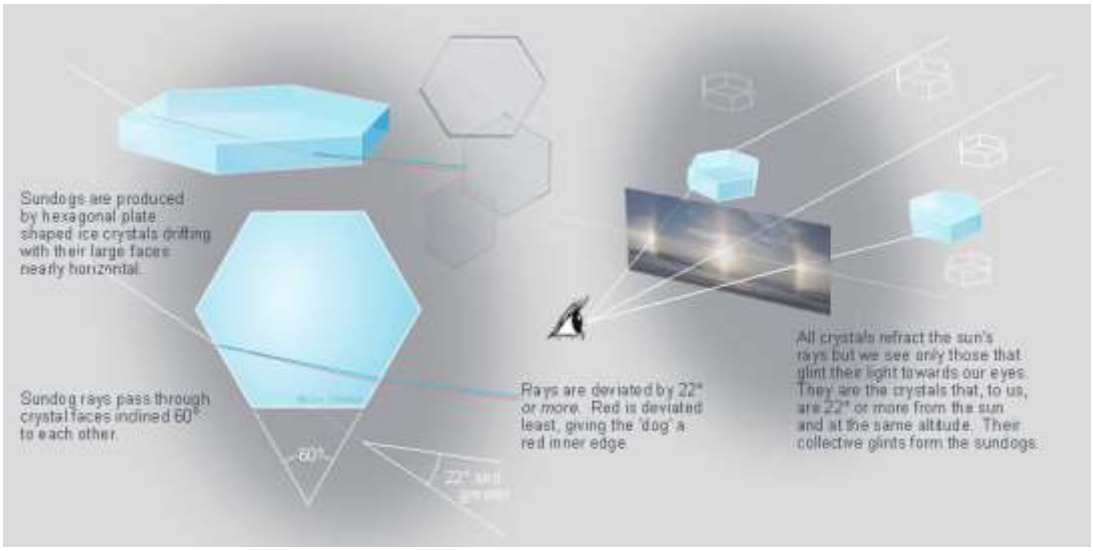

Figure 1-5: Hexagonal plates are associated to sundogs (7).

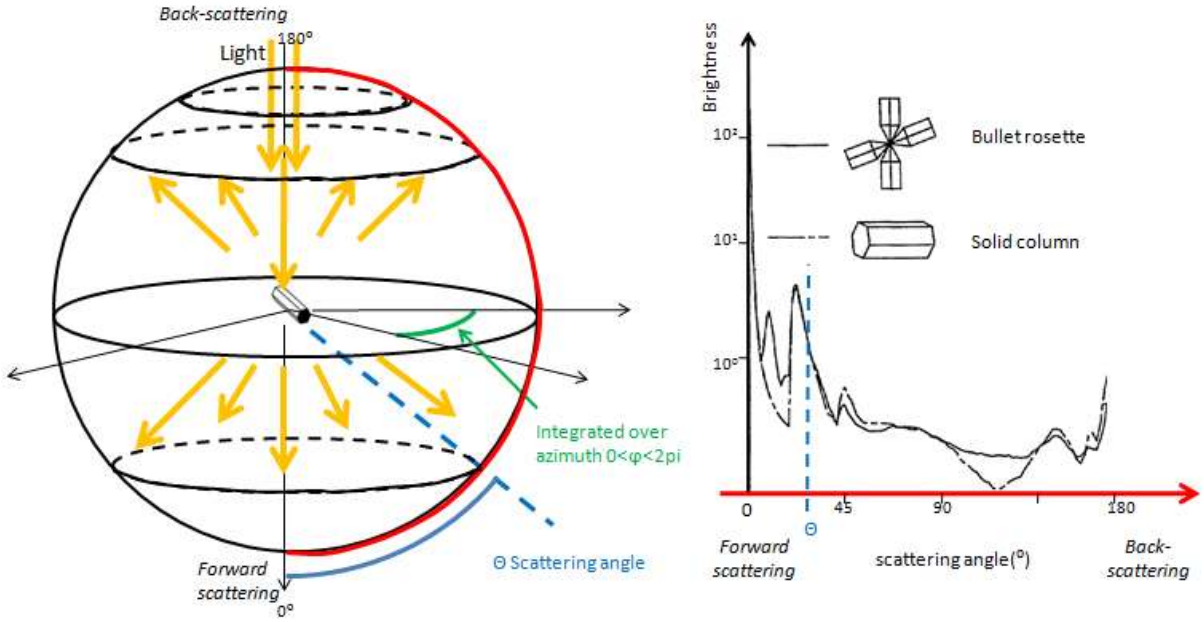

Figure 1-6: Scattering phase function.

In the coming paragraph cloud microphysics is discussed. The simpler case of liquid clouds will be considered at first. Average volume, surface area and mass of the particles will be derived from the particle size distribution (PSD). The focus will then turn to the more complex case of the ice cloud and to corresponding forms of the PSDs proposed in literature.

1.3.1 Cloud microphysics

One of the main differences between water and ice clouds is that the former are mostly formed of approximately spherical droplets whereas the latter of non-spherical ice crystals. Ice in cloudy media can take on many shapes. From the simple hexagonal column and plate to bullet-rosette, poly-crystals up to more complex aggregates. It is the significantly different microphysics of liquid and ice clouds that results in distinct optical and radiative properties. This has consequences on the cloud

radiative forcing which ultimately determines the impact of clouds on Earth's climate. Water droplet size may be on average 10 μm in non-precipitating clouds and larger than 1 mm in rain clouds (6). Given that there is no cloud characterized by mono-disperse water droplets, it is common practice to define a particle size distribution (PSD) $f(a)$ where a is the particle radius such that it normalizes as in Eq. 1.2 :

$$\int_0^\infty f(a)da = 1 \tag{1.2}$$

The fraction of particles per unit volume with radius between a_1 and a_2 is given by:

$$\int_{a_1}^{a_2} a\ f(a)\ da \tag{1.3}$$

In many cases f takes on the form of the lognormal or gamma distribution (9). Assuming the latter one, f can be expressed as in Eq. 1.4 :

$$f(a) = Ka^{\mu} e^{-\mu \frac{a}{a_0}} \tag{1.4}$$

where:

1. ***a* is the particle radius**
2. ***K* is a normalization constant**
3. **a_0 is where *f* is maximum**
4. **μ is a parameter that characterizes the width of the PSD**

The moments of the distribution are:

$$\langle a^n \rangle = \int_0^\infty a^n f(a)da \tag{1.5}$$

They can be calculated through Eq. 1.6

$$\langle a^n \rangle = \left(\frac{a_0}{\mu}\right)^n \frac{\Gamma(\mu + n + 1)}{\Gamma(\mu + 1)} \tag{1.6}$$

where Γ is the gamma function.
The average volume, surface area and mass of the particles, defined in Eq. 1.7, 1.8 and 1.9 respectively, can be easily calculated from Eq. 1.6.

$$\langle V \rangle = \frac{4\pi}{3} \int_0^\infty a^3 f(a)da \tag{1.7}$$

$$\langle S \rangle = 4\pi \int_0^\infty a^2 f(a)da \tag{1.8}$$

$$\langle M \rangle = \rho \langle V \rangle \tag{1.9}$$

where ρ = 1 g/cm^3 is the density of water. Characterizing cloud PSD through their moments is advantageous as they are in general retrieved from optical measurements (10). Other parameters worth mentioning are the effective particle radius a_{ef} and the coefficient of variance ξ of the PSD, expressed in Eq. 1.10 and 1.11 respectively.

$$a_{ef} = \frac{\langle a^3 \rangle}{\langle a^2 \rangle} \tag{1.10}$$

$$\xi = \frac{\sqrt{\int_0^\infty (a - \langle a \rangle)^2 \, f(a) da}}{\langle a \rangle} \tag{1.11}$$

The effective particle radius is proportional to the average volume to surface ratio of the particle. ξ is particularly important for narrow droplets distributions. Another important parameter in addition to size and shape is the number concentration *N* which is the number of particles per unit volume. It depends on the concentration of the condensation nuclei (CN) which varies widely from oceanic to continental regions. In general CN concentration is larger in continental regions. Satellite remote sensing shows marine clouds consisting of larger droplets due to this variation (11).
Despite being an average over the geometric thickness of the cloud (from cloud base x_b to top x_t), liquid and ice water path are also microphysical properties defined as follows:

$$LWP = \int_{x_b}^{x_t} \rho_{liquid} N \langle V \rangle dx \tag{1.12}$$

$$IWP = \int_{x_b}^{x_t} \rho_{ice} N \langle V \rangle dx \tag{1.13}$$

If we now turn our focus to ice clouds, plates, columns, needles, dendrites, stellars and bullets are some of the most typical ice crystals shapes found in crystalline clouds (12) (13) (14). In this respect it is worth to mention the work done by Magono and Lee who classified natural crystals into 80 different shapes spanning from the simple needle to the highly irregular germ (15). Ice crystal concentration spans from 50 to 50000 crystals per cubic meter, it varies with the height along the cloud extent with an average mass falling in the range $2x10^{-3}$g - $2x10^{-9}$g. Presence of cavities, bubbles and impurities makes it less than that of bulk ice (16). Crystals size is generally expressed in terms of its maximal dimension *D* which relates to the effective size (17). Ice crystals size can vary between 1 µm up to several thousands of microns (18) (19). Simple shaped crystals like hexagonal prisms can be characterized by two dimensions (length of the prism *L*, and diameter *D*). In this specific case the existence of empirical formulas linking *L* to *D* in natural clouds (20) can be used to express the PSD in terms of a single parameter. With respect to ice clouds it should be noted that this is not possible

because of the multitude of really complex shapes ice crystals can take on. However a way to define a PSD also for ice clouds consists in expressing it as in Eq. 1.14

$$f\left(\vec{a},\vec{b}\right)=\alpha\left(\sum_{r=1}^{N}c_r\,f_r\left(\vec{a}\right)+\sum_{i=1}^{M}c_i\,f_i\left(\vec{b}\right)\right) \tag{1.14}$$

where:

1. **f_r(a) is the size distribution for regular ice particles**
2. **f_i(b) is a statistical distribution of irregularly shaped crystals**
3. ***a* is a vector of some actual particle dimensions (would coincide with *L* and *D* in case of hexagonal prisms)**
4. ***b* represent statistical characteristic of the particle such as average radius**
5. **c_r and c_i are the concentrations of the single crystal habits**
6. **α is a normalization constant**

The introduction of a single irregularly shaped particle (fractal) as representative of all complex habits found in ice clouds proved to represent quite well the optical characteristics of ice clouds (21) (22) (6). In the coming paragraph some of the ice crystal habits more commonly used in the investigation of the optical properties of ice particles will be reviewed.

1.3.2 Ice cloud microphysics

Determining the size, shape, roughness and more in general characterizing ice crystals in terms of microphysical data is crucial if the impact of cirrus on Earth's climate is to be quantified. Given the high variability of such properties it is not possible to characterize them in terms of a single PSD as it has been done for water clouds. Pure ice clouds are found at temperatures lower than about 233 K (4). The way ice crystals form and grow depends on the environmental variables such as temperature and relative humidity (RH) in first place. Normally due to gravitation the larger crystals settle in the lower layers of the cloud where due to aggregation they may take on highly complex shapes like chains of hexagonal columns, plates, bullet-rosettes or ice aggregates. The longer the crystals take to fall the more time there is for them to grow through water vapour deposition and aggregation mechanisms (23) (24). Such processes may lead to irregular and difficult to classify ice aggregates (25). On the other hand the smaller particles are more likely to be found towards the cloud top where hexagonal columns, plates, bullet rosettes are often dominant although more complex shapes can occur. Also the latitude at which the cloud is found plays an important role. At mid latitudes, where cirrus forms into layered clouds, ice crystals complexity increases with the cloud depth relative to cloud top. In the tropics instead where up-draughts are stronger it is more likely to find larger, complex ice crystals toward the cloud top. Their size can vary from a few microns up to several millimetres in case of large aggregates. In the arctic regions where accessibility becomes more difficult ice crystals observations are less common. However, some studies suggest that ice crystals can grow up to 1000 µm (26) (27). PSD in general varies from layer to layer and it may be found bi-modal if co-existence of large and small particles occurs (24).
Figure 1-7, Figure 1-8 and Figure 1-10 show some of the ice crystal models used for investigating the light scattering properties of the larger crystals (>100 µm) found in cirrus (4). The hexagonal column, plate and the more common six-arms bullet rosette, shown in Figure 1-7 from left to right, have been proposed to model the simplest crystal shapes.

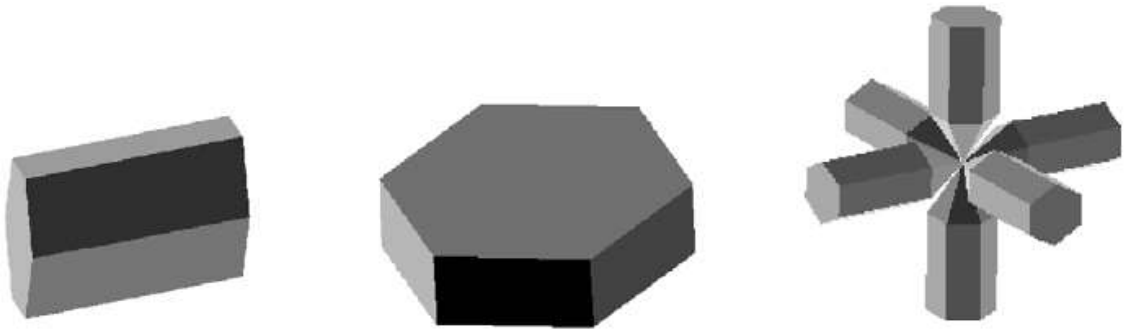

Figure 1-7: From left to right: hexagonal column, hexagonal plate, and bullet rosette (4).

The polycrystal (see Figure 1-8 - left) is one of the first attempts to represent the optical properties of ice aggregates (28) whereas the hexagonal ice aggregate (see Figure 1-8 - right) has been proposed to be representative of natural occurring compact aggregates (29).

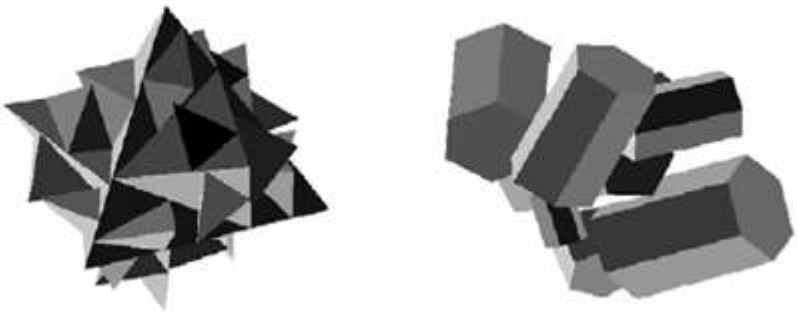

Figure 1-8: Poly-crystal and hexagonal ice aggregate (4).

The Inhomogeneous Hexagonal Mono-crystal (see Figure 1-9) was proposed to account for the observed air bubbles and aerosol inclusions (30).

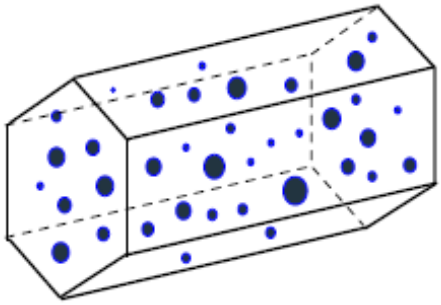

Figure 1-9: Inhomogeneous hexagonal mono-crystal (30).

The hexagonal plate and rosette aggregates (see Figure 1-10 - left and right) were proposed to improve the interpretation of remote sensed ice cloud properties (31) (32) while the spatial eight-chain aggregate (see Figure 1-10 - centre) for representing ice aggregates which appear spatial

rather than compact (33).

Figure 1-10: Chain of hexagonal plates, chain hexagonal ice aggregate, and rosette chain (4).

For what concerns particles smaller than 100 µm alternative idealized models have been proposed such as the Chebyshev model (34), the droxtal (35), the Gaussian random sphere (36) and the Bucky ball model (37). Habit mixture models have been introduced to better represent the optical properties of ice crystals. It is worth to mention the one from Baum (38) which accounts for a collection of different crystal habits and well reproduces the IWC consistently with the ice crystal aggregation relation which predicts the mass of ice to be proportional to the square of *D*. The ensemble model (39) also tries to represent the aggregation mechanism by means of a collection of habits progressively complex with *D*, each one distributed through a PSD which is obtained by means of moment estimation parameterizations. Baums's model on the other hand relies on PSD derived from in situ observations. They both proved to better predict CloudSat reflectivity (40) (41) and to have the capability to reproduce the aggregation process consistently with Eq. 1.15).

$$IWC \propto D^2 \tag{1.15}$$

1.3.3 Ice clouds - in situ measurements

In situ observations have been carried out over the years to retrieve the size and shape of ice particulate. Traditional probes are affected by optical limitations, inevitably taking place when the particle size goes down to a few microns. Acquiring high resolution images of single ice crystals is not possible because of optical aberration and diffraction. The latter in particular is responsible for making the particle look "rounded" when it actually may not be (42). A possible solution consists in looking at the way single ice crystals scatter light and retrieving morphological data by analysing the 2D scattering pattern so obtained (see Figure 1-11). This is conceptually known as the *inverse scattering problem*.

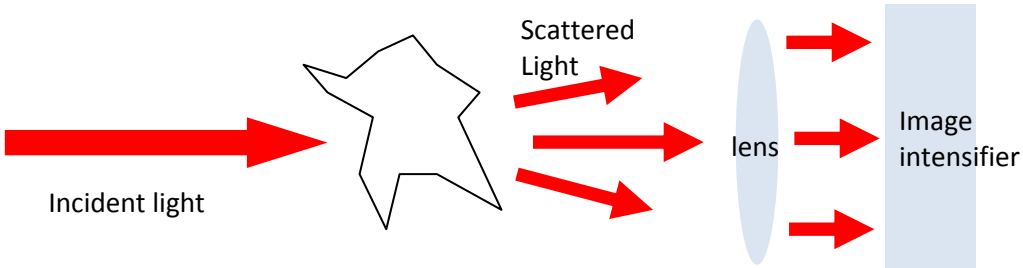

Figure 1-11: 2D scattering pattern obtained from generic particle.

Ice crystal shattering on the inlet of the probe (43) is an additional issue. The consequent overestimation of the actual number of small particles leads to a skewed PSD. Ice crystals smaller than 250 µm can be an artefact caused by shattering. Even if this issue has not entirely invalidated past in-situ observations, they have certainly boosted the focus into searching ways to circumvent these problems. Over the last ten years new generation probes for in situ-measurement have been introduced (44) (45) (46) (47). In this respect the Centre for Atmospheric and Instrumentation Research (CAIR), at University of Hertfordshire has developed the SID probes (Small Ice Detector - see Figure 1-12) which can be installed on aircraft (see Figure 1-13). SID3 in particular takes high resolution images of the light scattered by single ice crystals. Thanks to its open geometry it prevents ice crystal shattering from skewing the PSD.

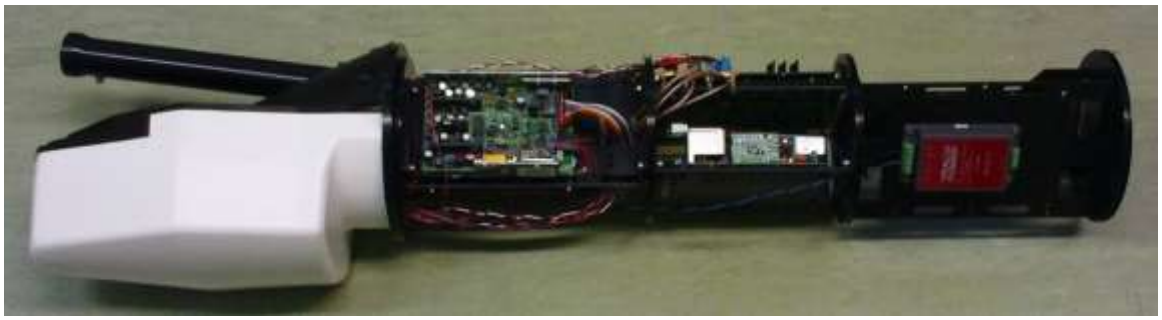

Figure 1-12: SID3.

Figure 1-13: SID3 on aircraft.

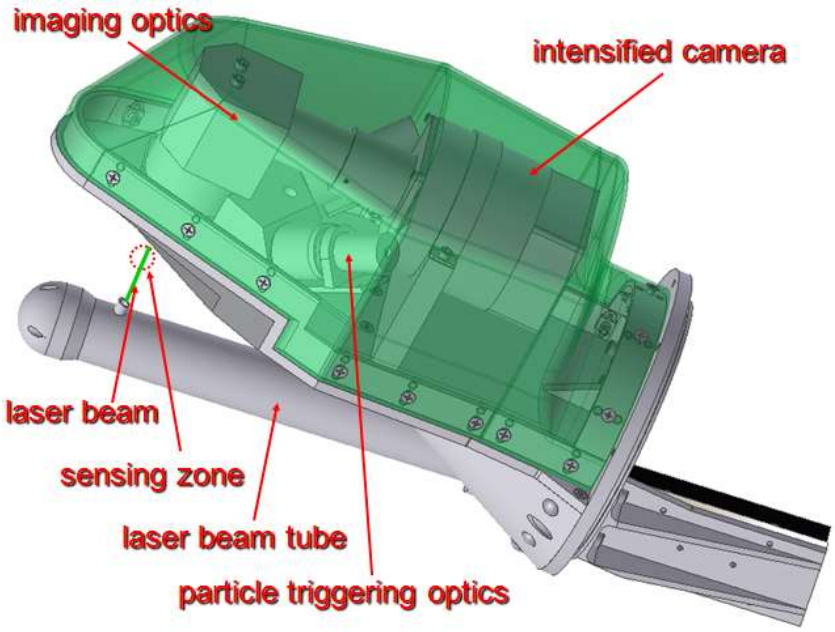

Figure 1-14: SID3 - close-up of head.

When the ice particle enters the sensing zone of SID3 (see Figure 1-14) a laser beam illuminates the particle, the light scattered travels through the optics and then reaches an intensified camera capable of taking a high-resolution image of the light scattered. Figure 1-15 shows typical SID3 2D scattering patterns (left) obtained when the scatterer is a hexagonal column and plate respectively (right).

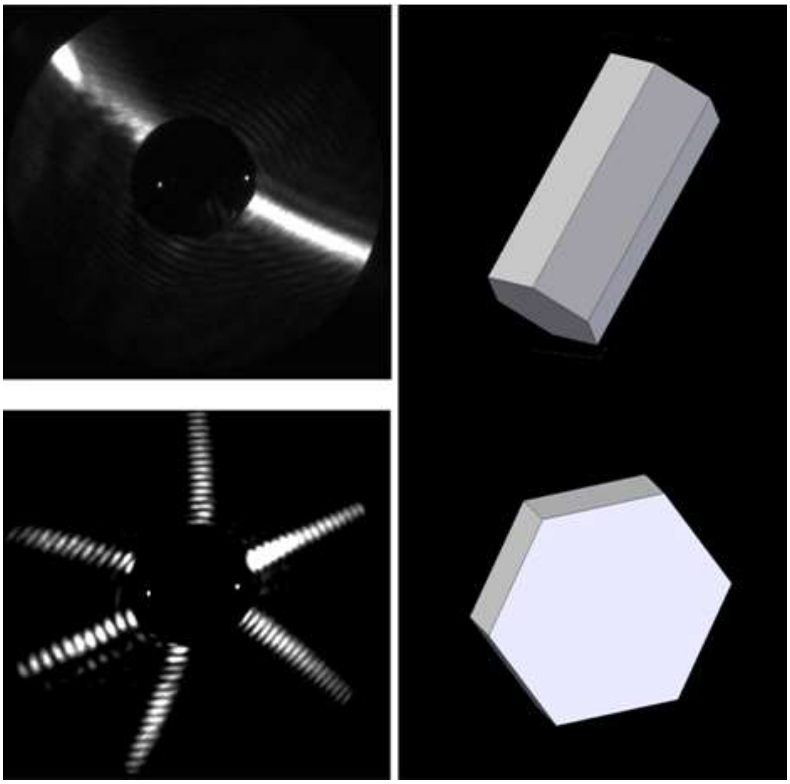

Figure 1-15: In situ 2D scattering patterns, from hexagonal column (top) and plate (bottom).

It is thanks to the modelling of light scattering from single particle that it is then possible to interpret the observed scattering pattern and associate it to the corresponding particle geometry. Some of the most common methods used for the modelling of light scattering will be covered in the coming paragraph.

1.3.4 Single ice crystals - modelling

Modelling the light scattering from single particles is essential if a correct interpretation of the observations is needed. The fact that the ice crystals found in cirrus are highly non spherical makes it very challenging. The Lorentz-Mie theory applies only to spherical particles and therefore over the last thirty years significant effort has been put into modelling light-scattering from non-spherical scatterers. The ray tracing approach applied in geometric optics has been used since the seventies (48) (49). Conventional geometric optics is based on the principle of localization which is applicable only to particles larger than the incident wavelength. Ameliorations have been achieved with the inclusion of diffraction, such as in improved geometric optics methods (50) or Ray Tracing with Diffraction on Facets (RTDF) (51) (52) (53) (54). These methods can incorporate the edge effect, which accounts for rays travelling tangentially and around the particle, and fundamental electromagnetic theories which lead to better results in the far field zone. They also allow illustrating that the halo peaks broaden and eventually disappear as the size parameter decreases, and in general compare better with exact calculations especially when it comes to single scattering properties such as extinction efficiency and phase matrix elements (50). The finite-difference time domain (FDTD) (55) (56) (57) is a numerical method in which the single particle is assumed to be enclosed in an absorbing boundary box and the electromagnetic fields are discretized over grid cells that individually contribute to the total scattered field, obtained as superimposition of the incident and scattered one (see Figure 1-16).

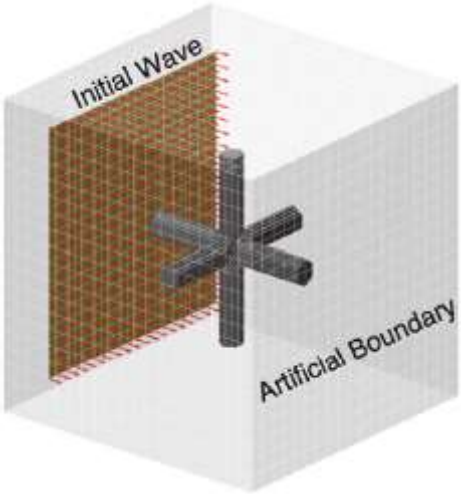

Figure 1-16: Conceptual FTDT diagram for the computation of the scattering of an electromagnetic wave by a non-spherical bullet rosette ice crystal (50).

Another approach which provides numerically exact solutions is the pseudo-spectral time domain method (PSTD) (58) (59) (60) which leads to modelling the optical properties of ice crystals by means of numerical integrations. As alternative to the aforementioned techniques the discrete dipole approximation (DDA) (61) assumes a particle to be a finite array of dipoles which respond to the incident wave front by emitting secondary radiation in turn interacting with the nearest neighbours (see Figure 1-17).

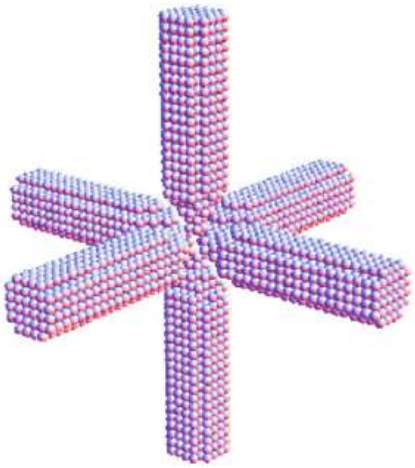

Figure 1-17: Schematic geometry to illustrate the approximation of a bullet rosette in terms of discretized dipoles (50).

DDA as opposed to FDTD and PSTD derives field solutions in the frequency domain. If on one hand FDTD, PSTD and DDA have comparable accuracy, on the other hand they are quite different in terms of computational efficiency. For refractive index smaller than 1.4 DDA was found to be faster than FDTD (62). For a given size parameter, there exist a certain index of refraction, over which PSTD results to be faster than DDA (63). Analogously for a fixed refraction index there is a certain size parameter over which PSTD is faster than DDA (64). In general FDTD and PSTD methods are considered preferable over DDA when it comes to particles with refractive index larger than 2. Often employed as accurate reference to assess numerical methods such as DDA and FDTD, the T-matrix method expands the scattered and incident waves into vector spherical wave functions. T matrix was first introduced in the 1965 (65) and then improved by several successive works (66) (67). In virtue of the linearity of Maxwell's equations is the T-matrix which links the scattered to the incident field. The T-matrix contains all the necessary information to derive the single scattering properties. There exists more than one method for deriving the T-matrix such as the extended boundary conditions method (EBCM), the null-field method with discrete sources, the generalized point-matching method, the superposition method, the discrete-dipole moment method for instance (50). The T-matrix method is in general computationally more efficient than DDA, FDTD and PSTD thanks to the independence of the T-matrix from the orientation of the particle with respect to the incident wave.
Modelling of light scattering is fundamental when it comes to interpret observed scattering patterns. Analogously to the interpretation of in-situ measures, the inverse problem is crucial to retrieve cloud optical properties from satellite remote sensed radiometric and polarimetric observations. These will be discussed in the coming paragraph.

1.3.5 Ice clouds - satellite remote sensing

Satellite observations are the best choice to determine ice clouds properties over large spatial and temporal scales. Parameters such as cloud top pressure, temperature, altitude and ice water path (IWP) have to be determined in order to characterize cirrus. IWP can be estimated from the effective ice particle size (EPS) and cloud optical thickness (COT). The effective particle radius can be inferred for a given particle size distribution by averaging over the ice habits. Among the most relevant satellite born instruments it is worth to mention the Advanced Very High Resolution Radiometer (AVHRR) imagers, the Moderate Resolution Imaging Spectroradiometer (MODIS), the Visible Infrared Imaging Radiometer Suite (VIIRS), the Cloud Aerosol Lidar with Orthogonal Polarization (CALIOP) and the Polarization and Anisotropy of Reflectances for Atmospheric Sciences coupled with Observations

from a Lidar (PARASOL) (50). Ice cloud characterization from satellite remote sensing is generally obtained through three different techniques:

1. **the solar-band based technique**
2. **the infrared-band based technique**
3. **and the polarization-based technique**

The solar and infrared band based cloud bulk scattering properties used in remote sensing applications are the extinction and scattering efficiencies, the single scattering albedo, the asymmetry factor and the phase matrix (68). Solar reflectance observed at a weakly absorbing wavelength (0.87 μm) is sensitive to COT whereas over a moderately absorbing wavelength (2.25 μm) it is sensitive to both COT and EPS. By comparison with look-up tables providing reflectances for varying COT and EPS it is possible to retrieve the cloud optical properties. In this respect radiative transfer calculations are essential for such purpose. They have to lead to consistent retrievals over the electromagnetic spectrum in particular from visible through to the infrared region. It is important to point out that the solar band based technique is not satisfactory for COT<1, it is limited to daytime, uncertainties are larger at high solar zenith angles and clouds have to be uniformly illuminated. An alternative way to infer COT and EPS is provided by the radiative properties of the near infrared 1.38 μm channel. At this wavelength water vapour is highly absorbing and therefore cloud reflectance is poorly contaminated by surface and lower clouds emission and it undergoes only little attenuation to reach the sensor. An additional advantage coming from using the infrared band based technique is that over this region of the spectrum, where absorption becomes dominant over scattering, sensitivity to ice crystal habit decreases. Observed ice absorption over two wavelengths (for instance 11μm-12μm) allows to retrieve COT and EPS by comparing the observations to simulated brightness temperature differences. This method provides good results only for COT<6 and is more sensitive to small particles (effective diameter < 50μm). However it is less sensitive to the modelled ice habit than the solar band based technique. Regardless of the technique used and the corresponding wavelength observed consistency in the inferred optical properties has to be achieved. Lidar and polarimetry provide global high resolution vertical profiles of clouds and aerosol. The attenuated depolarization ratio and backscatter coefficient have been found to be useful in discriminating horizontally and randomly oriented planar ice crystals (69). Active remote sensing techniques provide an useful means to validate passive sensors retrievals. PARASOL observed polarized reflectivities are sensitive to particle habit (70) and have become an important reference for light scattering modelling (71) (33). They have been used to infer ice particle habit and surface roughness (72). The introduction of surface texture in the ice particle habit model has brought calculations to better compare with observations (see Figure 1-18). However it is still necessary to improve the models if a better representation of the polarization properties of ice clouds has to be achieved. This is not trivial as the inclusion in the crystal model of enhanced complexities such as air bubbles, fractures and roughness makes light scattering and radiative transfer calculations more and more challenging. Some of the most relevant studies concerning ice crystal roughness will be briefly discussed in the coming paragraph.

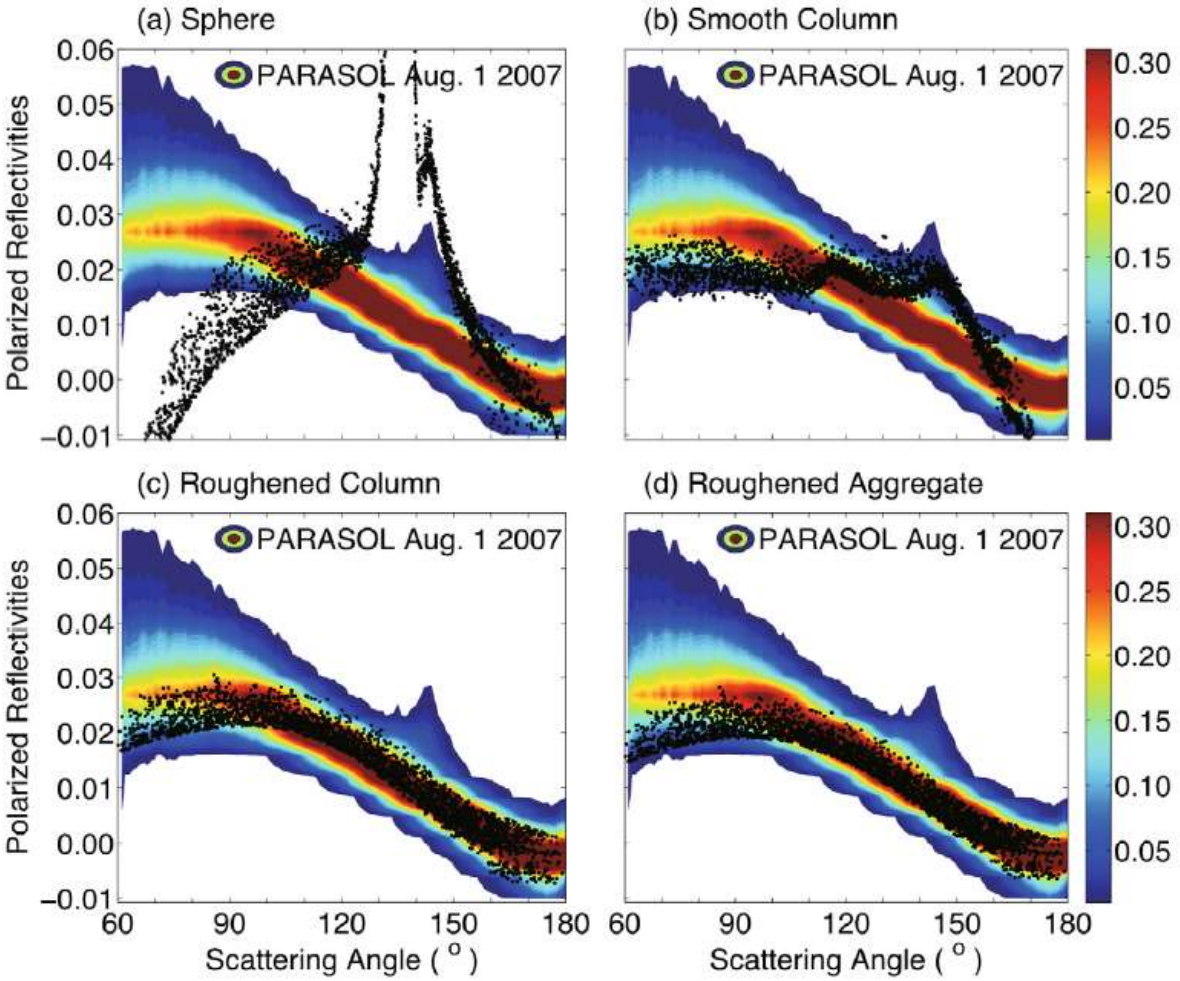

Figure 1-18: Comparison of normalized polarized reflectivities obtained from one day of PARASOL data over ocean in the color contour to numerical results based on different ice crystal habit models: (a) sphere; (b) smooth hexagonal column; (c) roughened hexagonal column; and(d) roughened aggregate (50).

1.3.6 Ice crystal roughness

The ice cloud optical properties parameterization is fundamental in numerical weather prediction (NWP) and general circulation models (GCMs). Significant discrepancies are still in place in the modelling of cloud radiative effects for different parameterization schemes. In one of the latest parameterizations proposed (73) the bulk properties of ice clouds are parameterized as a function of wavelength and ice water content (IWC) by assuming a mix habit model. Using a specific crystal habit such as spheres in place of roughened hexagonal columns leads to substantial differences in the calculations of the global cloud radiative effect. This is due to the significant difference in the asymmetry parameter (*g*) obtained with the two parameterizations. This remarks once more the importance of using appropriate representations of the optical and microphysical properties of ice clouds. Including crystal roughness in the habit model is a way to improve on this. Evidence of crystal shape complexity has increased thanks to the studies conducted over the last ten years. Back in 2006 single ice crystal angular scattering intensities were observed by means of the airborne polar Nephelometer in the southern mid-latitudes (74). Evidence of substantial ice crystal roughness and internal inclusions were apparent. Analogously high ice crystal irregularity is suggested by observations of cirrus radiances which show featureless phase functions inconsistent with idealized

geometries (75) (76). Similarly, the majority of the ice particles observed in mid-latitude stratiform clouds take on highly irregular shapes (77). Best fit to polarized reflectances from PARASOL (78), space borne depolarization LIDAR measurements (68) and Arctic ice cloud data (79) are obtained by accounting for roughness in the modelling of the ice crystal habit. Single scattering patterns obtained from electro-dynamically levitated sodium fluorosilicate ice analogues have also been investigated (42). Ice analogues, rough and smooth, randomly oriented in an electro-dynamic balance (see Figure 1-19) were illuminated by a laser beam. A fibre-optics laser diffractometer was used to measure the light scattered between 3^o and 177^o while a linear photodiode array measured the light intensity collected between 0.5^o and 5^o.

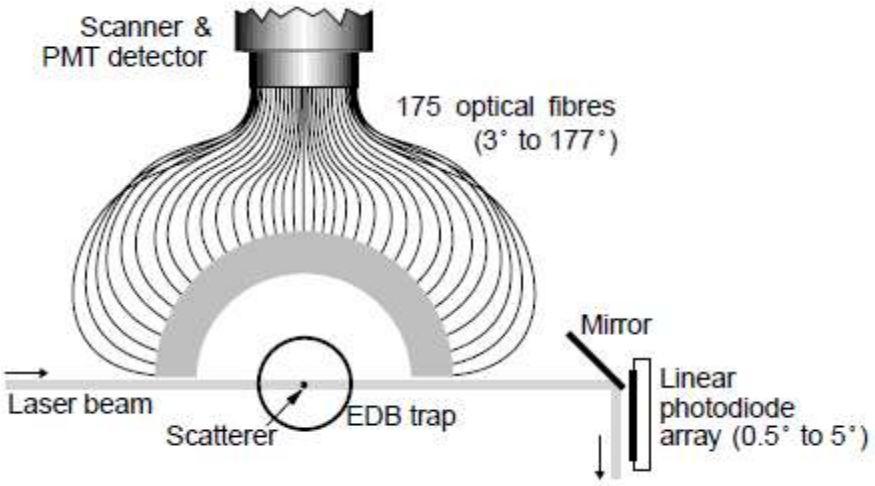

Figure 1-19: Experimental setup for measuring light scattering from levitated crystals (42).

Scattering phase function and degree of linear polarization were obtained for smooth and rough ice aggregates and rosettes. The asymmetry parameter was measured after having extrapolated the phase function for scattering angles smaller than 0.5^o. It was done analytically either by using the Lorenz-Mie theory (for some aggregates) or the Fraunhofer diffraction for highly non spherical particles (five branched rosette). The comparison of the phase functions of smooth and rough particles shows significant differences (see Figure 1-20). Smooth ice analogues give rise to enhanced forward scattering while rough crystals to larger side and back-scattering. Featureless scattering phase functions and lower (than the one obtained from their smooth counterparts) asymmetry parameter are associated to rough particles. This is consistent with the low asymmetry parameter observed in ice clouds by Garret et al. (80) and suggests that roughness may account for the rarity of ice halos observed (29). 2D scattering patterns also were observed (see Figure 1-21). They were obtained by recording through digital CCD camera the angular distribution of light scattered by single hexagonal column analogues glued on a thin carbon fibre. The light source was a 612 nm wavelength He-Ne laser. The 2D scattering patterns from smooth and rough analogues are significantly different. The smooth rosette shows azimuthal scattering pattern highly asymmetric as opposite to its rough counterpart and the light peaks associated to its arms are quite evident. 2D scattering patterns associated to rough particles exhibit a "speckle" pattern. The distinguishing features observed in the 2D scattering patterns together with those associated with the degree of linear polarization between 20^o and 35^o provide information on surface roughness.

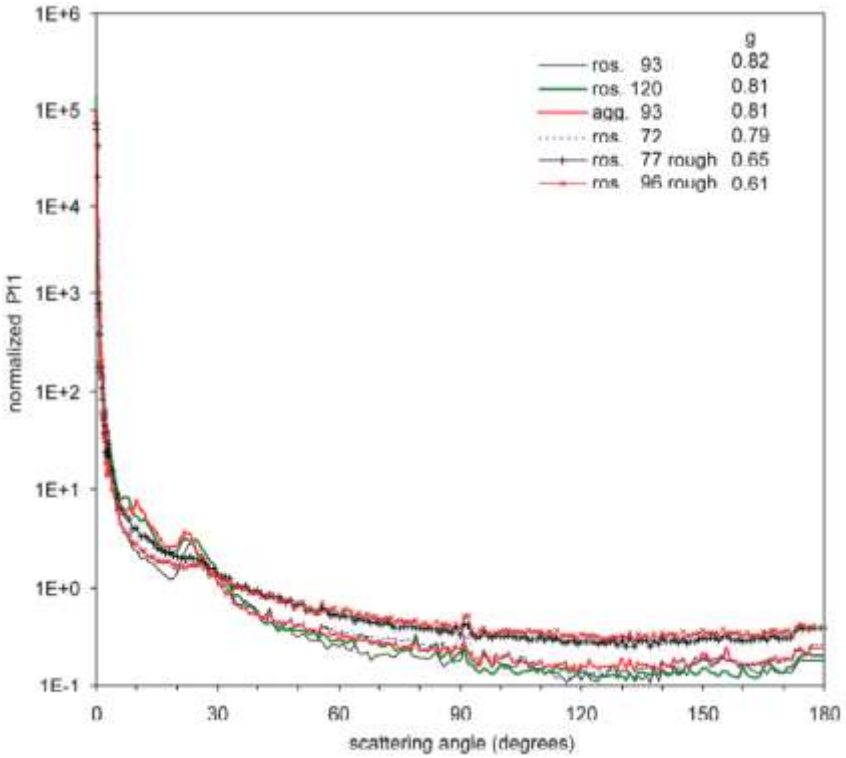

Figure 1-20: Normalized phase functions for the ice-analogues aggregate and five rosette, including two rough ones, at 514.5nm wavelength, in random orientation. The maximum dimension of each crystal in micrometers and the value of the asymmetry parameter g are shown in the legend (42).

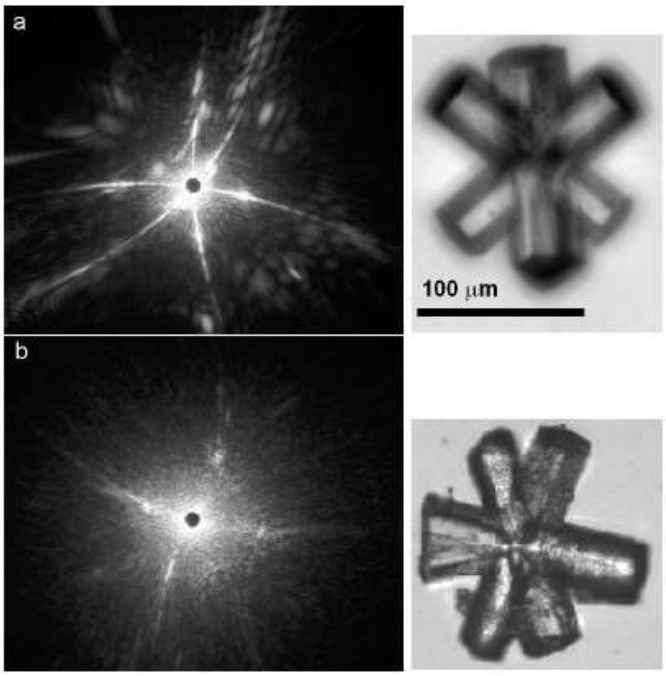

Figure 1-21: Scattering pattern from: (a) smooth 145μm 6-arm rosette, (b) 160 μm rough rosette (42).

Due to the optical limitations and the ice crystal shattering affecting traditional in situ probes only little is known about the surface texture of the particles composing ice clouds. It has to be quantified in virtue of the implications that it has on the radiative properties of the ice clouds. SID3 represents an example of a new generation probe which circumvents these issues. For the first time it provided in situ 2D light scattering patterns which by comparison with modelled ones, for example obtained through Ray Tracing with Diffraction of Facets (RTDF) (51) (81), allows discriminating ice crystals in terms of shape, size, orientation and roughness (42) (82). In situ cloud data were collected during the UK Met office CONSTRAIN campaign which took place in Scotland and south-eastern England between January and September 2010. The 2D scattering patterns analysed were from cirrus and mixed phase clouds. Five days back-trajectories allowed establishing the origin of the air masses. The open geometry of SID3 guarantees that shattering of ice crystals is negligible. The 2D patterns covered scattering angles ranging from 6^o to 25^o sufficient to observe the 22^o halo. The observed 2D patterns were compared to those obtained from test particles made in lab (see Figure 1-22) at varying level of roughness. Particle size was obtained from speckle analysis based on the fact that it is inversely proportional to the speckle area (45). Pattern texture measures were used to quantify roughness in both lab and in situ samples. Also the halo ratio (HR), which is the ratio of the light scattered at 22^o to the one scattered at 18.5^o, was measured. HR is a quantitative criterion for the occurrence of the 22^o halo and a measure of the regularity of the ice crystals. From the entire data set analysed frequency distribution of roughness measures were obtained. It turned out that most of the ice crystals observed were mostly highly irregular, complex and at times showing levels of roughness even larger than the roughest test particle available. HR was found to be negatively correlated with crystal roughness (see Figure 1-23) reinforcing the expectation that HR is positively correlated with the asymmetry parameter (83) (84). Lower roughness was observed and associated to the single case of continental cirrus examined. This suggests that higher concentration of ice nuclei may lead to lower roughness consistently with the reduction of homogeneous nucleation which, on the other hand, could potentially lead to higher complexity (85). The decreased reflectivity of smoother particles, observed in continental cirrus, arises doubts over the idea that ice nuclei seeding may favour a change of climate.

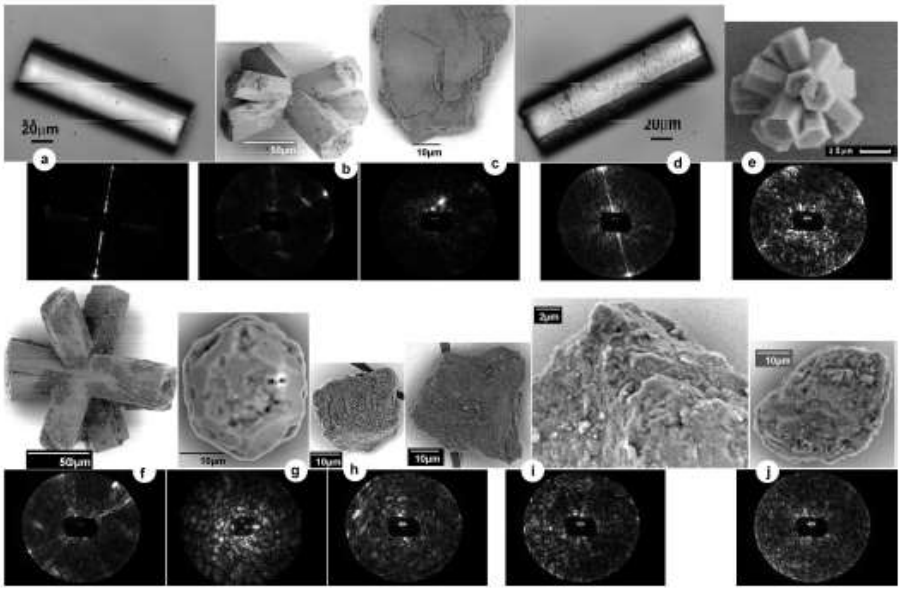

Figure 1-22: Upper rows: images of test particles from optical microscopy (ice analogue columns (a) and (d) only) or SEM, with size scales shown in insets – note that the magnifications vary; the dust grain (i) is shown in two magnifications. Lower rows: corresponding SID-3 scattering patterns.

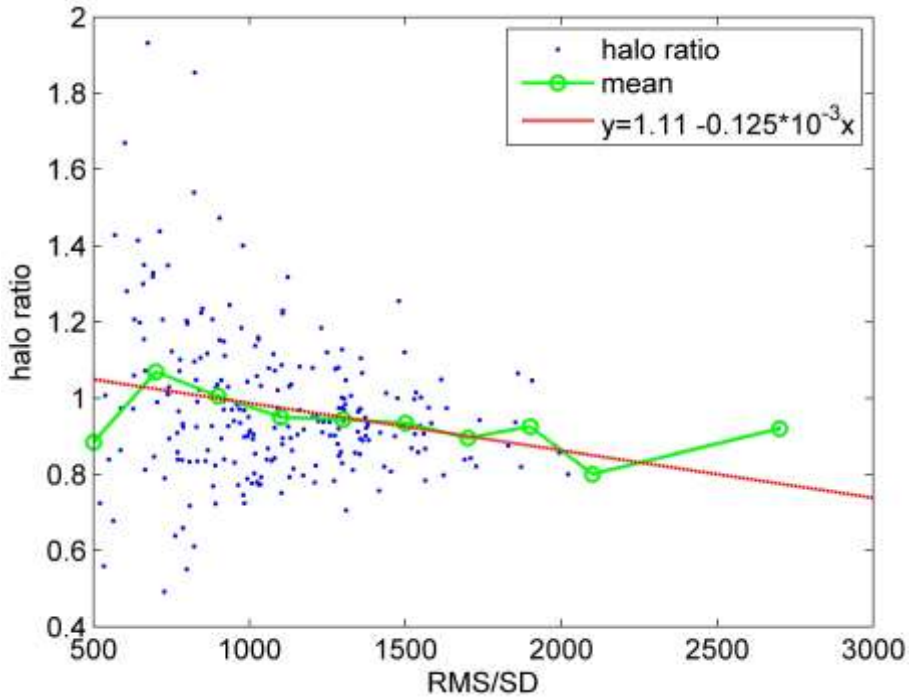

Figure 1-23: Halo ratio plotted against particle roughness measure RMS/SD, both determined from SID-3 patterns obtained in cirrus formed in marine air masses. Mean halo ratio calculated for fixed roughness intervals, and a least-squares regression line (coefficients) given in the legend) are also shown. The correlation coefficient was −0.22, significant at the 0.1% level, based on 239 data points.

If the existence of negative correlation between crystal roughness and asymmetry parameter were to be confirmed from future investigations, it would have important implications for climate modelling. It would improve our knowledge of cirrus which in turn would enhance our capability to quantify their impact on climate or in other words to reduce the uncertainty associated with the current NWPs and GCMs, by correctly representing the optical and microphysical properties of ice clouds in light scattering calculations.

Before we start tackling the problem of ground based cirrus detection, atmospheric absorption due to molecules and how it relates to the transmission properties of the atmosphere have to be discussed. This will be done in the coming paragraph 1.4.1. Particles contribution to absorption will be discussed in paragraph 1.4.2. In order to show analogies between molecular absorption and scattering and how they relate to each other the latter will be covered in paragraph 6.2 of the appendix. Paragraph 1.5 will begin with a short introduction to black-body radiation and how it relates to atmospheric emission. A short review of the observations of down welling thermal radiation under clear and cloudy skies and the implications for cirrus detection will then follow.

1.4 Atmospheric absorption

1.4.1 Absorption by molecules

When a beam of radiation interacts with a molecule, if the energy of the beam's photons is equal to the difference of energy between two atomic or molecular states the photon is absorbed and the molecule is excited to a higher energy quantum state. Similarly the same atom or molecule can be induced to emit radiation by decaying to a lower energy level. This process is called stimulated

emission. Also spontaneous emission can take place. Absorption and induced emission are opposite processes. All of these processes have to be in principle accounted for when measuring the net energy exchange. In general a molecule can undergo three types of energy transitions: electronic, rotational and vibrational. The energy levels of a molecule depend on the molecule structure and on the interactions it has with its neighbours. If E1 and E2 identify the energies of two energy states that a molecule can be found at, the frequency of the emitted photon is:

$$\upsilon_0 = \frac{E_1 - E_2}{h} \tag{1.16}$$

Given that a molecule is never isolated but always interacting with its neighbours and in motion the width of the line shape around ν_0 is never identically zero. While Doppler broadening is stronger at higher altitudes, in the lower layers of the atmosphere molecule interactions become dominant. Because of these two mechanisms molecules will reemit from perturbed energy states that give rise to the line broadening. Assuming a gas as a collection of identical molecules each with the same perturbed energy levels is a reasonable approximation because inter-molecule interactions are not as strong as they are in liquids and solids. It is also for this reason that for a gas it is possible to retrieve the absorption coefficient from the properties of the single molecule, bearing in mind that like temperature and pressure the absorption coefficient is a statistical quantity obtained as the average over an ensemble of molecules. Let us assume that a directional, monochromatic beam of irradiance *I* hits a single molecule. Part of the energy conveyed is absorbed, which means that it is transformed into other forms at a rate W_a proportional to *I*. Given that *I* has power per square metres unit and W_a is a power, the proportionality constant has to have units of area. The rate at which power is absorbed by the molecule is:

$$W_a = \sigma_a I \tag{1.17}$$

Where σ_a is the absorption cross section which is also the effective molecule's area that removes energy from the incident beam. Generally the absorption cross section is several orders of magnitude smaller than the actual geometric size of atmospheric molecules. Let us consider a thin slab of area *A* and thickness Δx filled with a gas populated by *N* identical molecules (per unit volume), each one with absorption cross section σ_a. Let a mono-chromatic beam hit normally to the faces of the slab. The decrease in transmitted power over the distance Δx is:

$$A\Delta I = -I\sigma_a NA\Delta x \tag{1.18}$$

As a consequence

$$\Delta I = -I\sigma_a N\Delta x = -Ik\Delta x \tag{1.19}$$

where *k* is the absorption coefficient, the product of the absorption cross section and the number concentration of molecules in the gas (see Eq. 1.20).

$$k = N\sigma_a \tag{1.20}$$

Even if all the molecules are identical they are not all oriented in the same way, therefore Eq. 1.20) should in general be rewritten as:

$$k = \sum_j N_j \sigma_{a,j} \tag{1.21}$$

where the sum is done over all possible orientations.
If the beam is assumed incoherent, interference can be neglected and if the molecules are randomly oriented the absorption coefficient is independent from the polarization. It can be shown that the irradiance *I* travelling through the slab of gas undergoes an attenuation due to absorption by molecules well represented by the law of the exponential decay:

$$I = I_0 e^{-kx} \tag{1.22}$$

It is worth noting that Eq. 1.22 is valid as long as the position of the molecules is not correlated or in other words it applies to a random distribution of absorbers.

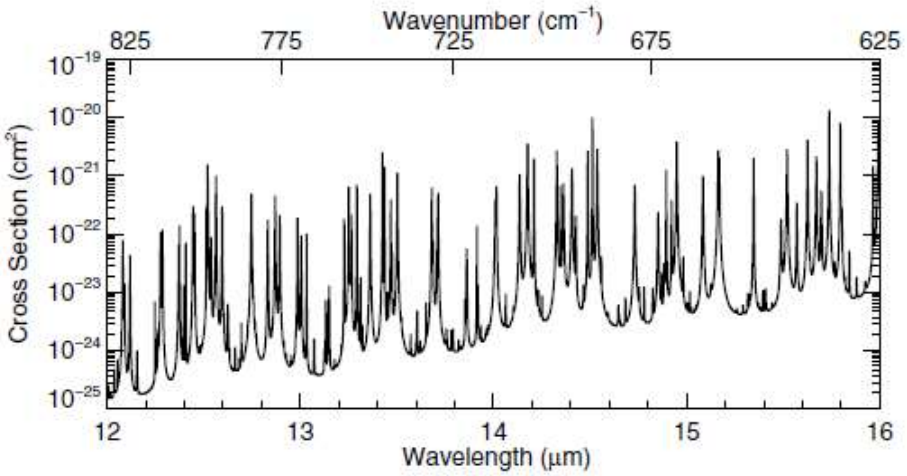

Figure 1-24: Absorption cross section of a water molecule for a temperature of 20°C and a total pressure of 1 Atmosphere. Copied from (86).

The absorption cross section of water vapour (see Figure 1-24) varies several orders of magnitude over the range of infrared frequencies. The peaks in the absorption cross section are found at those frequencies where the molecule absorbs the most. The origin of the absorption lines can be derived by classical physics principles. In fact, although a molecule is composed of an equal amount of positively and negatively charged particles that make it neutral, the centre of the negative electronic cloud and the centre of the positive charges might not coincide. This can be due to the molecular structure itself (permanent dipole) or to an external exciting field (induced dipole).
For a slab atmosphere (see Figure 1-25) of thickness *h* the emissivity ε along a path *s* making an angle ϑ with respect to zenith is given by Eq. 1.23

$$\varepsilon = 1 - e^{-kh/\cos\vartheta} \tag{1.23}$$

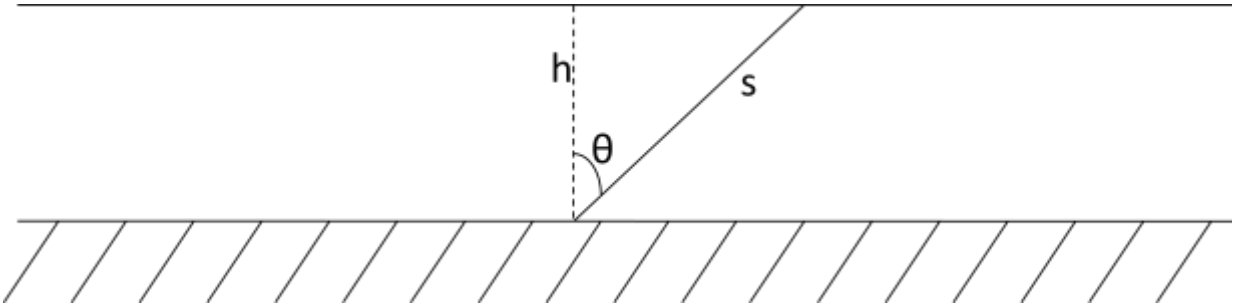

Figure 1-25: Slab atmosphere of thickness *h* and a path *s* making an angle *ϑ* with zenith.

If we take into account Eq. 1.20), the emissivity of a uniform layer of moist air of thickness *h*, along the vertical path becomes:

$$\varepsilon = 1 - e^{-Nh\sigma_a} \tag{1.24}$$

The term *Nh* can be rewritten as in Eq. 1.25 where the multiplicative factor, which is the number of liquid molecules per unit volume, has units of m^{-3}

$$Nh = \frac{\rho_w d}{m_w} = 3.3 \cdot 10^{28} \cdot d \tag{1.25}$$

where:

1. **ρ_w=10^3 Kg/m^3 is the density of liquid water**
2. **m_w=3*10^{-26} Kg is the mass of a water molecule**
3. ***d* is the precipitable water vapour (PWV) or in other words the thickness of the water layer that would be obtained if all the molecules of moist air were to condense. Notice that the integrated water vapour (IWV) which is the column integrated WV, the quantity that we measure with the GPS station discussed in section 3.3.2, when expressed in kg/m^2 is numerically equivalent to the PWV expressed in mm of liquid water.**

The argument in the exponential is the absorption optical thickness and the spectral dependence of the atmospheric emissivity arises from the absorption cross section of the water molecule.
The atmospheric transmission is calculated as the integral over the entire atmospheric column of the negative exponential of the absorption coefficient:

$$Tr = \int_0^{x'} e^{-k(x)} dx \tag{1.26}$$

In addition to the electronic, rotational and vibrational energy levels, the absorption coefficient depends on the pressure and to a lesser extent the temperature profile because they affect the line shape. In general, the absorption coefficient decreases with increasing temperature because the population of molecules in the lower energetic state decreases whereas the number of molecules in the upper state increases. It also depends on the profile concentration of the atmospheric gases. Figure 1-26 shows some of the most relevant in terms of their absorptive properties. Nitrogen

despite being the most abundant does not contribute significantly to absorption. Gas concentration varies with height.

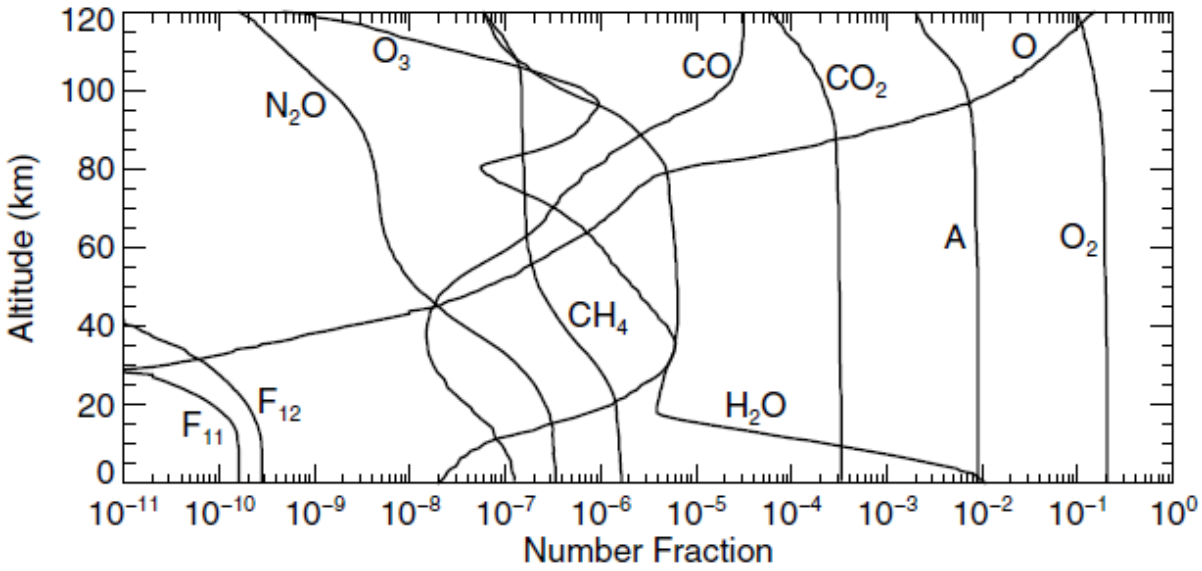

Figure 1-26: Average concentration profiles (expressed as a fraction of the total number density) of various atmospheric molecules. F_{11} and F_{12} denote the chlorinated fluorocarbons Freon-11 and Freon-12. Copied from (86).

In addition to the average air molecules scattering cross section Figure 1-27 (top panel) shows the absorption cross section of some of the most relevant atmospheric molecules. It is obtained as the ratio of the absorption coefficient to the number concentration. The absorption coefficient is calculated through line-by-line radiative transfer code, by dividing the spectrum into small intervals. Given that the lower the pressure the lower the line width, it is the lines corresponding to lowest pressure that determine how to divide the spectrum. The absorption cross section varies hugely with wavelength from ultraviolet through visible and infrared up to the microwave spectral region. By multiplying the number concentration profiles (of all molecular species taking part in the absorption) times the corresponding specie's absorption cross section at a specific wavelength and by summing up over all the species it is possible to obtain a profile of the total absorption coefficient at that specific wavelength. The integration of the negative exponential of the spectral absorption coefficient over the entire atmospheric column is the transmissivity at that specific wavelength. By repeating over the entire spectrum it is possible to obtain the total atmospheric transmissivity shown in Figure 1-28.

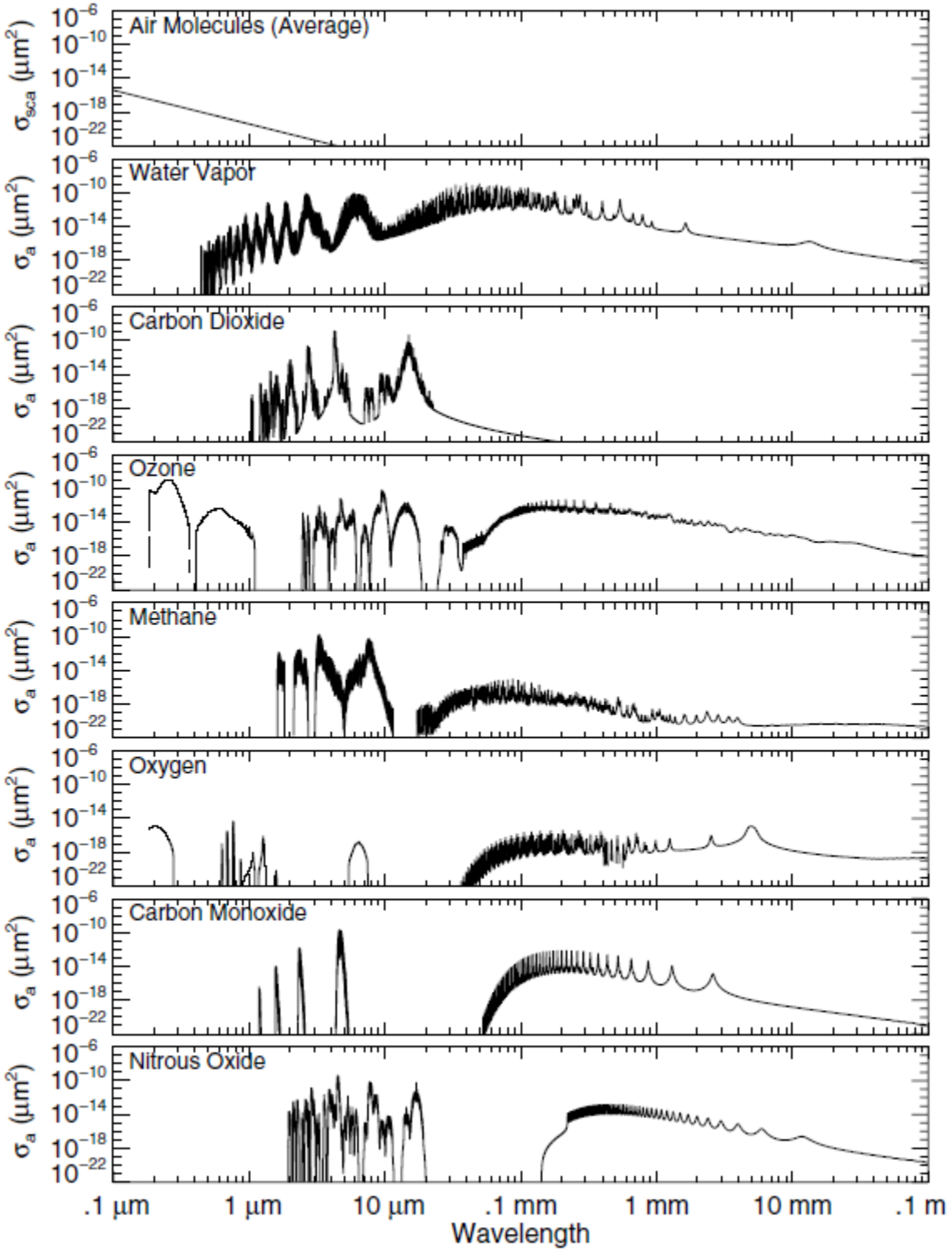

Figure 1-27: Absorption cross section for some of the atmospheric gases most relevant in terms of absorption.

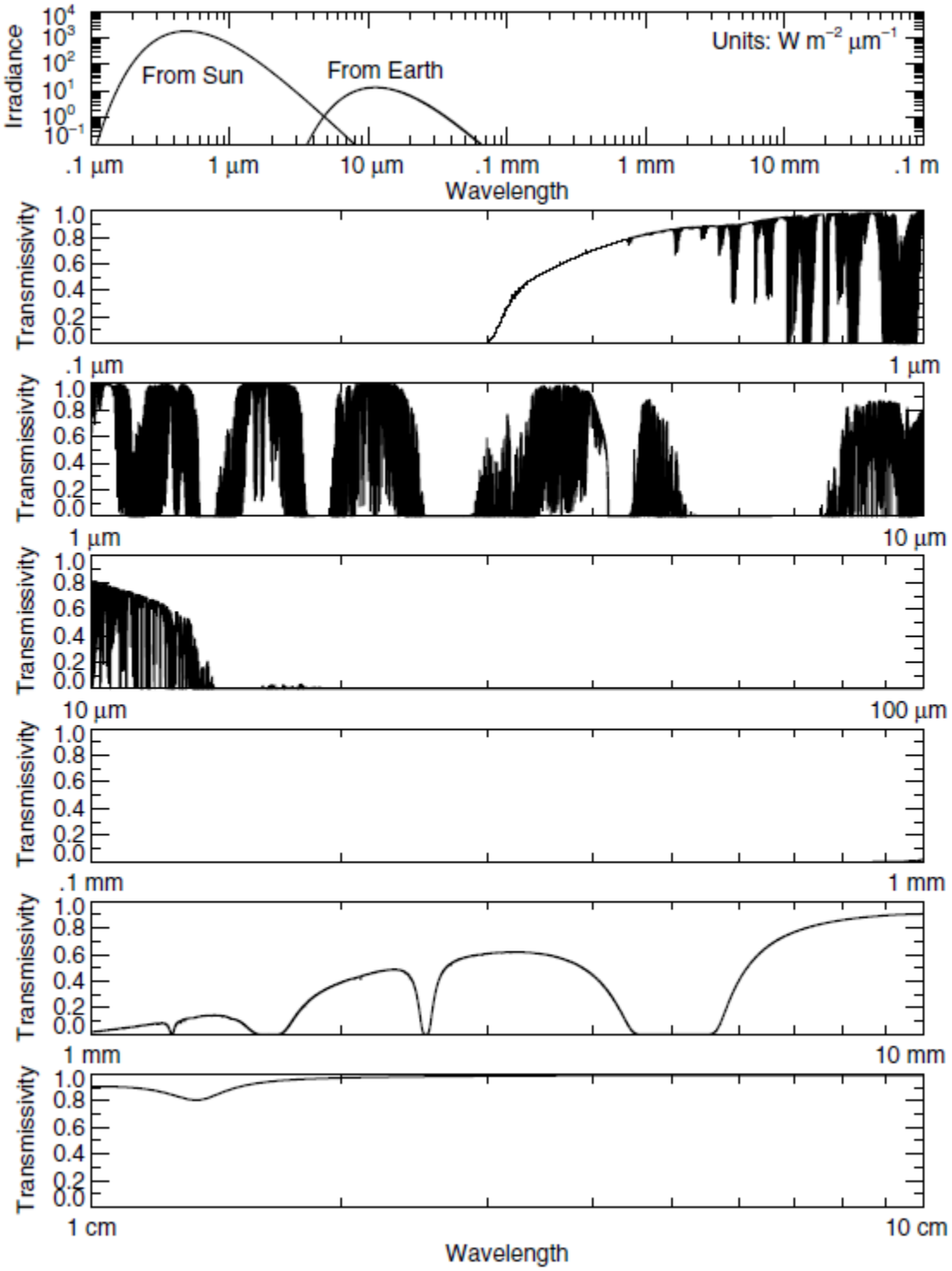

Figure 1-28: Transmissivity along a vertical path through the entire atmosphere. Each panel is one wavelength decade. The top panel shows approximate solar and terrestrial irradiances. Copied from (86).

1.4.2 Absorption by particles

Unlike molecules particles have a definite volume *v*. If C_{abs} identifies the absorption cross section of a particle it is possible to define its *volumetric* cross section. For *N* identical particles per unit volume the absorption coefficient is:

$$k = NC_{abs} = Nv\frac{C_{abs}}{v} = f\frac{C_{abs}}{v} \tag{1.27}$$

where:

1. ***f* is the volume particle fraction, that is the fraction of the total volume occupied by particles**
2. **C_{abs}/v is the volumetric absorption cross section**

For non identical particles it follows that:

$$k = f\left\langle\frac{C_{abs}}{v}\right\rangle \tag{1.28}$$

where the average is done over all possible orientations, sizes and composition.
A simple way of representing a particle is a slab of optically homogenous medium, with thickness *d* and area *A*. Let *λ* be the wavelength of a monochromatic beam hitting normally to the surface *A*. *λ* is assumed to be much smaller than the slab's dimensions which makes interference negligible. For reflections to be negligible we assume that the optical properties of the environment surrounding the slab are similar to the slab's ones.

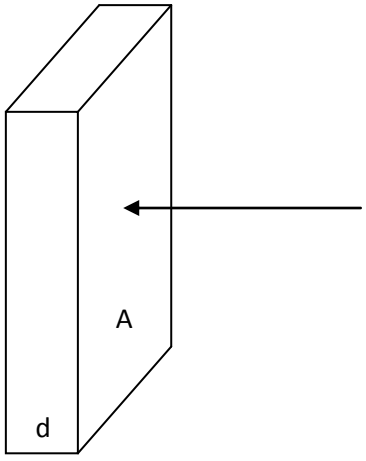

Figure 1-29: Slab of optically homogenous medium.

The rate at which the incident energy is absorbed is:

$$W_a = IA\left(1 - e^{-k_b d}\right) = I\sigma_a \tag{1.29}$$

where k_b is the bulk absorption coefficient.
As a consequence in the regime of weak absorption $k_b d \ll 1$ Eq. 1.29 turns into Eq. 1.30

$$W_a \approx IA(k_b d) \approx I\sigma_a \tag{1.30}$$

From which it follows that

$$Ak_b d \approx \sigma_a \tag{1.31}$$

Therefore for weak absorption the *volumetric* absorption cross section becomes

$$\frac{C_{abs}}{v} = \frac{\sigma_a}{Ad} \approx k_b \tag{1.32}$$

on the other hand in the regime of strong absorption when $k_b d >> 1$ it results

$$\frac{C_{abs}}{v} \approx \frac{1}{d} \tag{1.33}$$

However Eq. 1.28 should be used with caution when it comes to dense particle suspensions. When the particles fill all the space (f=1) the absorption coefficient should approach the bulk coefficient k_b. However, this is not the case in the limit of strong absorption when this is dominated by the particle size according to Eq. 1.33.
This is true in particular for metals and to a lesser extent for quartz and ammonium sulfate, insulating crystalline materials more commonly found in the atmosphere. Interestingly Eq. 1.32 and 1.33 give good approximation for water. When the particle size of water droplets is sufficiently small the volumetric cross section is approximately the bulk absorption coefficient and is independent from the diameter. However as the diameter increases the volumetric cross section decreases as the inverse of d. A more realistic representation of the absorption coefficient for dense gas suspensions (f≈1) would be the one for a porous material for which it holds:

$$k = fk_b \tag{1.34}$$

It is worth noting that absorption spectra of molecules and particles small compared to the wavelength show some similarities which vanish for larger sizes. Despite having completely different origins, weakly absorbing particles whose diameter becomes comparable to the wavelength, exhibit narrow lines in the spectrum, caused by interference, which might resemble a molecular one. Even if a molecule can be thought of as a particle of zero dimensions, it is essentially impossible to obtain the absorption cross section of particles through quantum mechanics.

1.5 Clouds and black body radiation

We are interested in how much radiation is emitted by matter in each wavelength interval, also known as the spectral distribution of radiation. For an ideal gas sealed in a container, held at a fixed temperature T (see Figure 1-30), the distribution of the kinetic energies of the molecules is specified by a probability distribution function $f(E)$ which, like all distribution functions, is defined by its integral properties, that is,

$$\int_{E_1}^{E_2} f(E)dE \tag{1.35}$$

Eq. 1.35 is the fraction of molecules having kinetic energies between any two energies E_1 and E_2

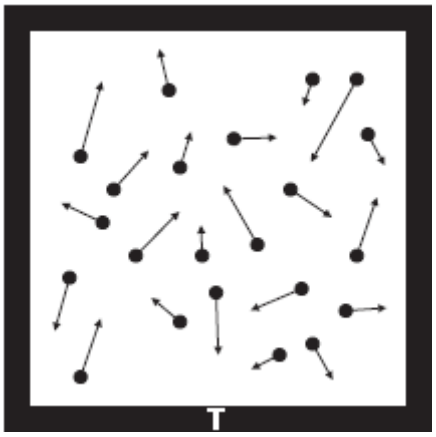

Figure 1-30: At equilibrium, ideal gas molecules in a closed container at absolute temperature T have a distribution of kinetic energies determined solely by this temperature. Copied from (86).

If *f* is continuous from the mean value theorem of integral calculus it results Eq. 1.36 .

$$\int_{E_1}^{E_2} f(E)dE = f(\overline{E})(E_2 - E_1) \tag{1.36}$$

where $\overline{E}$ lies in the interval (E_2,E_1) and if we substitute E_1 with E and E_2 with $E+\Delta E$ we have Eq. 1.37

$$f(E) = \left(\frac{1}{\Delta E}\right)\int_{E}^{E+\Delta E} f(x)dx \tag{1.37}$$

f(*E*) is often called *probability density. f*(*E*) is zero if the limits of the integral are the same which is consistent with the fact that the probability that a continuous variable takes on exactly a particular value over the range on which it is defined must be zero. *f*(*E*)Δ*E* is *approximately* the fraction of molecules lying between *E* and *E*+Δ*E* where the approximation gets better the smaller the value of Δ*E*. Gases within a sealed container held at temperature T evolve to an equilibrium state determined solely by this temperature. In this state the distribution function for molecular kinetic energies is the *Maxwell-Boltzmann distribution* (see Eq. 1.38).

$$f(E) = \left(\frac{2(E)^{\frac{1}{2}}}{(\pi)^{\frac{1}{2}}(k_b T)^{\frac{3}{2}}}\right)\exp\left(-\frac{E}{k_b T}\right) \tag{1.38}$$

where

1. k_b **is the Boltzmann's constant**

and *f* is normalized such that:

$$\int_{0}^{\infty} f(E)dE = 1 \tag{1.39}$$

Because matter continuously emits radiation, a container with walls so thick that no photons leak from it will fill with a gas of photons (see Figure 1-31). At equilibrium photons have not all the same energy and frequency but are distributed about a most probable value.

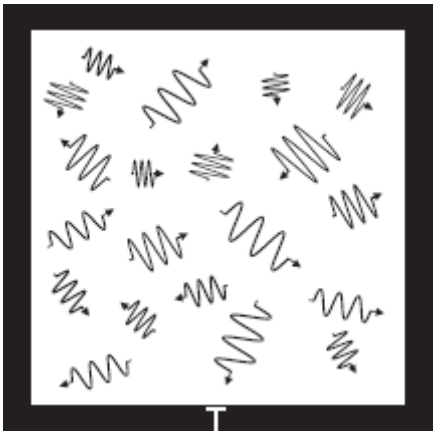

Figure 1-31: An opaque container at absolute temperature T encloses a gas of photons emitted by its walls. At equilibrium, the distribution of photons energies is solely determined by this temperature. Copied from (86).

Imagine a plane surface (*S*) in the container (see Figure 1-32) held at a fixed temperature *T*.

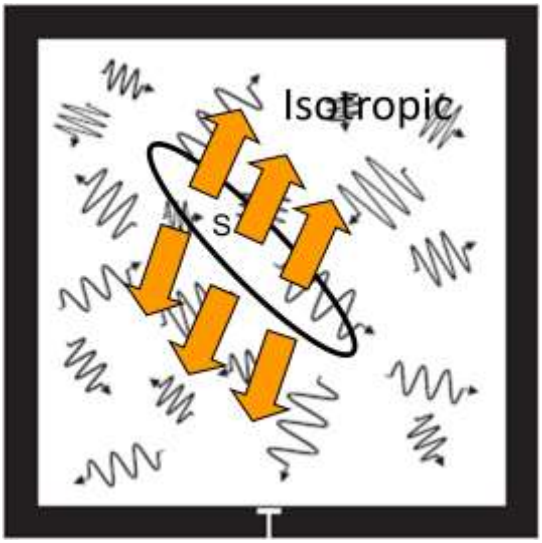

Figure 1-32: as Figure 1-31 but including a plane surface.

At equilibrium, the radiation field is isotropic, so regardless of how the surface is oriented the same amount of radiant energy crosses unit area in unit time. We consider only that radiant energy (photons) propagating in a hemisphere of directions either above or below the surface. The energy distribution function (or spectral distribution) is given by the Planck distribution or Planck function (see Eq. 1.40) (86)

$$P(\omega) = \frac{\hbar\omega^3}{4\pi^2 c^2} \frac{1}{e^{\frac{\hbar\omega}{k_b T}} - 1} \tag{1.40}$$

where

1. ***ω* angular frequency**
2. ***c* speed of light**
3. $\hbar$ **Planck's constant over 2π**
4. k_b **Boltzmann's constant**
5. ***T* temperature**

Eq. 1.40 can also be seen as the spectral radiance (*R*) emitted by a body, in thermal equilibrium, at a given temperature and wavelength. It can be rewritten as a function of wavelength (*λ*) (see Eq. 1.41) after the necessary change of variable (see Eq. 1.42)

$$R(\lambda) = \frac{2\,\pi\,h\,c^2}{\lambda^5} \frac{1}{e^{\frac{hc}{\lambda k_b T}} - 1} \tag{1.41}$$

1. ***λ wavelength***
2. ***h Plank's constant***

$$\int_{\omega_1}^{\omega_2} P(\omega) d\omega = \int_{\lambda_1}^{\lambda_2} P\{\omega(\lambda)\} \frac{d\omega}{d\lambda} d\lambda \tag{1.42}$$

A section specifically dedicated to the concept of radiance has been included in the appendix 6.1 for further details.
The higher the black body temperature *T*, the shorter the wavelength *λ* that the Planck's distribution peaks at (see Figure 1-33).

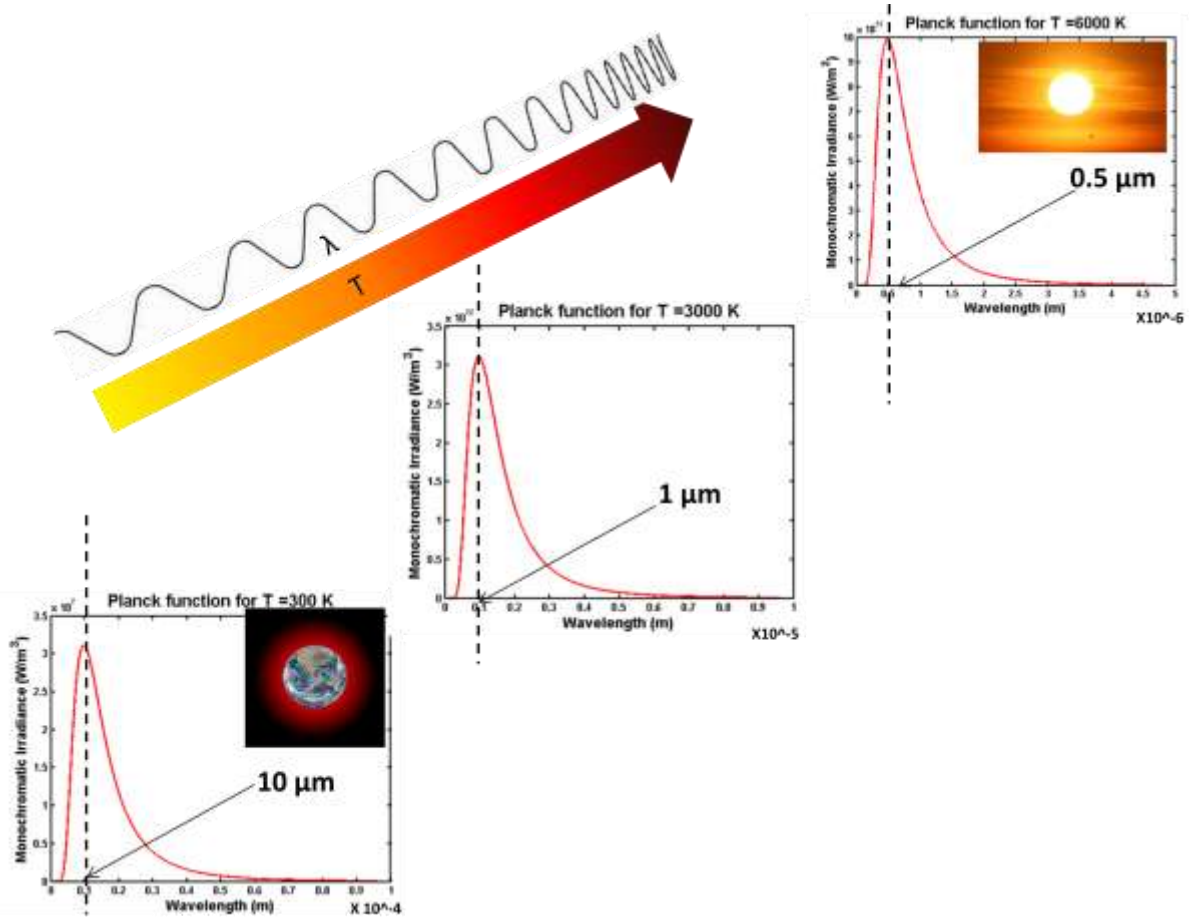

Figure 1-33: Black body curve peak shifts to smaller wavelengths for higher T.

In its more general form the right side of Eq. 1.41 is multiplied by the emissivity (ε_λ) of the radiating object. The emissivity, that is the ratio of the radiance emitted by a body at a given temperature and wavelength to that emitted by a black body at the same temperature, is 1 for a black body and is less than 1 for any real object. If we solve 1.41 for *T* the brightness temperature (BT) at the wavelength λ is obtained. BT is the radiative body temperature, which is a measure of the body radiance at the given wavelength. BT coincides with the physical temperature of a body whose emissivity, at the measuring wavelength, is 1 (a black body). It is an underestimation of the actual physical temperature for emissivity smaller than 1 (a grey body).

Clouds and more in general Earth's atmosphere emit and absorb thermal radiation. One aim of this investigation is detecting cirrus clouds by observing sky thermal emission. Measurements of down-welling thermal radiation (between 4 and 15 µm) were performed already back in the fifties (87) and even earlier (88). An optical device for collecting sky radiation, consisting of an adjustable mirror enabling to point at zenith angle (*z*), allowed comparing sky emission to a reference black body source (close to absolute zero temperature blackbody). A spectrograph was used for dispersing radiation into its spectral components and a thermocouple turned radiant flux differences into a recorder deflection which quantified the sky signal provided that the intensity of the blackbody source emission could be reduced to "zero" (87). By pointing the instrument at zenith, recorder deflections were measured at different wavelengths. The atmosphere is highly absorbing over some portions of the spectrum. The well-known atmospheric CO_2 absorption bands at 15 µm and 4.3 µm, the water vapour (WV) absorption band at 6.3 µm and the ozone absorption band at 9.6 µm appear as minima in the solar spectrum (87). Overlapping absorption bands of WV and CO_2 are associated with the strong peak at 2.7 µm. Rotational absorption lines of WV give rise to the small minima

observed between 10 and 14 µm. Analogously, the minima occurring between 7 and 9 µm are associated with the 6.3 µm vibration-rotation band (87). On a clear day with moderate humidity and ground-level air temperature T_0= 20.0°C, typical zenith sky spectra (see Figure 1-34 - solid line) were obtained. The first thing to notice is that deflection maxima are observed in correspondence of the minima present in the solar spectrum. These deflection maxima are ascribable to the thermal emission of the atmospheric gases. Strong emission bands appear in the sky spectrum at 4.3 µm, 6.3 µm, 9.6 µm and 15 µm.

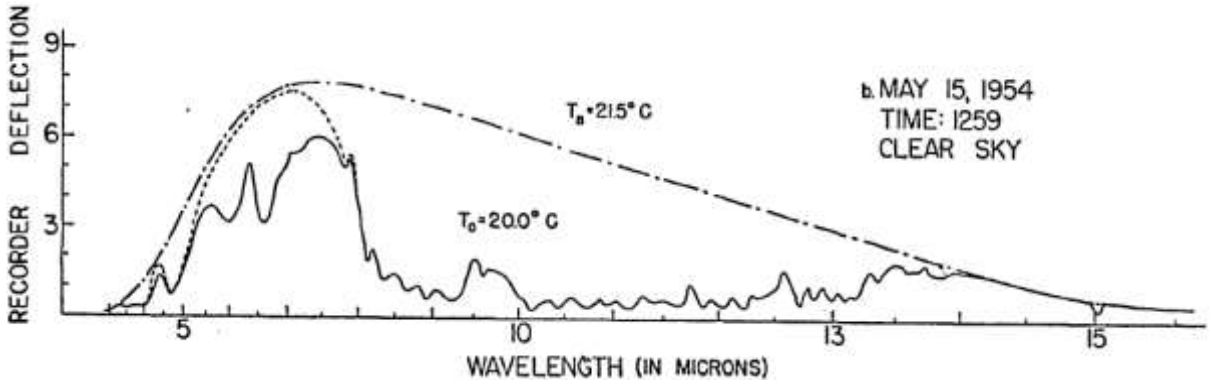

Figure 1-34: Typical zenith sky spectra The dashed curve above each tracing was obtained with a laboratory blackbody of temperature T_B. The "ground temperature" T_0 was measured by automatic recording in a standard screen. Water-vapour concentrations (g/m^3) six feet above ground level was 9.3- Copied from (87).

The dashed line in Figure 1-34 represents a reference black body emission curve at temperature T=21.5°C (representative of close to ground temperature) corrected for WV and CO_2 absorption that radiation undergoes on its way to the spectrograph entrance. Analogously, the dotted line is an attempt to correct sky radiation for the same effect. WV is probably the cause of the relatively strong emission maxima observed between 7 µm and 14 µm (87). CO_2 vibration-rotation bands are associated with emission maxima observed between 13 µm and 14 µm. The emission maximum at 12.6 µm in particular is associated to a weak CO_2 vibration-rotation band which has been identified in high-dispersion solar studies (87). At night, the zenith sky spectrum shows a striking similarity to the one observed during day time. The only clear evidence of scattered solar radiation for wavelengths longer that 3 µm is found between 3 and 4 µm. On a cold and dry night, when WV concentration near the ground is 5.9 g/m^3, (see Figure 1-35 top plot) decreasing intensity in the emission of WV around 6.3 and between 8 and 13 µm is readily apparent. A closely resembling black body spectrum (see Figure 1-35 middle plot) is observed on an overcast day when cloud base is found 600-700 feet above ground (87). On a hot and really humid day, when WV concentration near the ground is 20.3 g/m^3 (see Figure 1-35 bottom plot) the increased emission of WV is evident.

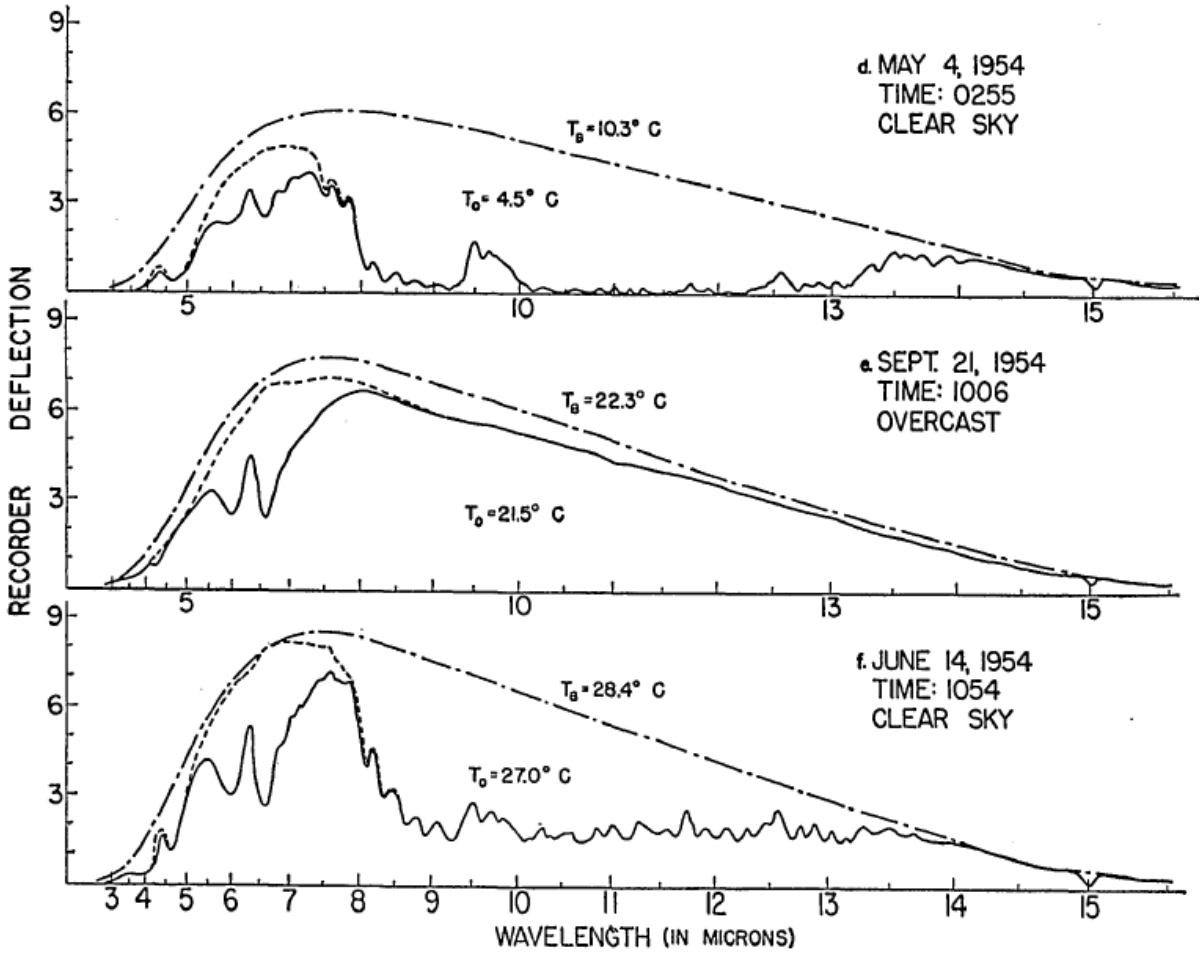

Figure 1-35: As Figure 1-34, top - sky spectrum observed on a very dry night, middle - overcast day with cloud base at 600-700 feet above ground, bottom - very hot and humid day- Copied from (87).

What we have seen is that clear sky spectra significantly deviate from the black body one, especially in those regions of the spectrum where gas absorption is low and conversely transmission is high. On the other hand under cloudy skies when cloud emissivity approaches 1 as is the case for integrated water vapour column larger than 0.1 mm (89), small deviations from the spectrum of a black-body at close to ground temperature are observed. Optically thick clouds closely approximate black body radiation irrespectively of wavelength. In the presence of optically thin cirrus and for ice water path less than 0.1 mm the cloud emissivity is significantly lower than 1 (90). In this case sky emission spectra are significantly different from the spectra of an ideal black body (91) (92) (93) (at screen level temperature) and are hard to distinguish from clear sky. Another essential aspect to notice is that near ground temperature may be representative of the actual sky emitting radiative temperature. This is evident in particular in regions of high absorption, where the sky spectrum deviates the least from the black-body reference. Despite the temperature profile generally decreasing with altitude, this change is not dramatic if most of the gas species actually contributing to absorption and emission are contained within the lower atmospheric layers. In this respect it should be remarked that WV, among the principal atmospheric gases (CO_2, O_3) contributing to thermal emission, plays the most important role and it is mostly confined within the first kilometre of the troposphere. Within high transmission regions, where the down-welling radiation originates also from high altitude layers whose temperature may substantially differ from near ground, deviations are larger. In this respect sky spectra would resemble those of a black-body at a

temperature which is an average over the entire atmospheric column. Empirical models (94) (95) (88) (96) (97) (98) attempting to reproduce the down-welling long-wave irradiance under clear and cloudy skies typically make use of temperature and or vapour pressure close to ground to reproduce the down-welling thermal radiation. This is estimated through the Stephan-Boltzmann law by expressing the clear-sky apparent emissivity as function of either one screen level parameter such as water vapour density, vapour pressure, dew point temperature, air temperature or a combination of the latter and vapour pressure for instance. Parametric coefficients appearing in the analytical form are normally fitted over clear sky data. These studies (94) (95) (88) (96) (97) (98), even if carried out over a broad spectral range (1 μm < λ < 40 μm), show that screen level temperature and column integrated WV can be adequate proxies for the effective emissivity of the atmosphere. Using column integrated WV in place of its screen level counterpart is motivated by the fact that emission does not originate only from the lower layers. Radiation transfer calculations nowadays available provide an accurate solution to the estimation of down-welling thermal radiance under clear skies. This is derived by using detailed spectral profiles of the atmospheric constituents and corresponding radiative properties as input to radiative transfer equations. LOWTRAN, FASCODE, MODTRAN, MOSART are examples of existing complex algorithms which, however, are rarely used (99) (100) (101). Figure 1-36 and Figure 1-37 show MODTRAN5 calculated zenith radiances in case of clear sky with 1 cm of precipitable water vapour (PWV) (Figure 1-36 left plot), clear sky with 2 cm of PWV (Figure 1-36 right plot), cirrus cloud base at 10 km altitude (Figure 1-37 left plot) and low level cloud (Figure 1-37 right plot) respectively. PWV expresses the millimetres of liquid water that would be obtained by condensing the total amount of WV present in the atmospheric column. The integrated water vapour (IWV) which is the column integrated WV, when expressed in kg/m^2 is equivalent to the PWV expressed in mm of liquid water. The dashed line represents the black body emission for a temperature of 288 K that is typical for the air temperature (AT) near ground. It would be the radiance observed as if the atmospheric emissivity were 1 over the entire spectrum. Under clear sky, the largest deviations from the black body emission are mostly associated with low emissivity portions of the spectrum (high transmission).

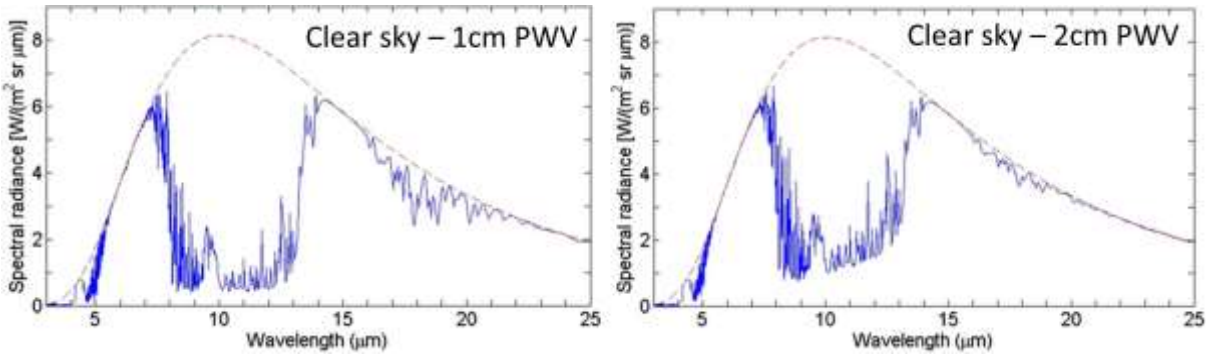

Figure 1-36: Atmospheric emitted radiance (solid blue line) and 288 K blackbody radiance (dashed red line) plotted versus wavelength for (a) 1 cm PWV and (b) 2 cm PWV. Both spectra were calculated with Modtran5 for a zenith path from sea level to space through a 1976 US Standard Atmosphere model. Copied from (91).

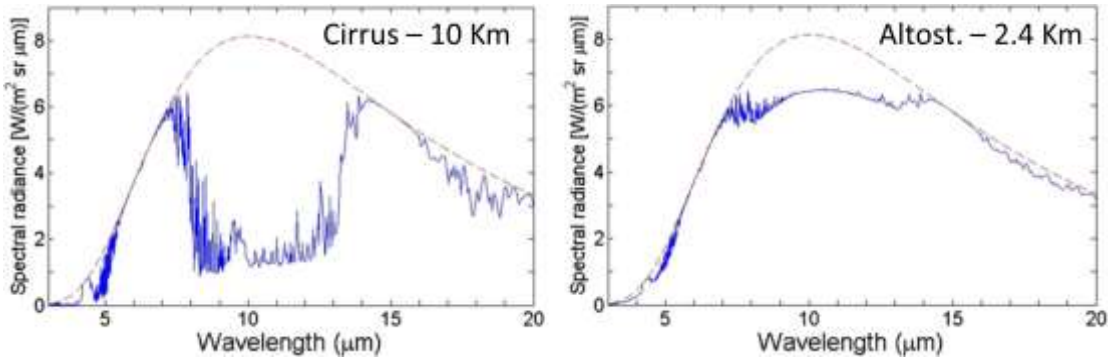

Figure 1-37: Emission spectra of clouds observed at the zenith from ground, modelled with Modtran5 for the 1976 US Standard Atmosphere: (a) cirrus with 10 km base altitude, 2 km thickness, and 0.28 extinction; and (b) optically opaque altostratus cloud with a 2.4 km base and 3.0 km top. Copied from (91).

Regions of the electromagnetic spectrum characterized by high absorption are not the ideal choice for cloud detection because the atmospheric gases would absorb direct emission originating from the atmospheric layers up above. On the other hand, observing in high transmission regions, where optically thick clouds have a significantly larger emissivity compared to the atmosphere, reduces the problem of cloud detection to discriminating atmospheric gases from optically thin clouds. It is thanks to their peculiar high transmission properties that atmospheric windows are important for cloud detection. There are four of these regions within the portion of the electromagnetic spectrum spanning from visible to far infrared: the visible (0.4–0.7 μm), short-wave infrared (SWIR from 1 to 2 μm), mid-wave infrared (MWIR from 3 to 5 μm), and long-wave infrared (LWIR from 8 to 14 μm) window. The LWIR window represents the one relevant for this study (see Figure 1-38).

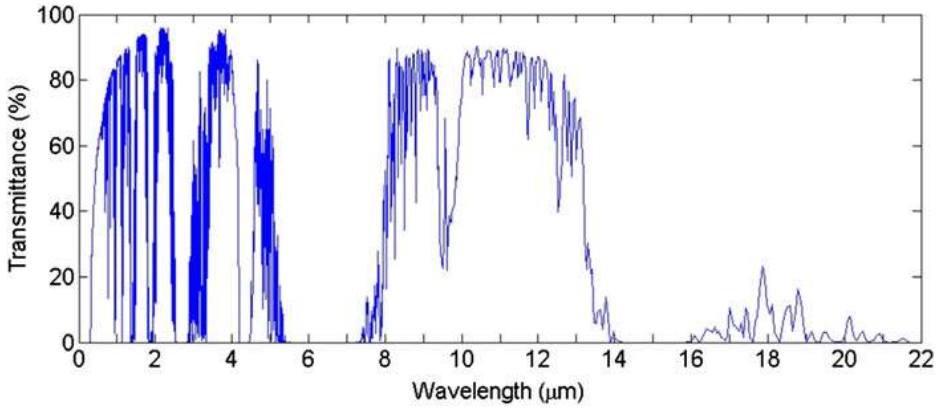

Figure 1-38: Atmospheric transmittance versus wavelength, calculated with Modtran5 for a zenith path from sea level to space through a 1976 US Standard Atmosphere model. Copied from (91)

Over this transmission window the spectral radiance is mainly dominated by the amount of WV present in the atmosphere (91) and cloud detection simplifies to discriminating clear sky (gases emission) from cirrus or more generally optically thin clouds while optically thick clouds are readily sensed. For detecting cirrus the fluctuations of the BT will be quantified through De-trended Fluctuation Analysis (DFA) which has already been used in cloud detection investigations (102) (103). DFA is very sensitive to cloud presence except to very optically thin clouds. Furthermore it is unable to alone distinguish between cirrus and other clouds. Another method is necessary to distinguish cirrus from warmer clouds. This can be done if cloud temperature can be measured via BT corrected

for the atmospheric conditions. On theoretical grounds the radiative temperature BT and the actual thermodynamic temperature of a body do coincide only if the body's emissivity is 1. For bodies whose emissivity is less than 1, the thermodynamic temperature that they need to be at for emitting the same radiance of a black body at the same wavelength is higher than the black body temperature. In remote sensing applications for non-contact temperature retrieval the measured BT will never coincide with the actual thermodynamic temperature not even for black bodies because of the attenuating medium between target and observer. In other words the irradiance impinging on the measuring instrument does not coincide with the radiant emittance of the source. It should also be pointed out that if the emissivity setting of the measuring instrument is set to 1 then the BT measured is always an underestimation of the actual temperature because the atmospheric emissivity is generally less than 1 except for optically thick clouds whose emissivity can be approximated to 1. For this subcategory of clouds a better estimate of cloud temperature can be obtained by correcting the actual cloud emissivity for the sky transmittance. It is the knowledge of the emissivity which allows the correction. On the other hand for optically thin clouds, whose emissivity is generally unknown this correction cannot be done. Modelling clear sky BT with sufficient accuracy would mean knowing the atmospheric transmittance and emissivity through which one could correct the measured BT. This would provide a correction for the presence of the atmosphere, which being an attenuating and emitting medium makes an exact calculation of the source properties impossible unless the atmospheric contribution is accounted for. Instead of having recourse to detailed radiative transfer calculations, we propose to model clear sky down-welling irradiance as a function of the IWV and close to ground temperature (CGT), based only on first principles. In its more general form the model would also account for direct cloud emission, however only atmospheric gases' contribution, or in other words clear sky, will be considered at this stage. This will be discussed in section 3.6. DFA will be covered in section 3.5 and will be used for identifying clear sky periods. It will be shown that DFA may fail in discriminating clear sky from very optically thin clouds. The cirrus detection algorithm will ultimately result in a two-steps scheme. A first step to quantify BT fluctuations which will allow to identify the presence of clouds and a second step for discriminating warm and cold clouds, by comparing clear sky BT to the observed BT. The departure from clear sky BT due to the presence of cirrus can be estimated if assumptions on cloud emissivity and temperature are made. Assuming an optically thick cirrus and a temperature representative of the boundary of cirrus would provide an estimate of the maximum departure of BT from clear sky BT ascribable to ice clouds. This would allow us to set a threshold corresponding to the transition from ice to mixed phase.

2 All-sky Imaging

In this chapter we will first review the various applications that all sky imaging finds in the field of atmospheric physics. We will then see how such a technique can be used to interpret all sky images in terms of scattering phase function, provided that the necessary image transformation and corrections are applied. These consist in reconstructing the original image in the light-source-centred system of coordinates and correcting for air mass and vignetting. The use of a back-ground mask, needed to exclude non-sky pixels from the averaged sky brightness, will also be proposed. With all the necessary corrections available, an example of scattering phase function measure will be discussed in paragraph 2.10. The effect of each correction on the measured sky brightness will be at first accounted for individually, to analyse the effect that each correction has on the SPF, to then be applied altogether and provide the measuring method, employed in chapter 4, for the retrieval of the HR.

2.1 Whole-sky imagers

The first work on whole sky photography started around the beginning of the 20th century with the main purpose of determining cloud cover. Three types of Whole Sky Imagers (WSIs) have been devised since: refracting, reflecting and moving film systems. An example of moving film system is the Mueller's cloud camera, developed in 1905, whose description appears in literature in June 1915 in an article written by Fassig (104). A full view of the sky dome was projected onto an automatically revolving film, inclined at an elevation of 45^{o}, while the camera assembly revolved around the vertical axis (105). The rates of rotation of the film and the camera base were perfectly coupled to make the image stationary with respect to the film (105). Reflecting systems, on the other hand, can be obtained by mounting a camera on top of a convex mirror. The first description of such a device able to capture the whole-sky view was published in 1933 (106). In this respect it is worth to mention the work done by Greenler and Mallmann who used silvered Christmas tree ornaments to photograph halos (107) and the one by Winn et al. who captured lightning flashes on whole-sky images (108). Wide-angle reflective devices are generally simpler than refractive ones as construction is simpler since they do not need correction for chromatic dispersion. Regardless of the system in use, projecting a whole hemisphere into a camera plane is inevitably associated with image distortion. Pin-hole camera images are distortion-free but only a limited portion of the sky dome can be viewed. It was just at the beginning of the twenties that the problem of image distortion became well known; R. Hill is the first one to describe the differences between gnomic, stereographic, orthographic and equidistant methods and to point out the importance of selecting the best projection method (109). C. E. Deppermann in 1949 concludes that, for reflecting systems, no projection can accomplish the mapping without distortion (110). He also states that by preserving directions the equal angle projection is more suitable for cloud photography and meteorology than the equal area projection. For reflecting systems the image distortion is fully determined by the shape of the mirror surface whose geometry determines the way the image is projected onto the camera plane. It has been shown that spherical and paraboloid mirrors can be used to obtain near equidistant projection (111). It is still in 1949 that Deppermann suggests that to get an exact equidistant projection the shape of the mirror should be slightly prolate (110). The same author illustrates also what the shape of the mirror should be to get an equal area projection. However, the need of accurate camera alignment and quite large reflecting surfaces prevented the reflecting systems from becoming widespread amongst the scientific community. Refractive systems, exploiting the ability of fish-eye lenses to see wide-angle field of views, are the most common to come across in literature. The first ever attempt to obtain a whole sky image through a refractive camera, dating back to 1911 (112), is by professor R. W. Wood, experimental physicist at John Hopkins University. He illustrates how to construct a fish-eye camera by making use of the different refraction indexes of air and water. Basically Wood's camera is a water-filled pinhole camera

consisting of a light-tight, water-tight box filled with water and a 3 cm hole in the centre of one the box faces. The need of immersing the photographic plate in water is the main disadvantage associated with Wood's camera. Projecting the sky dome into a plane is conceptually analogous to projecting the Earth surface into a paper sheet. Cartography in this respect provides methods of flattening into a plane a continuous curved surface. Imaging the sky dome onto a plane surface corresponds to what in cartography is classified as an azimuthal projection. Only radial distances are distorted and in such a way that is specific to the type of projection that the optics is designed for. The stereographic projection preserves shape while the orthographic one gives a prospective view; with the equidistant projection the distance from the image centre is proportional to the zenith distance whereas with the equal area projection equal areas on the image correspond to equal solid angles over the sky dome. These last two projections are the more common to find in use. However the equidistant one finds wider applicability as it makes it easier determining angular distances while the equal area one is more suitable for cloud photography because better reproduces the way a surface observer would quantify cloud cover. With the beginning of the seventies several works (113) (114) (115) (116) focussed on the determination of cloud-free lines of sight through the atmosphere. These investigations were based on a three year dataset collected through the Nikon fish-eye system described by Pochop and Shaklin (117) which makes use of a fish-eye lens mounted on a Nikon camera. Cloud cover, generally retrieved by means of a grid, for these specific works did not account for the distortion caused by the camera. One of the most extensive investigations over cloud cover comes with the work by Holle and Mackay who analysed more than four thousand whole-sky images taken between 1963 and 1974 from a site on the island of Barbados and on board United States research ships. They used two different grids: a linear one which uses an equal solid angle approach (105) and a non linear one which instead accounts for the fact that clouds of the same geometric extent when closer to the horizon cover a smaller solid angle (118) (119). Cloud-free line of sight statistics has also proved to be essential for ground-based laser weapon applications (120) (121) and, more in general, WSIs have been used in support of military test sites and satellite tracking stations (122) (123). Around the mid seventies whole sky imaging has found application in auroral photography (124) and the retrieval of cloud heights and velocity by means of two or more all-sky cameras. In this regard it is worth to mention the work done by Lyons, back in 1971, who, by combining the use of three whole-sky cameras, determined cirrus clouds height and velocity allowing a better interpretation of satellite retrieved wind speed and direction obtained by using cirrus as tracers (105) (125). By the end of the seventies and throughout the eighties whole-sky imaging has been employed to perform radiometric measurements of the distribution of diffused solar radiation over the sky dome (126), to establish the view factor in complex radiation environments such as forests, and valley bottoms (127) (105) and to measure plant leaf cover (128). From the mid-nineties multispectral digital sky imagers have been developed for a variety of uses. The total sky imager (TSI) (129), for instance, was meant for assessing the impact of cloud cover on surface solar irradiance whereas a daylight WSI sensitive to visible and near infrared light (VN-WSI) was developed in the late nineties in support to investigation over the impact of ozone to UV radiation (130). This was an improved version of the daytime whole sky imager (day-WSI) fielded in the eighties by the same Atmospheric Optics Group (AOG) of University of California (130). Successive to the day-WSI and VN-WSI is the day and night WSI (D/N-WSI). D/N-WSI was developed to provide 24-h coverage (130). Since the introduction of VN-WSI a series of day time WSIs were developed over the years for multiple purposes such as solar energy application (131), weather forecasting (132) and cloud fraction retrieval (133). Many of these devices use the same cloud detection algorithms based on the red/blue ratio that was first introduced with the day WSI. The algorithm developed in the mid eighties (134) (135) used a fixed red/blue ratio to identify opaque clouds (130). Towards the end of the eighties AOG implemented also a thin cloud algorithm which made its first appearance in literature at the beginning of the nineties (136). Accounting for the instrument site, solar zenith angle, look angle and amount of haze a clear sky blue/red ratio was extracted. Field images were divided by the haze-corrected clear sky ratio and a threshold was set

for determining the presence of thin clouds. It was found that uniform thin clouds give rise to a 20% increase in the same ratio lending themselves to detection. In a more recent version of the same algorithm, opaque cloud detection is based on a fixed NIR/blue threshold whereas the thin cloud one on a haze/aerosol-corrected clear sky NIR/blue ratio image. Such algorithms automatically correct for aerosol/haze variations and hardware artefacts (130). Night time cloud detection algorithms are also available, under both moonlight and starlight. They are based on star light transmittance and whole clear sky radiance. Presence of clouds is determined based on how much attenuation the star beam undergoes. With respect to a specific pixel, the presence of thin clouds gives rise to an observed radiance which is lower than the one due to clear sky and larger than opaque cloud radiance. Corrections for the amount of aerosol and haze and for variations in radiance of the Milky Way are also accounted for (130). Cloud classification through imaging is another field of active investigation. Automatic algorithms for cloud classification have been proposed such as the one from Heinle et al. based on statistical features of the colour and texture of images (137). WSIs bring several advantages in the field of atmospheric science if compared to alternative techniques: thermal IR systems have to cope with presence of WV to sense optically thin clouds and also are unlikely to provide space-to-Earth beam transmittance measurements; LIDARs and RADARs cannot achieve a full view of the sky dome and the large and simultaneous amount of measures that WSIs do; satellites, on the other hand, have a limited spatial and temporal resolution. Mention to all the work done about the calibration of all-sky cameras should not be forgotten. Generally it relies on the use of several images of some known pattern. In this respect C. Hughes et al. have introduced a simple fish-eye lens calibration method to extract distortion centre and equidistant parameter *f*. From a checkerboard diagram, used as calibration image, a set of distorted lines are selected; these lines are chosen on both vertical and horizontal edges and arbitrary points are extracted along each curve; circles passing through these points and corresponding to parallel scene lines converge into vanishing points whose position is used to determine the distortion centre; the equidistant parameter *f*, on the other hand, is obtained by a procedure of minimization of area distortion (138). The same authors have also introduced, for a generic fish-eye camera, a new method to extract the radial distortion curve, which relates rectilinear and fish-eye projections, by using a standard checkerboard calibration diagram. Some of the most common fish-eye projection models (Equidistant, Equisolid, Orthographic, Stereographic) in addition to the fish-eye radial lens models such as the "Polynomial Fish-eye Transform", the "Fish-eye Transform" and the "Field of View Model" have been fitted to the extracted distortion curves obtained for five different fish-eye cameras. The accuracy of the models in reproducing the actual camera projection has been quantified. It has also been shown that the inclusion of additional parameters to the basic models improves the fit to the extracted distortion curves. In particular this can be done by appending polynomial elements to the basic model (139). In this regard it should be noticed that some lens elements can cause the distortion curve to deviate from the nominal one that the lens was designed to adhere to. This can be due to the specific manufacturing process. With a similar approach to the one used by C. Hughes et al., F. Yue et al. (140) do calibrate an equidistant fish-eye camera by means of a single image and two sets of parallel lines from the scene. Alternatively to the use of fixed patterns, cross diffractive optical elements (CDOEs) have also been used to generate an accurate virtual grid for camera calibration. First introduced in 2008 (141) this laser-based technique does not suffer from random errors due to the measurement errors of the calibration target (142). Using 3D control points in a calibration room (143) or single views of a planar calibration object (144) are alternative calibration techniques. Camera intrinsic parameters can also be retrieved by using a set of point pairs in a sequence of images (145). A full MATLAB implementation of an algorithm for estimating both intrinsic and extrinsic camera parameters is also available (146) and has already been used by other authors (147) for camera calibration purposes. It makes use of a set of images of a checker-board pattern which are used for corners detection. The camera intrinsic parameters, which allow to retrieve the centre of the image, are obtained through a minimization routine, which leads to the determination of the parameters of a polynomial and the elements of a transformation

and translation matrices. In addition to the geometric calibration, the same authors (147) perform white balancing and chromatic corrections which can be particularly significant especially for WSIs sensitive to visible and near-infrared radiation as the one they have used. Chromatic aberration is due to the fact that, depending on the wavelength, rays converge on different points on the sensor. Also correction for vignetting is accounted for and measured by means of an integrating sphere whose interior is coated with a reflecting film. The radial darkening due to vignetting, non negligible especially for wide-angle lenses, is measured by taking images from within the sphere. With the general purpose of measuring sky brightness and in particular to characterize cirrus, two equidistant fish-eye cameras for day and night time vision are used and described in detail in the coming sections. They are used for measuring sky brightness and in particular to measure the SPF associated with ice clouds. The camera details and specifications will be given in section 2.3. The camera calibration has been done by detecting the position of stars and implementing a minimization procedure similarly to what done by Tohsing et al. (148) for the validation of the projection function of their CCD camera. With respect to the daytime camera, the aperture has been increased from the usual f/16 to f/4. It has then been left to take images over the course of a clear night. A set of bright stars was plotted as circles on an image, based on their position in the middle of the exposure and the theoretical f-theta system of the lens. The parameters of the camera were then adjusted until the errors between the calculated and true position of the stars on the image were minimised. This was verified by using a number of different images across the night. The same procedure has been applied for both night and day time cameras. The testing of the projection is discussed in paragraph 2.4.1 where the performance of the lens model in reproducing stars and planets trajectories, with the cameras parameters obtained from calibration, has been assessed. A method for measuring the sky brightness and in particular the ice clouds SPF from which the HR is measured is covered in paragraph 2.5. This method is based on the transformation of coordinates which goes from the zenith-centred system of coordinates to the light-source-centred reference system where eventually the original image is interpolated. Correction for air mass (see paragraph 2.6), which gives enhanced image brightness towards the periphery of the image, and for vignetting (see paragraph 2.7) are also proposed.

2.2 Measuring Sky Brightness

Sky images from the continuously operating all-sky cameras (one for night time, one for day time) available at the observatory of Bayfordbury have been examined and analysed. With a fixed time between exposures of twenty seconds the daytime camera provides approximately three images per minute. The time between exposures for the night time camera is set accordingly to how dark the sky is. It varies between twenty and sixty seconds providing from a minimum of one to a maximum of three images per minute. Sky imaging doesn't allow us to detect cirrus clouds in case of very thin optical thickness. However, it is valuable if one is interested in observing optical phenomena like halos, one example of which is shown in Figure 2-1.

Figure 2-1: Night Time Halo. Bayfordbury 29th December 2009, 00:26 (149).

One question that we want to answer is what proportion of cirrus clouds gives rise to this type of optical phenomenon. Also, we want to determine the sky brightness. To do so we have to take into account that the All Sky cameras are equipped with a fish-eye lens that make up a part of the optics. This type of lens is able to span angles as wide as 185 degrees. While on the one hand we get such a large field of view, on the other hand the image gets necessarily distorted when projected onto the camera sensor plane. This is evident when we look at the halo shape which is clearly not circular as shown in Figure 2-1. Image processing is necessary if we want to measure the sky brightness. This implies measuring the image brightness as a function of the scattering angle ϑ (with respect to the light source centre). For achieving this the image brightness has to be averaged over the azimuth angle ϕ over pixels which are equidistant in terms of scattering angle from the light source centre. Figure 2-2 shows source centred coordinates where ϑ_j (for a fixed j from 1 to 3) do not represent points at constant scattering angle, because the lens projection is radially symmetric with respect to zenith. Equidistant points in terms of pixels would be at the same scattering angle only if the light source centre coincided with zenith (approximately the image centre).

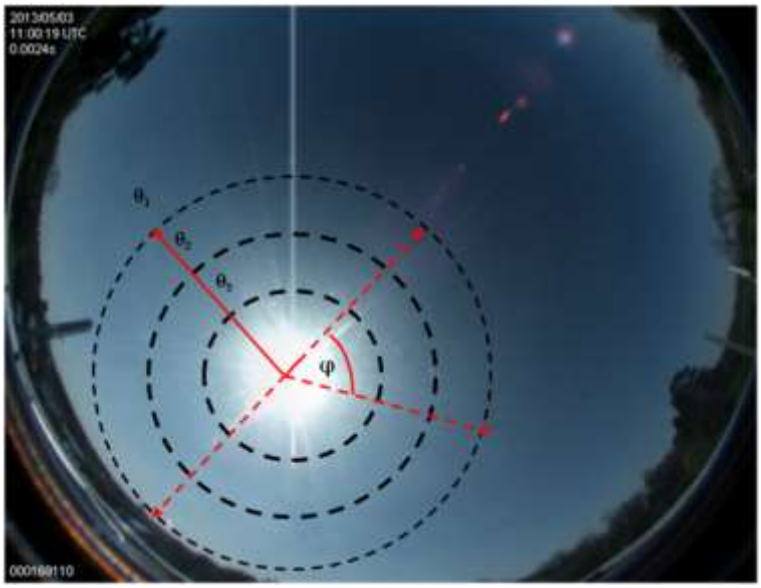

Figure 2-2: Source centred coordinates: θ_j (j=1:3) do not represent points at constant scattering angle because the light source centre is not at zenith, Bayfordbury 03-May-2013, 11:00 am (149).

2.3 Camera details and specification

The camera used is the third version of the All Sky camera manufactured by the Santa Barbara Instrument Group (SBIG). Called the All Sky-340, the optical system consists of a Kodak KAI-0340 CCD sensor and a Fujinon FE185C046HA-1 lens. The KAI-0340 is a VGA resolution (640x480 active pixels) 1/3" format CCD with 7.4 µm size square pixels. The FE185C046HA-1 is a wide angle fish-eye lens with a focal length of 1.4 mm and a focal ratio range of f/1.4 to f/16, fixed open at f/1.4 in the AllSky-340 night camera and closed down to f/16 in the day camera. This combination gives a field of view of 185°×144°47' and average resolution of 18' per pixel. Assuming the camera is aimed at the zenith, a maximum of 95.0 % of the area of the sky can be imaged, with 2.52% cut off at the top and bottom. The areas around the edges are most affected by light pollution and not suitable for any measurements so this loss is not too detrimental. The camera is located on the roof of the East of England Science Learning Centre (see Figure 2-3), next to the University of Hertfordshire's astronomical observatory at Bayfordbury, Hertfordshire (51.776N 0.096W). The elevated vantage point from the roof gives it a clear view of the skies, uninterrupted by most of the surrounding trees.

Figure 2-3: Bayfordbury, East of England Science Learning Centre roof.

Figure 2-4: All Sky camera 340 (150).

The camera is connected to a computer inside the Science Learning Centre, via an RS-232 serial cable. Whilst a RS-232 link is slower than USB, it has the advantage of faring better over longer distances, as the cameras are often located far from a computer. Using a USB-serial adapter at the PC end the maximum download speed of 460.8 Kbaud could be achieved. At this rate the average download time of an image is 16.5 seconds for the gray camera. The colour one is connected to a slower serial port which allows a download time of 48 seconds (150). The All Sky 340 camera, illustrated below in Figure 2-5, incorporates the SG-4 Camera inside an aluminium enclosure with an acrylic dome to protect the fisheye lens (151).

Figure 2-5: All Sky camera.

The two cameras are identical except for a mosaic arrangement of photo-sensitive elements placed over the pixel sensors of the daytime camera, called Bayer filter, a schematic of which is shown in Figure 2-6. The advantage of using one mosaic arrangement is that it enables to use only one matrix of photo-sensitive elements instead of three (one for each colour) (152).

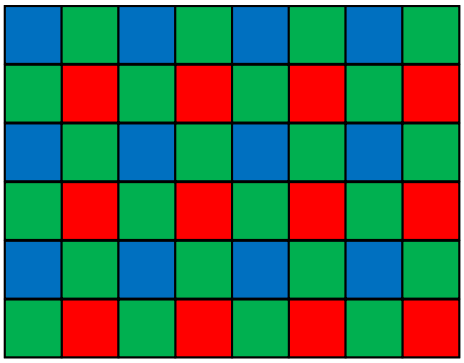

Figure 2-6: Bayer filter.

The Bayer filter is used for discriminating the red, blue and green wavelengths respectively. A demosaicing algorithm has to be applied to the raw image data captured by the image sensor to reconstruct the full colour image (see Figure 2-7).

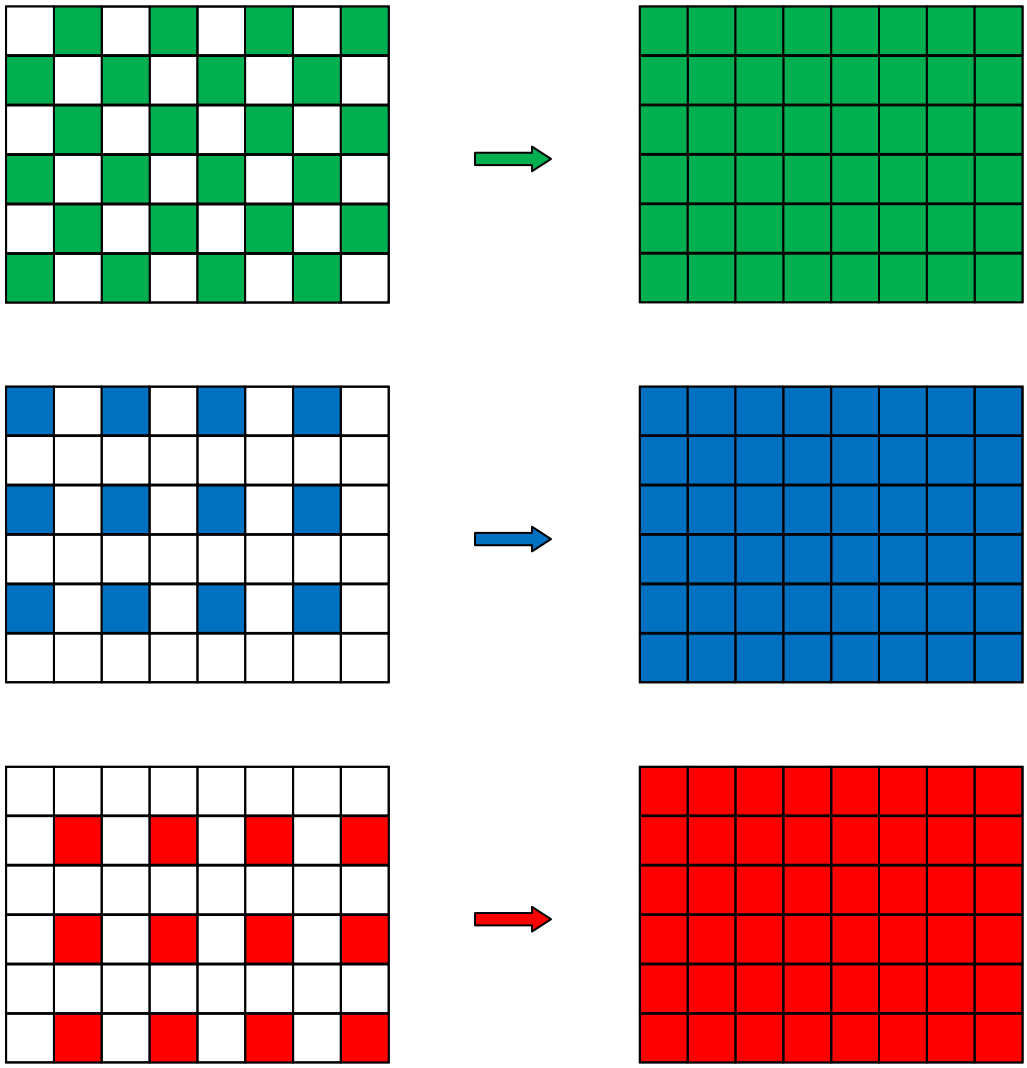

Figure 2-7: Interpolation of colour planes.

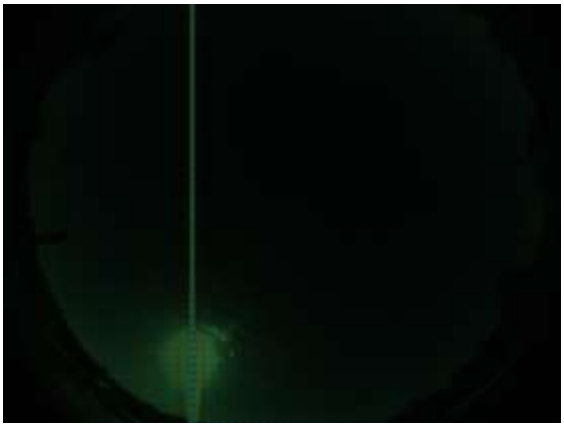

Figure 2-8: Day time image before demosaicing.

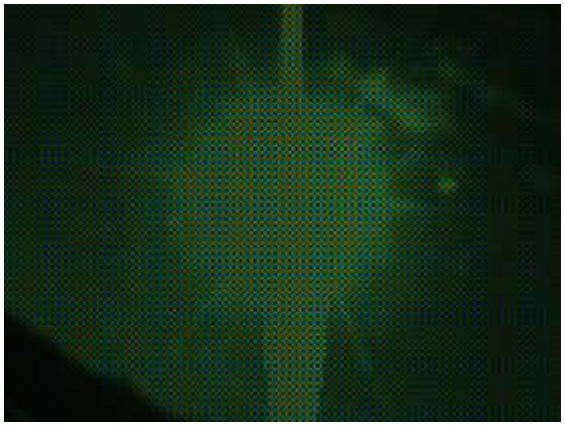

Figure 2-9: Zoom around the light source.

Figure 2-10: Day time image after demosaicing.

Figure 2-11: Zoom around the light source.

Figure 2-8 shows an example of raw image data before demosaicing. From Figure 2-9 it is evident the "blue-green-green-red" Bayer pattern. For this specific project the Matlab built-in function "demosaic" that allows image demosaicing has been used. Figure 2-10 is the final outcome and Figure 2-11 a zoom in around the light source.
It should be highlighted that the absolute quantum efficiency of the daytime camera is provided by the manufacturer (153) and shown below (see Figure 2-12) as extracted from its datasheet. This information is essential if independent observations have to be compared.

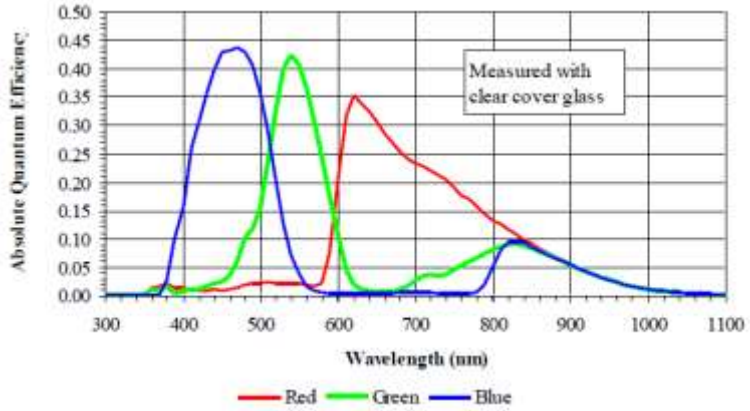

Figure 2-12: Colour with Microlens quantum efficiency (153).

2.4 Fish-eye lens projection

The fish-eye lens that forms part of the optics of the two All-Sky cameras enables sky observation over a field of view (FOV) as large as 187°59' along ENE-WSW and as large as 142°38' along SSE-NNW as shown in Figure 2-13 for the night time camera. Slightly larger is the FOV of the day time camera along ENE-WSW. It measures 189°53' (see Figure 2-14). This difference is due to the slightly different alignment of the lens relatively to the camera plane. This is also reflected on the position of the zenith with respect to the camera plane centre.

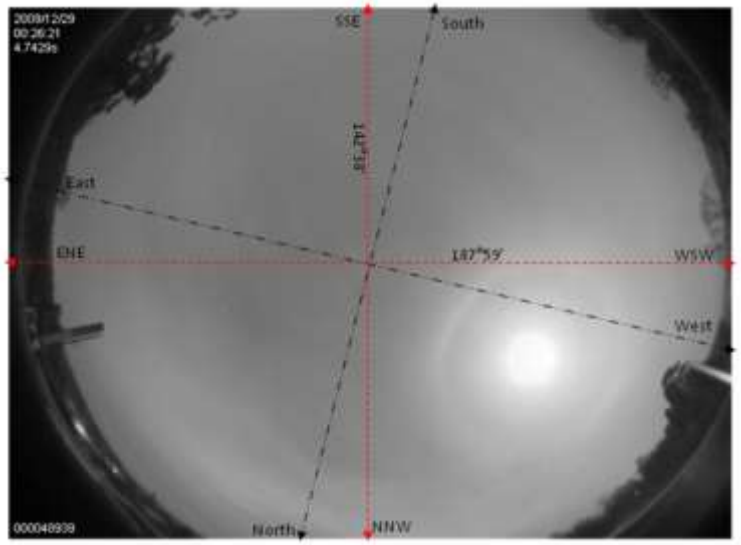

Figure 2-13: All-Sky night time camera FOV (149).

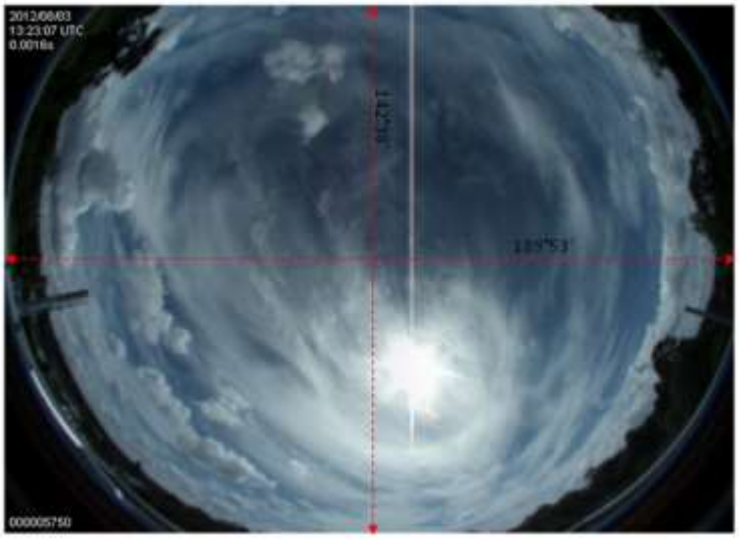

Figure 2-14: All-Sky daytime camera FOV (149).

The camera centre (CC) of both cameras does not coincide with the position of the projection of the true zenith on the camera plane (CP), shown in Figure 2-15, to which we refer to as the lens focal axis (LFA). An offset of 14 pixels in the *x* direction and 12 pixels in the *y* direction that corresponds to about 4^{o} and 3.5^{o} respectively has been measured for the night time camera. The same quantities become about 1^{o} and 9.5^{o} for the daytime camera.

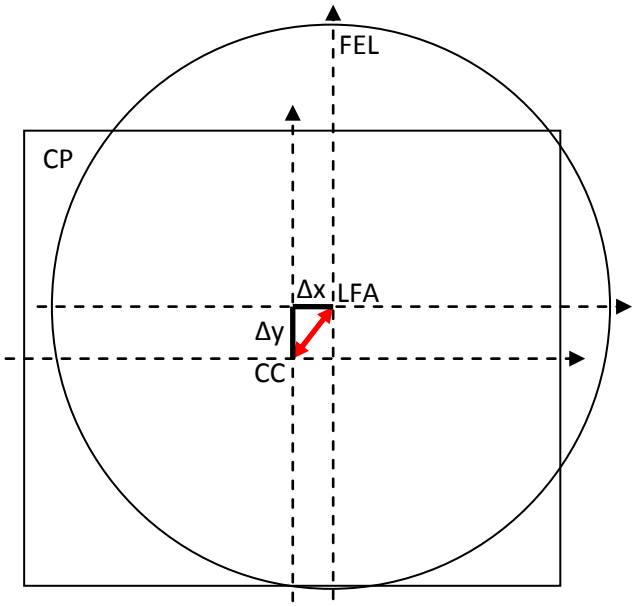

Figure 2-15: Camera plane - lens offset is the distance between LFA and CC.

Our fish-eye lens uses an 'f-theta' system which means that the distance in pixels of the object projected onto the camera plane from the optical centre of the image is simply a scaling factor *f* (3.365 pixels/degrees) multiplied by the zenith angle *z* of the object expressed in degrees (see Figure 2-16). This type of projection is called *equidistant* (154) (155).

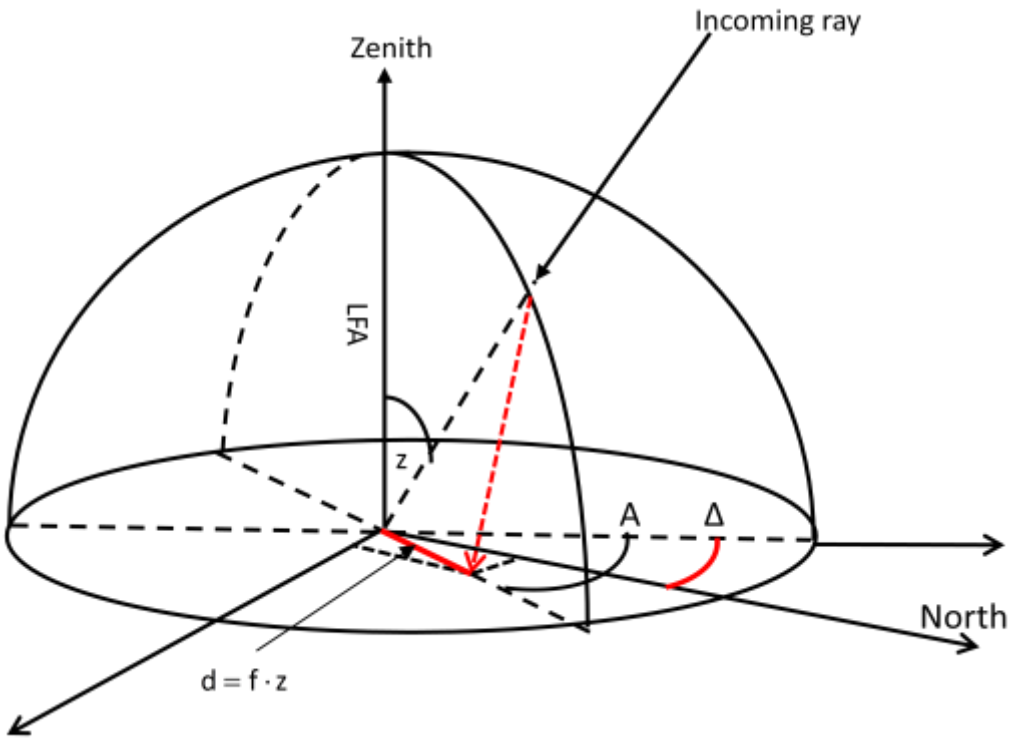

Figure 2-16: f-theta lens projection.

It should be noticed that the lens sees below the horizon as shown in Figure 2-17. This has to be accounted for when image processing is performed.

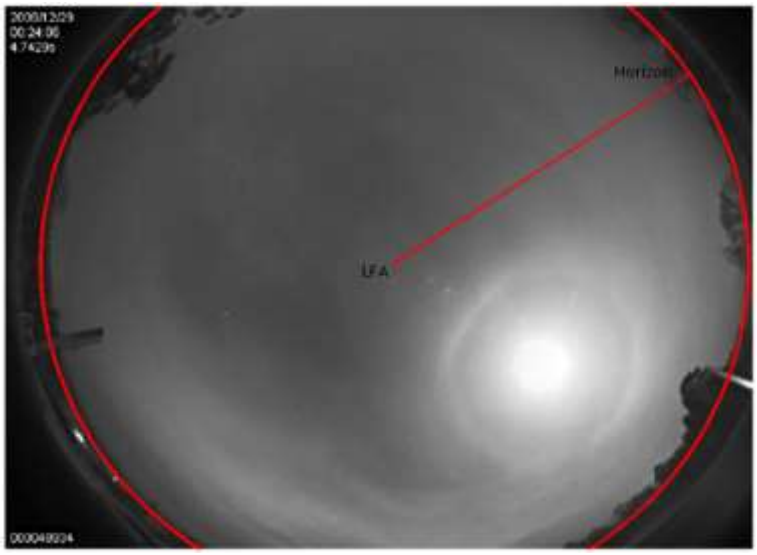

Figure 2-17: All sky night time camera horizon (red solid circle).

To verify that the camera projects the objects into the camera plane according to the equidistant projection, planets and stars trajectories have been considered. Linear simultaneous equations (2.1 and 2.2) are expected to predict the image position of starts and planets given their azimuth (*A*) and zenith distance (*z*) coordinates;

$$x = f\, z \sin(A - \Delta) + x_0 \tag{2.1}$$

$$y = f\, z \cos(A - \Delta) + y_0 \tag{2.2}$$

Eq. 2.1 and 2.2 give the *x* and *y* pixel coordinates by knowing that:

1. ***f* is a scale factor that expresses the conversion from degrees to pixels**
2. ***z* is the zenith distance in degrees from zenith (from Table 2)**
3. ***A* is the azimuth in degrees from North (from Table 2)**
4. ***Δ* is the rotation of the camera from North expressed in degrees**
5. ***x_0* and *y_0* are the coordinates of the optical centre (true zenith) expressed in pixels**

In accordance with Eq. 2.1 and 2.2 and with respect to Figure 2-18 the true zenith (z=0) is projected into the camera plane at (x_0,y_0).

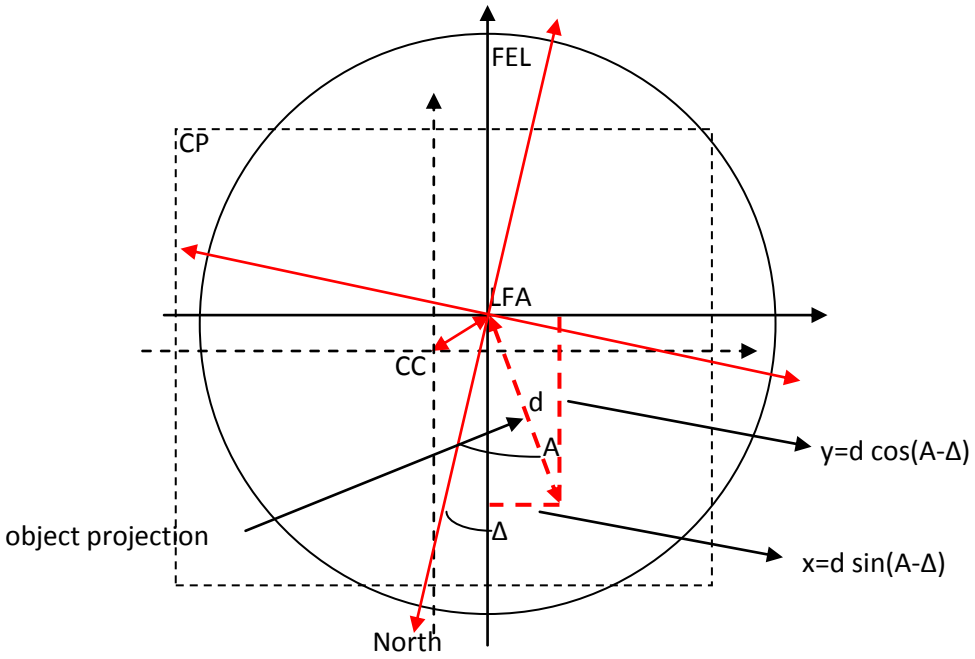

Figure 2-18: Object projection in the All-Sky camera plane: *d* is the pixel distance from LFA, *A* is the azimuth measured from north and *Δ* is the rotation of the camera from north.

Zenith distance and azimuth on minute basis have been taken into account as shown for one specific case in Table 2 (156).

Betelgeuse

Apparent Topocentric Positions
Local Zenith and True North

(no name given)
Location: E 0°05'44.8", N51°46'31.4", 0m
(Longitude referred to Greenwich meridian)

Date (UT1)	Time h m s	Zenith Distance ° ' "	Azimuth (E of N) ° ' "
2013 Feb 14	23:00:00.0	55 45 42.8	232 15 29.1
2013 Feb 14	23:01:00.0	55 53 05.2	232 31 09.5
2013 Feb 14	23:02:00.0	56 00 29.0	232 46 47.4
2013 Feb 14	23:03:00.0	56 07 54.5	233 02 22.9
2013 Feb 14	23:04:00.0	56 15 21.4	233 17 56.0
2013 Feb 14	23:05:00.0	56 22 49.9	233 33 26.8
2013 Feb 14	23:06:00.0	56 30 19.8	233 48 55.1
2013 Feb 14	23:07:00.0	56 37 51.3	234 04 21.0
2013 Feb 14	23:08:00.0	56 45 24.2	234 19 44.6
2013 Feb 14	23:09:00.0	56 52 58.5	234 35 05.8
2013 Feb 14	23:10:00.0	57 00 34.3	234 50 24.7
2013 Feb 14	23:11:00.0	57 08 11.5	235 05 41.2
2013 Feb 14	23:12:00.0	57 15 50.2	235 20 55.5
2013 Feb 14	23:13:00.0	57 23 30.2	235 36 07.4
2013 Feb 14	23:14:00.0	57 31 11.7	235 51 17.0
2013 Feb 14	23:15:00.0	57 38 54.5	236 06 24.4
2013 Feb 14	23:16:00.0	57 46 38.7	236 21 29.5
2013 Feb 14	23:17:00.0	57 54 24.3	236 36 32.3
2013 Feb 14	23:18:00.0	58 02 11.2	236 51 32.9
2013 Feb 14	23:19:00.0	58 09 59.4	237 06 31.2
2013 Feb 14	23:20:00.0	58 17 48.9	237 21 27.3
2013 Feb 14	23:21:00.0	58 25 39.8	237 36 21.2
2013 Feb 14	23:22:00.0	58 33 31.9	237 51 12.9
2013 Feb 14	23:23:00.0	58 41 25.3	238 06 02.5
2013 Feb 14	23:24:00.0	58 49 20.0	238 20 49.8
2013 Feb 14	23:25:00.0	58 57 16.0	238 35 35.0
2013 Feb 14	23:26:00.0	59 05 13.2	238 50 18.1
2013 Feb 14	23:27:00.0	59 13 11.7	239 04 59.0
2013 Feb 14	23:28:00.0	59 21 11.3	239 19 37.8
2013 Feb 14	23:29:00.0	59 29 12.2	239 34 14.5
2013 Feb 14	23:30:00.0	59 37 14.3	239 48 49.1
2013 Feb 14	23:31:00.0	59 45 17.5	240 03 21.6
2013 Feb 14	23:32:00.0	59 53 22.0	240 17 52.1
2013 Feb 14	23:33:00.0	60 01 27.6	240 32 20.5
2013 Feb 14	23:34:00.0	60 09 34.4	240 46 46.8
2013 Feb 14	23:35:00.0	60 17 42.3	241 01 11.2
2013 Feb 14	23:36:00.0	60 25 51.3	241 15 33.5
2013 Feb 14	23:37:00.0	60 34 01.5	241 29 53.8
2013 Feb 14	23:38:00.0	60 42 12.8	241 44 12.1

Table 2: Zenith and azimuth celestial coordinates for Betelgeuse (156).

Our goal is comparing the actual position of stars and planets on the image with the one predicted by the linear simultaneous equations to test the reliability of 2.1 and 2.2.

2.4.1 Testing of the lens projection

Before starting with any quantitative analysis it has been necessary to select clear sky nights. Reading the time when the image was taken is essential for synchronization. For this purpose if only "JPG"* data is available a specific function that read the time directly from the image has been written in Matlab. A red rectangle, drawn in Figure 2-19, indicates date and time when the JPG was taken. The main part of the function consists of an optical character recognition algorithm that detects the white pixels (by contrast with the black background) forming the date and time. In case of "FITS"**(flexible image transport system) data the date and time are specified in the header of the file so no specific function is required. Figure 2-19 and Figure 2-20 show the same image in the two different formats.

*jpgs data are available in gray-scale for night-time data whereas in true colour for the day-time ones

**The FITS file format is the standard data format used in astronomy, endorsed by both NASA and the International Astronomical Union (IAU). A data file in FITS format can contain multiple components, each marked by an ASCII text header followed by binary data (184).

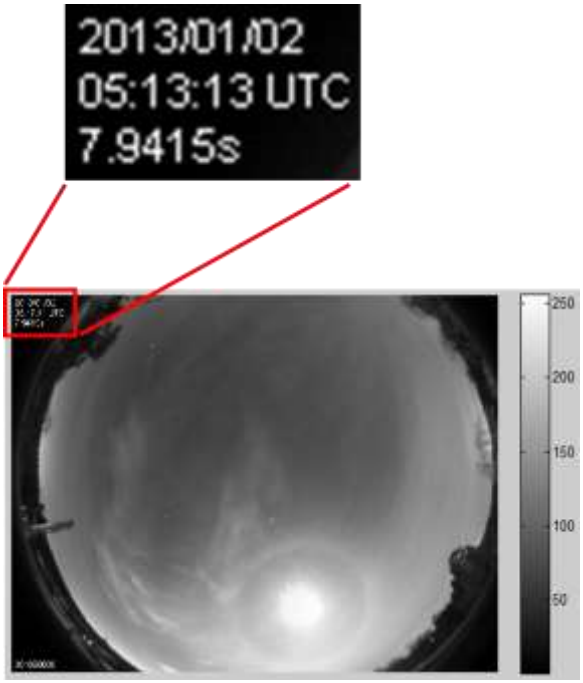

Figure 2-19: JPG format - Bayfordbury 2nd of January 2013, 05:17 am.

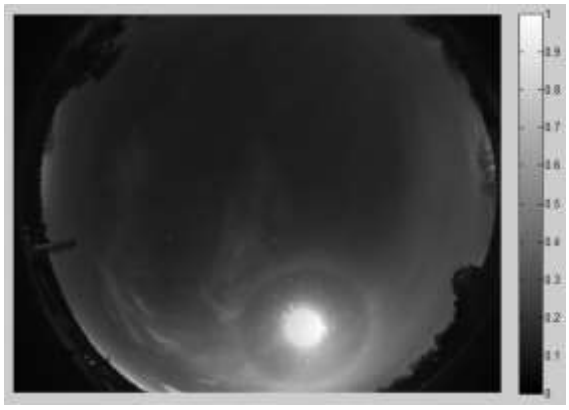

Figure 2-20: FITS format - Bayfordbury 2nd of January 2013, 05:17 am.

Once the time has been read and a specific celestial object among those present in the sky has been chosen, by reading a lookup table as the one shown in Table 2, it is possible to associate each image to the corresponding *A* and *z* coordinates of the celestial body centre and then through Eq. 2.1 and 2.2 it is possible to find its pixel coordinates *x* and *y*. To measure the actual position of stars/planets a detection scheme has been applied; it is based on locating the bright spot that defines the star/planet position. For this purpose JPG images from the night-time camera have been used. By selecting an appropriate brightness threshold and turning the image into binary it is possible to identify all the bright spots present in the sky and representing stars and planets (see Figure 2-21). With respect to the specific planet or star chosen, its pixel coordinates as predicted through Eq. 2.1 and 2.2 are known.

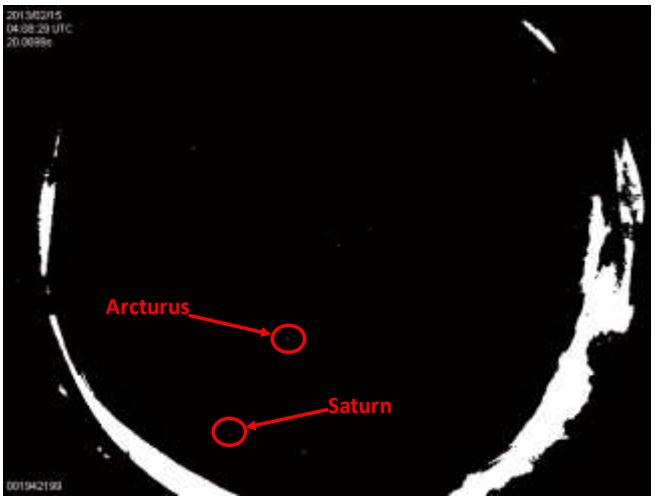

Figure 2-21: Binary image, based on threshold - the white spots represent the actual position of stars/planets.

From the binary image a square region centred where the star is predicted to be (*x*,*y*) has then been taken into account (see Figure 2-22). This region should be sufficiently large to include the white spot representing the actual position.

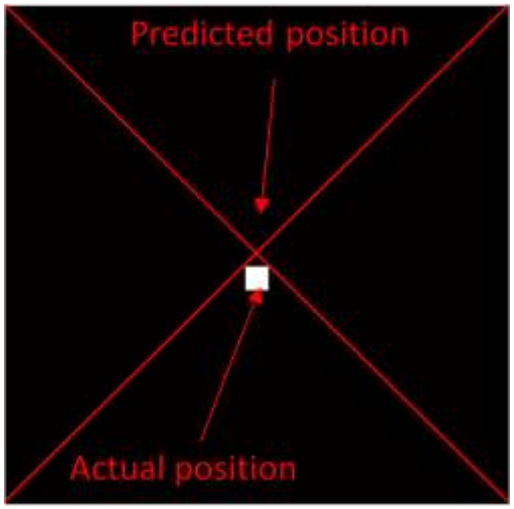

Figure 2-22: The white spot represents the star/planet position: in general the white spot doesn't coincide with the black region centre that individuates the predicted star location.

The centre of mass of the white spot will represent the actual position of the star/planet. The procedure described for detecting the actual planet/star position has been coded in a script written in Matlab.

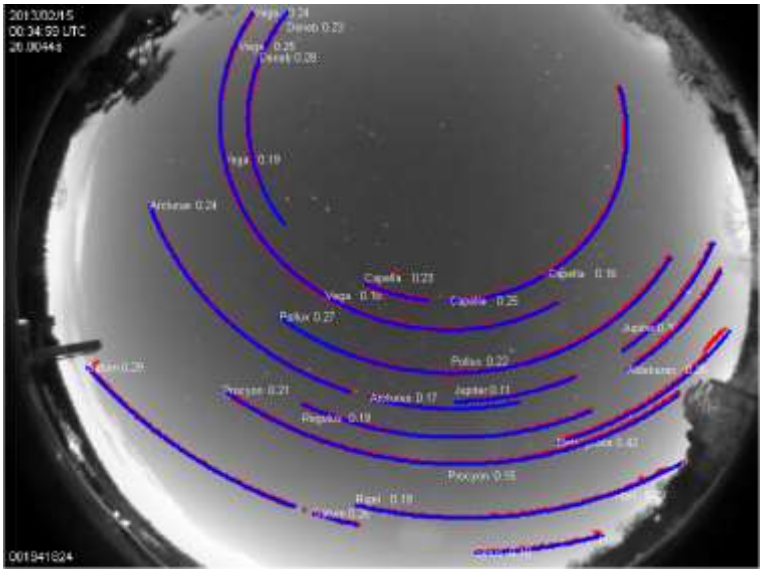

Figure 2-23: Predicted (blue dots, from eq. 1 and 2) and actual (red dots) Stars and planets trajectories comparison.

In Figure 2-23 predicted (blue dots) and actual object positions (red dots) are shown. The mean difference between predicted and actual position is less than 0.5^{o}. By knowing that the actual position could be evaluated with more accuracy and also that the accuracy of the method goes down as we approach the horizon because of the light coming from the surrounding towns, it seems reasonable to state that the lens projection is well replicated by the linear simultaneous equations (2.1 and 2.2). However the fact that the lens uses a linear projection does not solve the fact that the

light source centre and zenith never coincide. It is essential for us to take this into account if we are interested in evaluating correctly the SPF (more precisely the image brightness against the scattering angle) of the ice cloud or in other words the light scattered by the cirrus as a function of the angular distance from the light source centre.

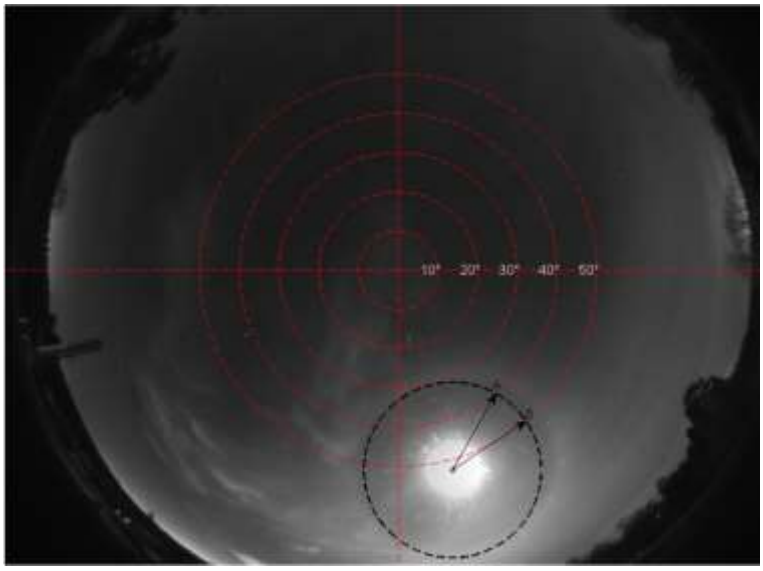

Figure 2-24: Lens projection and light source off zenith (149).

Figure 2-24 shows that a geometric correction is needed. Any pair of points (A,B) equidistant in terms of pixels from the light source centre do not represent points at the same scattering angle. This means that we cannot average their corresponding pixel brightness. This will be the case every time that the light source is off zenith.

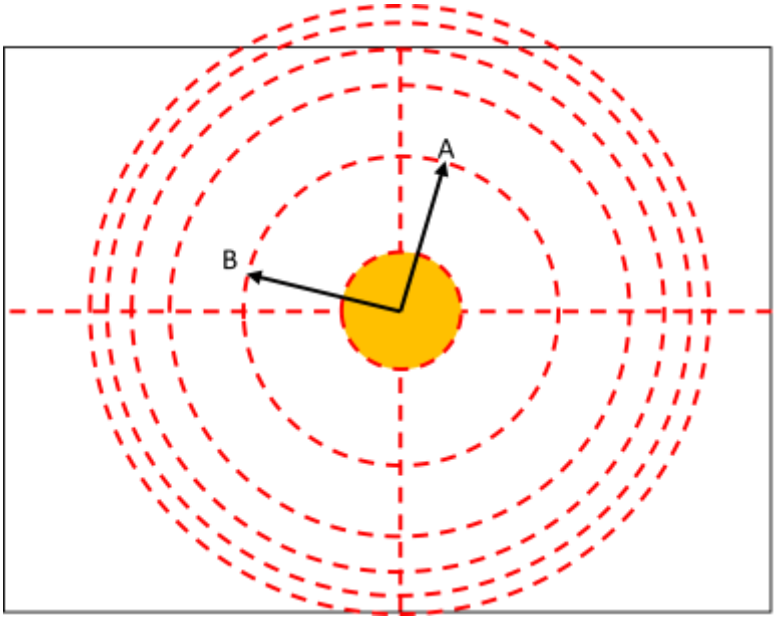

Figure 2-25: Lens projection and light source at zenith.

If we look at Figure 2-25 instead we notice that if the light source centre coincides with the zenith, A and B will then represent points which are equidistant in terms of scattering angle. In the next paragraph a solution to the image distortion problem is presented.

2.5 Geometric distortion problem (method)

In order to solve the issue of the distortion several steps have to be implemented; the general idea consists of transforming the all-sky image as if the light source were located at zenith; what we expect is that the halo would then look circular, as shown in Figure 2-26. This would confirm that the transformation is working correctly.

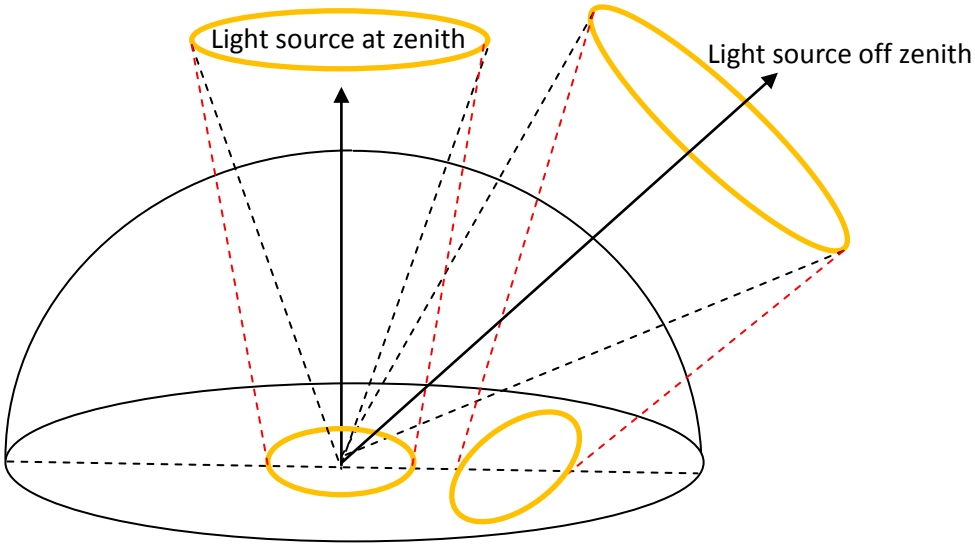

Figure 2-26: Halo shape would be circular if the light source were at zenith.

What we have seen by following the stars/planets trajectories is that any incoming ray travelling along a direction specified by *z* is projected onto the camera plane at a distance from the optical centre (OC=LFA) of the image that is proportional to the zenith distance of the corresponding incoming ray as Figure 2-27 shows.

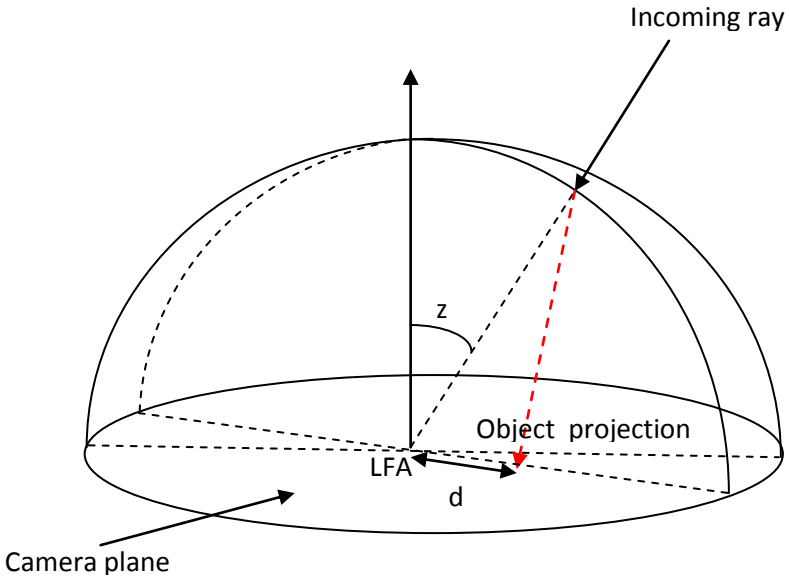

Figure 2-27: Camera projection: rays coming from zenith distance *z* will be projected at a pixel distance from the LFA proportional to *z*.

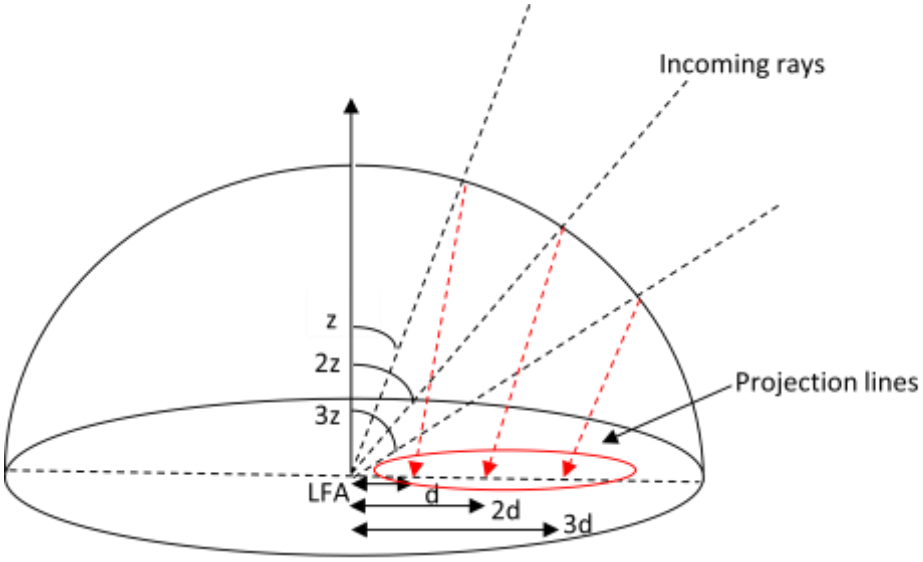

Figure 2-28: Equidistant projection camera.

This type of projection is called "equidistant" projection (see Figure 2-28) because rays coming from zenith distances *z*, 2*z*, 3*z* respectively will be projected onto the camera plane at distances, from the optical centre (LFA), that are directly proportional to the *z*. What we want to do is to implement a rotation of the light source in such a way that its centre coincides with the zenith. In other words we want to remap the image in such a way that it will appear as if the light source were at zenith (see Figure 2-29).

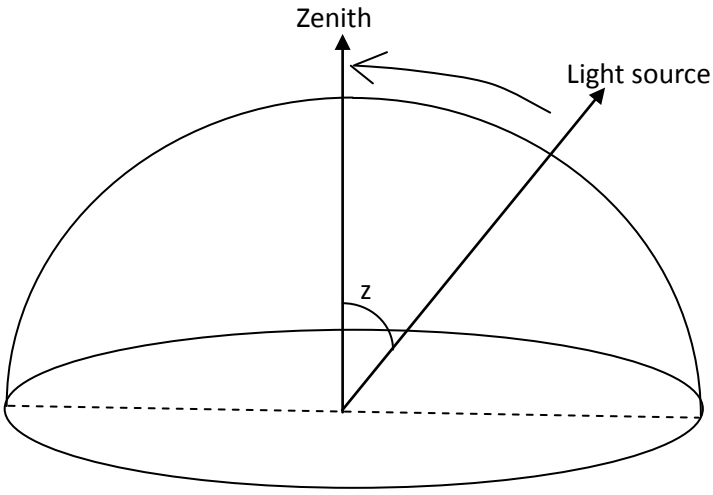

Figure 2-29: Rotation on the sphere.

Before implementing such a rotation in spherical coordinates a further step must be implemented; it consists of changing the projection from being "linear" with respect to *z* to being proportional to the "*sine*" of *z* (see Figure 2-30). In other words we want to remap the original image onto a sphere. This is essential if we want to rotate the image in spherical coordinates by using a rotation matrix.

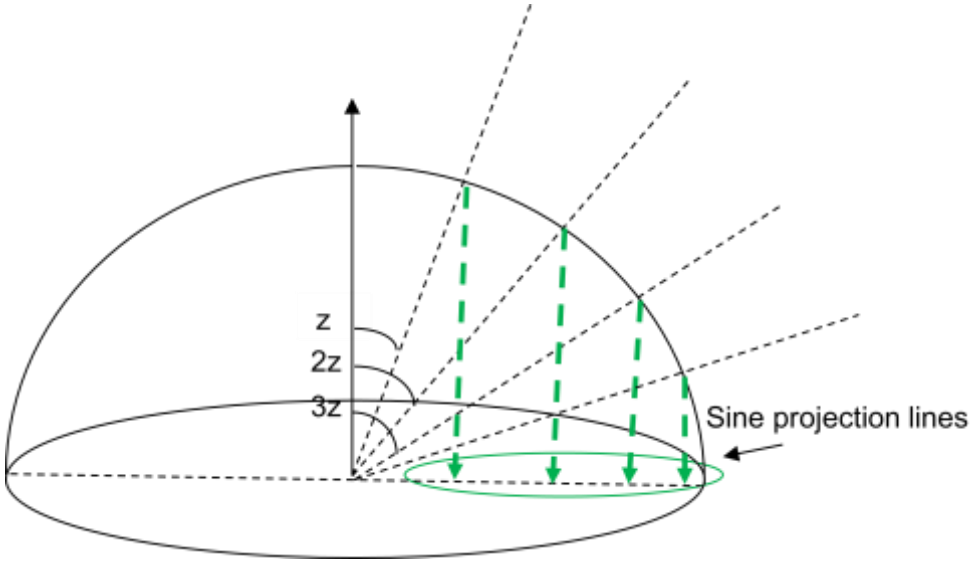

Figure 2-30: Sine projection: this is equivalent to mapping the original image onto a sphere of arbitrary radius.

For changing projection every pixel in the original image has to be associated with the corresponding *z* coordinate. This is done by means of Eq. 2.3. Given that the lens sees objects below the horizon as demonstrated by the presence of trees those points have $z > 90^{o}$. The change of projection can be seen as the wrapping of the image around a sphere of arbitrary radius *R*. With respect to Figure 2-17 the periphery of the image which is below the horizon will be projected in the southern hemisphere while all the points above the horizon will appear in the northern hemisphere. Figure 2-31 and Figure 2-32 show the original image above (a) and below (b) the horizon.

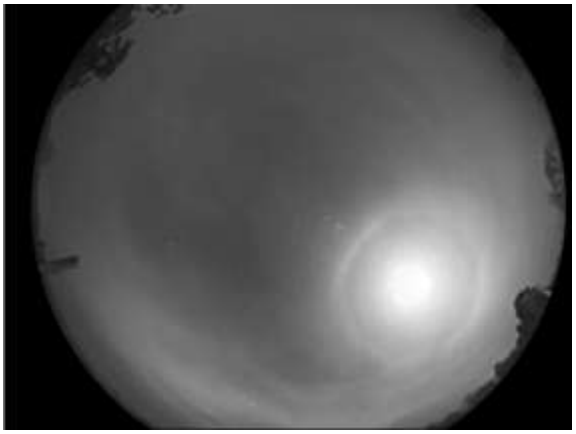

Figure 2-31: Original image above the horizon.

Figure 2-32: Original image below the horizon.

$$d(px) = fz(^{\circ}) \tag{2.3}$$

Once *z* is evaluated for each pixel (see Eq. 2.3) the new position is recalculated as the product of the sine of *z* times *R* by means of Eq. 2.4

$$d_{new}(px) = R\sin(z(rad)) \tag{2.4}$$

The next step consists of rotating the image in spherical coordinates; given that this rotation takes place in three dimensions, we have to give each image pixel (defined by a pair of *x* and *y* coordinates) an additional *Z* coordinate (see Figure 2-33);

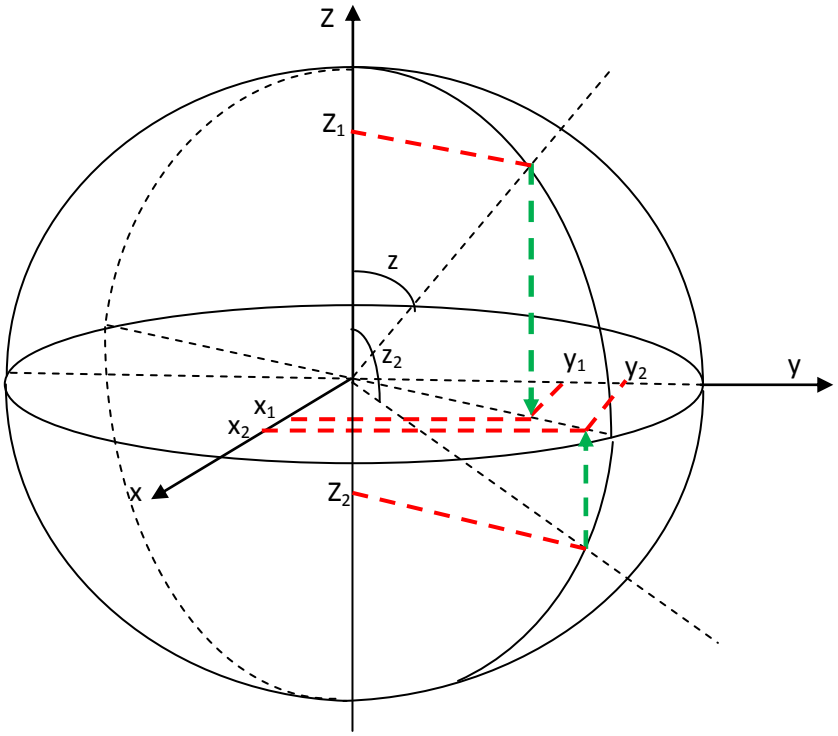

Figure 2-33: Spherical coordinates.

From the above reasoning it should be clear that the part of the original image that is below the horizon has to be associated to a negative *Z* while the other way around for points above the horizon. Once every image pixel is associated to the proper triple (x_1, y_1, Z_1) a rotation matrix **R** (see Eq. 2.5) has to be used to perform the rotation around the unit vector *u* that is perpendicular to the line linking LFA and the light source (LS) (see Figure 2-36).

Two methods have been used to implement such a geometric transformation:

1. **Re-mapping**
2. **Interpolation**

2.5.1 Re-Mapping method

A possible approach to change the projection of the image consists of remapping pixel by pixel the original image onto a new one; in the new image the new pixel location is calculated according to Eq. 2.4 which implies a redistribution of the pixels over a sphere of radius *R* as Figure 2-35 shows. It is the portion of the original image above the horizon wrapped around the sphere. In this respect pixels found below the horizon (see Figure 2-34) would be seen in the southern hemisphere and should be taken into account if a full reconstruction of the image after rotation has to be achieved. For sake of clarity this will be shown for this specific case.

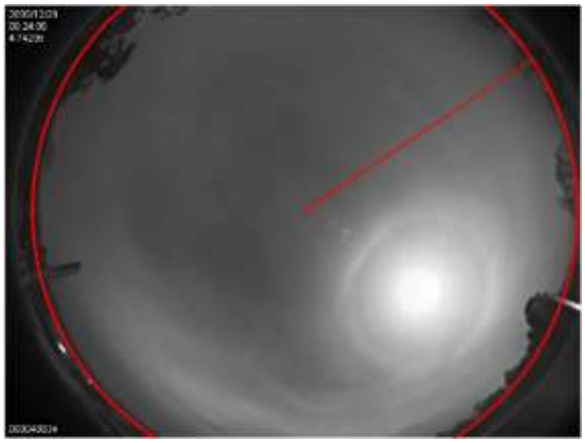

Figure 2-34: Original JPEG image.

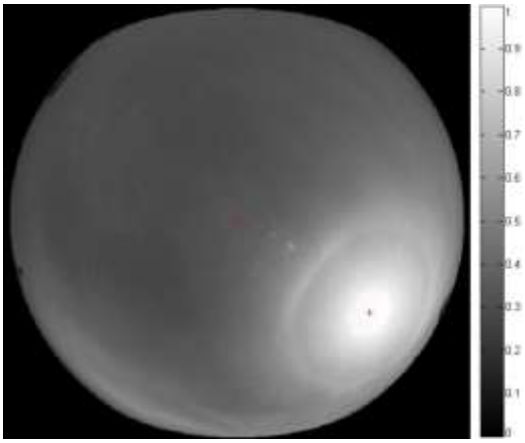

Figure 2-35: Sine projected image.

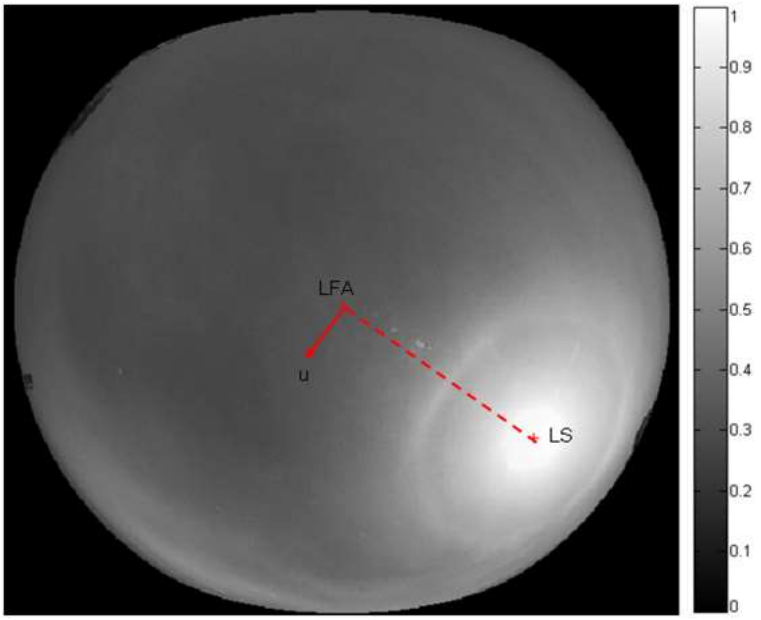

Figure 2-36: Unit vector identifying the direction around which rotation has to take place.

The rotation angle will depend on the light source position and its angular distance from zenith. The position of the light source is calculated through equations 2.1 and 2.2 as explained in section 2.4 and recalculated in the new coordinates system.

$$R = \begin{Bmatrix} \cos\theta + u_x^2(1-\cos\theta) & u_x u_y(1-\cos\theta) - u_z \sin\theta & u_x u_z(1-\cos\theta) - u_y \sin\theta \\ u_x u_y(1-\cos\theta) - u_z \sin\theta & \cos\theta + u_y^2(1-\cos\theta) & u_y u_z(1-\cos\theta) - u_x \sin\theta \\ u_x u_z(1-\cos\theta) - u_y \sin\theta & u_y u_z(1-\cos\theta) + u_x \sin\theta & \cos\theta + u_z^2(1-\cos\theta) \end{Bmatrix} \quad (2.5)$$

With the application of the rotation matrix **R** the outcome of the image transformation, for the northern hemisphere, is the one Figure 2-37 shows. Pixels that belong to those portions of the image that after rotation would be below the horizon are visible in the southern hemisphere (see Figure 2-38). It is essential to account for these regions of the image if a measure of the SPF for SA > 90^o is

needed. However being interested in the measure of the HR, over the next paragraphs calculations of the SPF will be limited to SA <= 90^{o}.

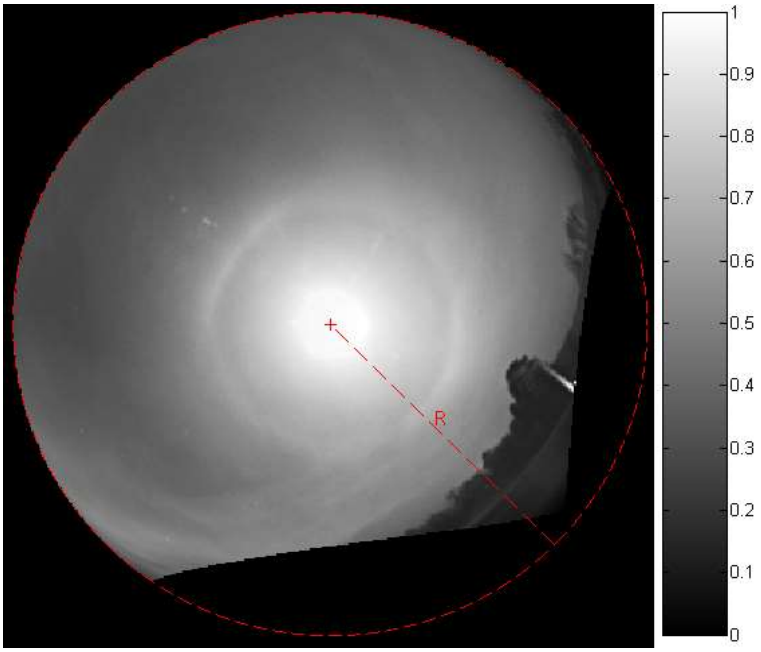

Figure 2-37: Image after remapping and rotation (northern hemisphere) - notice the radius R of the sphere the image is wrapped around.

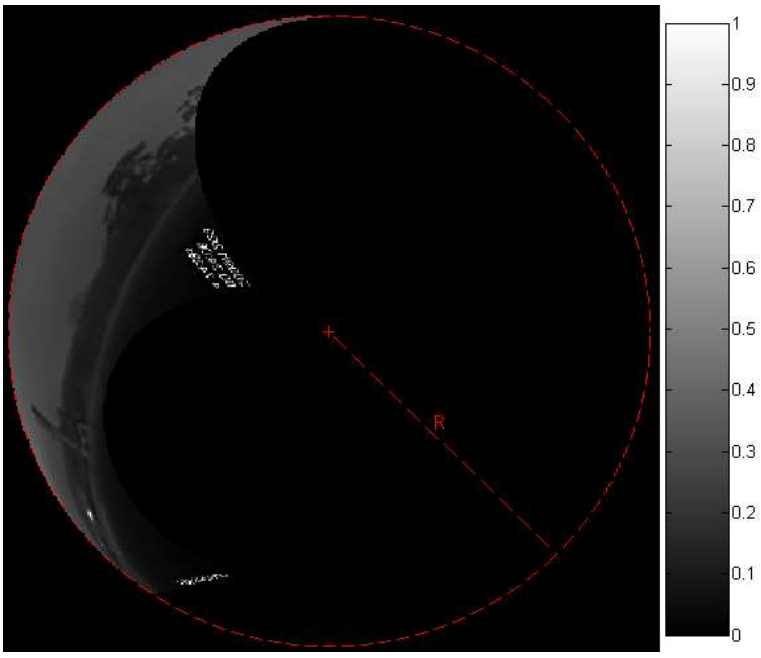

Figure 2-38: Image after remapping and rotation (southern hemisphere) - R is the radius of the sphere the image is wrapped around.

Once the rotation has been implemented, we can use the transformed image to calculate the brightness as a function of the distance from the light source centre.

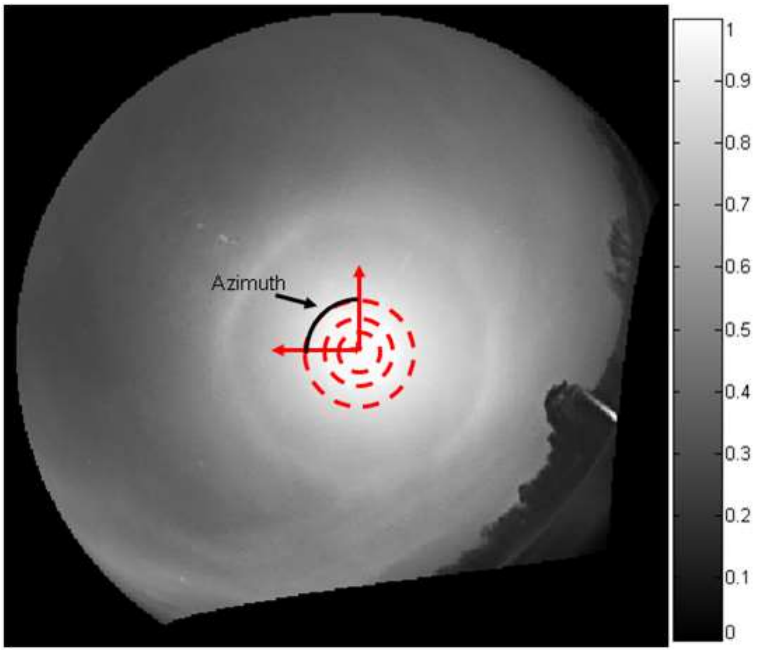

Figure 2-39: Image after both the change of projection and the rotation.

A system of coordinates has to be centred in the light source centre and then the brightness averaged over *A* (see Figure 2-39). It should be specified that the scattering phase function so measured is not the phase function of a single particle but it is rather the phase function for a cloud, which is an average phase function representative of the ice crystal habits composing the cloud, and includes phenomena such as multiple scattering, geometric influences such as airmass (to be corrected for later in this chapter), or ground reflections.
Figure 2-40 shows the comparison between the brightness obtained by using off zenith source centred coordinates (original image) and zenith source centred coordinates (geometric corrected image).

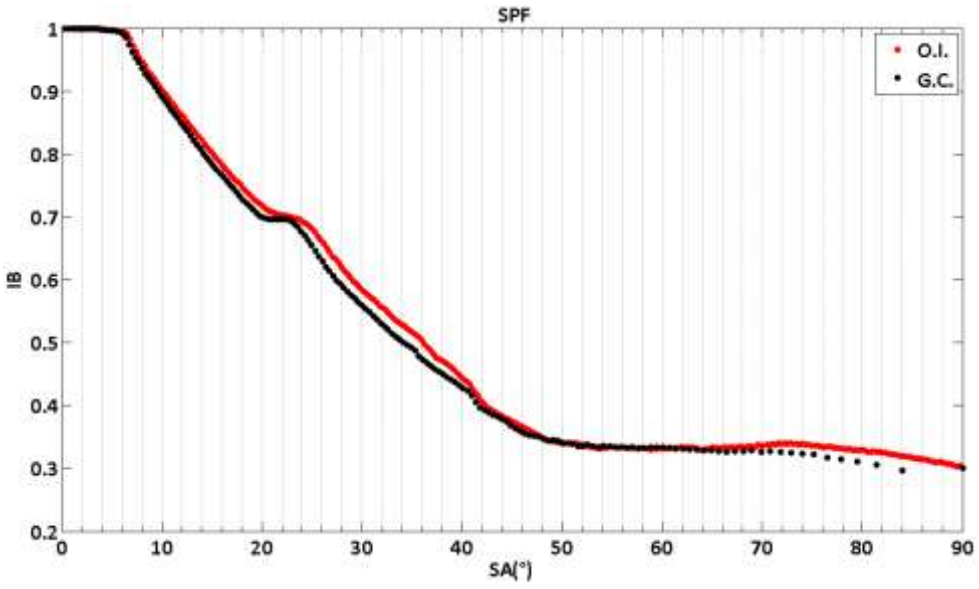

Figure 2-40: Phase function before (red dot) and after (black dot) geometric correction (from JPEG image -Figure 2-34).

Transforming the image in such a way that the light source coincides with the zenith allows us to get a sharper halo peak. However, one additional distortion is present where JPEG images are the only available ones. This reflects on the fact that the image brightness is 1 for scattering angles up to 6º while the angular size of the light source is smaller than that. The dynamic range, insufficient to cover the spread of intensity values, associated with saturation at low angles, and the characteristic compression that JPEGs undergo, due to "digital development" processing (DDP), do not allow many orders of magnitude of intensity to be captured across the image. A larger brightness range and a sharper halo peak are obtained when FITS data are used. To show the difference arising from using one type of data rather than another, the mapping method has been applied to the same image for both types of data for comparison (see Figure 2-41 and Figure 2-42). This is an image taken at the observatory of Bayfordbury on January the 2nd, 2013 at 05:17 am.

Figure 2-41: JPEG original data - image taken on the 2nd of January 2013 05:17 am.

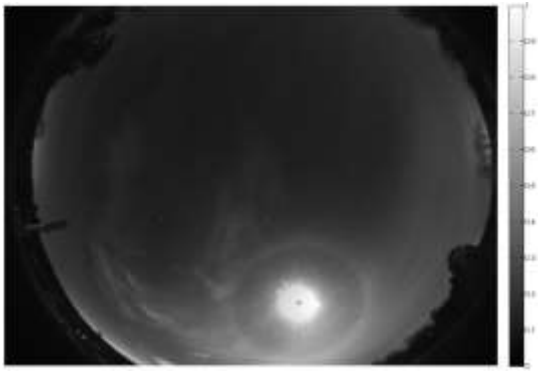

Figure 2-42: FITS original data - image taken on the 2nd of January 2013 05:17 am.

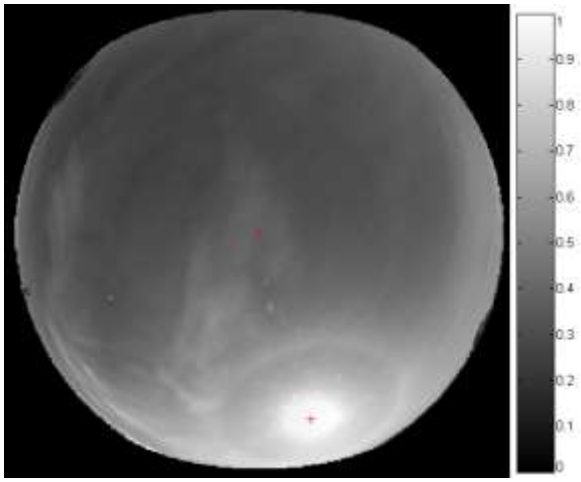

Figure 2-43: JPEG sine projected.

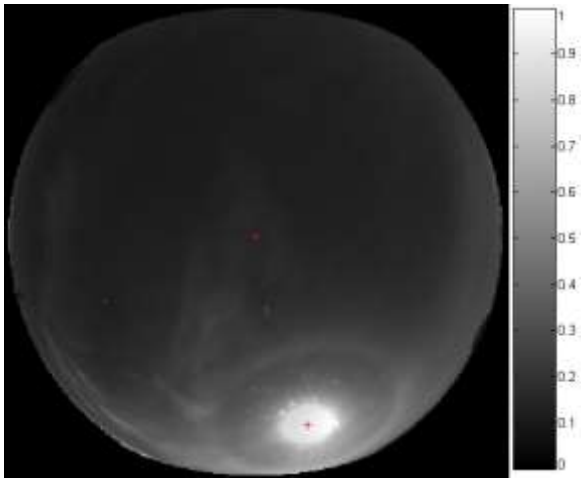

Figure 2-44: FITS sine projected.

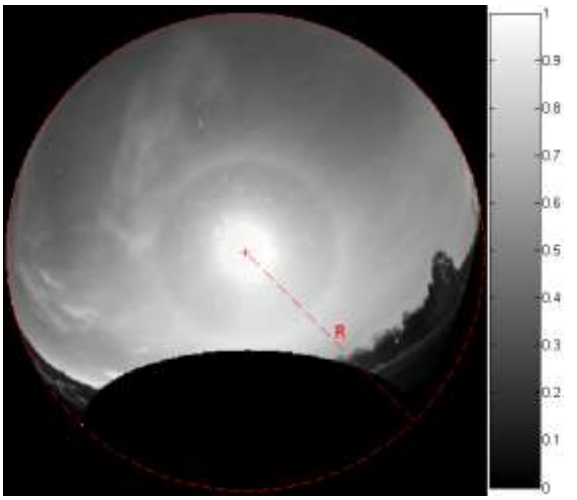

Figure 2-45: JPEG after rotation.

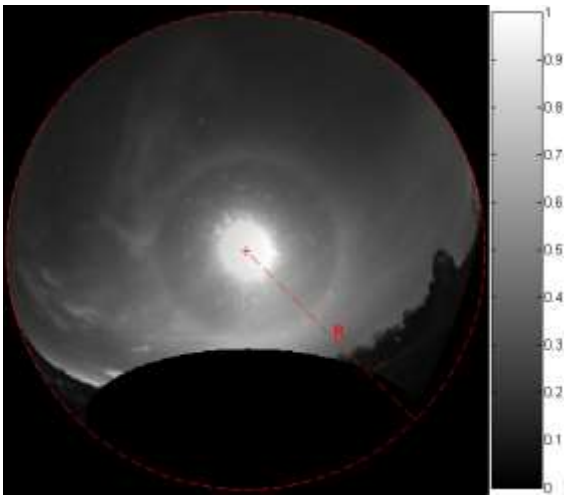

Figure 2-46: FITS after rotation.

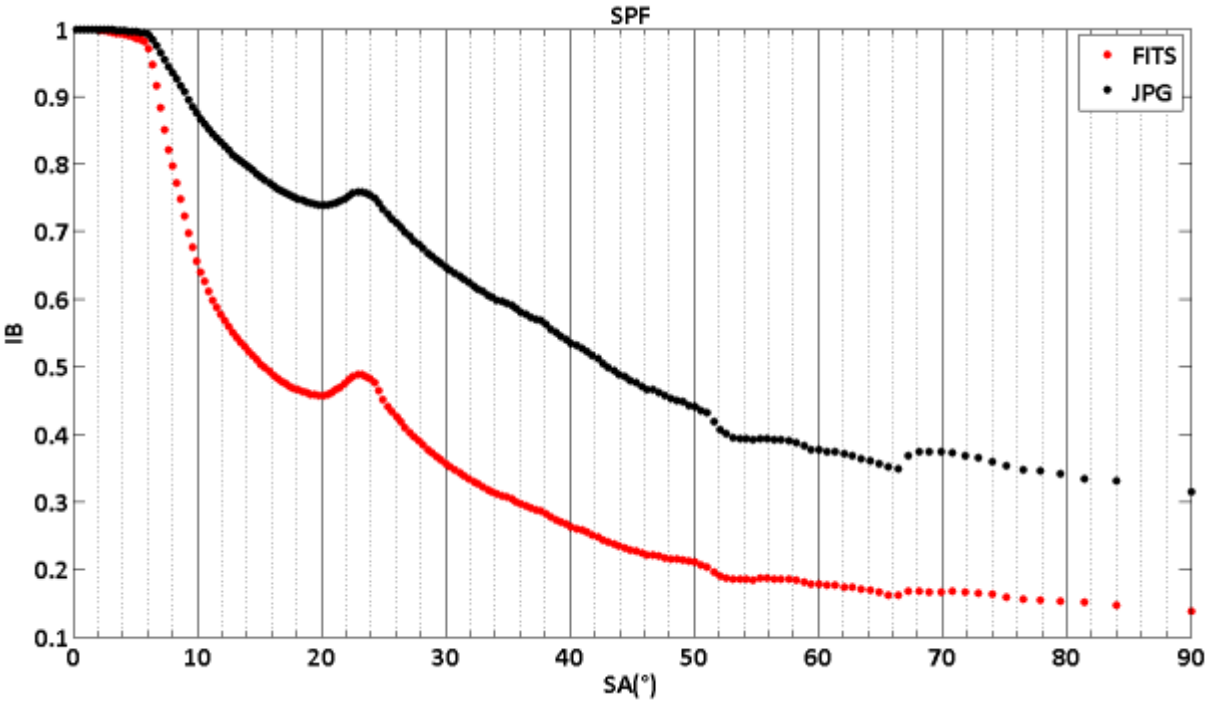

Figure 2-47: Image brightness vs scattering angle comparison.

The main difference is that JPG brightness has much narrower dynamic range than FITS. This is due to DDP applied to JPG images. For this reason, when available, FITS data have been preferred to JPG data. However, in the coming paragraph 2.5.2 the phase function corresponding to the 28th of Dec 2009 at 00:24 am (see Figure 2-53) and the 03rd of Aug 2012 at 01:24 pm (see Figure 2-67) have been calculated using the respective JPG images (see Figure 2-51 and Figure 2-52 for the 28th of December and Figure 2-58, Figure 2-59 and Figure 2-60 for the 03rd of August respectively) being FITS data not available for these specific cases. On the other hand Figure 2-48 and Figure 2-49 are the FITS images corresponding to the phase function shown in Figure 2-50 and analogously Figure 2-54, Figure 2-55, Figure 2-56 are the FITS images corresponding to the phase function shown in Figure 2-57.

2.5.2 Interpolation method

With this alternative method it is possible to implement the same image transformation that has been presented in the previous paragraph with the remapping method.
It can be achieved in two main steps:

1. **Coordinate transformation**
2. **Interpolation to get the transformed image**

The coordinate transformation can be divided into three sub-steps:

1. **Generation of a grid of Cartesian coordinates coinciding with the image and centred in the optical centre of the image x_0, y_0**
2. **Switching from Cartesian to polar coordinates and transformation of the radial coordinate through Eq. 2.4 to obtain the "sine projection"**
3. **Switching from polar to Cartesian coordinates to rotate the coordinate system using the same rotation matrix R shown in Eq. 2.5 (before rotating the image a *Z***

coordinate has to be associated with each image pixel analogously to what was shown in section 2.5)

The interpolation itself can be divided into two sub-steps:

1. **Definition of a set of grid points where we want the image to be interpolated**
2. **Interpolation of the image, for example by using the Matlab built-in function "griddata"**

Figure 2-48 shows the same night-time image (2nd of January 2013 at 05:17 am) as Figure 2-42. This time it is interpolated (see Figure 2-49) and the SPF, calculated with both methods, compared in Figure 2-50. Very close match is apparent.

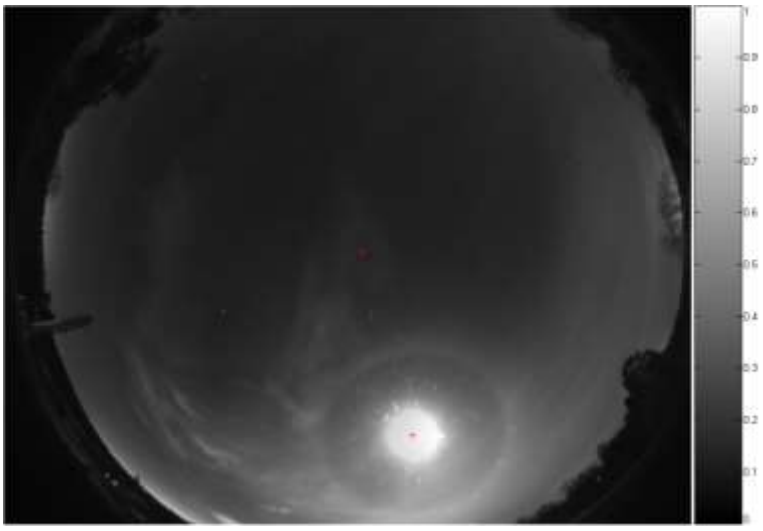

Figure 2-48: Original FITS data: 2nd of January 2013 at 05:17 am.

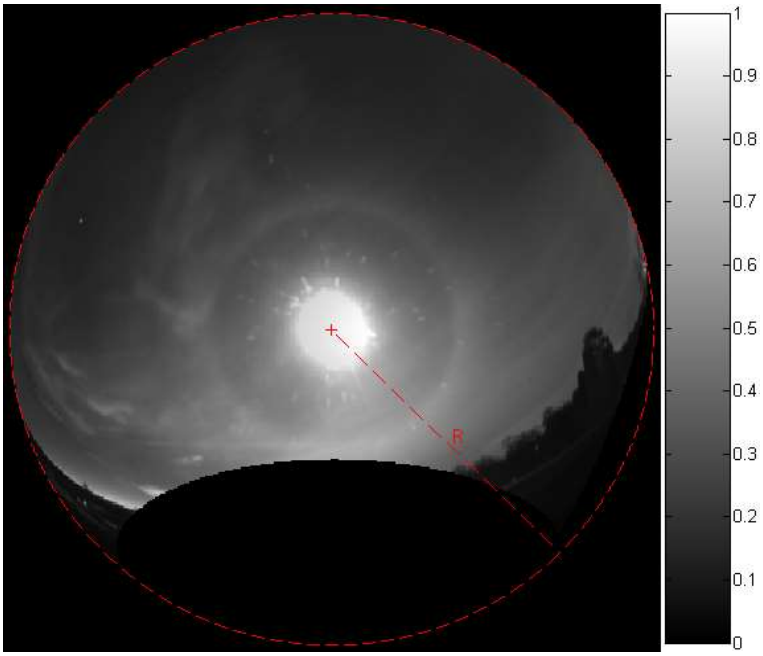

Figure 2-49: Interpolated FITS image corresponding to Figure 2-48 (Cartesian representation).

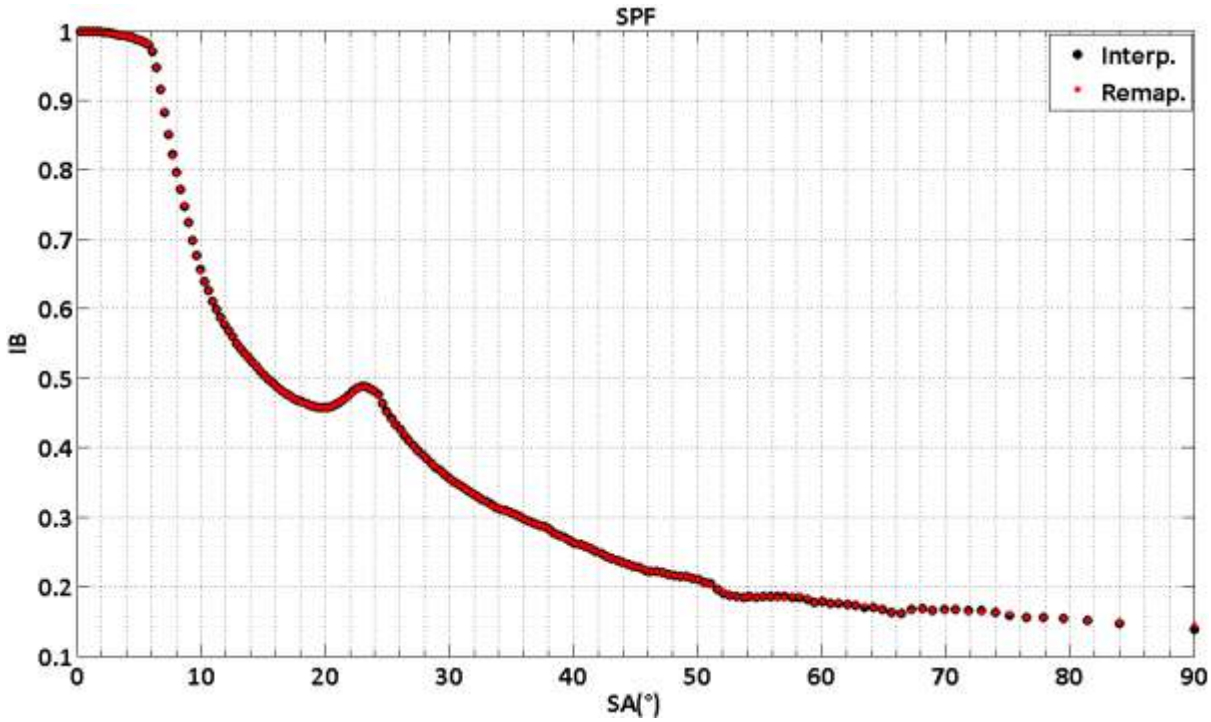

Figure 2-50: Comparison between remapping and interpolation methods when applied to the image of Figure 2-48 (FITS image - 2nd of January 2013 at 05:17 am).

Analogously the two methods have been applied to the image data that Figure 2-34 shows. Figure 2-51 is the transformed image obtained by the remapping method, Figure 2-52 the one obtained

through interpolation and Figure 2-53 the comparison of the corresponding SPFs. Results are in close agreement.

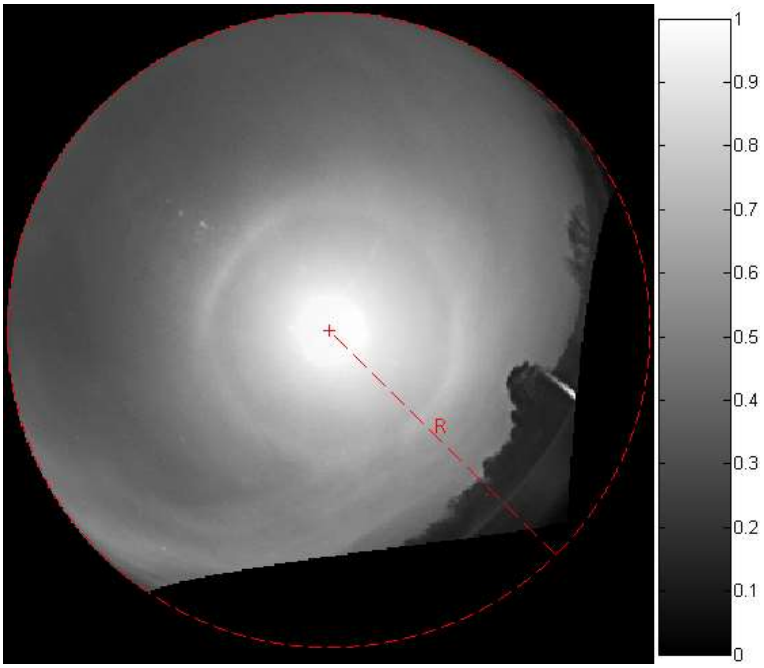

Figure 2-51: Remapped JPEG image corresponding to Figure 2-34.

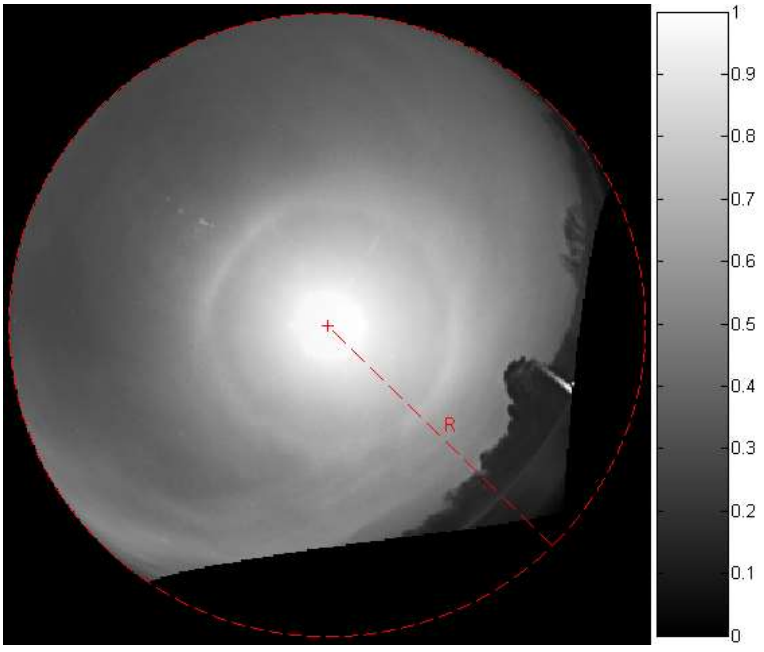

Figure 2-52: Interpolated JPEG image corresponding to Figure 2-34.

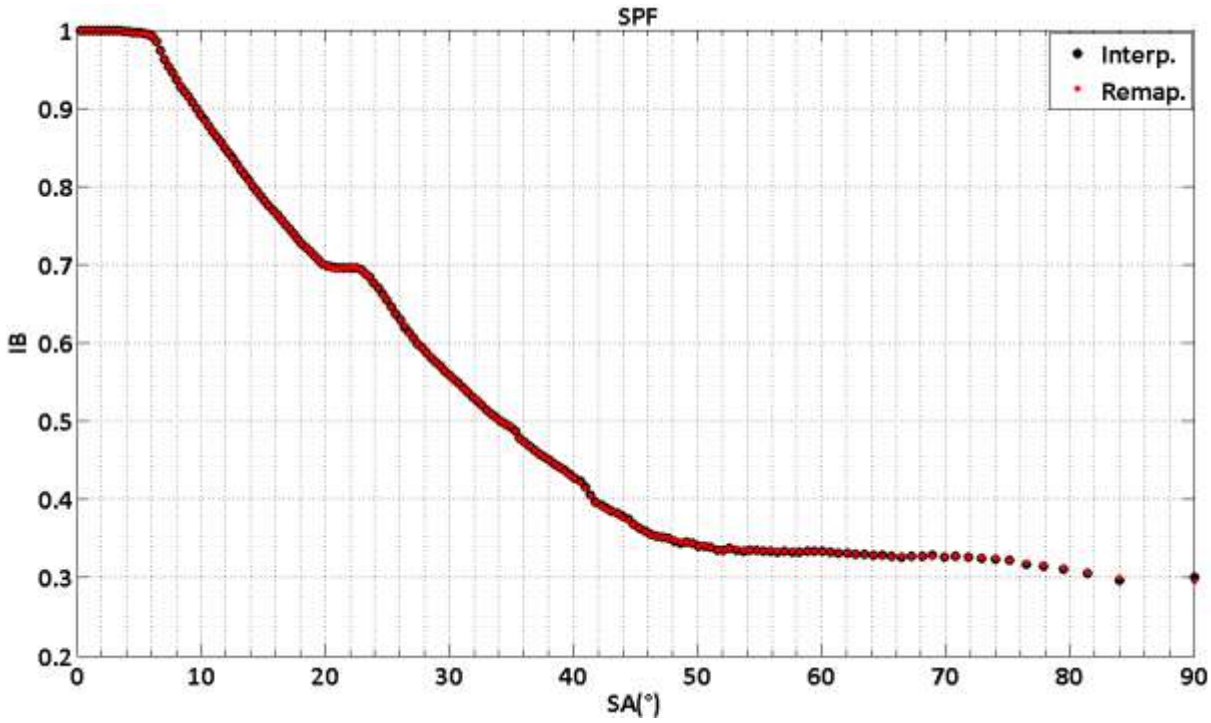

Figure 2-53: Comparison between remapping and interpolation methods when applied to the image of Figure 2-34 - (JPEG image - 28-Dec-2009 - 00:24 am).

The same comparison has been done for the image taken on the 01st of Nov 2009 at 09:16 pm (Figure 2-54) and on the 03rd of Aug 2012 at 01:24 pm (Figure 2-58). Figure 2-55, Figure 2-56 and Figure 2-57 show the outcome of the remapping method, the image after interpolation, and the corresponding SPFs comparison for the first case whereas Figure 2-59, Figure 2-60 and Figure 2-67 for the second case respectively. Significant differences between the SPFs calculated through the two methods are not observed. However, as far as remapping is concerned, due to rounding errors multiple pixels in the original image can happen to correspond, according to the transformation of coordinates, to the same pixel in the destination image. This can cause the presence of empty pixels in the transformed image unless iteration were done over the pixels of the destination image and the inverse transformation were used in place of the direct one, which would further complicate calculations. Hence between the two methods, interpolation is the preferable choice.

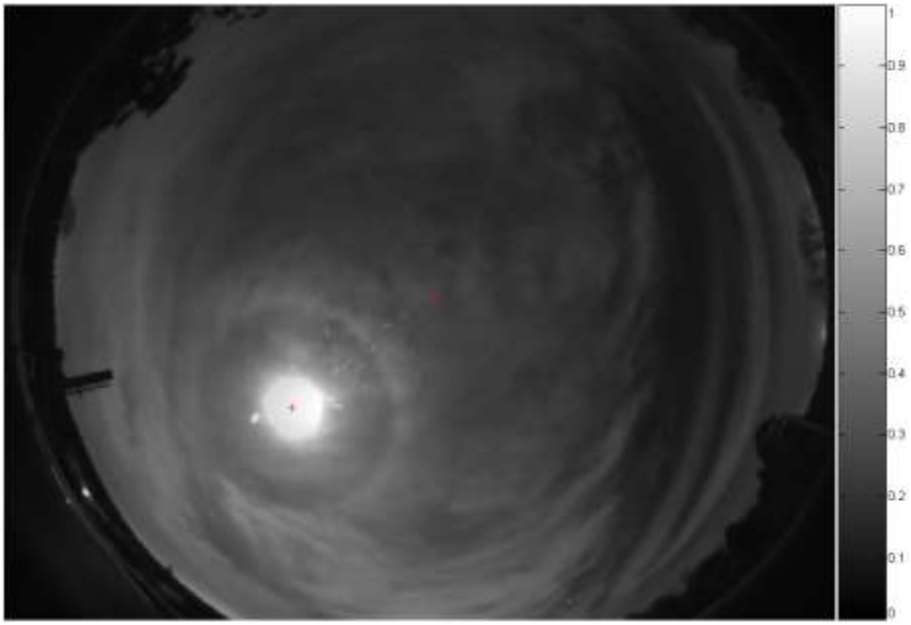

Figure 2-54: Original FITS image 01-Nov-2009-09:16 pm.

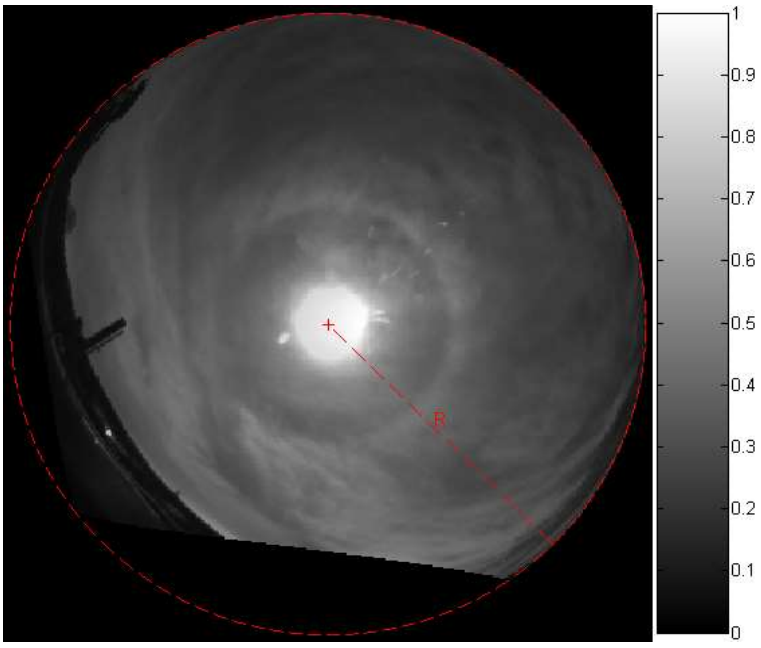

Figure 2-55: Remapped FITS image corresponding to Figure 2-54.

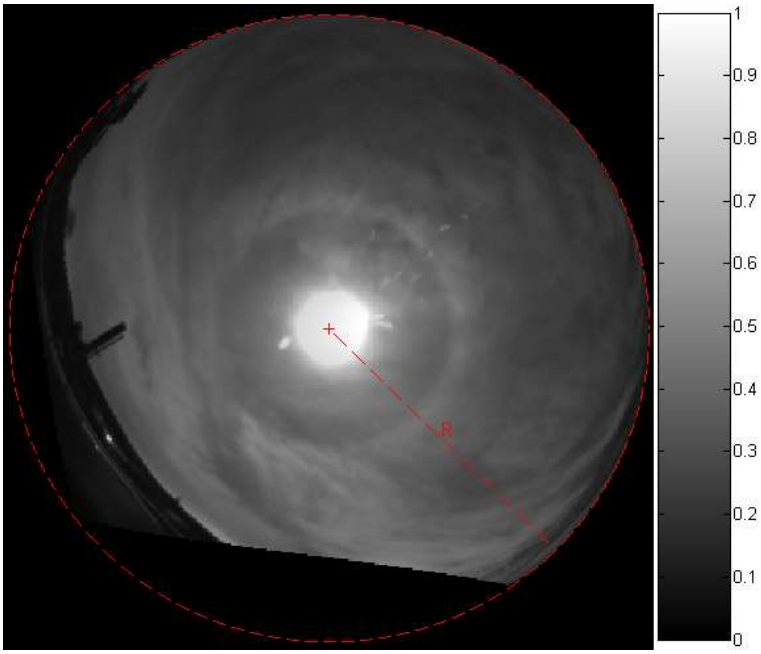

Figure 2-56: Interpolated FITS image corresponding to Figure 2-54.

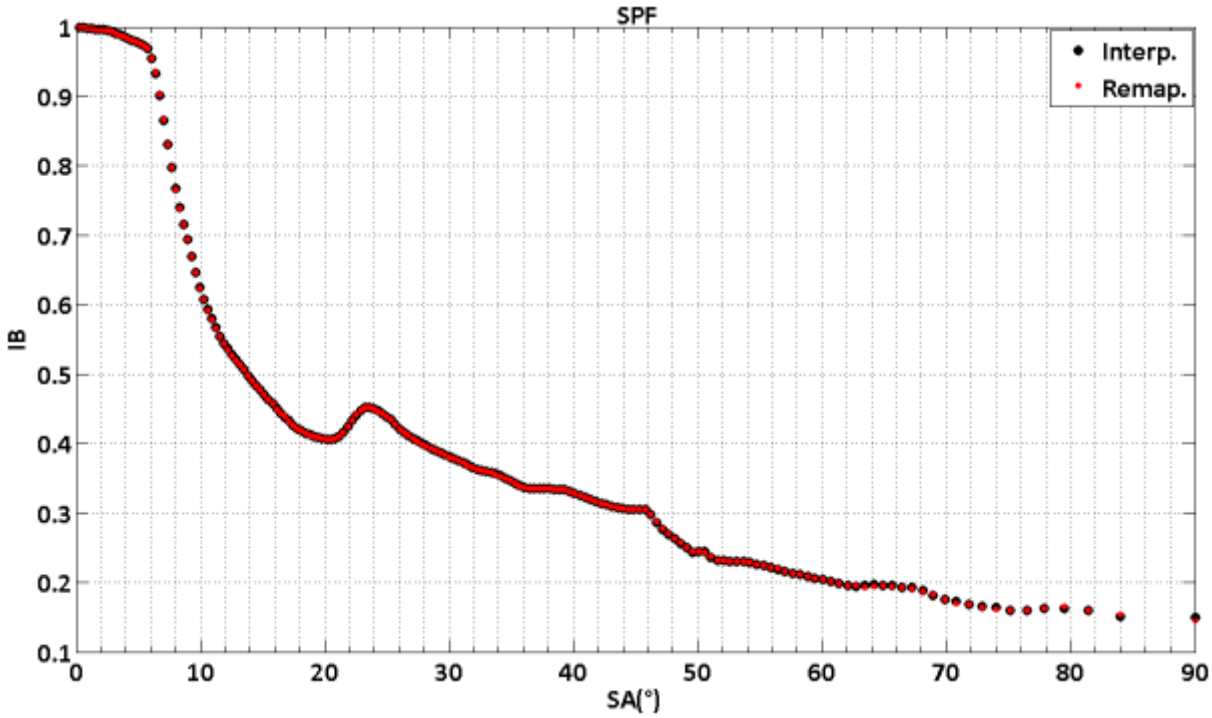

Figure 2-57: Comparison between the remapping and the interpolation methods when applied to the image of Figure 2-54 (FITS image - 01-Nov-2009 - 09:16 pm).

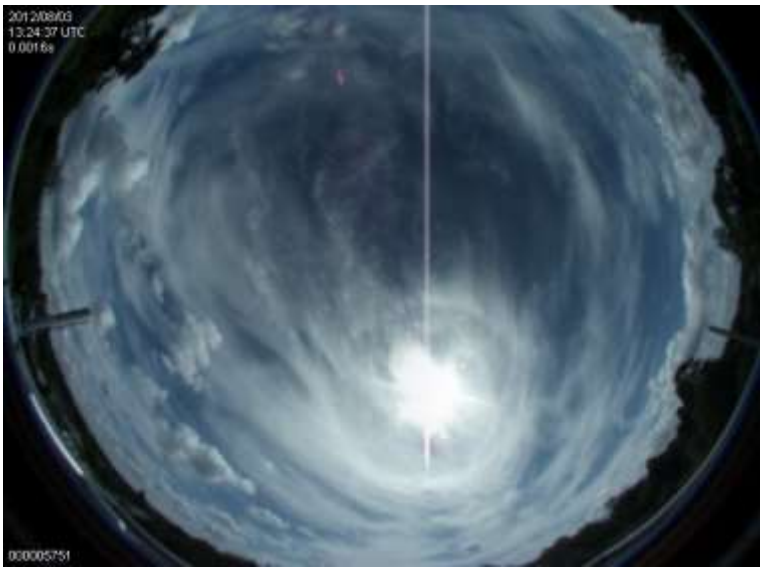

Figure 2-58: Original JPEG image(03-Aug-2012-01:24 pm).

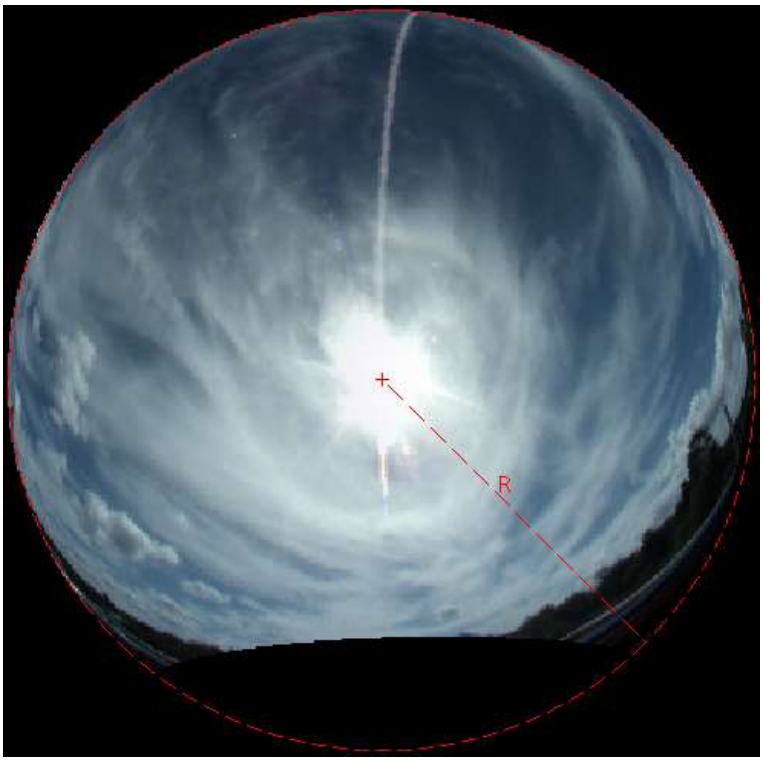

Figure 2-59: Remapped JPEG image corresponding to Figure 2-58.

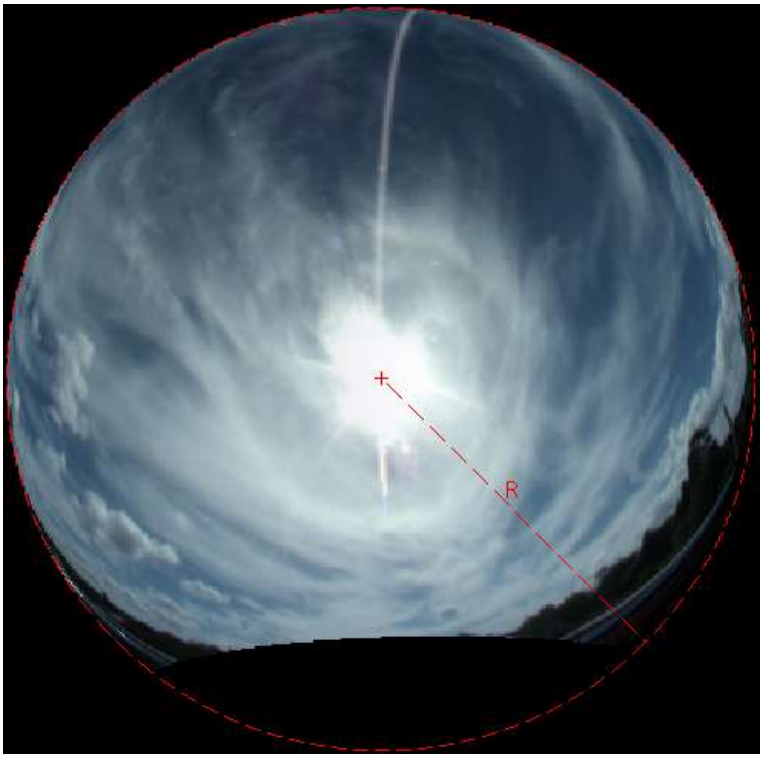

Figure 2-60: Interpolated JPEG image corresponding to Figure 2-58.

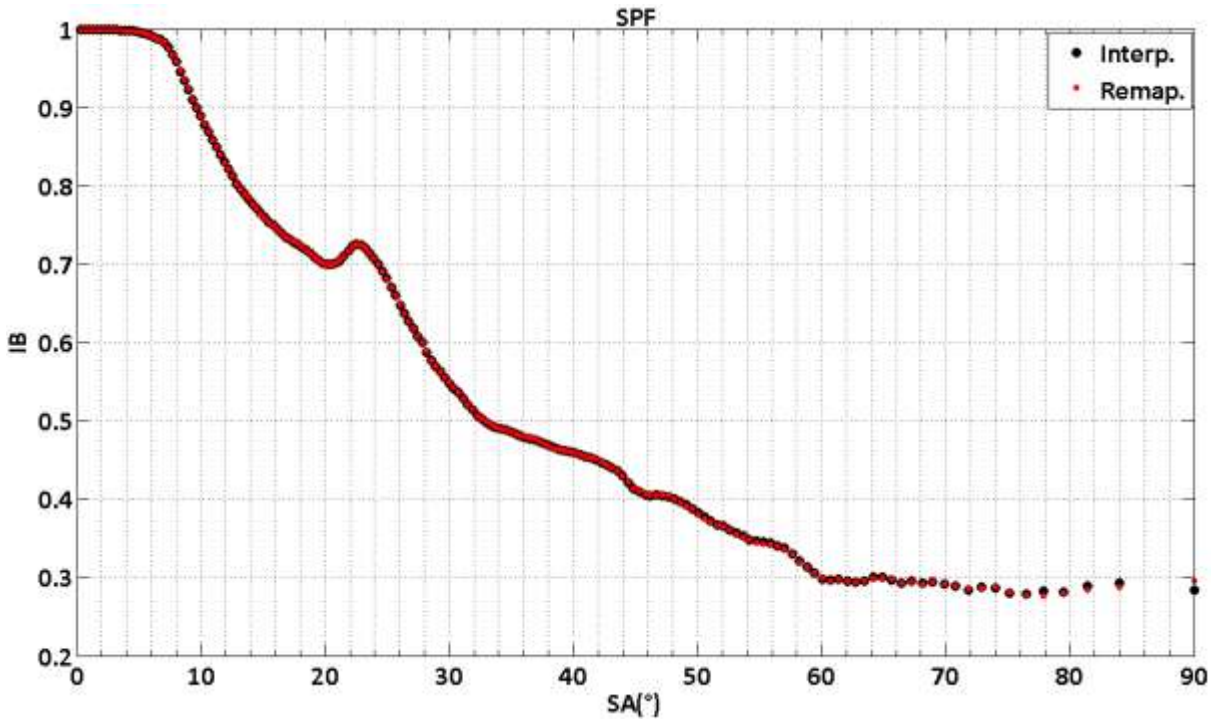

Figure 2-61: Comparison between the remapping and the interpolation methods when applied to the image of Figure 2-58 (JPEG image - 03-Aug-2012 - 01:24 pm).

2.6 Air mass correction

In addition to the geometric distortion issue we should also take into account that the image brightness depends on the amount of air mass (AM) found along the viewing direction between the observer and the source (see Figure 2-62).

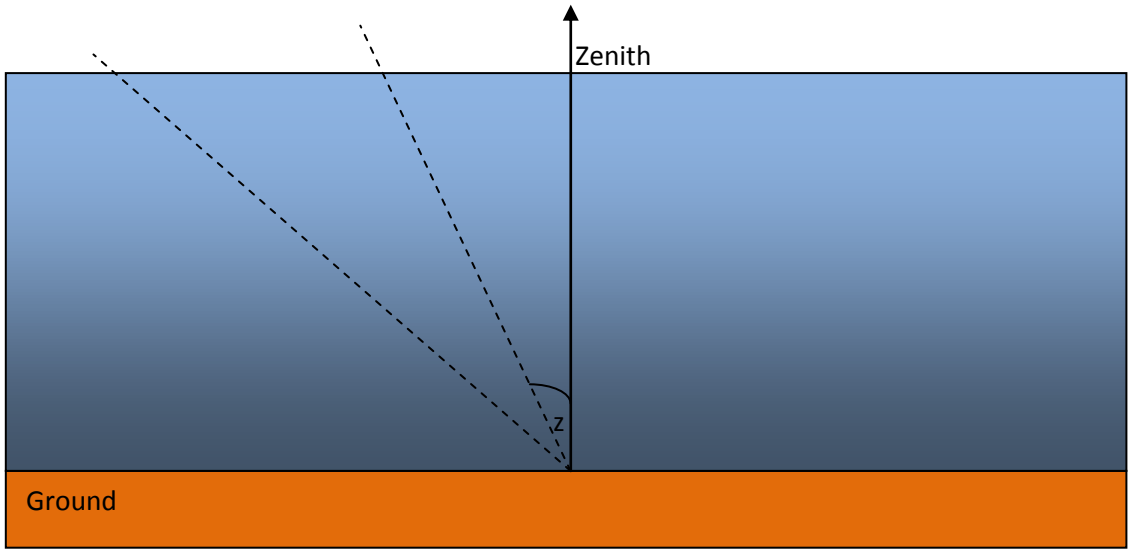

Figure 2-62: Air mass increases with the zenith distance.

The fact that AM increases with *z* implies that the light travelling from the source to the observer undergoes enhanced forward scattering when the source gets close to the horizon. Figure 2-63 shows the variation of AM with *z* assuming a plane parallel atmosphere. When *z* is 89^o AM is nearly sixty times as much as at zenith (AM = 1) for then increasing to infinity towards the horizon (*z* = 90^o). It increases the brightness of those pixels which are closer to the periphery of the image.

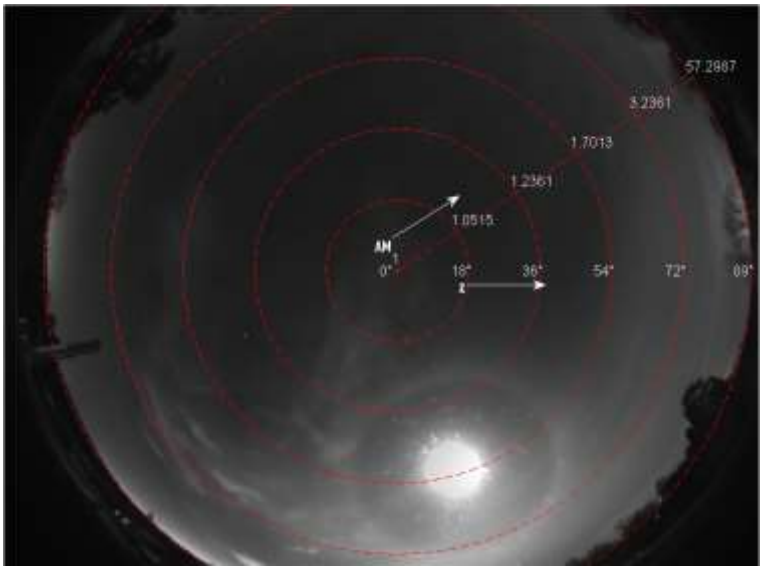

Figure 2-63: Original FITS image, zenith distances(red dashed lines) and corresponding AM for a plane parallel atmosphere.

Several functional forms have been suggested to define the air mass (157). The simplest approach in this respect is assuming a plane, homogeneous (ρ = constant) parallel atmosphere. This is a reasonable assumption if we compare the earth's radius (R_E = 6371 km) to the thickness of the atmosphere (≈10 km). Figure 2-64 shows a schematic of a plane parallel atmosphere.

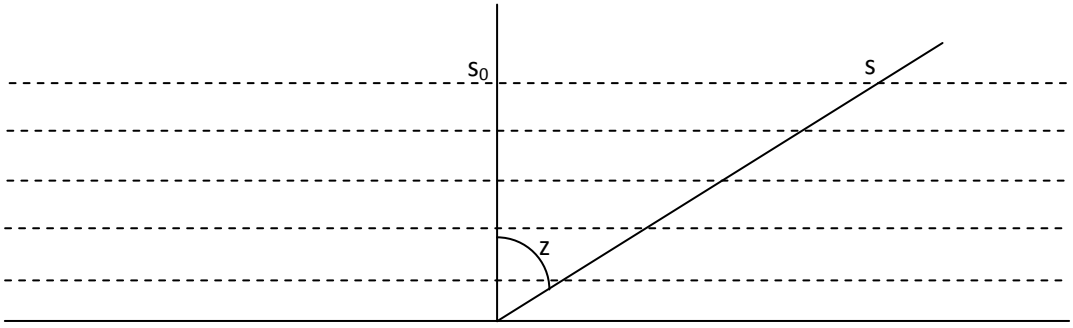

Figure 2-64: Schematic of plane parallel atmosphere.

Where s_0 is the zenith depth of the atmosphere and *s* is the atmospheric path at zenith distance *z*. In general the absolute optical air mass (along the direction specified by *z*) can be defined as the integration of the atmospheric density ρ along the path (*s*) linking the observer to the source as specified in Eq. 2.6 (158):

$$M = \int_S \rho(s) ds \tag{2.6}$$

With relative air mass or more simply air mass (AM) it is indicated the ratio of M calculated along *z* to the zenith air mass M_0 (see Eq. 2.7).

$$AM = \frac{\int_{s} \rho(s) ds}{\int_{s_0} \rho(s) ds} = \frac{M}{M_0} \tag{2.7}$$

It should be noticed that no elementary function exists that is the solution to the integral of Eq. 2.7. Functional forms that aim to be representative of AM have been suggested. In general AM is a function of *z* and parameters which can be obtained from a set of physical variables like height, pressure and temperature at the observation site. Several atmospheric models like the exponential density profile or the quartic profile (often used in atmospheric delay of radio signal studies) have been adopted to test the reliability of such analytical forms and to fit the above mentioned parameters (157). For a homogeneous plane parallel atmosphere AM becomes the ratio of *s* to s_0 which from trigonometry coincides with the secant of *z* as expressed in Eq. 2.8.

$$AM = \frac{s}{s_0} = \frac{s}{s\cos(z)} = \frac{1}{\cos(z)} = \sec(z) \tag{2.8}$$

Figure 2-65 shows AM for a plane parallel atmosphere as a function of *z*.

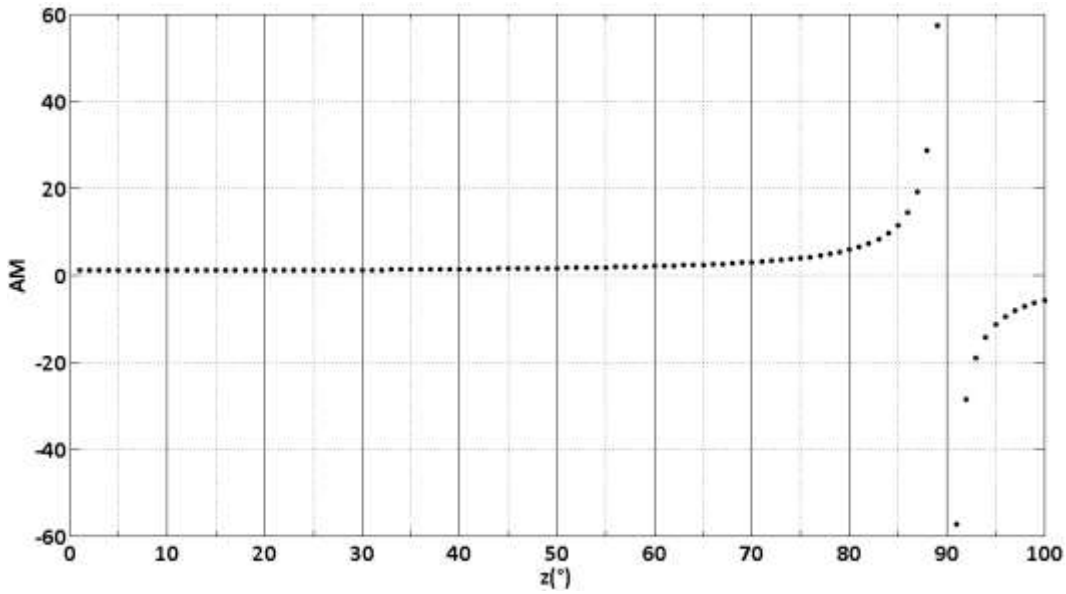

Figure 2-65: AM for a plane parallel atmosphere.

One of the main issues is that sec(*z*) diverges at the horizon, it is reliable up to 80 degrees and also it changes sign when *z* > 90. However, given the pixel distance from the optical centre (LFA), from Eq. 2.3 it is possible to work out *z* from which the corresponding AM(z) is calculated by using Eq. 2.8. Finally the original pixel brightness is reduced by dividing each pixel by the corresponding AM(*z*). For the reasons set out above this can be done only for pixels such that *z* < 90. Figure 2-66 and Figure 2-67 show the night time sky corresponding to January the 2nd 2013 at 5:17 am without and with air mass correction respectively. The red line defines the actual horizon beyond which it is not possible to apply Eq. 2.8.

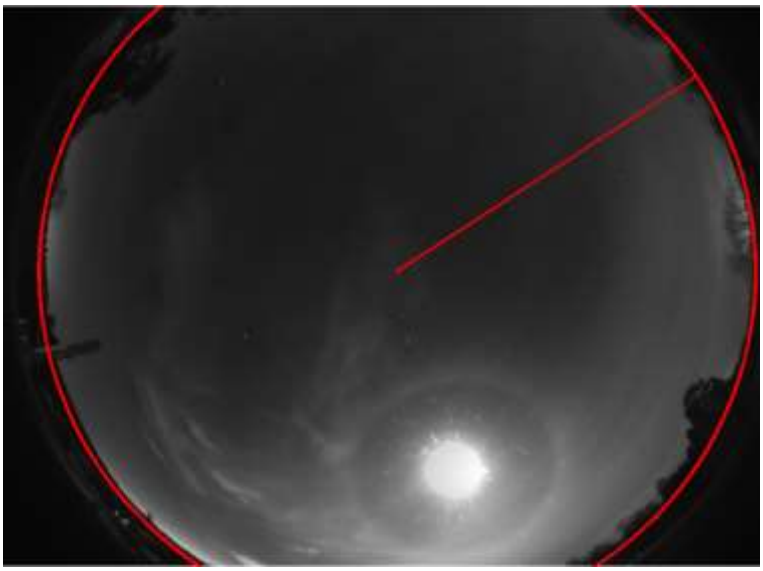

Figure 2-66: Raw FITS data - January the 2nd 2013 at 5:17 (red lined horizon).

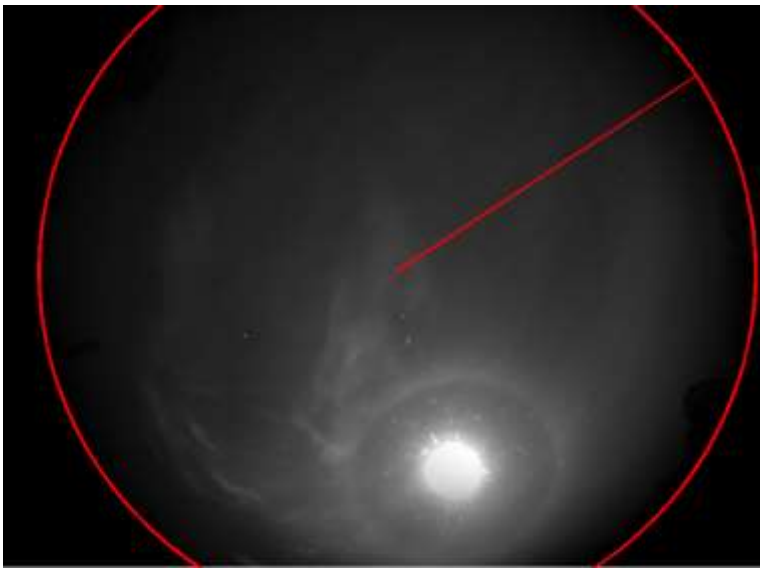

Figure 2-67: January the 2nd 2013 at 5:17 air mass corrected assuming the plane parallel model.

However a more realistic formula for the air mass can be obtained by thinking of the atmosphere as a homogeneous layer of thickness h_{atm} (see Figure 2-68) having spherical symmetry.

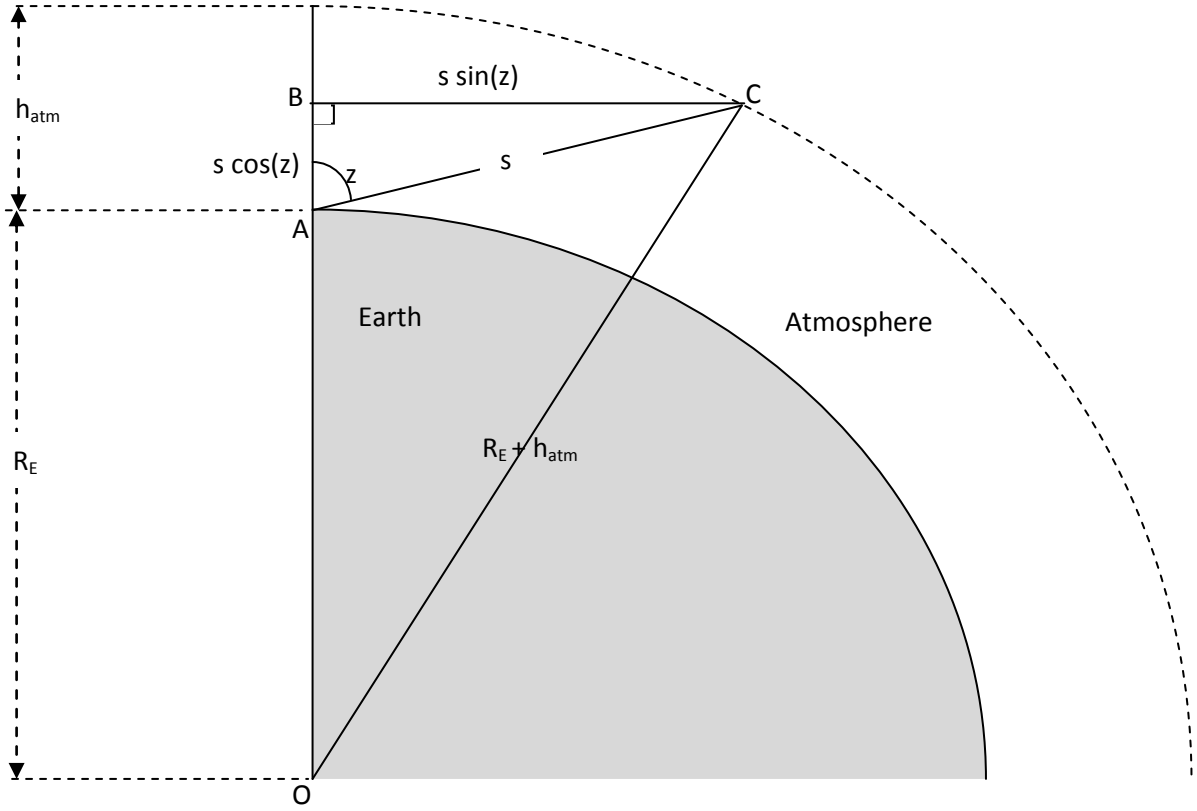

Figure 2-68: Radially symmetric homogeneous atmosphere.

According to Figure 2-68 for a homogeneous atmosphere, the AM is by definition expressed as in Eq. 2.9.

$$AM = \frac{s}{h_{atm}} \tag{2.9}$$

By applying the Pythagoras theorem to the right angle triangle OBC (see Eq. 2.10), and by solving for *s* (see Eq. 2.12), the AM is obtained in Eq. 3.14.

$$\left(R_E + h_{atm}\right)^2 = \left(R_E + s\cos(z)\right)^2 + \left(s\sin(z)\right)^2 = {R_E}^2 + 2R_E s\cos(z) + s^2 \tag{2.10}$$

$${h_{atm}}^2 + 2R_E h_{atm} = 2R_E s\cos(z) + s^2 \tag{2.11}$$

$$s = \frac{\left[-2R_E\cos(z) + \sqrt{\left(2R_E\cos(z)\right)^2 + 4\left({h_{atm}}^2 + 2R_E h_{atm}\right)}\right]}{2} \tag{2.12}$$

$$s = \sqrt{\left(R_E\cos(z)\right)^2 + 2R_E h_{atm} + {h_{atm}}^2} - R_E\cos(z) \tag{2.13}$$

$$AM = \frac{s}{h_{atm}} = \sqrt{\left(\frac{R_E}{h_{atm}}\cos(z)\right)^2 + 2\frac{R_E}{h_{atm}} + 1} - \frac{R_E}{h_{atm}}\cos(z) \tag{2.14}$$

If we take into account that the Earth's radius is R_E=6371 km and by assuming a non-refracting homogeneous radially symmetric atmosphere of thickness h_{atm} = 9000 km the AM so calculated at the horizon is less than 40 as it is expected (157).

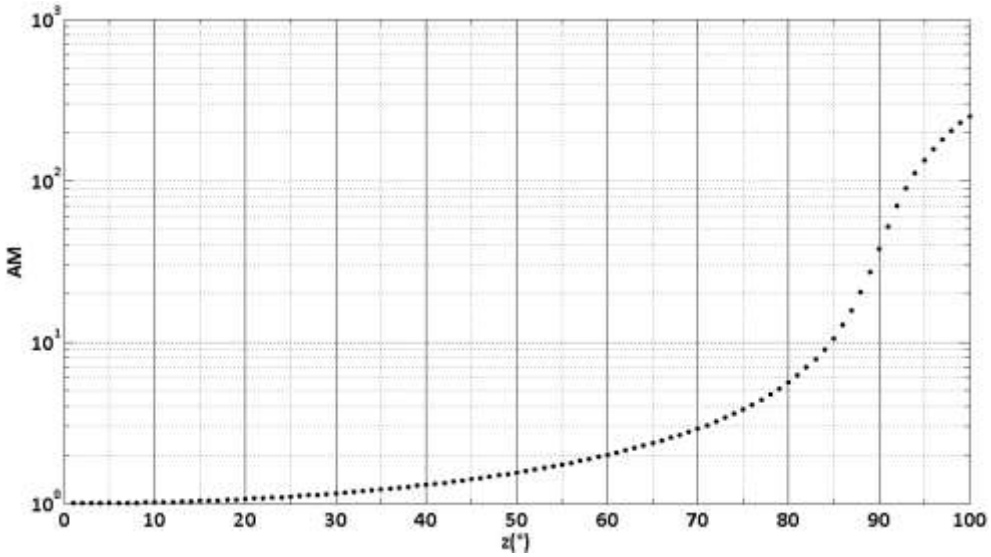

Figure 2-69: AM for an atmosphere with spherical symmetry.

If we correct the original image by means of this alternative AM Figure 2-70 becomes the output. Comparison of Figure 2-67 and Figure 2-70 shows no significant difference. This is consistent with what we see by comparing the two models (see Figure 2-71).

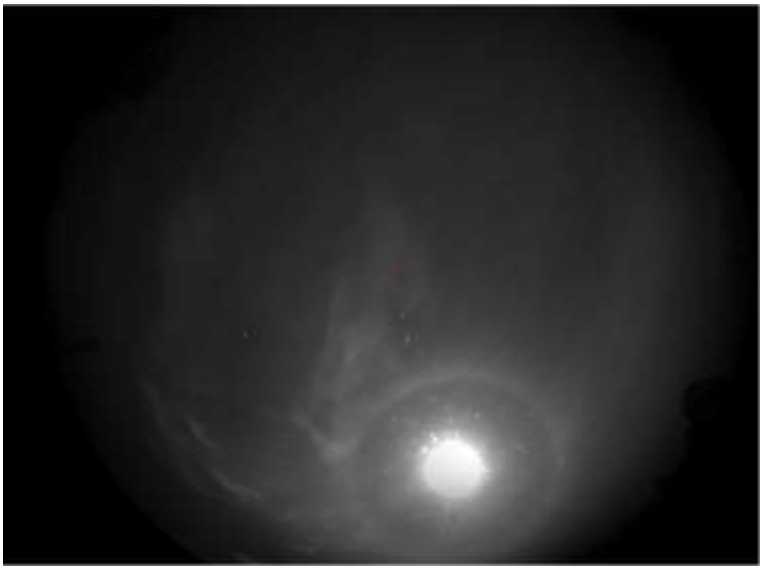

Figure 2-70: January the 2nd 2013 at 5:17 air mass corrected assuming the spherical symmetry model.

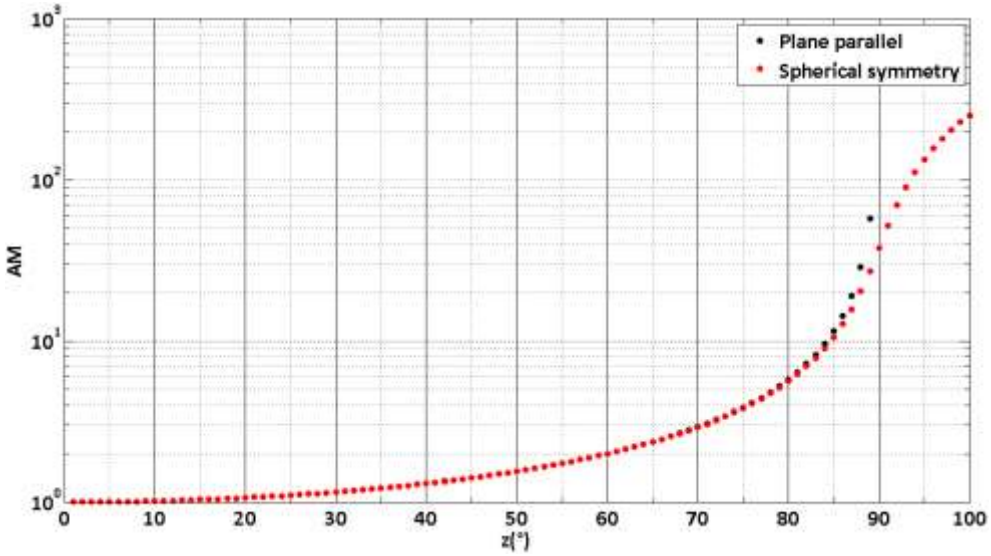

Figure 2-71: AM comparison between plane parallel (black) and spherically symmetric (red) atmosphere.

In addition to not deviating substantially from the parallel plane model the spherical symmetry provides more realistic values of AM in particular at the horizon and beyond it. Therefore it seems to be the preferable option.

2.7 Vignetting

Vignetting is a falloff of luminance increasing with the distance from the centre of the image. It especially involves those pixels close to the periphery (see Figure 2-72) and takes place in nearly every digital photograph, in all optical lens systems, in particular wide-angle and ultra wide-angle lenses like fisheye lenses (159).

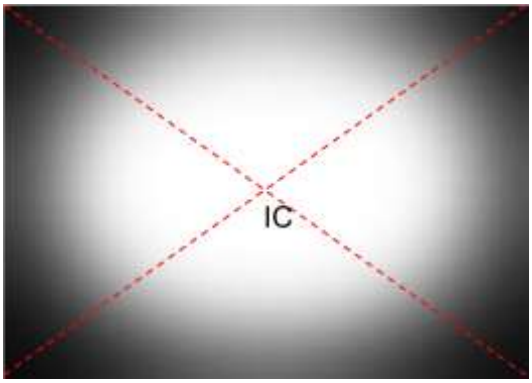

Figure 2-72: Vignetting.

Vignetting may arise from multiple sources. The blocking of light rays due to external objects such as thick or stacked filters and secondary lenses or hoods attached to the front of the lens body which is known as mechanical vignetting. Optical vignetting is the one caused by the lens aperture which causes light paths to be blocked inside the lens body depending on the changing shape of the clear aperture of the lens as it is viewed from different angles. The shape of the entrance pupil varies with the aperture and the angle of incidence. Natural vignetting is due to geometric optics which causes

different regions of the camera sensor to receive different irradiances. This radial falloff (RFO) is often modelled as the fourth power of the cosine of the angle ϑ at which the light ray exits from the rear of the lens (160).

$$RFO = \cos^4(\theta) \tag{2.15}$$

Pixel vignetting – which affects only digital cameras – is due to the interconnects between filters and camera sensor which create a geometric well the walls of which cast a shadow on the photosensitive elements. This is especially problematic for light incident at an oblique angle (see Figure 2-73).

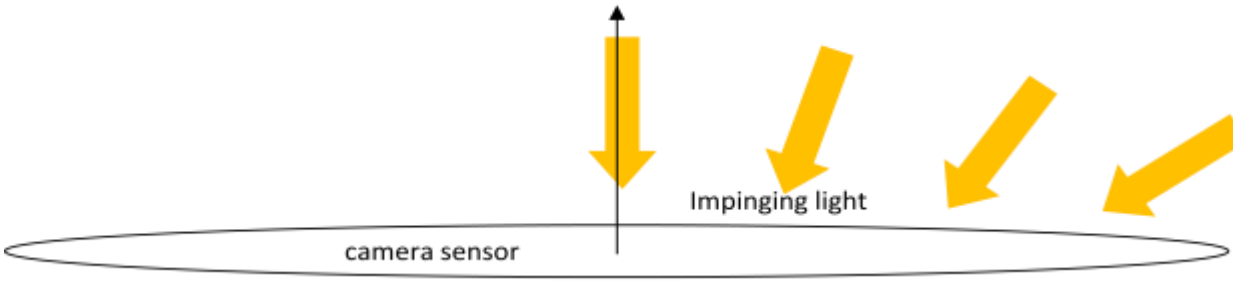

Figure 2-73: Light impinging the camera sensor.

Because of the multiple origins of vignetting it is difficult to predict for a given lens and setting the expected vignetting. In general it increases with aperture and decreases with the focal length.
Details of a possible way of removing this effect will be presented in the coming sections. The idea consists of comparing daytime image data with sun photometer data under clear sky. While the camera is affected by vignetting, the sun photometer is not. For this reason the ratio of the sky brightness (SB) measured with these two instruments over the same spectral range is expected to provide a measure of the vignetting parameter. In this respect it must be said that an occulting disk made by CAIR (Centre for Atmospheric and Instrumentation Research) has been mounted on the daytime All Sky camera to prevent stray light from affecting the measure. Figure 2-74 shows the All Sky camera and the occulting disk while on operation on the roof of the science learning centre.
It consists of an opaque disk, 10 cm in diameter, connected to a T shaped rigid arm whose long and short arms are 60 cm and 20 cm long respectively. The other end of the arm is attached to the base which fits on the camera and is free to rotate thanks to a stepper motor. A GPS module which provides time and position of the sun allows the occulting disk to track the sun when it is above 5 degrees altitude. At sunset it moves slightly below the horizon and waits for the sun to rise again. There's no information if it's cloudy, so the mechanism simply tracks all the time when the sun is up.

Figure 2-74: Daytime All-sky camera and occulting disk, night camera (right) and Cimel sun-photometer CE318-N (left on background).*

In the coming paragraph 2.8 after a short presentation of the Cimel sun-photometer CE318-N, its components and the principal plane measurement (PPM) will be discussed.

2.8 Sun photometer

Sun photometry is one of a series of remote sensing techniques available at the observatory of Bayfordbury. Figure 2-75 shows the multiband Cimel sun-photometer operated by CAIR.

Figure 2-75: Sun Photometer operated by CAIR at Bayfordbury observatory.*

CE318-N measures the optical properties of the atmosphere by quantifying sun irradiance and sky radiance. It provides a large number of variables which are calculated from the measurements. This makes possible for instance the quantification of the aerosols, the measure of the Aerosol Optical Depth (AOD) for both fine and coarse particles, the determination of the amount of precipitable water vapour. Due to its very low power consumption technology, to its self-powered system and to

*D. Campbell

its rugged design, the CE318-N fully meets the operational requirements of continuous monitoring in terms of reliability, long lifetime and very low maintenance cost. The "Cimel" is still the benchmark device for most aerosol observing networks and more specifically for the international federation of AERONET (161) (162). CE318-N does also principal plane measurements (PPM). It is a measure of the sky radiance performed along the plane containing the sun and the zenith. It is this measure that will be used to quantify the vignetting and will be discussed in the coming paragraphs after an overview of the system components.

2.8.1 System components

CE318-N consists of the following parts (see Figure 2-76):

1. **A sensor head, which allocates the actual sensitive parts of the instrument receives the radiation coming from the source (sun, sky, soil, sea) and send the data to the control unit (see Figure 2-78). The sensitive materials are silicon and InGaAs an alloy of indium, gallium arsenide. The latter is sensitive to near-infrared wavelengths**
2. **A collimator focuses the light into the sensor head and minimizes the amount of stray light**
3. **A robot is the component on which the sensor is mounted and that permits to point at any direction with high accuracy**
4. **A protection case (see Figure 2-77) contains the control unit which is where all the data acquired by the optical head are stored, two rechargeable batteries, a solar panel (the blue rectangle at the front) and a wet sensor (highlighted by a red circle) which permits to stop the operation when it rains**

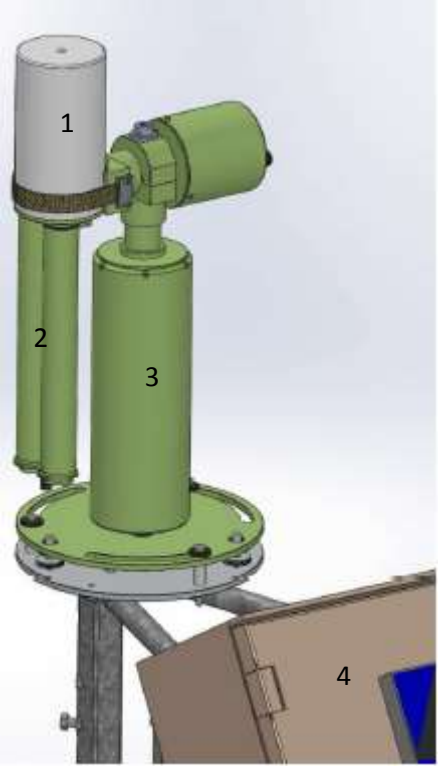

Figure 2-76: CE318-N in parking position.

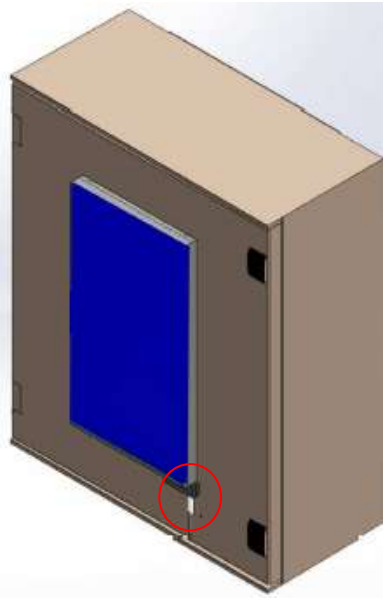

Figure 2-77: Protection case.

Figure 2-78: Control unit.

2.8.2 Sun photometer principal plane measurement

CE318-N has been operating in automatic mode. In such a configuration PPM is performed every hour over the following wavelengths, 1.0205, 1.6385, 0.8682, 0.6764, 0.5015, 0.4403 µm, in this order at about 35 s apart from each other. It operates during daytime and only if the sky is not overcast. Figure 2-79 shows the principal plane and the directions that the sun-photometer points at on operation.

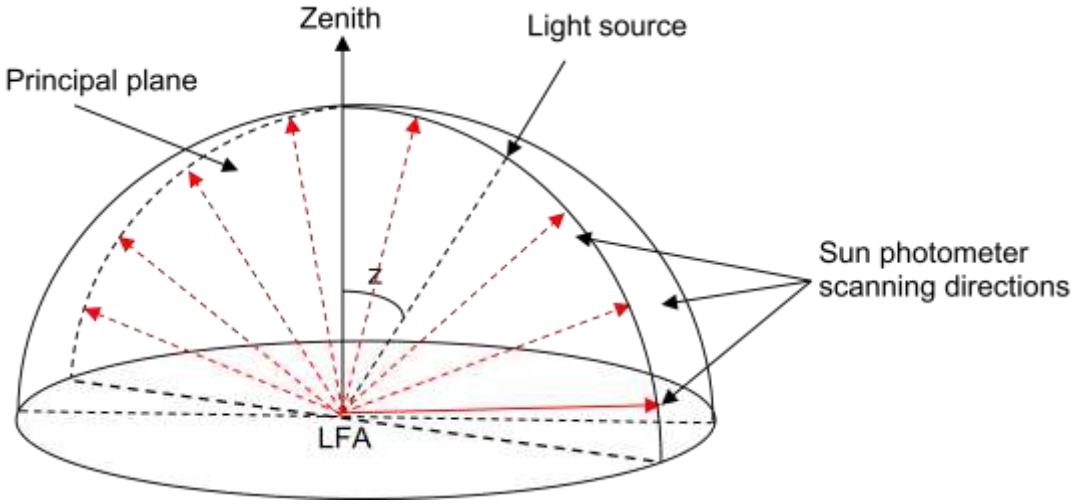

Figure 2-79: Principal plane sun photometer scan.

Figure 2-80 shows the measured sky brightness (SB) over a range of zenith angles as large as 180 degree (from -100 to +80 degrees). Plotted is the average of the SB observed at the visible wavelength of 0.5015 µm and 0.4403 µm on the 2nd of November 2015 at 2:57pm when the sky was clear (see Figure 2-81).

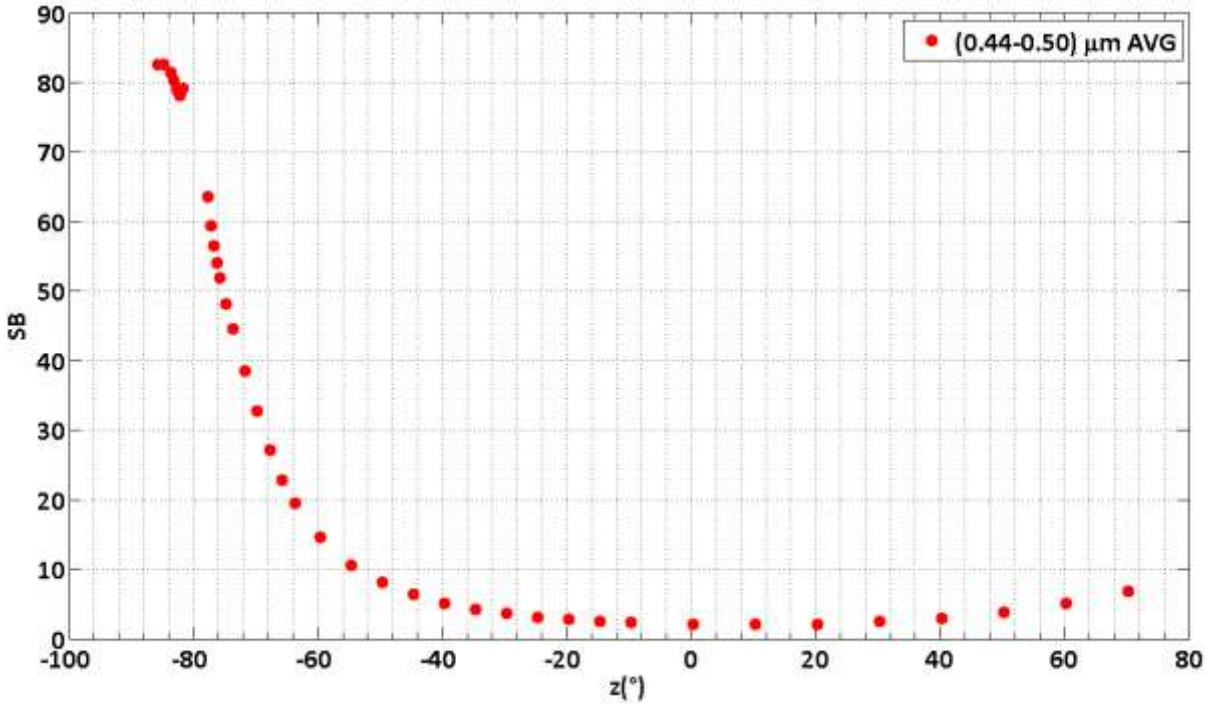

Figure 2-80: Sun photometer principal plane measurement corresponding to the 2-Nov-2015, 14:57 pm - 0.5015 µm.

Figure 2-81: Bayfordbury all-sky daytime JPEG image, 2/11/2015, 14:57 pm (149).

2.9 Vignetting removal

In order to quantify vignetting several steps have to be implemented as follows:

1. **First thing to do is to select a clear sky daytime case and make sure that synchronized image and sun photometer data are available**
2. **Once the FITS image has been selected the Matlab "demosaic" function is used in order to get the corresponding demosaiced RGB image that Figure 2-82 shows**

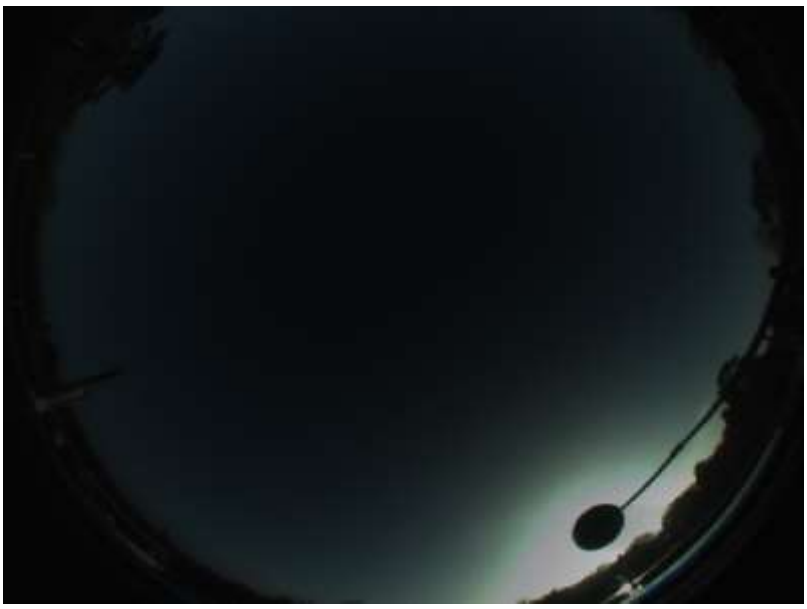

Figure 2-82: RGB daytime image after having used the Matlab "demosaic" function.

3. **The blue channel is then extracted from the RGB image just obtained (see Figure 2-83). With a quantum efficiency peaking at 0.46 μm the blue channel is the one which matches best the available operational wavelengths of the sun photometer**

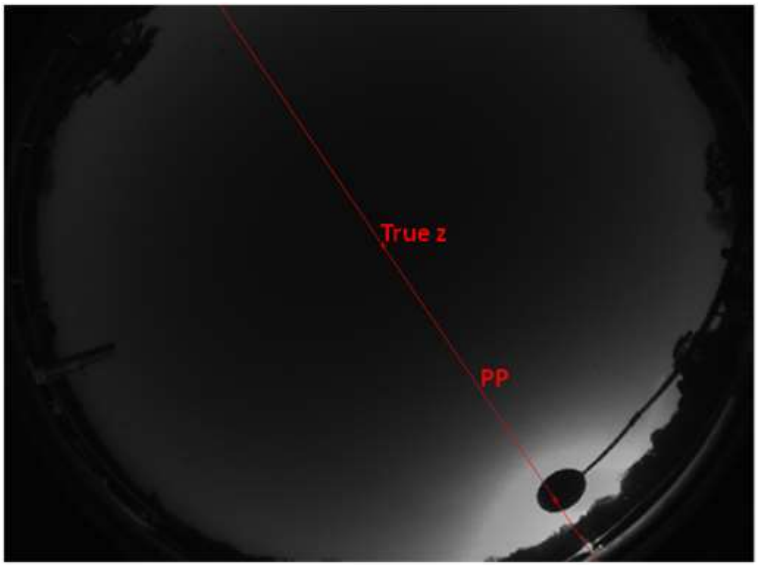

Figure 2-83: Blue channel image profile to be compared to PPM.

4. **Extract the image brightness along the principal plane as plotted in Figure 2-84 (PP is the red line drawn on Figure 2-83)**

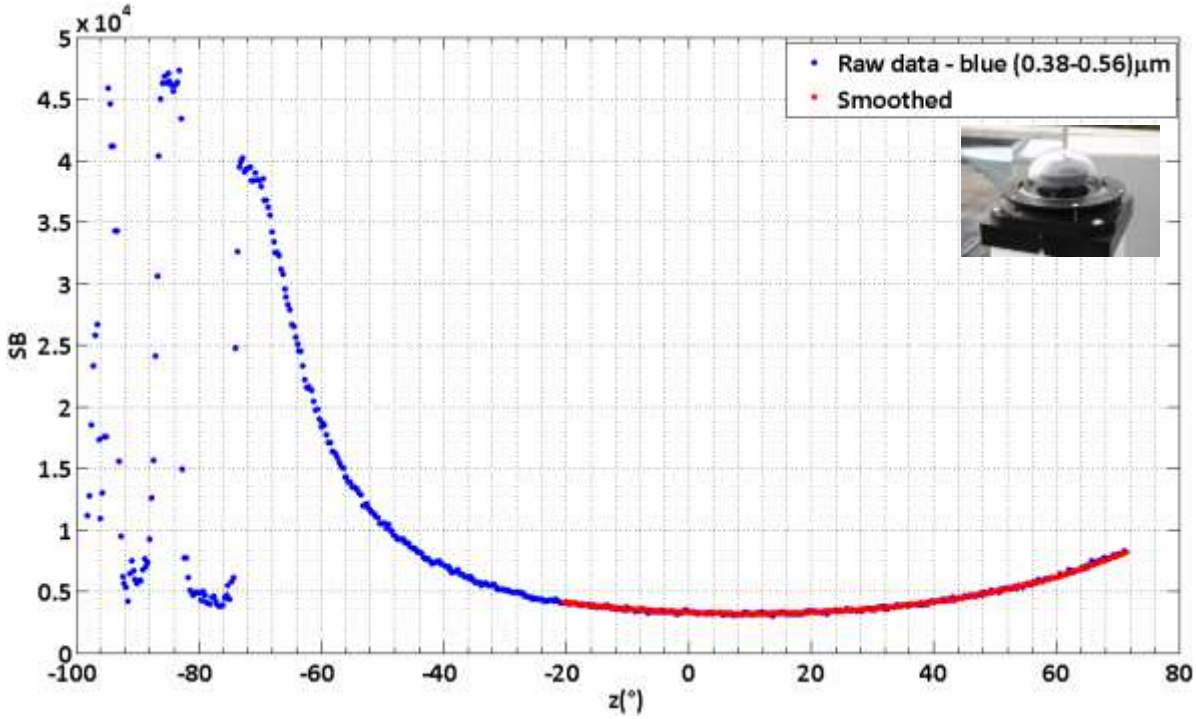

Figure 2-84: Image brightness profile corresponding to the red line drawn in Figure 2-83.

5. **Take the corresponding PPM at 0.4413 µm and 0.5015 µm respectively. Figure 2-85 shows the average of the two**

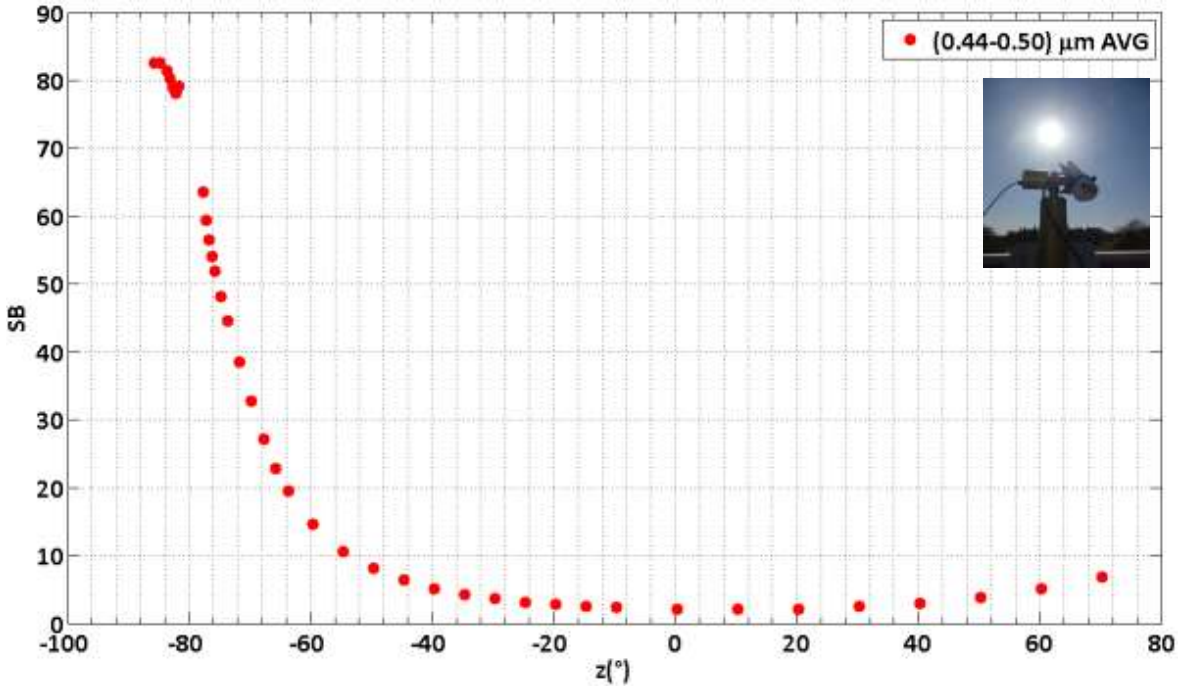

Figure 2-85: Sun photometer data, Bayfordbury 02-Nov-2015, 14:57 pm, averaged of 0.4413 and 0.5015 um channels.

6. **Consider only data from zenith (the optical centre) to the horizon (the opposite direction to the sun). The vignetting effect is expected to be a function of the *z* only and to be zero at zenith while increasing with *z*. With respect to Figure 2-85 we are only interested in the portion of the data that have been LOWESS (locally weighted scatterplot smoothing) smoothed (163), fitted and plotted as Figure 2-86 shows. The coefficients *a*, *b*, *c* and *d* of the fitting polynomial are approximately $4*10^{-6}$, $9*10^{-4}$, -0.02 and 2.1 respectively.**

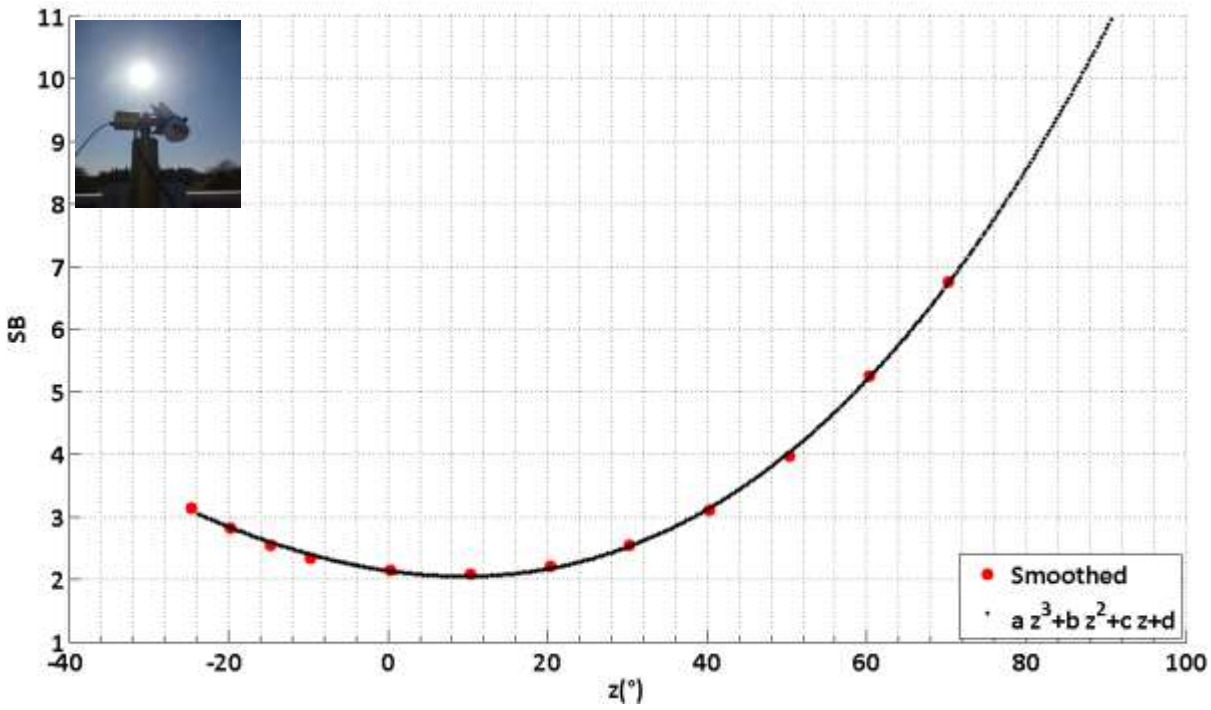

Figure 2-86: LOWESS smoothed PPM and corresponding fit.

7. **Fit the LOWESS smoothed image data (see Figure 2-87). The coefficients *f*, *g*, *h* and *i* of the fitting polynomial are approximately $6*10^{-3}$, $8*10^{-1}$, -21.2 and $3.3*10^{3}$ respectively.**

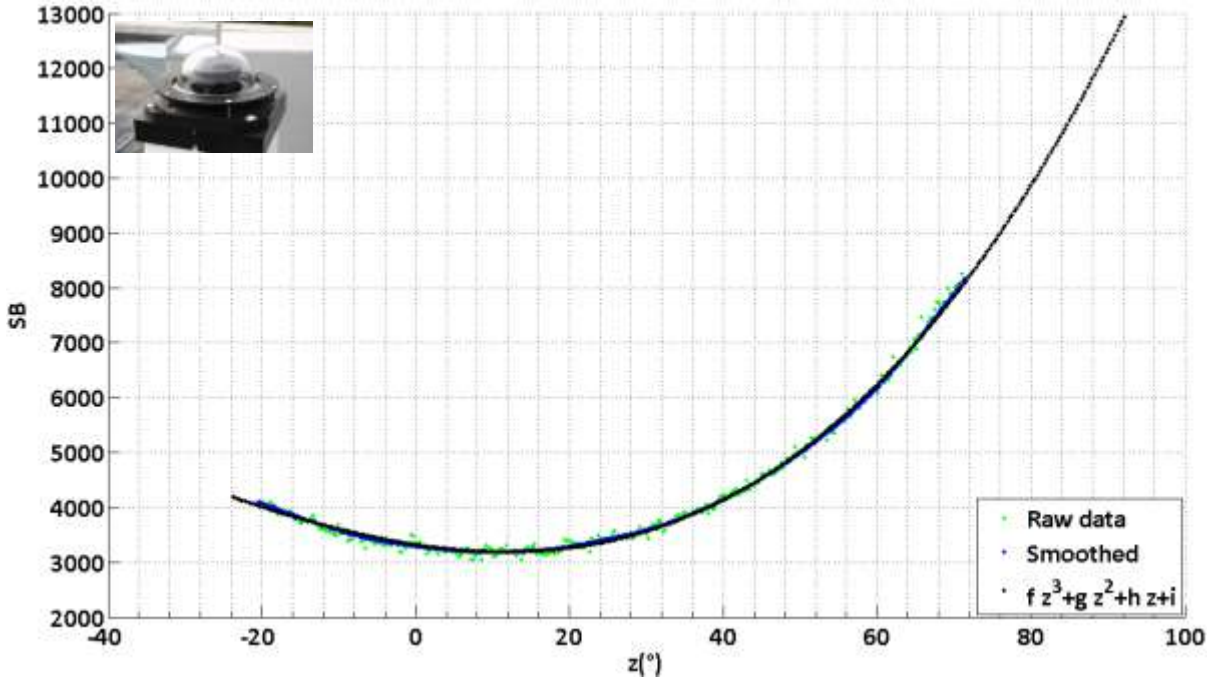

Figure 2-87: Row image data, LOWESS smoothed and fitting polynomial.

8. **Calculate the ratio between the two fitting polynomials (camera to sun-photometer) after normalization. This will result in the de-vignetting coefficient (DC) (see Figure 2-88)**

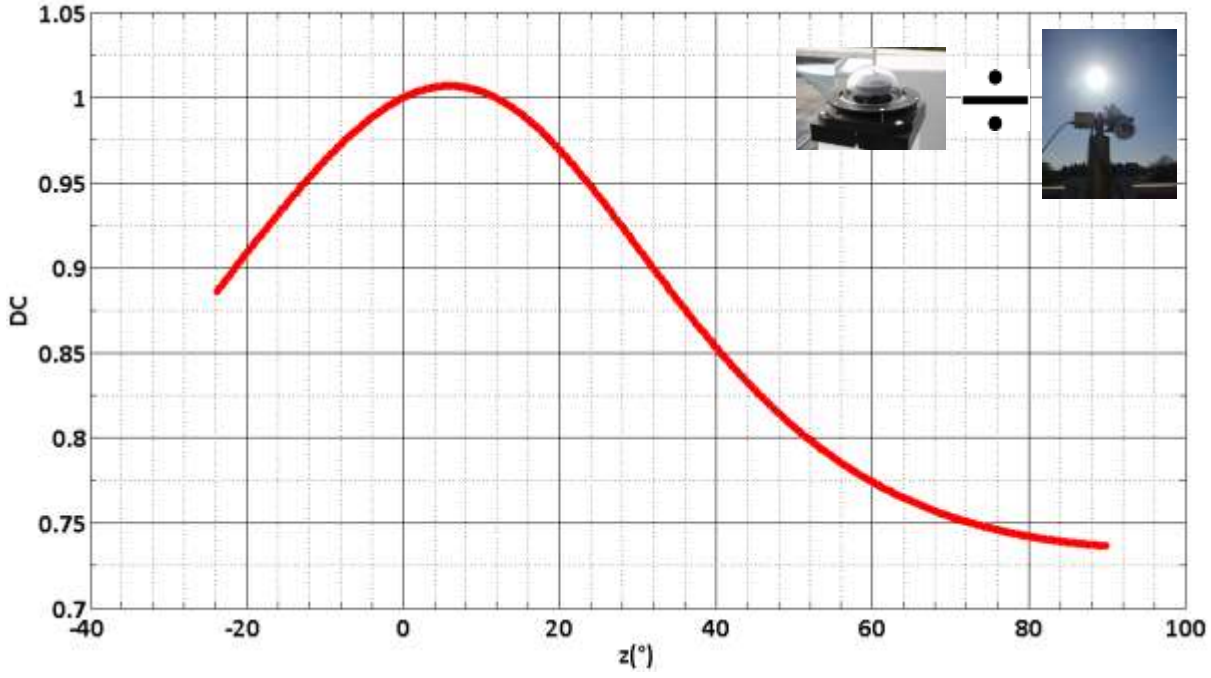

Figure 2-88: De-vignetting coefficient.

The presence of an unexpected peak in the de-vignetting coefficient located roughly 8 degrees from zenith has been investigated. The use of the occulting disk permits to exclude the possibility that this is caused by stray light. The simplest explanation comes from noticing that such an off-set, corresponding to around 27 pixels, is consistent with a displacement as small as 0.2 mm between the lens focal axis and the aperture centre. Given that the correction has to be symmetric with respect to the camera zenith it has been decided to "stretch" the original curve to coincide with the original one at 90° while the peak gets shifted to a mirror position with respect to zero. Then a function symmetric with respect to zero, a Gaussian of the form shown in Eq. 2.16, has been used to fit the two curves. In this way the correction is symmetric with respect to the camera zenith. Figure 2-89 shows the original curve (red line), the stretched one (green) and the best fit obtained (black).

$$f(z) = A + B\,e^{-\left(\frac{z^2}{C^2}\right)} \tag{2.16}$$

A, *B*, *C* so obtained are 0.73, 0.26 and 40.03 respectively.

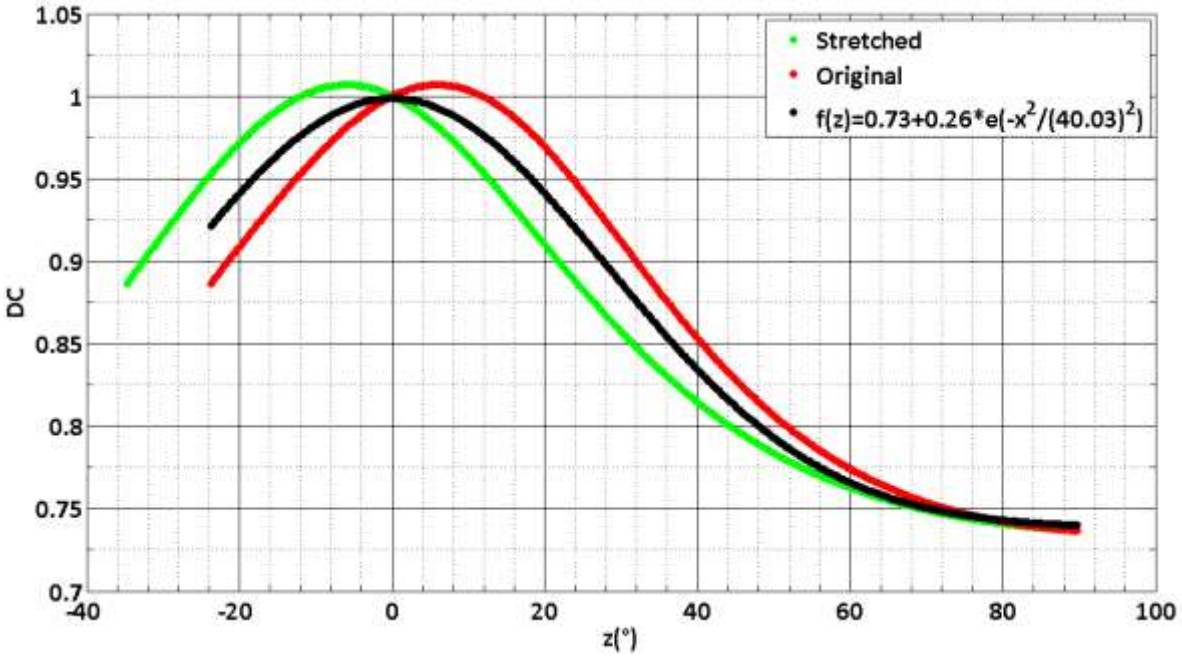

Figure 2-89: De-vignetting coefficient and fitting curve

The fitting curve provides a working approximation of the actual de-vignetting parameter. This is correctly normalized at zenith and has the expected monotonic decay with *z*. The original image brightness is divided by the de-vignetting coefficient to compensate for the radial fall-off of luminance.

2.10 SPF - preliminary analysis

With the available corrections the measure of the HR is now possible. However, before measuring the SPF, two additional aspects have to be taken into account. Points of the image which do not coincide with sky pixels should not be accounted when the SPF is averaged over the azimuth. Two masks, one for the background, and one for the stray light shade have been used. The former has been obtained by considering a summer time image, when vegetation is thicker (see Figure 2-90). An algorithm written in Matlab, whose details are given in section 6.4.5 of the appendix, has been

implemented in order to obtain a dynamic mask for the occulting disk. An example corresponding to the stray light shading of Figure 2-91 is shown in Figure 2-92.

Figure 2-90: Background mask.

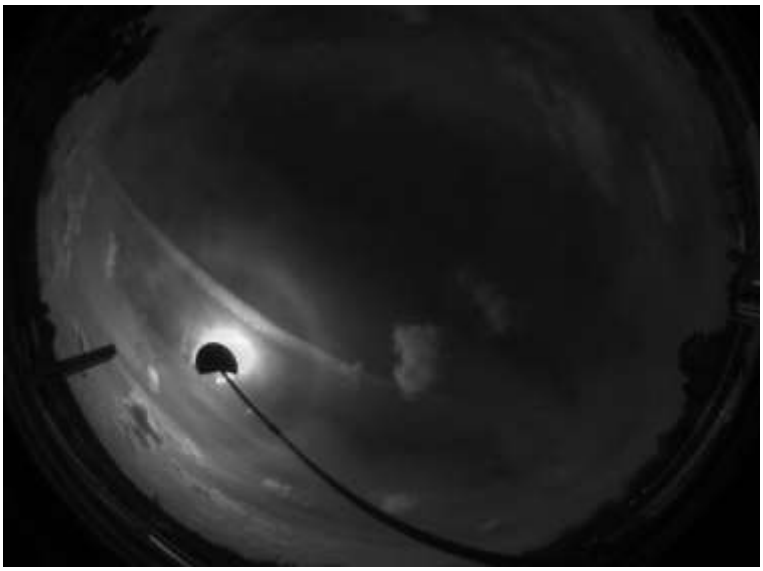

Figure 2-91: Stray light shading.

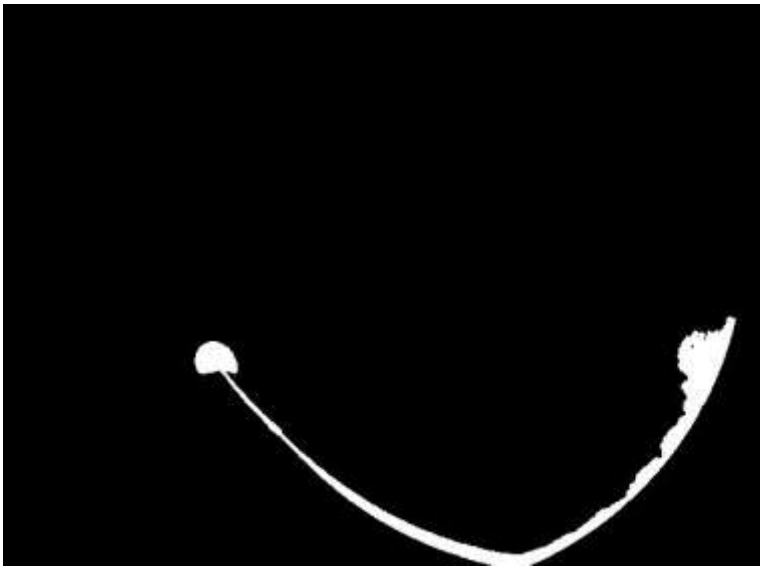

Figure 2-92: Occulting disk mask.

For illustrative purposes, the SPF corresponding to the 10th of April 2016 at 10am (see Figure 2-93) has been measured. The contributions of each individual correction have been separated: Figure 2-94 shows the transformed image when only the geometric correction (GC) is accounted for; Figure 2-95 is the outcome when also the background mask (BM) is included; if the AM correction (AMC) is incorporated (within the edge of the mask -up to about z = 88° see Figure 2-96) Figure 2-97 becomes the end result; this turns into Figure 2-98 allowing also for vignetting correction (VC). A comparison of the corresponding normalized SPFs is shown in Figure 2-99 (black dot: SPF after GC; red dot: SPF after GC and BM; blue dot: SPF after GC, BM and AMC, green dot: SPF after GC, BM, AMC and VC). The first noticeable thing is that the presence of the mask gives rise to a plateau in the SPF located at a scattering angle of about 38° (see red dotted SPF) which corresponds to the edge of the mask (see Figure 2-100). This is caused by the inclusion of the mask which removes from the azimuth average those relatively dark pixels which otherwise would significantly lower the mean value of the image brightness. When also the AM within the edge of the mask is accounted for a sudden kink at approximately the same scattering angle is observed (see blue dotted SPF). This is ascribable to the large value that the AM takes on when z is larger than about 82° (notice from Figure 2-96 that the edge of the mask begins approximately at 88°). Values of the AM ranging between 12 and 22 as highlighted in the rotated reference system (see Figure 2-101) cause the image brightness to drop too rapidly as the edge of the mask approaches. One way of getting around this issue consists in excluding values of the AM larger than 7, or in other words excluding pixels such as z>82°. If this is the case the kink gets significantly reduced as Figure 2-102 shows.
However, it should be specified that the measure of HR (see eq. 2.17 and 2.18 - where M_1 and M_2 are the number of data points available between 21.5° and 22.5° and between 18° and 19° respectively, excluding the initial one), discussed in chapter 4, will be limited to images such that z < 65° and z > 75°. This is done in order to prevent the mask edge from being found within the region of the SPF (between 18° and 22°) from which the measure of the HR is derived.

$$HR = \frac{SPF\left(22^\circ\right)}{SPF\left(18.5^\circ\right)} \tag{2.17}$$

$$HR = \frac{\left(\sum_{j=1}^{M_1} SPF\left(21.5^\circ + \frac{j-1}{M_1 - 1} \right) \right) / M_1}{\left(\sum_{j=1}^{M_2} SPF\left(18^\circ + \frac{j-1}{M_2 - 1} / \right) \right) / M_2} \tag{2.18}$$

The SPF does not change substantially when also the devignetting correction is applied. The corresponding correction parameter calculated in the rotated reference system is shown in Figure 2-103 for sake of completeness. Despite getting a slightly smaller HR, the same conclusions are drawn when the above comparison is repeated with the inclusion of the occulting disk mask (see Figure 2-104). This might suggest that the corresponding correction plays only a marginal role.
In chapter 4 time series of HR, BT, and solar irradiance (from pyranometer measurements) corresponding to specific test cases will be plotted together with the purpose of characterizing cirrus.

Figure 2-93: Original FITS image: Bayfordbury 10-Apr-2016, 10:00 am.

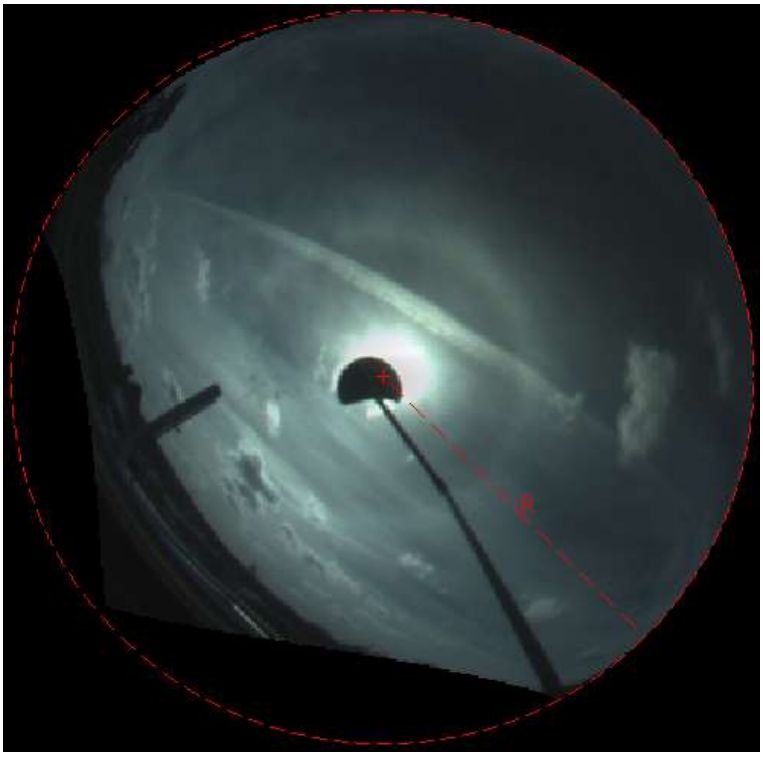

Figure 2-94: Original image after geometric correction (GC).

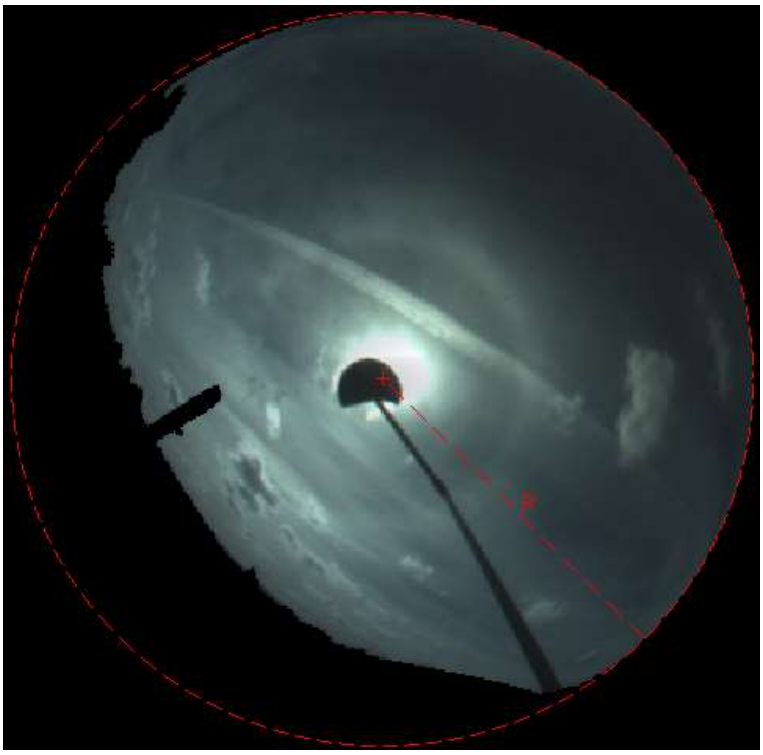

Figure 2-95: Original image after geometric correction (GC) and the inclusion of the background mask.

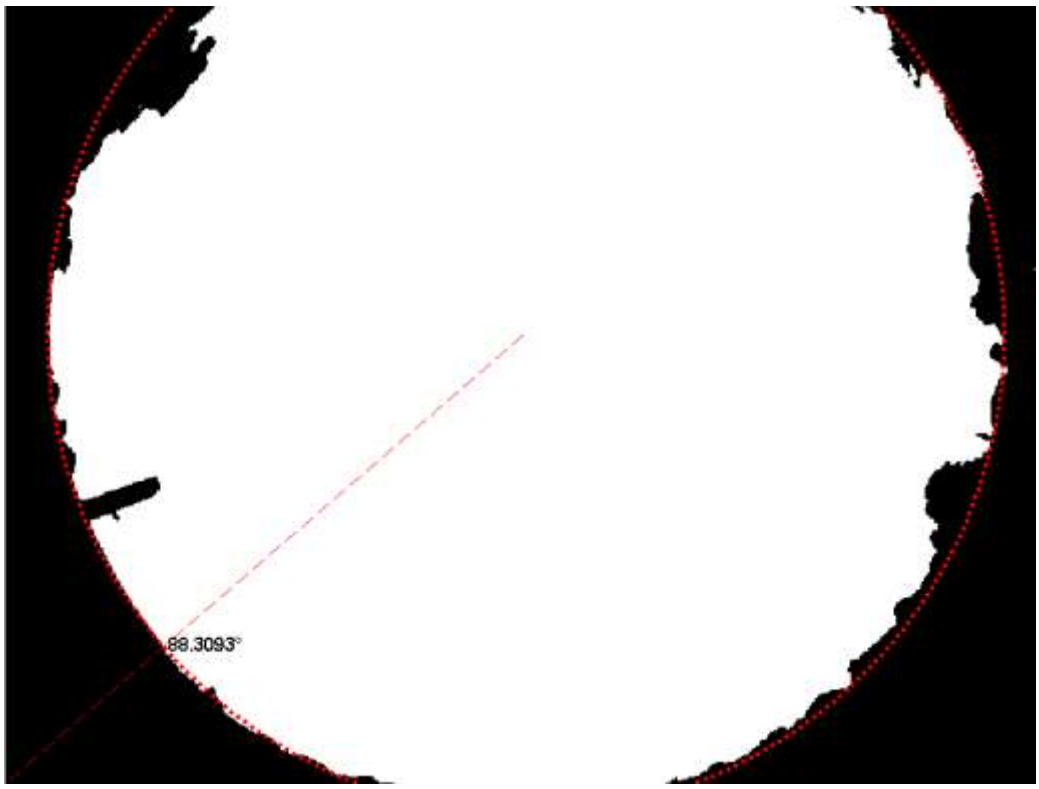

Figure 2-96: Edge of the mask.

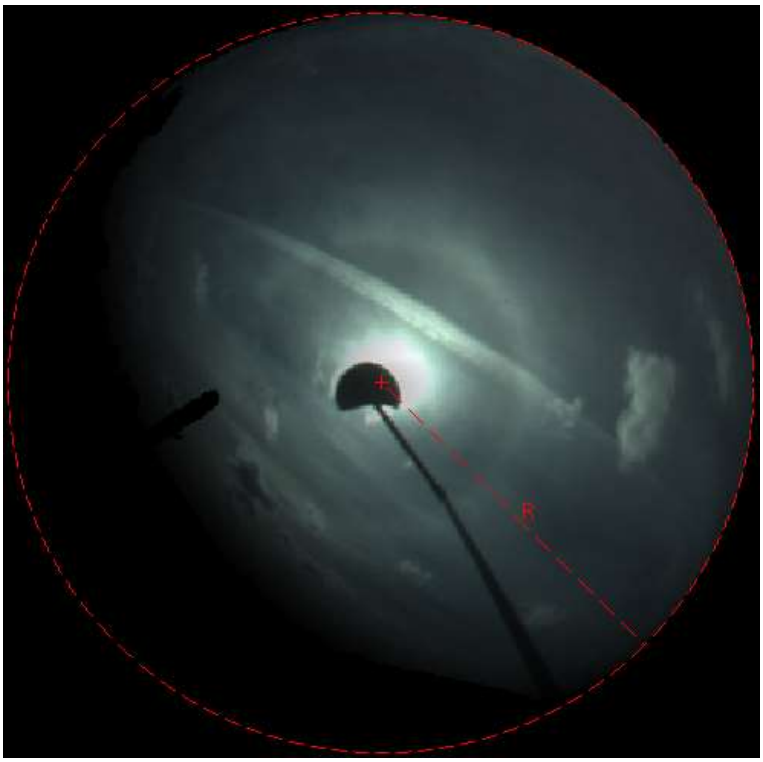

Figure 2-97: Original image after geometric correction (GC), the inclusion of the background mask and AM correction accounting for AM up to the mask edge.

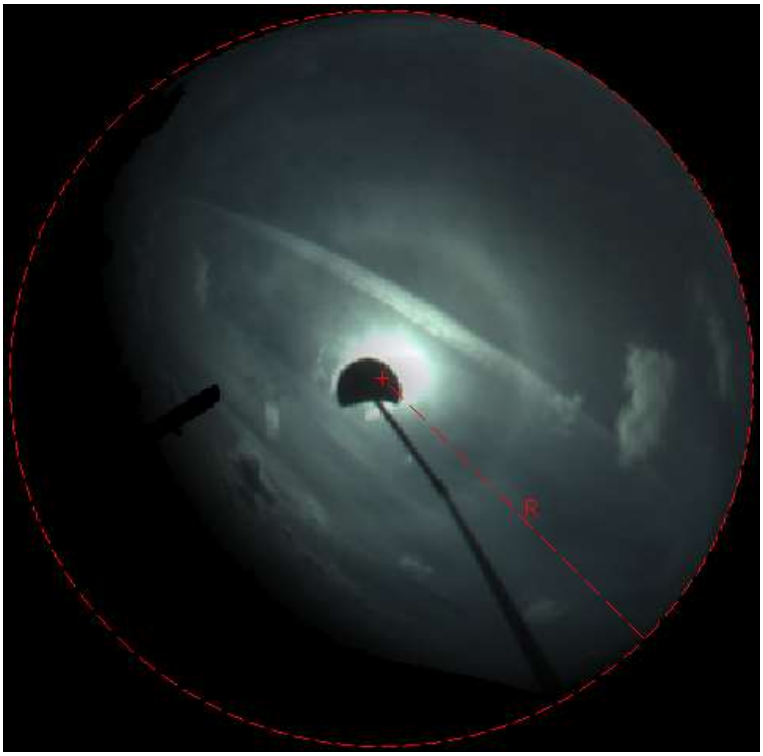

Figure 2-98: Original image after geometric correction (GC), the inclusion of the background mask, AM and devignetting correction.

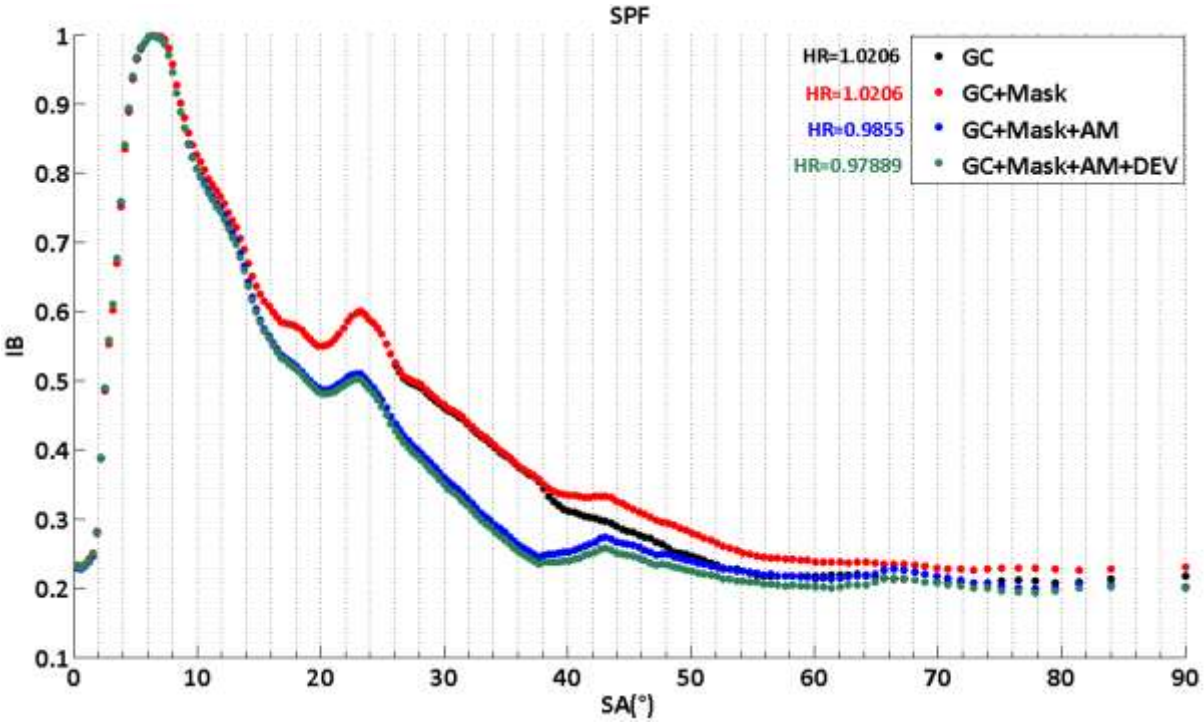

Figure 2-99: SPF comparison: geometric correction only (GC), including mask (GC+mask), including mask and AM corrected (GC+mask+AM), including devignetting correction (GC+mask+AM+Dev).

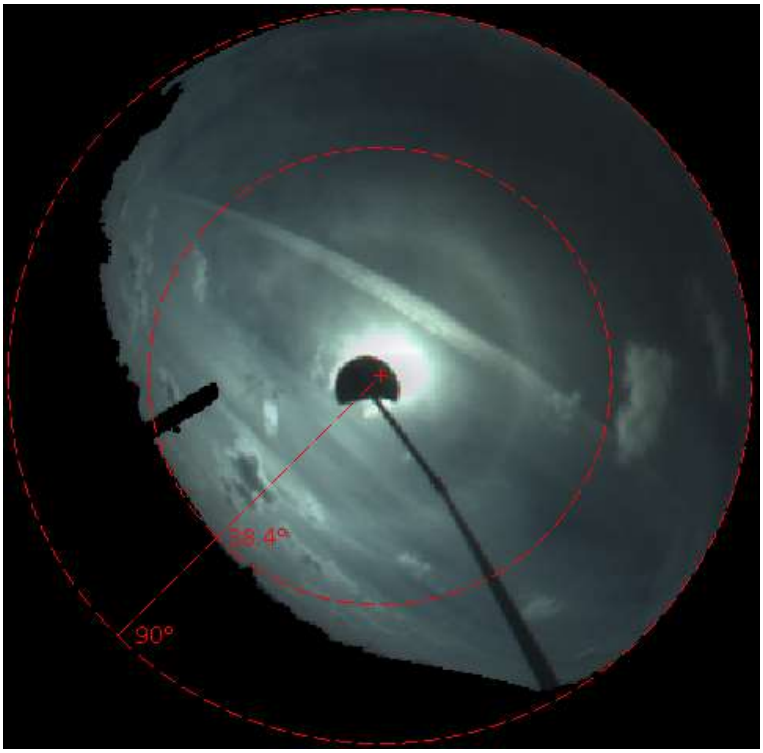

Figure 2-100: Original image after geometric correction and the inclusion of the background mask. The inner red circle shows the edge of the mask whereas the outer one shows the 90° scattering angle.

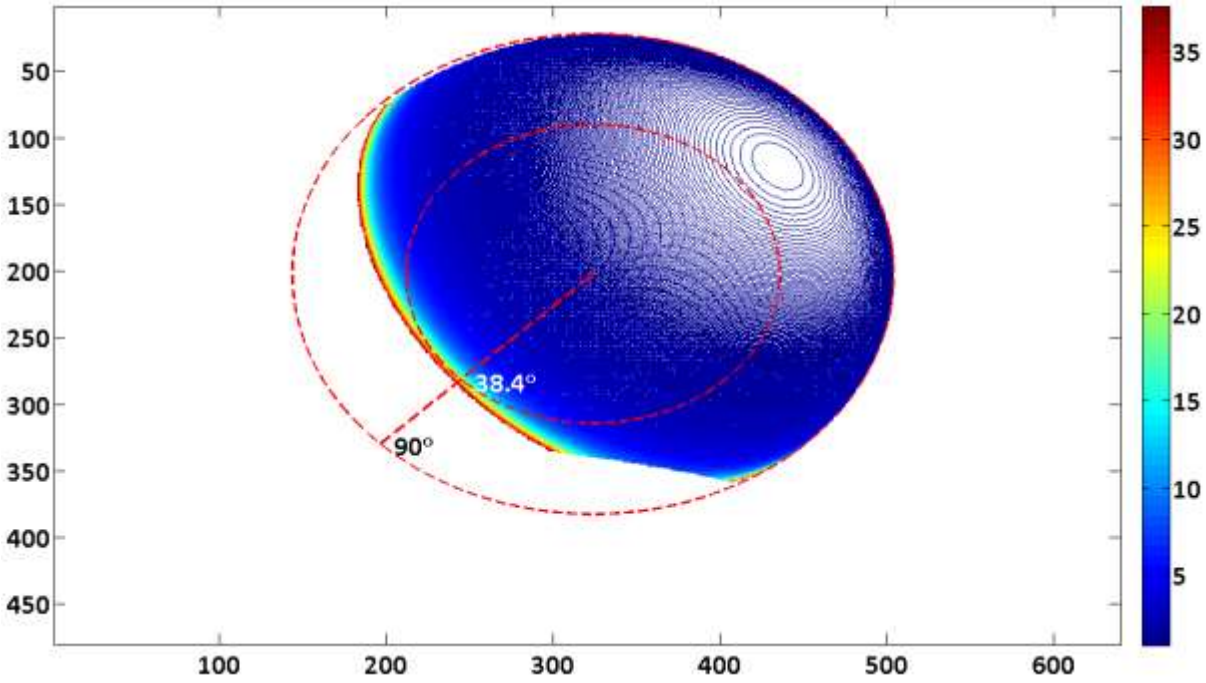

Figure 2-101: AM in the rotated reference system when AM is accounted up to the mask edge.

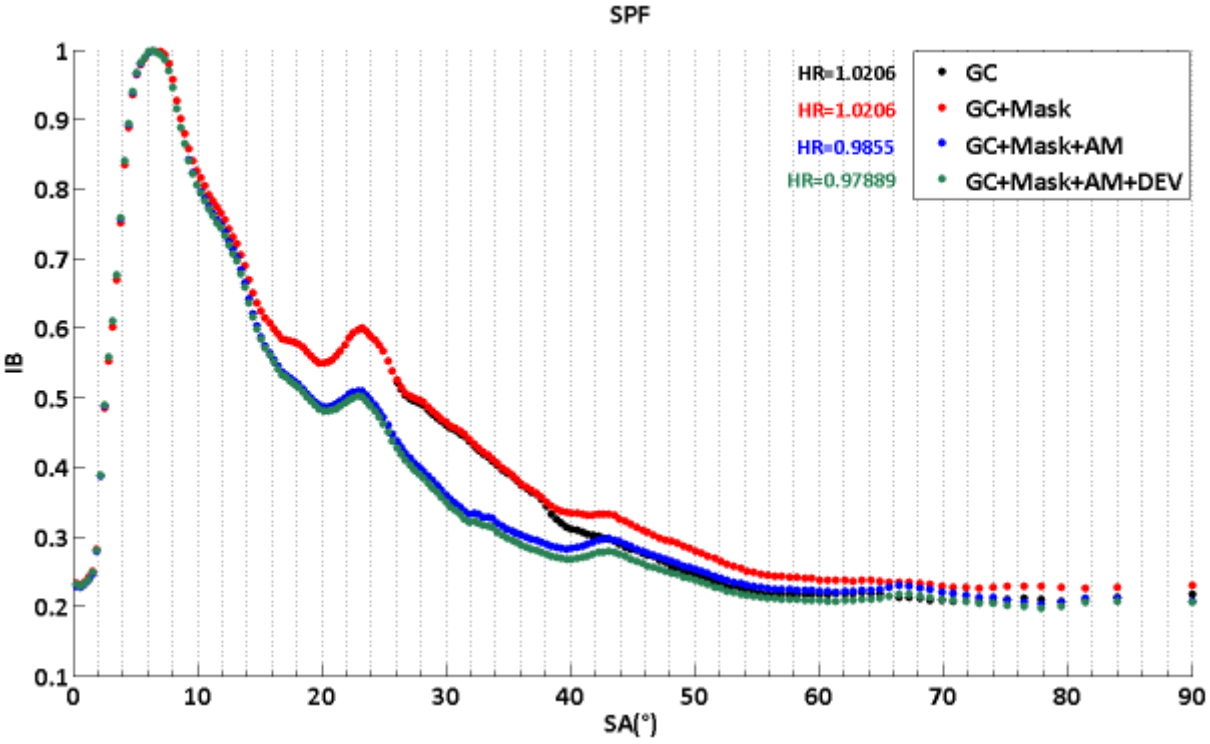

Figure 2-102: Like Figure 2-99 but with AM<7.

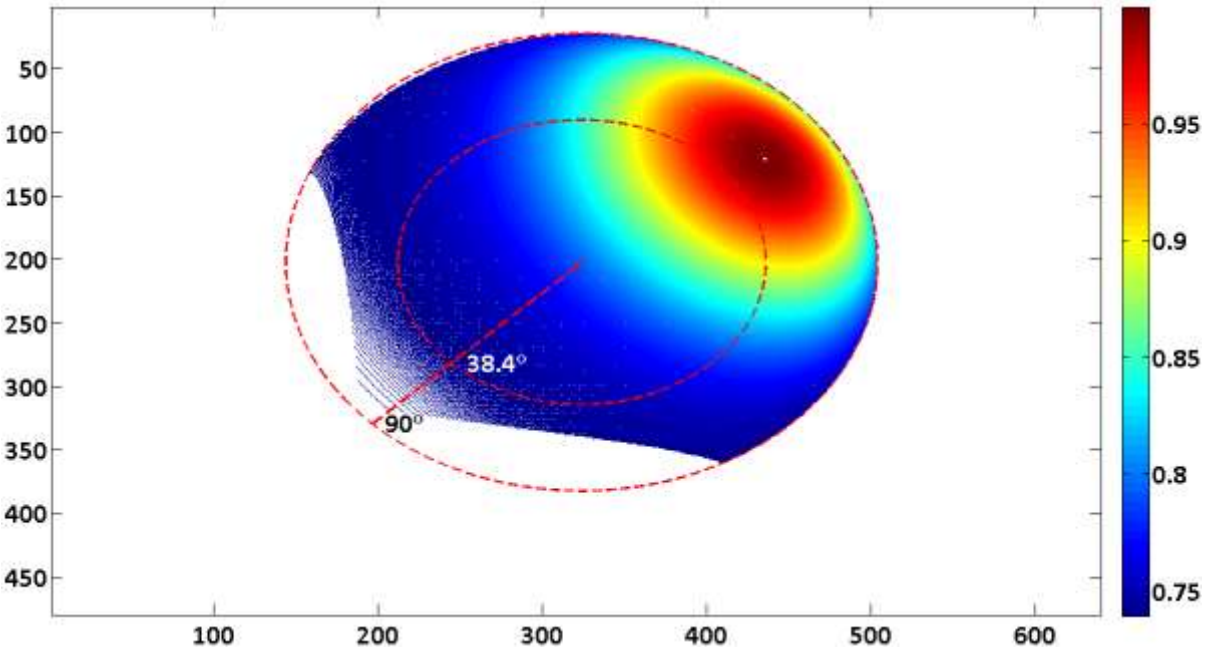

Figure 2-103: Devignetting parameter in the rotated reference system.

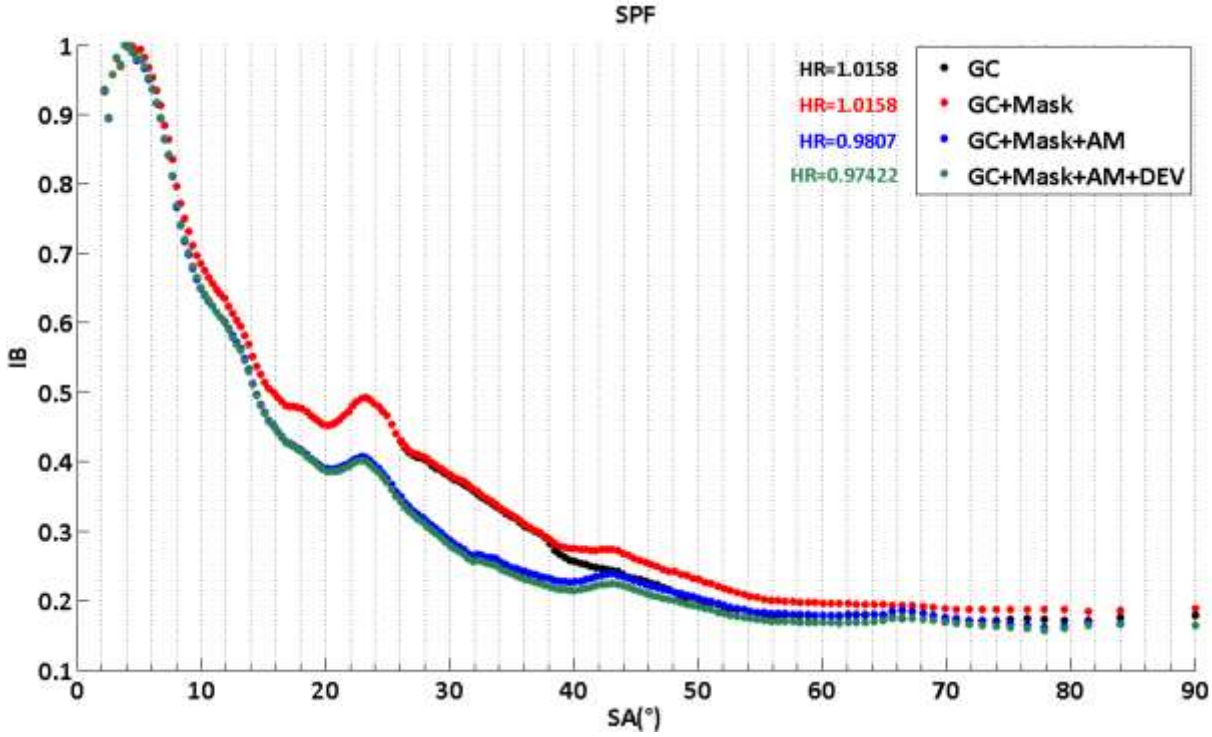

Figure 2-104: Like Figure 2-99 but with AM<7 and the inclusion of the occulting disk mask.

In this chapter we have provided a method to interpret all sky images in terms of scattering phase function. The necessary geometric transformation and corrections for the air mass, for vignetting and for the background have been proposed. This sets us up to measure with some accuracy the SPFs of cirrus clouds from which the HR measure is retrieved. HR time series, under different atmospheric conditions, corresponding to several test cases will be discussed in chapter 4. This has not been done before in all sky imaging to the best of my knowledge.

3 Ice cloud detection through radiometry

In this chapter we will first see what the instruments proposed for detecting cirrus are. We will begin by giving instruments purpose, location and some of their technical characteristics. We will see how a radiation pyrometer can be used for measuring sky downwelling thermal radiation; basics of GPS meteorology and how this applies to the retrieval of columnar integrated water vapour will also be provided. De-trended Fluctuation Analysis, its application for clear sky detection and its limitations in discriminating clear sky from optically thin clouds will then be discussed. We will then turn to the mathematics of a simple analytical model for downwelling thermal radiation under clear skies and see how this leads to the estimation of an effective atmospheric absorption cross section. In section 3.7 we will then discuss the deviation of the model from the observed sky irradiance and look for possible correlations which might allow to reduce such a discrepancy. We will also modify the basic analytical form of the model by including coefficients determined through an optimization routine. In section 3.8 a cirrus detection method will be proposed and the corresponding limitations discussed. Finally, in paragraph 3.9, conclusions to this chapter and recommendations for further work will be given.

3.1 Measurements

What we have seen in section 1 is that cirrus detection is not easy because the downwelling radiation under clear sky and under cirrus, when optically thin, are very similar. Furthermore DFA which in itself is very sensitive to presence of clouds (unless optically thin) does not distinguish between warm and cold clouds. Modelling clear sky thermal emission would help in discriminating between liquid (or mixed phase) and ice clouds. An attempt to do so is discussed in this chapter. Clear sky and cirrus spectra are similar and both significantly deviate from the black body spectrum. However the black body distribution can be used after correcting it by introducing an analytical form for the atmospheric emission. Clear sky emission is mainly governed by WV emission, the amount of which has a diurnal and seasonal variability. First of all, atmospheric temperature governs the amount of emitted IR radiation directly. Moreover, the amount of WV that the atmosphere can contain is determined by the temperature: the greater the temperature the higher the vapour mixing ratio or specific humidity for a given relative humidity. With the purpose of modelling clear sky downwelling thermal radiation the instruments available at Bayfordbury for measuring WV and CGT are:

1. **A weather station for measuring CGT**
2. **A GPS station for IWV soundings**

CGT and IWV are sampled every 1 and 15 minutes respectively. The observed sky BT is measured through an infrared radiation pyrometer which together with the GPS and weather station will be described in the next section.

3.2 Infrared radiation pyrometer (KT15.85 II)

An infrared radiometer (KT15.85 II) has been installed at Bayfordbury for cirrus detection purposes. An example of a generic model belonging to the KT15 series is shown in Figure 3-1.

Figure 3-1: Radiometer KT15 Series (164).

The radiometer pointing at zenith is attached to the wall of a hut about 2 meters above ground (see Figure 3-2).

Figure 3-2: KT15.85 II location.

At its top a white cylindrical shield keeps sunlight out. This has a gap at the bottom to allow airflow in and prevent condensation, it also contains an electric circuit with a few resistors to keep it slightly warmer and prevent dew from forming. Wrapped over that is cling-film (polyethylene), which was the most transparent of the materials tested. This is at an angle to allow rain to run off. The cling-film is replaced periodically to prevent it from breaking and rain from entering. The radiation pyrometer is a measuring transducer, which receives the infrared radiation emitted by the measured object and transforms it into a standardized output signal. If the emissivity is known, the

temperature of the object can be determined. The KT15.85 uses a constant emissivity of 1.0 for sky and clouds. KT15.85 II spectral sensitivity $S(\lambda)$ is centred at around 10.5 µm (see Figure 3-3). The sensitivity spectrum spans from 9.4 to 11.8 µm where the atmospheric transmissivity is very high and no weakening of the infrared radiation due to CO_2 or to WV contained in the air is to be expected. The KT15.85 IIP unit at Bayfordbury has been customized for the -100 to +200°C temperature range. The working principle of infrared radiation pyrometers uses optical modulation of thermal radiation intercepted by an infrared detector. Sometimes this is accomplished by an optical chopper (mechanical blades driven by an electric motor), which periodically interrupts the incident radiation from the measured target to the detector. During each interruption the detector is exposed to an internal blackbody reference source having a defined temperature. Infrared detectors of the pyroelectric type must be operated with the "chopped radiation" method because they respond to radiation differences and not to absolute radiation intensities. The detector intercepts infrared radiation emitted by the measured target and, at the same time, radiation emitted by the detector enclosure. During the short chopping cycles, in the millisecond range, the temperature of the pyrometer's housing does not change. The bias is thus eliminated and substituted by the reference signal, which can be easily measured or controlled within the specified reference accuracy over the operational ambient temperature range. Thus, the "chopped radiation" method eliminates thermal drift and automatically provides a modulated signal with a precisely defined frequency (165).

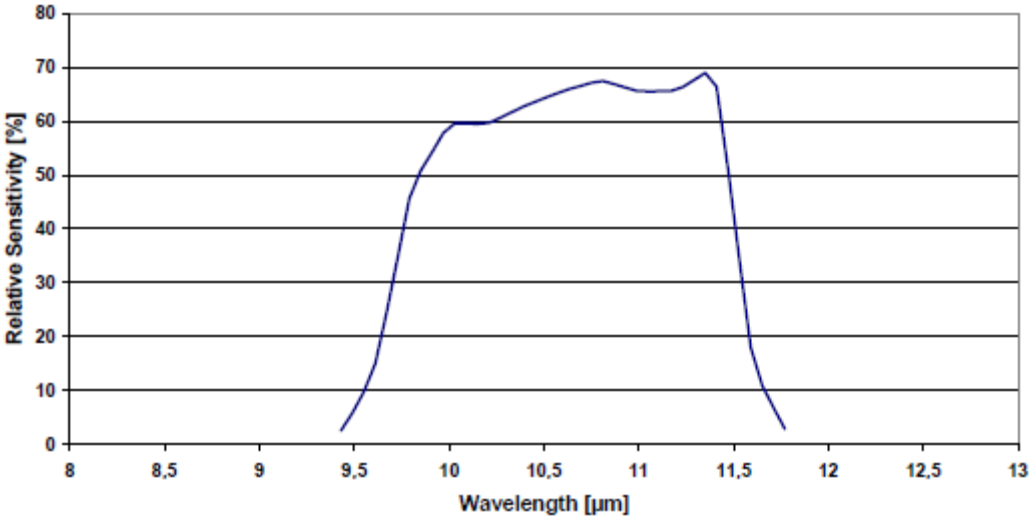

Figure 3-3: KT15.85 spectral response (164).

The impinging irradiance recorded by the instrument, if ε_λ is set to 1, can be thought of as the result of the following integration:

$$I = \int_{\Omega} \int_{\lambda_1}^{\lambda_2} S(\lambda) R(\lambda, T) d\lambda \tag{3.1}$$

The observed irradiance is obtained as the convolution of the Planck's distribution curve (see Eq. 1.41) over the spectral response $S(\lambda)$ and the FOV of the instrument.
The solid angle Ω subtended by KT15.85 is specified by its manufacturer Heitronics (164). Figure 3-4 shows a corresponding diagram.

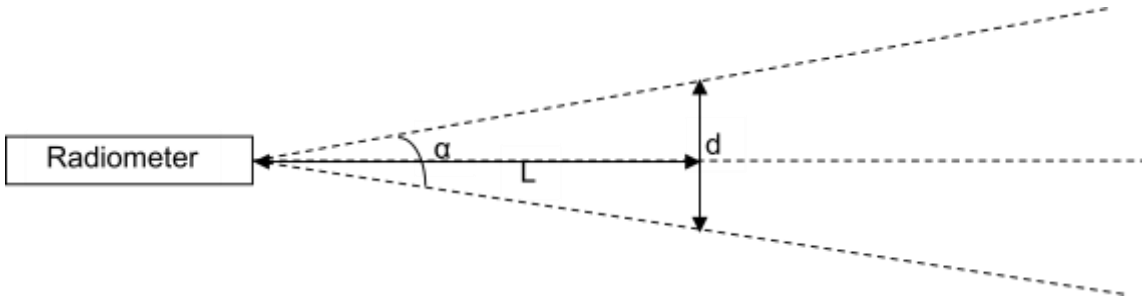

Figure 3-4: KT15.85 field of view.

According to the manufacturer, depending on the detector type and the lens adopted, the ratio of the target diameter to the distance from the lens varies as in Figure 3-5.

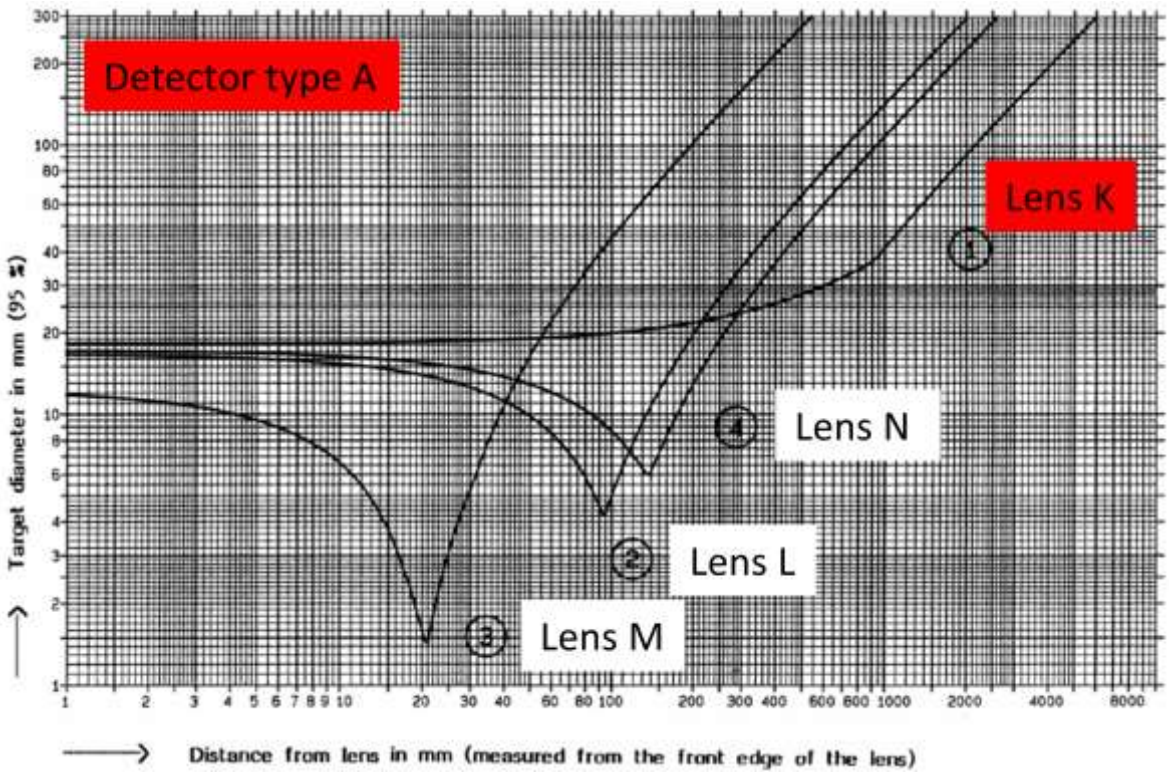

Figure 3-5: Target diameter for the KT1585 radiometer (164).

In our specific case the detector type is A and the lens type is K. After 1 m distance from the lens the ratio of the target diameter *d* to the distance from the lens *L* becomes constant and equal to 0.05 (see Eq. 3.2). From trigonometry (see Eq. 3.3) and after integration over ϑ and φ the solid angle subtended by KT15.85 has been estimated (see Eq. 3.4). At 10 km altitude the size of the target would be as large as 500 m.

$$\frac{d}{L} = 0.05 \tag{3.2}$$

$$\frac{d}{2} = L\tan\left(\frac{\alpha}{2}\right) \Rightarrow \frac{\alpha}{2} = \arctan(0.025) \Rightarrow \alpha \approx 2.86° \tag{3.3}$$

$$\Delta\Omega = \int_0^{2\pi} d\varphi \int_0^{\frac{\alpha}{2}} d\theta \sin\theta = 2\pi\left(1 - \cos\frac{\alpha}{2}\right) = 1.9 \cdot 10^{-3}\ sr \tag{3.4}$$

3.2.1 Observed sky BT

Figure 3-6 shows a schematic diagram of KT15.85 field of view and its zenith pointing layout. The atmosphere is assumed to be plane parallel (dashed lines), which is a reasonable approximation given its relatively small thickness with respect to the Earth's radius.

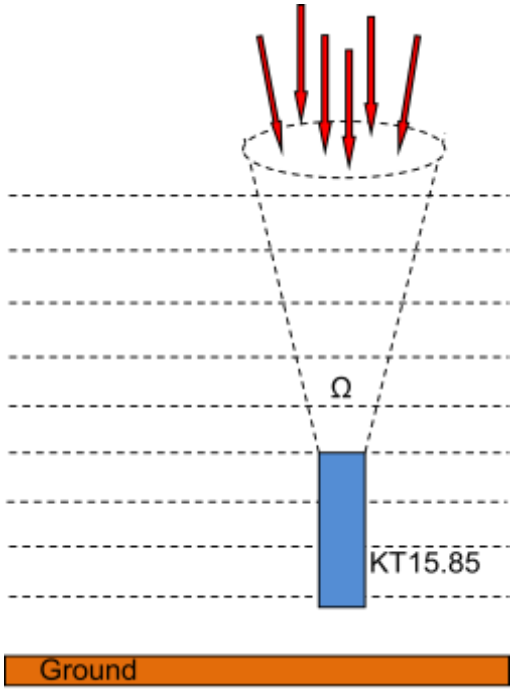

Figure 3-6: Schematic diagram of KT15.85 field of view.

From the radiometer, text data files listing BT as a function of time are obtained. Time and BT are recorded with a frequency of 1 Hz. The temperature resolution of the instrument is ± 0.65 K if emissivity and response time are set to 1 and 1 sec respectively (164). BT is very sensitive to the fast changing atmospheric conditions. If we look at its annual variation (see Figure 3-7 - one minute resolution), we can notice its large variability embedded in the slowly varying seasonal trend consistent with the variation in atmospheric temperature and pressure (103). It should be noticed that interpolated values appear where gaps in the data occur. In winter, sky BT can be as low as -70 ^{o}C. Superimposed on BT is the annual variability of WV and CGT as observed from our measuring site. The high frequency variation is mostly due to clouds. When optically thick clouds are in the field of view of the radiometer, variations in BT, from that of the background clear sky that are, as large as 40 ^{o}C are observed. Determining variations in the observed BT associated with WV and CGT seasonal

variability is the purpose of this investigation. Our aim will be modelling BT under clear skies, which will provide a "baseline" BT for the more general case when clouds are present.

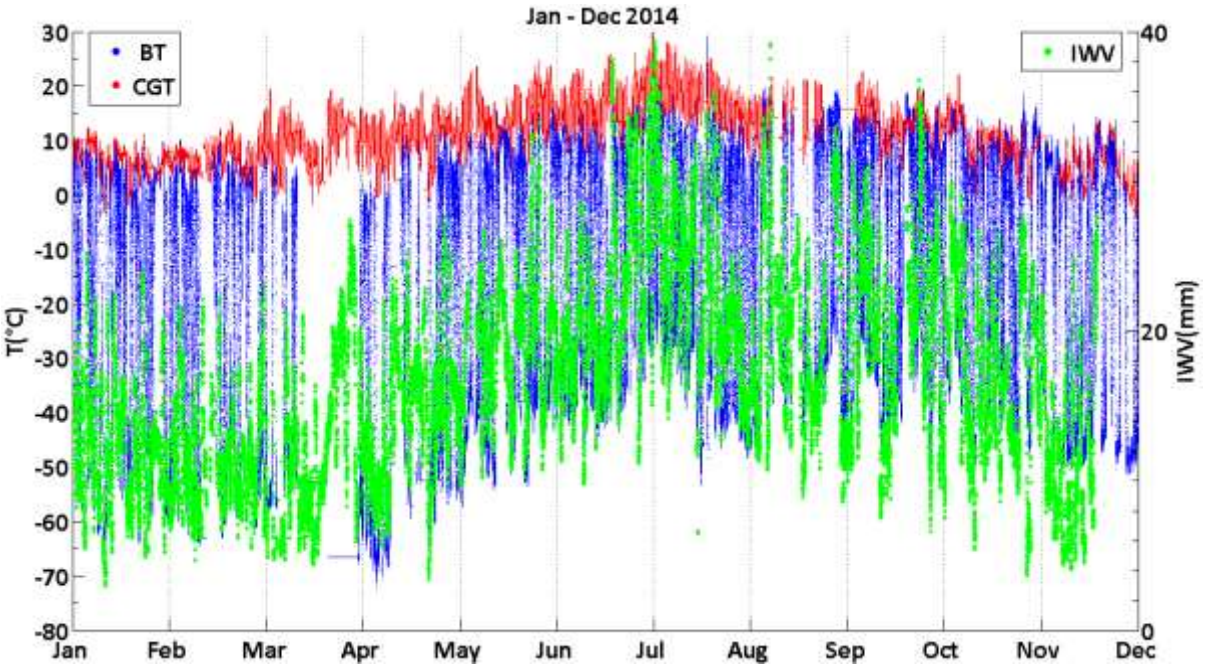

Figure 3-7: Time series of the measured BT over one year (2014) period.

Figure 3-8 shows the observed BT corresponding to the time period ranging from April the 27th to May the 5th 2013 with the corresponding CGT and WV time series.

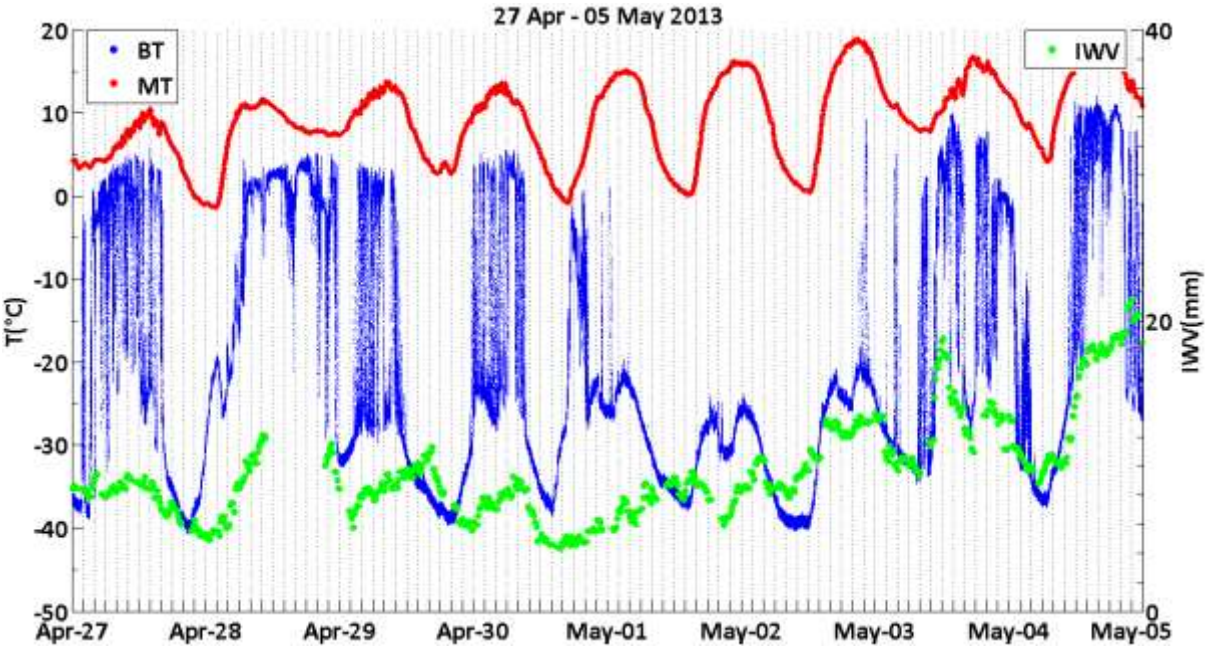

Figure 3-8: Time series of the observed BT, CGT and WV from April the 27th to May the 5th 2013.

Over those time intervals when no clouds are in the field of view of the radiometer (BT<-20^{o}C) the downwelling atmospheric thermal emission seems to follow the diurnal change of CGT. If we look at the behaviour of the corresponding WV time series, increases and decreases in the observed BT are

mostly accompanied by corresponding variations in the WV observed. Maxima and minima do not always coincide with those observed in the CGT time series. However, this should not come as a surprise as it is a measure of the WV contained over the entire atmospheric column and therefore not only affected by CGT but potentially by the entire T profile. Failure in the uploading or in the processing of the observed GPS receiver zenith delays can give rise to gaps in the WV time series as the one occurring between the 28th and 29th of April.
Figure 3-9 shows the observed BT over the time period ranging from July the 5th to July the 10th 2013 and the corresponding CGT and WV time series. Presence of data gaps as the one between the 8th and 9th of July are due to the occurrence of brownouts.

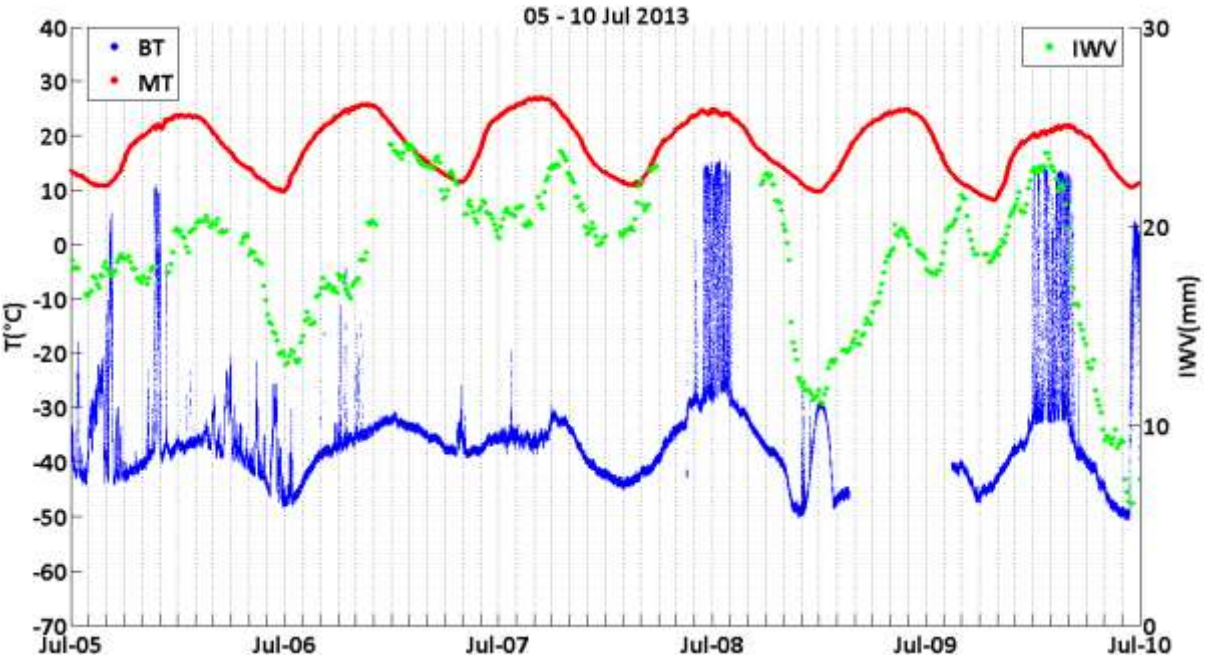

Figure 3-9: Time series of the observed BT from July the 5th to July the 10th 2013.

In analogy to the previous case when no clouds are in the field of view of the instrument the atmospheric column seems to be radiating proportionally to CGT. In particular if we look at the WV maxima and minima they match with the corresponding peaks and dips observed in the BT time series more than they did in the previous case. This could be due to the relatively higher WV average observed during this period compared to the one observed in April. If detecting optically thick clouds seems to be straightforward, this is not true for optically thin clouds because of the seasonal and diurnal WV variation. BT recorded in the presence of optically thin clouds over a dry atmosphere can be comparable to BT observed under clear skies over a humid atmosphere. This is also why setting a fixed threshold for cloud detection would not be sufficient. At the current stage it has been decided to not have recourse to numerical radiative transfer models accounting for all the important processes occurring when radiation and atmosphere interact. Building a physical, analytical model of the observed sky BT, using first principles (i.e. black body radiation etc.) is the approach chosen which significantly simplifies calculations. In fact, it does not require the detailed spectral profiles of the atmospheric constituents and their radiative properties to derive the atmospheric radiance, but relies only on screen level parameters. In section 3.6 this is what is done for clear sky. This is relevant for ice cloud detection, because if we can predict how BT varies with the atmospheric variables under clear skies (taking into consideration the amount of WV, air temperature close to ground, relative humidity, dew point) or in other words if we can model clear sky BT with sufficient accuracy then we would have an additional tool for discriminating cirrus.
Based on the reasons set out so far and on the instruments available at the observing site, WV and CGT will be used to determine downwelling thermal emission under clear skies. These two quantities

are the ones which have been measured and are discussed in the coming sections. The instrument chosen for WV sounding is a GPS receiver which will be described in section 3.3.2. In the next section the basic principles of GPS meteorology will be discussed. In section 3.3.1 an overview of the EUMETNET GNSS (Global Navigation Satellite System) water vapour programme will be given. The weather station which provides us with the observed CGT is discussed in section 3.4.

3.3 GPS meteorology

When signals travel through the atmosphere they travel slower and along a curved path because of the variable atmospheric refraction index along the ray path. The delay in signal arrival time can be stated in terms of an equivalent increase in travel path length. This excess path length is given by

$$\Delta L = \int_S n(s)ds - G \tag{3.5}$$

where:

1. ***n*(s) is the refractive index as a function of position *s* along the curved ray path *L***
2. ***G* is the straight-line geometrical path length through the atmosphere (the path that would occur if the atmosphere was replaced by a vacuum).**

Equivalently

$$\Delta L = \int_S [n(s)-1]ds + [S-G] \tag{3.6}$$

where:

3. ***S* is the path length along *L***

The first term on the right is due to the slowing effect whereas the second term to the bending. The bending term [*S* - *G*] is much the smaller, about 1 cm or less, for paths with elevations greater than about 15°. For vertical rays, the ray path is a straight line and the bending term vanishes (166). Saastamoinen et al. (167) showed that the zenith total delay (ZTD) can be partitioned into a large quantity which depends only on surface pressure, called the "zenith hydrostatic delay" (ZHD), which has been fairly accurately modelled, and a smaller quantity which is a function of water vapour distribution and is called the "zenith wet delay" (ZWD). It is possible to derive an approximate relationship between the vertically integrated water vapour (IWV) and the observed ZWD (166), as in Eq. 3.7.

$$IWV \approx k \cdot ZWD \tag{3.7}$$

where

$$\frac{1}{k} = 10^{-6}\left(\frac{k_3}{T_m} + k_2\right)R_v \tag{3.8}$$

1. **R_v is the specific gas constant for water vapour**
2. **T_m is the average temperature of the atmosphere weighted by the pressure of water vapour**
3. **k_3 is (3.776±0.004)10^5 K^2mbar^{-1}**
4. **k_2 is 17±10 K $mbar^{-1}$ (166)**

The constant *k* should be estimated using a value for T_m that is "tuned" to the specific location and season (166). The zenith hydrostatic delay (ZHD) is subtracted from the ZTD and an estimate of the IWV can then be obtained.

3.3.1 The E-GVAP program

EUMETNET is the network of European Meteorological Services. E-GVAP, the EUMETNET GNSS water vapour programme, was set up, in April 2005, to provide its EUMETNET members with European GNSS delay and water vapour estimates for operational meteorology in near real-time (168). The NRT GNSS delay data contain information about the amount of water vapour above the GNSS sites. Water vapour plays a key role in atmospheric processes by providing half of the energy of the atmosphere through latent heat, contributing to its dynamics and as we have seen in the previous section amongst green-house gases is the most important one. Given the lack of water vapour observations, a ground based network of GNSS has been set up to improve on this (see Figure 3-10) (168). For the moment the E-GVAP network consists of more than 1500 GNSS sites, mainly in Europe, but recently processing and distribution of global GNSS data has started, since many E-GVAP members run global NWP models. For the same reason E-GVAP welcomes collaboration with both European and non European institutions, in order to densify the GNSS meteorological observing network (168).

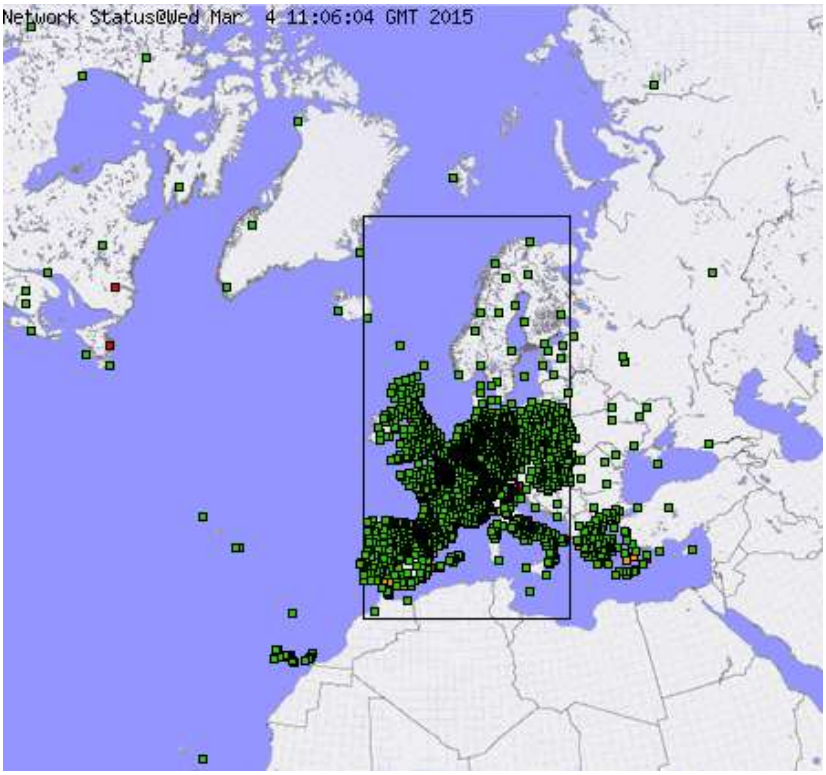

Figure 3-10: The current status of the NTR (Near Real Time) network (168).

The vast majority of high quality permanent GNSS sites are installed for positioning purposes, by geodetic institutions and private firms. To them the atmospheric delay is a noise term. The core of E-GVAP is a close collaboration between geodesy and meteorology. Raw data from GNSS sites are collected by more than ten GNSS analysis centres, which process the data to estimate ZTDs and other parameters. The British Isles continuous GNSS Facility (BIGF), hosted at the Nottingham Geospatial Institute, a centre for related postgraduate teaching and research, at The University of Nottingham (UK) is the analysis centre which provided the BGF2 solution used in this investigation for WV sounding (169). The archive comprises RINEX data from GPS and GLONASS satellites, from a high density network of around 160 continuously recording stations, sited throughout mainland Britain, Northern Ireland and Ireland. IES2 is the sub group of the entire NRT network from which BIGF retrieve ZTDs and IWV estimates (see Figure 3-11) (169).

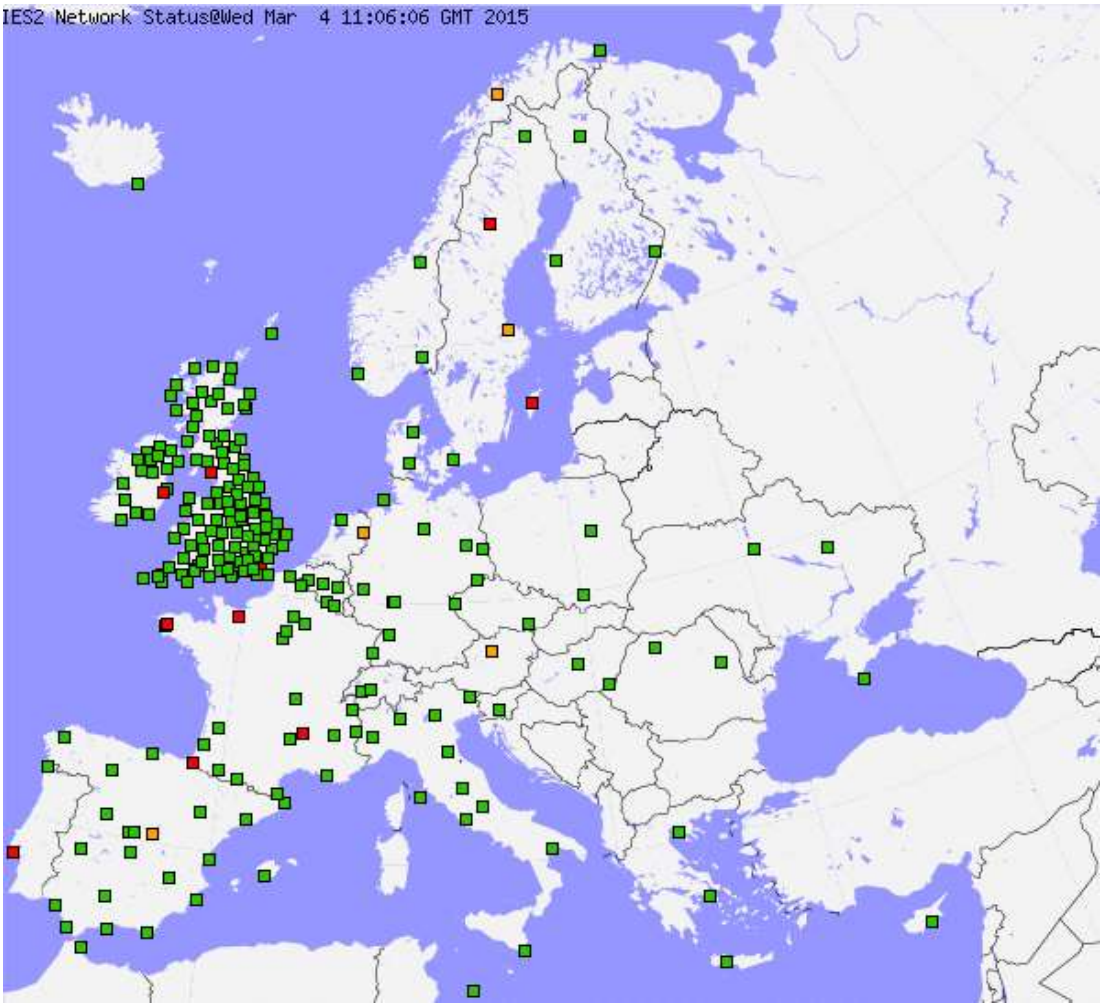

Figure 3-11: IES2 Network status, locations of the latest estimates, Wed 4th Mar 11:06 GMT 2015 (168).

	No Data or before **03/02 12h**
	between 03/04 09h and 03/04 12h
	between 03/04 06h and 03/04 09h
	between 03/04 06h and 03/02 12h

Figure 3-12: Arrival time window of observations.

By clicking on a coloured square the time series of IWV and ZTD is presented in a separate window. Figure 3-13 shows an example corresponding to the observing station of Stevenage (UK) (STEE).

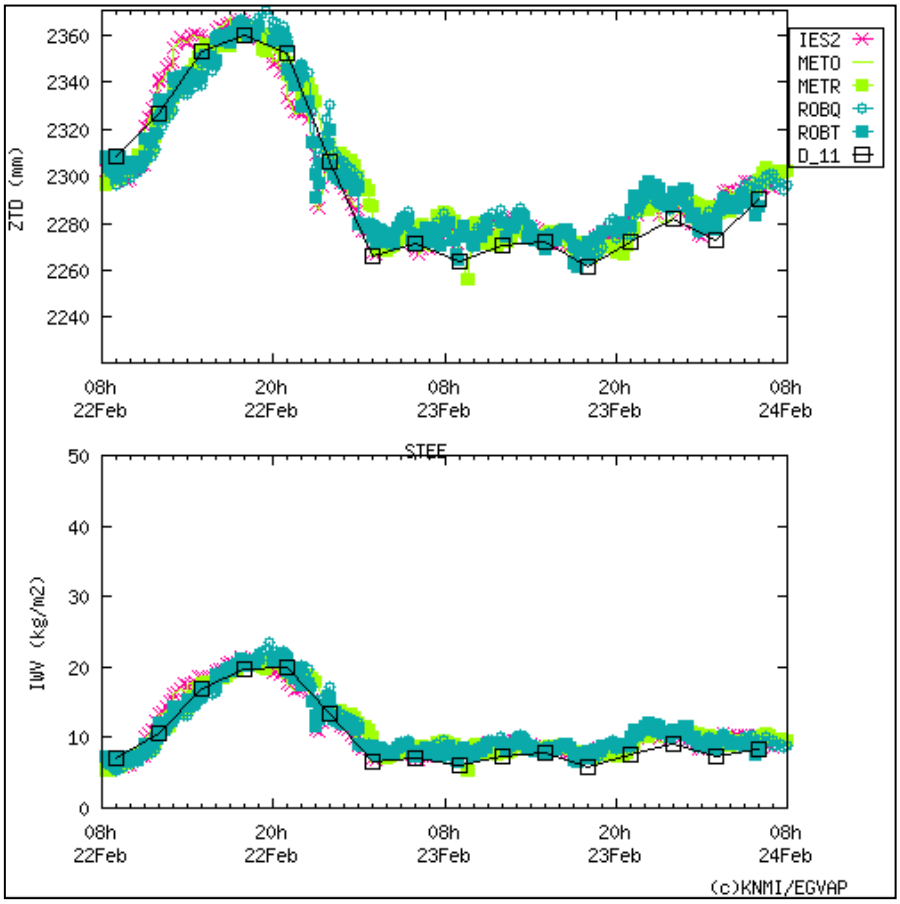

Figure 3-13: ZTD and IWV time series obtained by clicking the square corresponding to STEE (Stevenage) site; the time series represent WV estimates for the period ranging from February the 22nd at 08 am up to Feb the 24th at 08 am.

The University of Hertfordshire has recently contributed to expanding this network of ground based recording stations by acquiring one.

3.3.2 The GPS receiver

A GPS receiver has been installed, about 1 meter away from the radiometer KT15.85, 3.8 m above the ground, attached to the hut with a rigid steel frame (see Figure 3-14).

Figure 3-14: Observatory of Bayfordbury, GPS station attached to the hut by a rigid steel frame.

A list of the parameters obtainable from BIGF analysis, together with the corresponding description, units and format are given in Table 3.

Parameter Name	Description	Units	Format
Time	Time stamp of sample in UTC to 1s (hours, minutes & seconds)	hr/min/sec	3I3.2
Product Confidence Data (Data)	A set of summary bit flags describing the quality of the data sample	flag bits	Z9.8
Zenith Total Delay	ZTD to 0.1mm	mm	F7.1
Error in ZTD	Estimated error (standard deviation) in ZTD to 0.1mm	mm	F7.1
Zenith Wet Delay	ZWD to 0.1mm (when surface pressure available)	mm	F7.1
Integrated Water Vapour	IWV to 0.1kg.m^{-2} (when ZWD, Temp & RH available)	kg.m^{-2}	F7.1
Pressure	Pressure used for ZWD to 0.1hPa	hPa	F7.1
Temperature	Temperature used for IWV to 0.1K	K	F7.1
Relative Humidity	RH used for IWV to 0.1%	percent	F7.1
Gradients	N/S & E/W delay gradients to 0.01mm	mm	2F7.2
Gradient errors	Estimated errors (standard deviations) in delay gradients to 0.01mm	mm	2F7.2
TEC	Vertically integrated Total Electron Content (1 TECU = 10^{16} electrons per m^2) to 0.001 TECU	TECU	F8.3

Table 3: List of products obtained from BIGF ZTDs analysis.

WV has a seasonal variability. It spans from about 5 mm in winter, when CGT is lower on average, to 35 mm in summer when down-welling solar flux significantly intensifies. If we focus on the year 2014 only, Figure 3-15 shows the time series corresponding to the WV raw and LOWESS smoothed data measured at Bayfordbury.

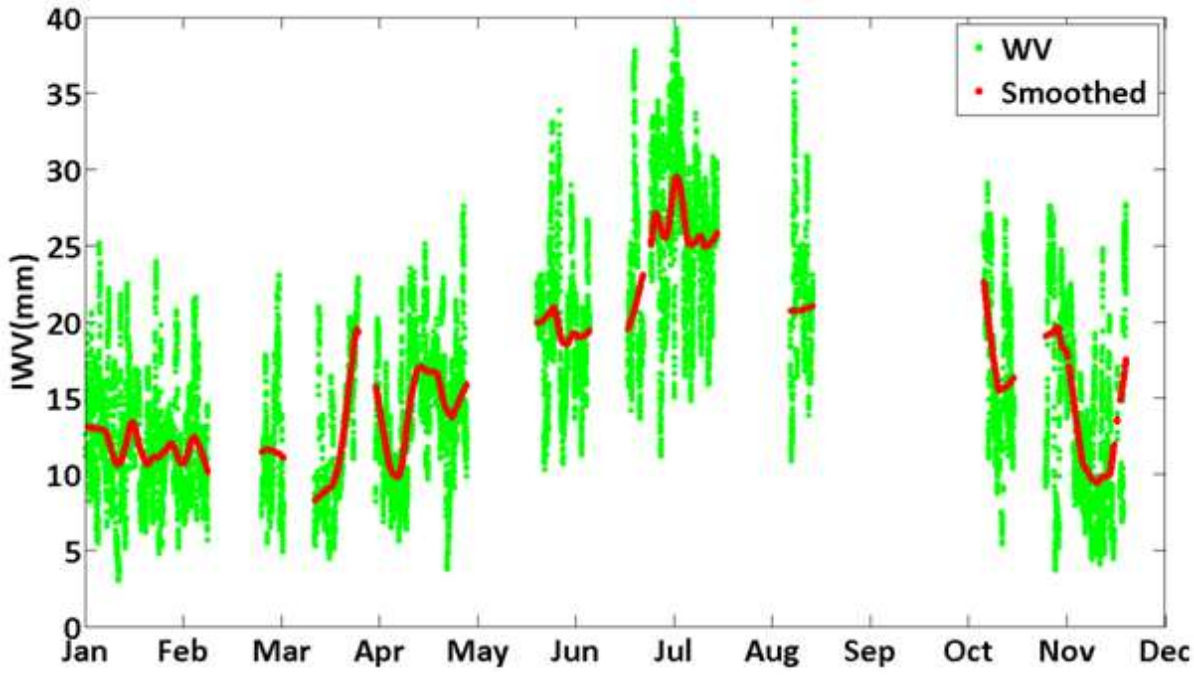

Figure 3-15: WV observation - Bayfordbury(UK) - from 1st of Jan 2014 to 31st of Dec 2014.

Figure 3-16 and Figure 3-17 are the observed 2014 WV time series for the nearby sites of Stevenage (STEE) and Stratford (STRA) respectively.

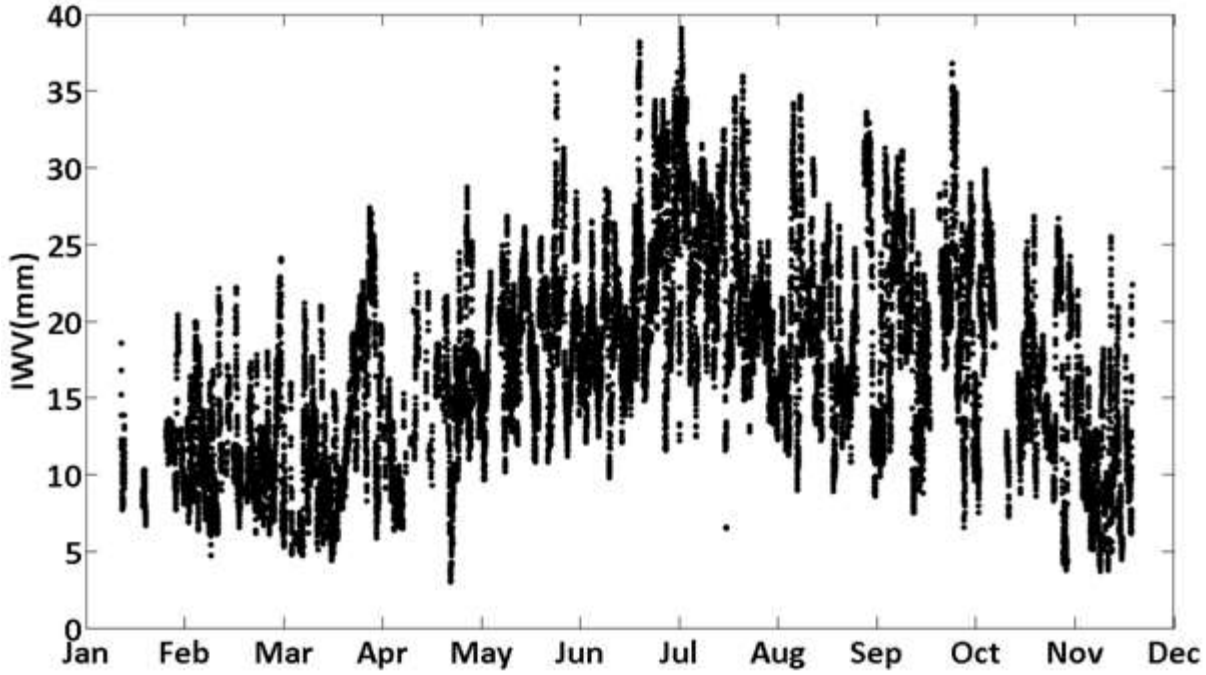

Figure 3-16: WV observation - Stevenage(UK) - from Jan the 1th 2014 to Feb the 1th 2015.

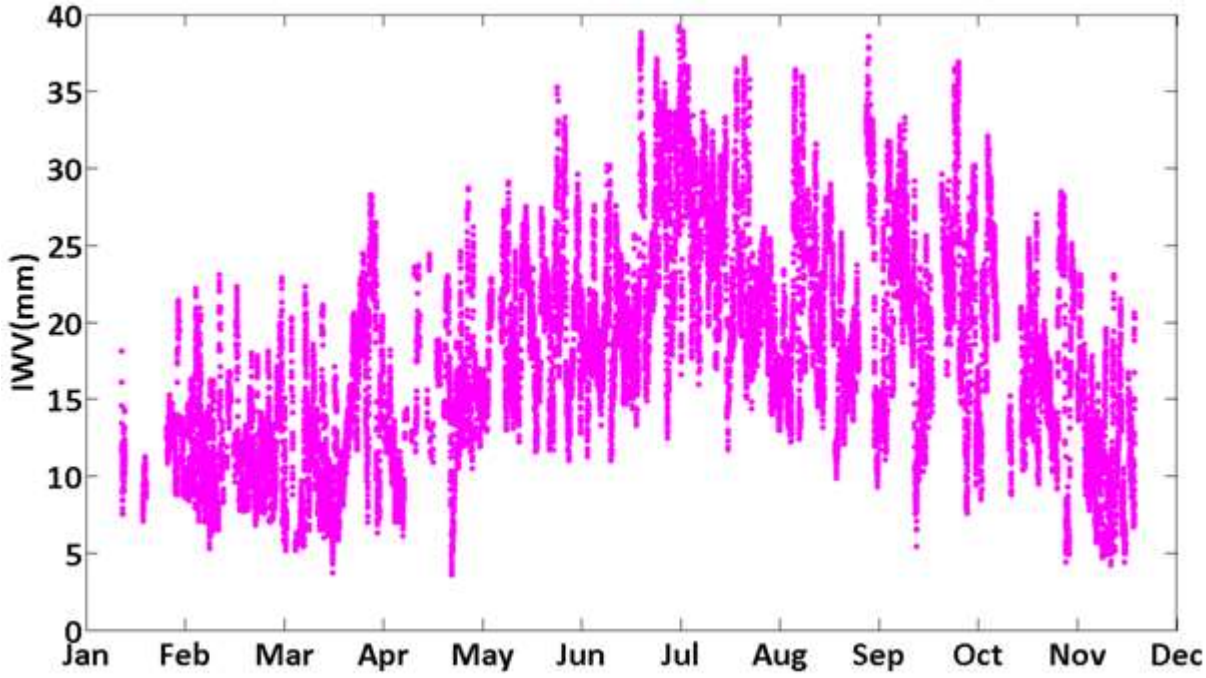

Figure 3-17: WV observation - Stratford(UK) - from Jan the 1th 2014 to Feb the 1th 2015.

The mean absolute deviation (MAD) between the WV observed at Bayfordbury and Stevenage and Bayfordbury and Stratford calculated through Eq. 3.9 is 0.91 mm and 0.99 mm respectively.

$$MAD = \frac{\sum_{j=1}^{N} \left| WV_{ref} - WV_{nearbysite} \right|}{N} \tag{3.9}$$

This implies that in case of data gaps in the Bayfordbury WV soundings, data from STEE can be taken as second preferable choice.

3.4 The weather station

A weather station (see Figure 3-18) which records air temperature, humidity (inside the hut and outside), air pressure, wind direction, wind speed, rain rate, solar radiation and UV index has been installed 10 m south of the building where the radiometer is installed. The temperature sensor is 2 m above the ground. The air temperature sensor is rated ±0.5°C, and has a number of solar radiation shields so it is not affected directly by the sun. The measured height above ground is 2.12 m.

Figure 3-18: the weather station.

Before discussing the clear sky BT model it is necessary to find clear sky data points to test the model with. In the coming section the DFA algorithm which in first place permits to sense cloud presence irrespective of cloud phase and optical thickness will be used for identifying clear sky spells. It will be shown that DFA is very sensitive to the presence of clouds although it may fail to identify very optically thin ones. DFA is the initial step of the cirrus detection algorithm whereas the comparison of BT and clear sky BT is the second step which allows to screen out warm clouds and indirectly to discriminate cirrus.

3.5 Clear sky detection

Clear sky data have to be selected if a model (which will be discussed in the next section) for downwelling radiation under clear sky has to be tested. Ideally the model would manage to reproduce the observed BT with sufficient accuracy to assure that even when optically thin clouds are in the field of view of the instrument, BT observed is larger than the modelled clear sky BT. In other words the accuracy of the model has to be such that even when the thinnest cloud is present the modelled BT within the margins of uncertainty is below the observed BT. The latter in itself is not

sufficient for clear sky detection as we have seen that under clear skies BT can be as low as it would be in presence of optically thin cirrus. Measuring the fluctuations of the observed BT is an additional tool for discriminating clear sky (102).

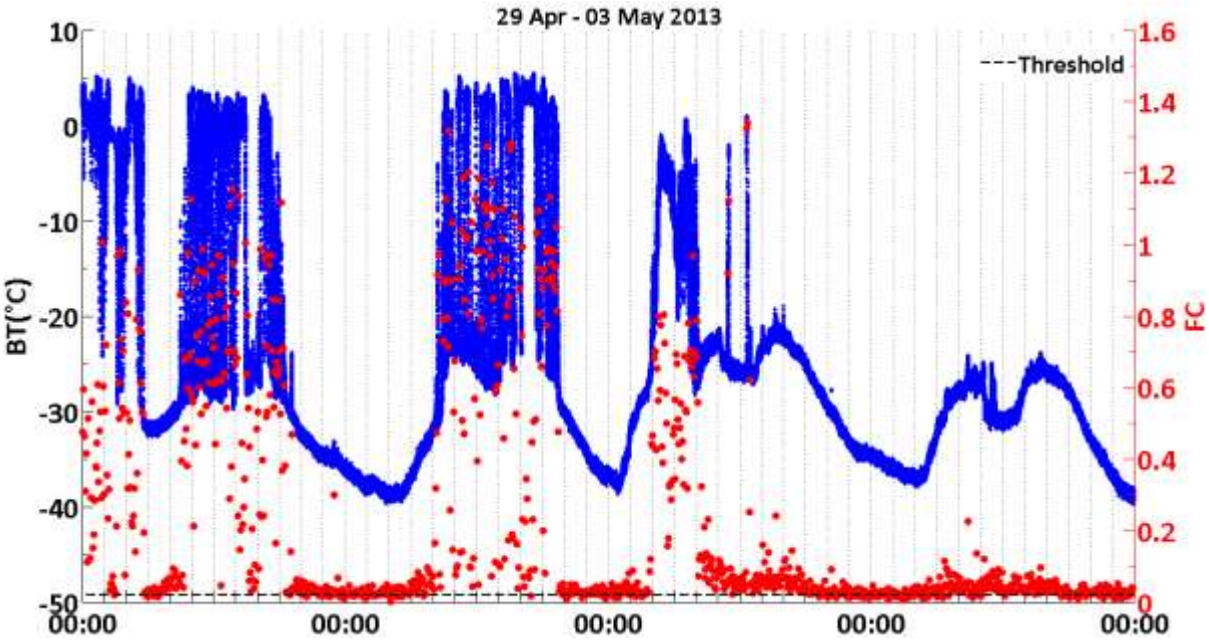

Figure 3-19: BT and corresponding DFA fluctuation coefficient time series. The time axis starts at midnight (00:00) on the 29th of April 2013 and shows the time label at the beginning of each day. The time interval ends at midnight on the 3rd of May 2013. Dotted vertical grid lines, separated by 2 hours, are also shown.

The Detrended Fluctuation Analysis (DFA) is an algorithm that when applied to a time series gives a measure of the temporal fluctuations of the time series itself. Such measure is the fluctuation coefficient (FC). DFA has already been applied in similar contexts and implemented into cloud detection algorithms (102) (103). For this particular investigation a DFA algorithm has been written in Matlab. If we look at Figure 3-19 and Figure 3-20 the FC (red dot) is proportional to the fluctuations in the observed BT (blue dot). When the fluctuation is minimum as it is the case under clear skies FC also takes on its minimum which is 0.02 based on the DFA output calculated over a year of observations (if its resolution is set to 5 minutes and the time scale over which the FC is calculated ranges between 20 and 60 seconds). Therefore a threshold (black dashed line - which in general is function of the time scale chosen) has been set to discriminate clear sky. DFA does not account for the absolute value of BT. Therefore DFA in itself does not tell us around which mean value of BT the time series is fluctuating. To give broader context to the data in Figure 3-19 and Figure 3-20 the respective clear sky data points so selected have been scatter plotted against CGT and shown in Figure 3-21 and Figure 3-22. Correlation coefficients of 0.61 (April-May) and 0.65 (July) are observed and would confirm what has been stated in section 3.2.1 on qualitative grounds about the fact that the atmosphere under clear skies can be thought of as a gray body whose temperature is proportional to CGT. Despite the above discussed (see paragraph 1.5) significant departure of clear sky spectra from the black body one, these findings seem to suggest that clear sky emission can be formulated in terms of gray body radiance.

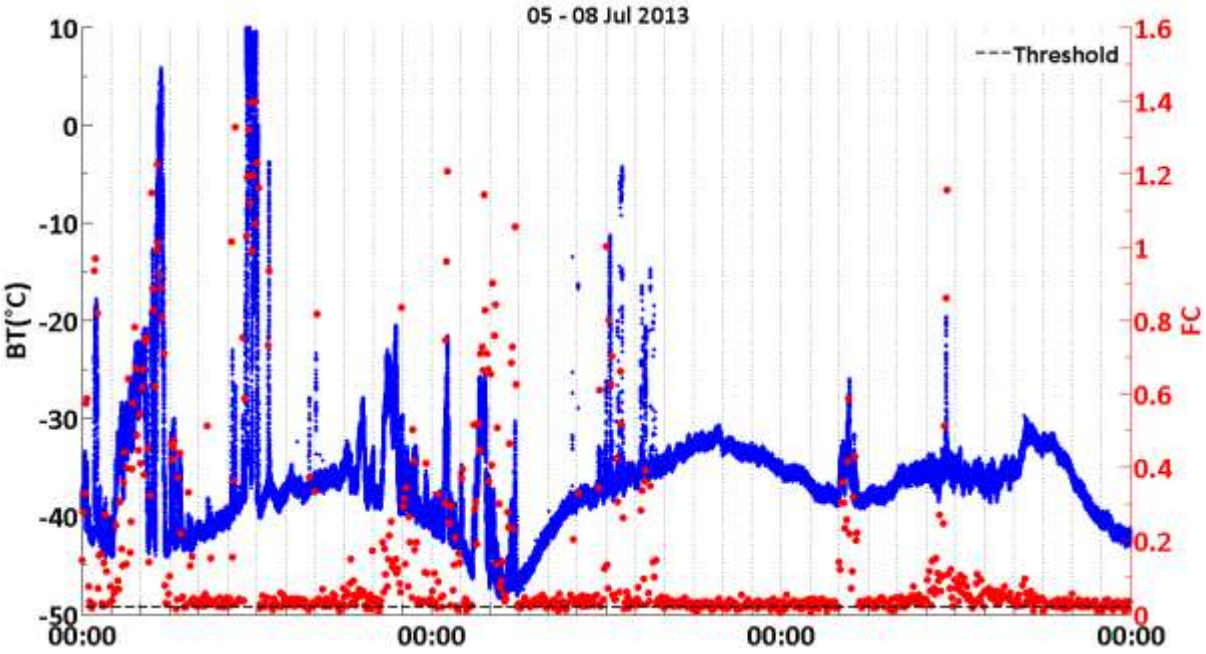

Figure 3-20: BT and corresponding DFA fluctuation coefficient time series. The time axis starts at midnight (00:00) on the 5th of July 2013 and shows the time label at the beginning of each day. The time interval ends at midnight on the 8th of July 2013. Dotted vertical grid lines, separated by 2 hours, are also shown.

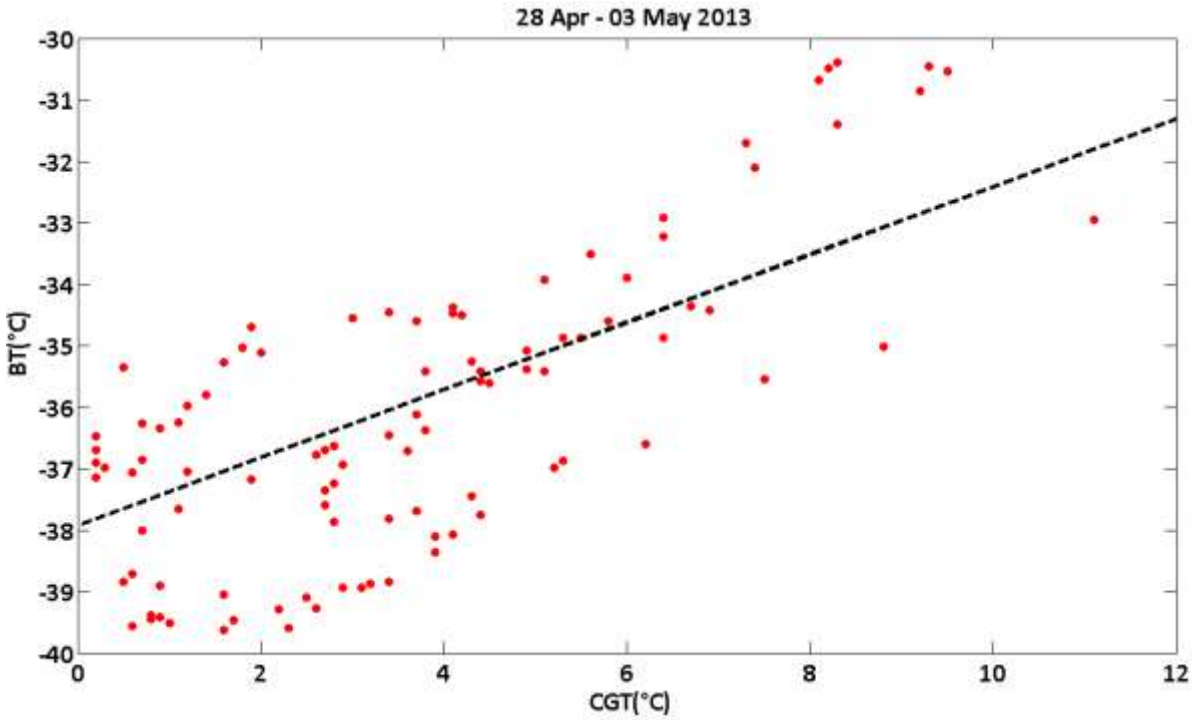

Figure 3-21: BT vs CGT for clear sky data points selected through DFA and corresponding to Figure 3-19.

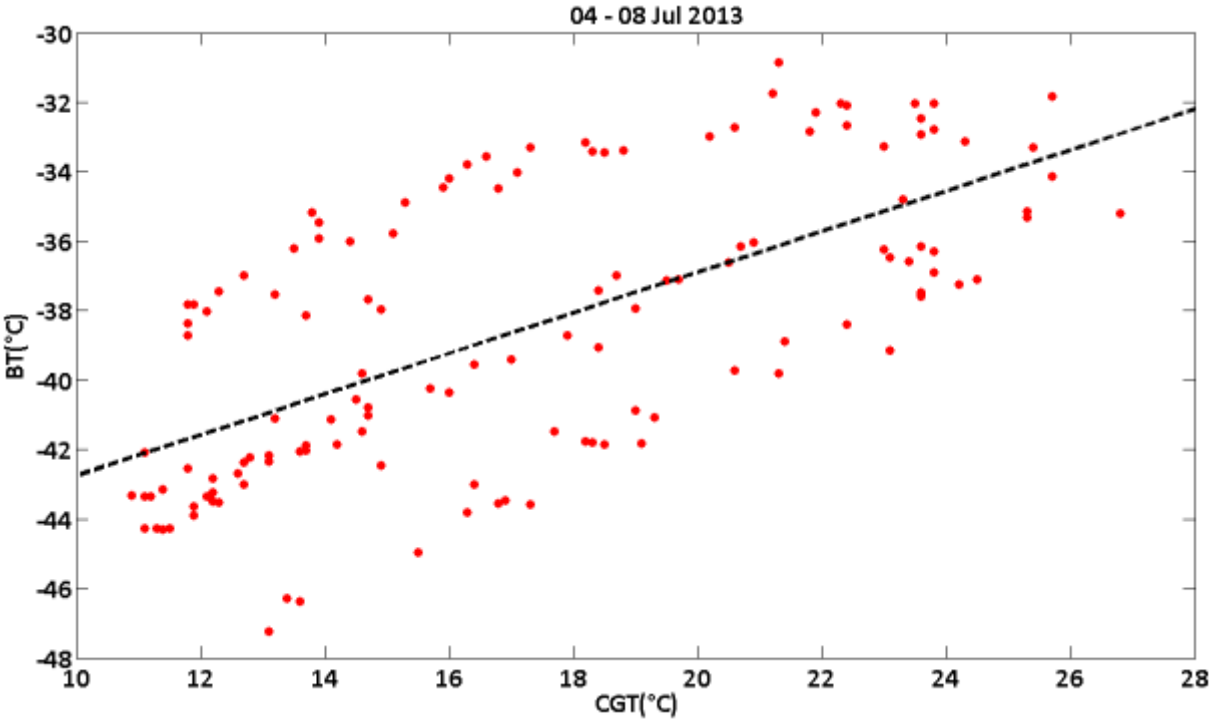

Figure 3-22: BT vs CGT for clear sky data points selected through DFA and corresponding to Figure 3-20.

With respect to Figure 3-19, and in particular to the small peak observed in the BT time series at about 11 pm on the 29th of April, it is worth noticing how sensitive DFA is to BT fluctuations as small as a few degrees. The corresponding All-sky image (see Figure 3-23) shows the presence of a small cloud grouping passing over the observation site.

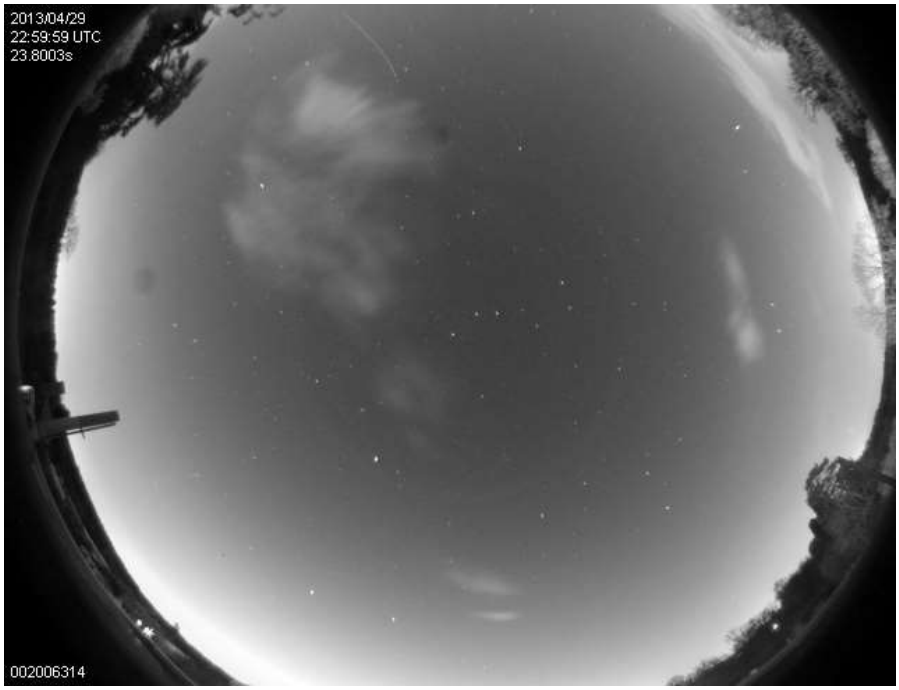

Figure 3-23: 29 Apr 2013 10:59pm.

However it should be pointed out that DFA is not always successful in discriminating clear sky. In this context three cases have been compared. A case of optically thick clouds, thin cirrus and clear sky observed on the 9th of July 2014 at 1:54pm, the 14th of Jan at 12:00 and on the 20th of Aug 2014 at 8:00 am respectively. Figure 3-25, Figure 3-27 and Figure 3-29 represent the corresponding all-sky images. The BT time series corresponding to a time interval of 15 minutes centred at the respective observation times have been plotted along with the FC and a threshold set to 0.02. Figure 3-24, Figure 3-26 and Figure 3-28 are the corresponding time series for the three cases. This is a typical example of DFA failure; in fact the FC, despite being larger in presence of optically thick clouds, in presence of cirrus is less than under clear sky. The reason why this happens is made more clear by looking at the plot of the DFA functions. Figure 3-30 and Figure 3-31 show the DFA functions for the three cases analysed for a time interval of 15 and 5 minutes respectively. The FC is the slope of the regression line calculated over the time scale chosen. This has been set to 60-150 and 30-60 seconds when the time interval is 15 and 5 minutes, respectively. For a given time interval the DFA function has been calculated over several test cases. The time scale has then been chosen as the time range over which the DFA function is relatively stable and the slope of the DFA function, or in other words the FC, is as sensitive as possible to the presence of clouds. Basically the slope of the DFA functions in the presence of clear sky or optically thin clouds is comparable and this is what makes it hard to discriminate clear sky. The resolution of the clear sky BT model is 15 minutes as this is the rate that the WV has been sampled at. Therefore if we want to test the model, we must establish whether the sky is clear around these data points. The time interval chosen over which the FC is calculated is 20 minutes. This time length should increase the likelihood of cloud screening the data point without excluding potentially good clear sky data by seeing fluctuations which are far from the observation time. Considering the issue just discussed, there is no guarantee that the whole data set which will be used to test the model will be cloud free. It should also be clear that there is no guarantee that DFA will be able to exclude aerosol cases. In order to further cloud screen the data the standard deviation (STD) of the BT time series has also been taken into account. In this respect data already cloud-screened through DFA and covering the period from November 2013 to November 2015 have been further cloud-screened by observing (see Figure 2-67) that STD is on average expected to be below 0.5^{o}C for clear sky. These cases will be used in section 3.7 where the deviation of the model from the observed BT will be discussed.

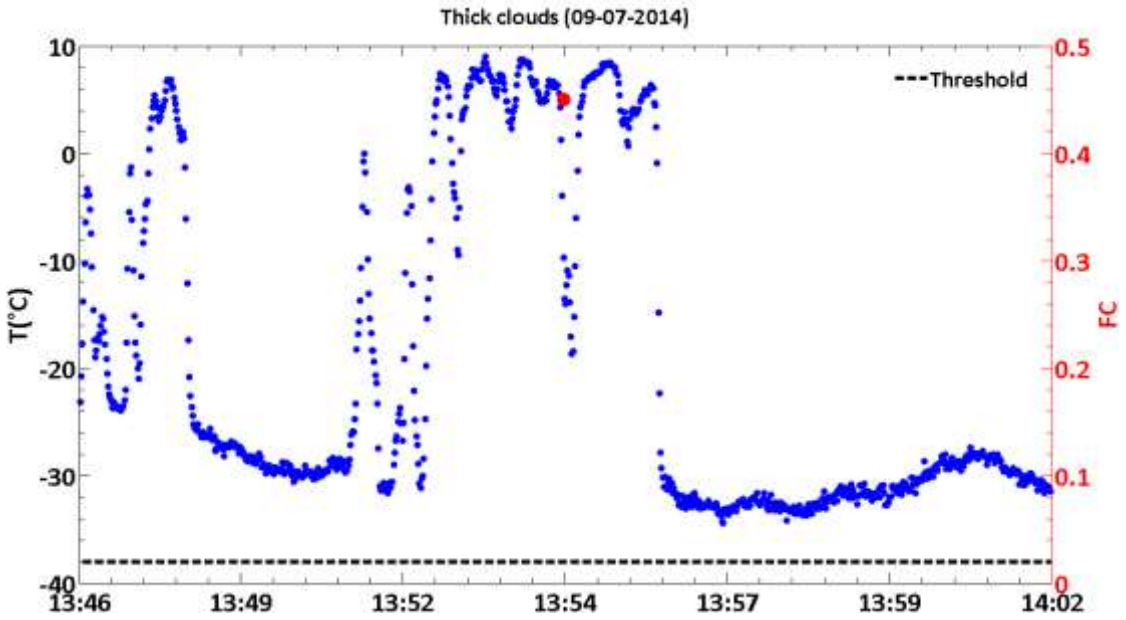

Figure 3-24: Thick clouds observed on the 9th of July 2014.

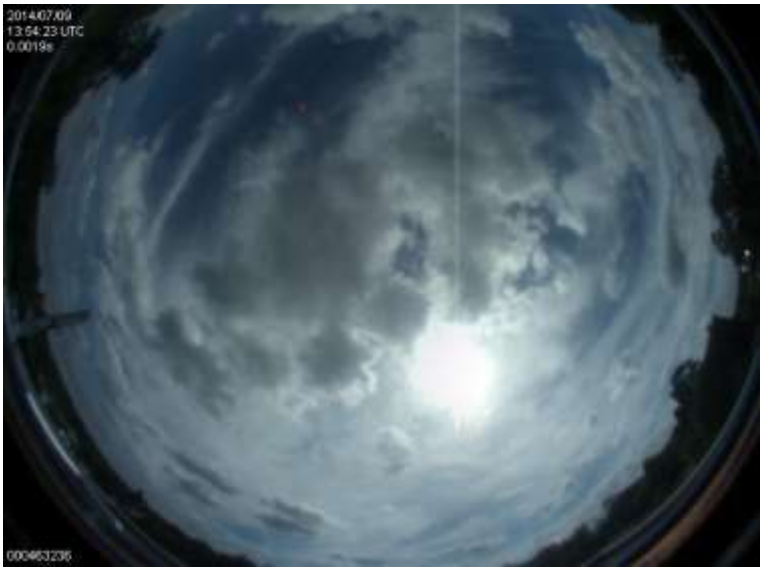

Figure 3-25: Thick clouds observed on the 9th of July 2014.

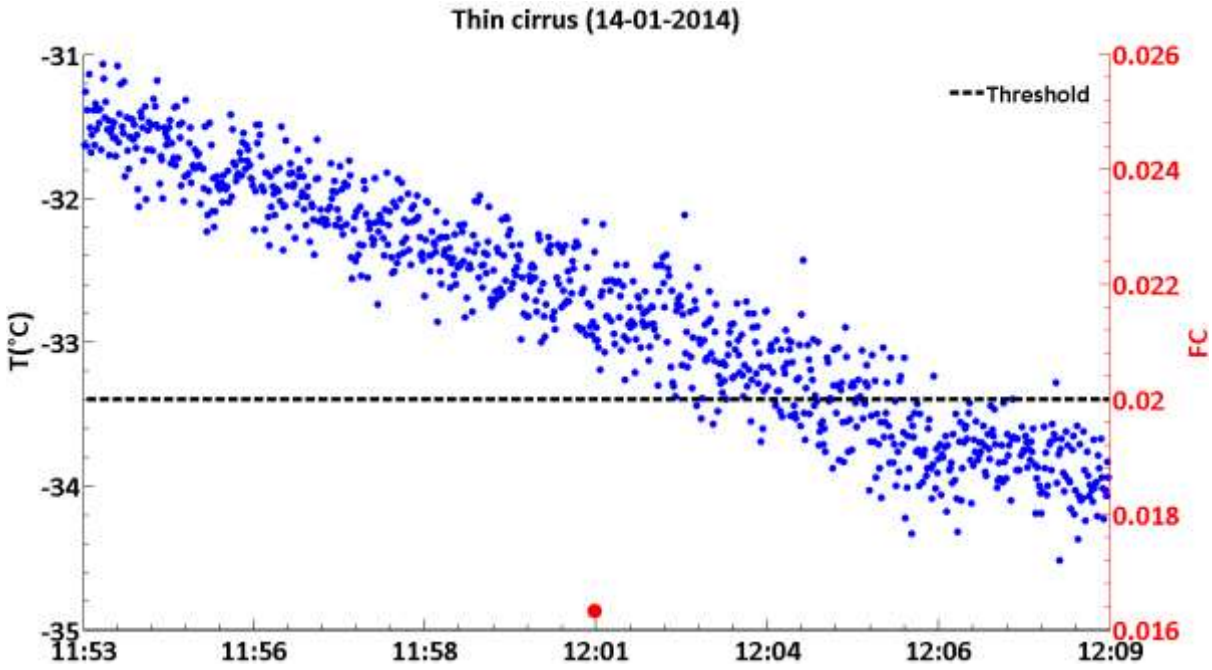

Figure 3-26: Thin cirrus observed on the 14th of Jan 2014.

Figure 3-27: Thin cirrus observed on the 14th of Jan 2014.

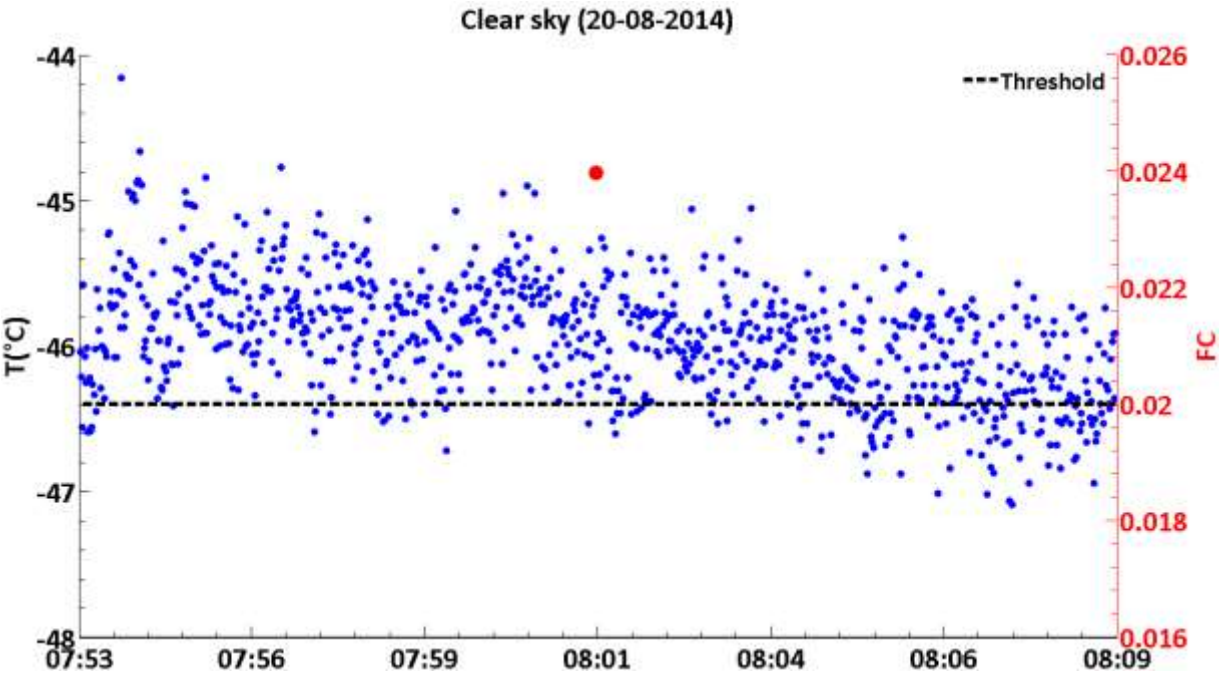

Figure 3-28: Clear sky observed on the 20th of Aug 2014.

Figure 3-29: Clear sky observed on the 20th of Aug 2014.

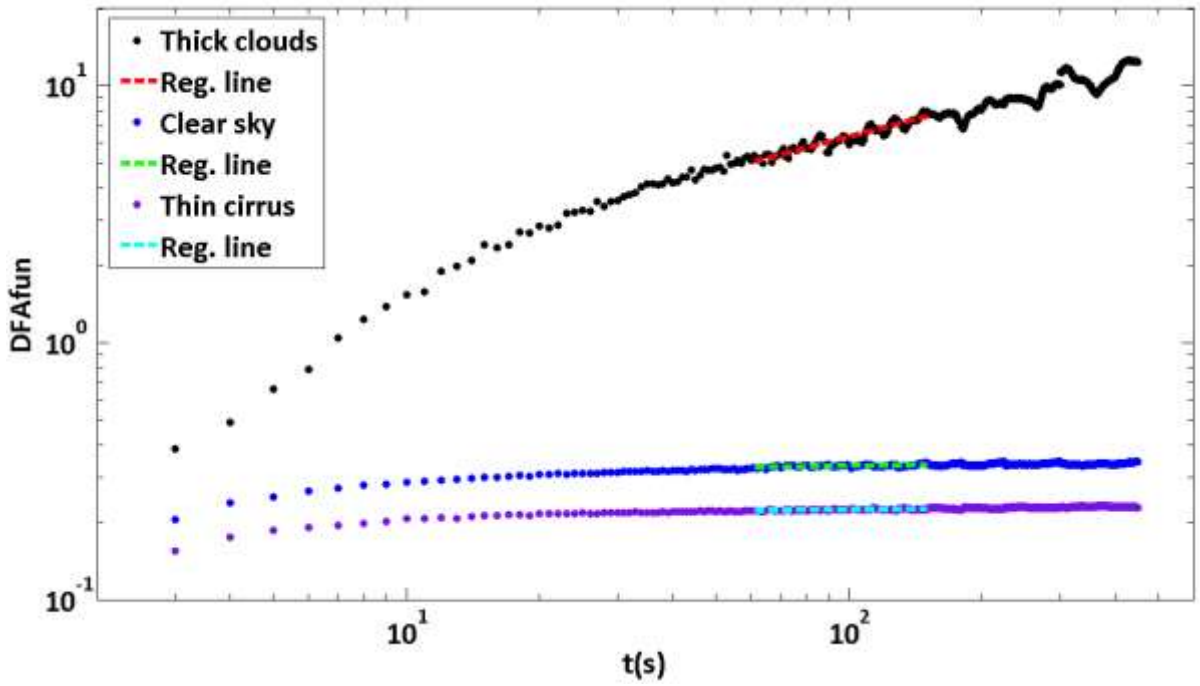

Figure 3-30: DFA functions corresponding to the observed cases and corresponding regression lines for a time window of 15 minutes.

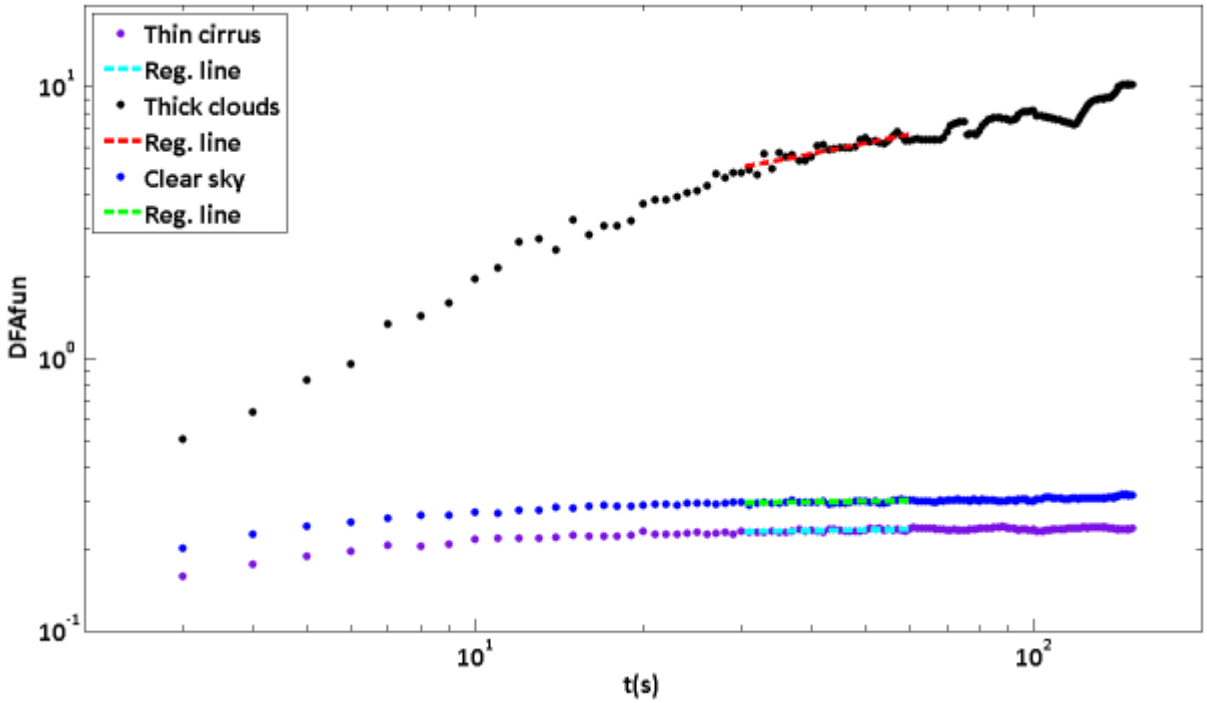

Figure 3-31: DFA functions corresponding to the observed cases and corresponding regression lines for a time window of 5 minutes.

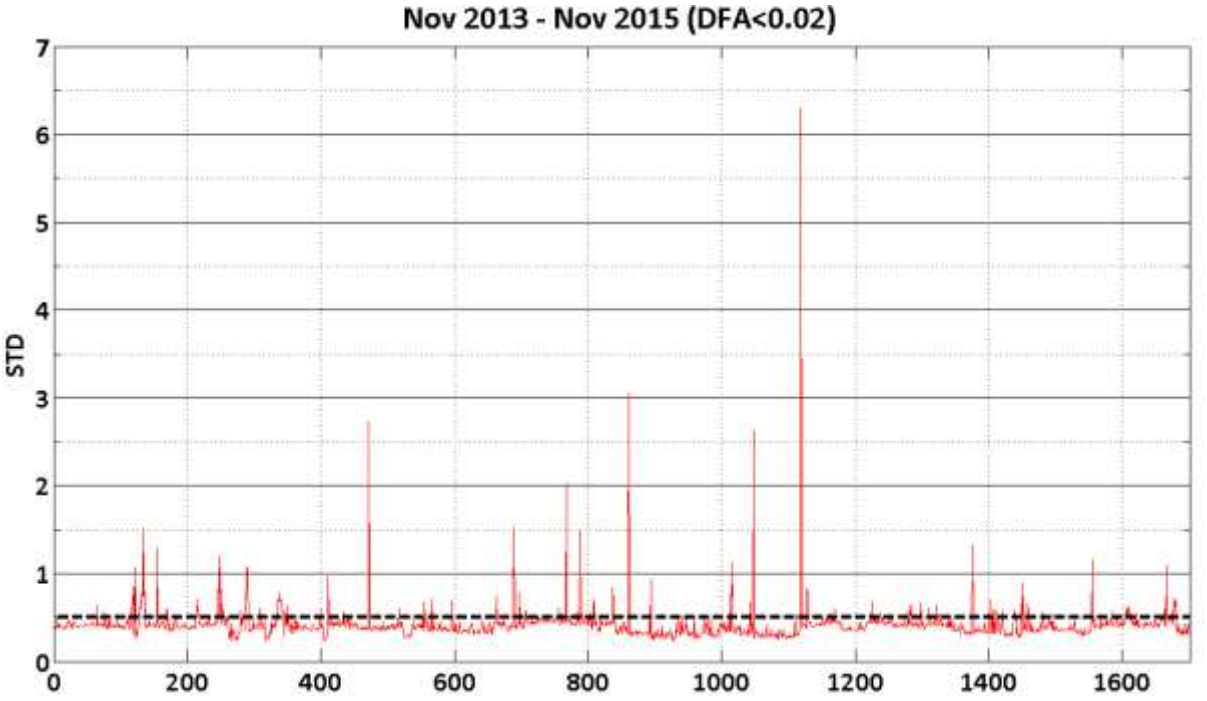

Figure 3-32: STD corresponding to points such that FC<0.02.

In the next section a clear sky down-welling radiation model based only on black body first principles will be covered.

3.6 Down-welling thermal emission (The modelling)

3.6.1 Model assumptions

In the following formulation we will assume that the Earth's atmosphere can be approximated as a set of plane parallel layers stacked on top of each other. Also, that the absorption and emission of radiation are the dominant radiation-atmosphere interaction mechanisms in the instrument sensitivity spectrum (scattering is considered negligible). WV is assumed to be the dominant emitting (absorbing) gas in the spectral window of our instrument and to be confined to the planetary boundary layer (we are neglecting CO_2 contribution). We will pretend that the WV is contained within a planar slab. The presence of a single optically thin cloud layer, far above the WV, that radiates as a "gray body" is also taken into account. For simplicity we assume that the absorption coefficient *k* of the atmosphere does not depend on the altitude.

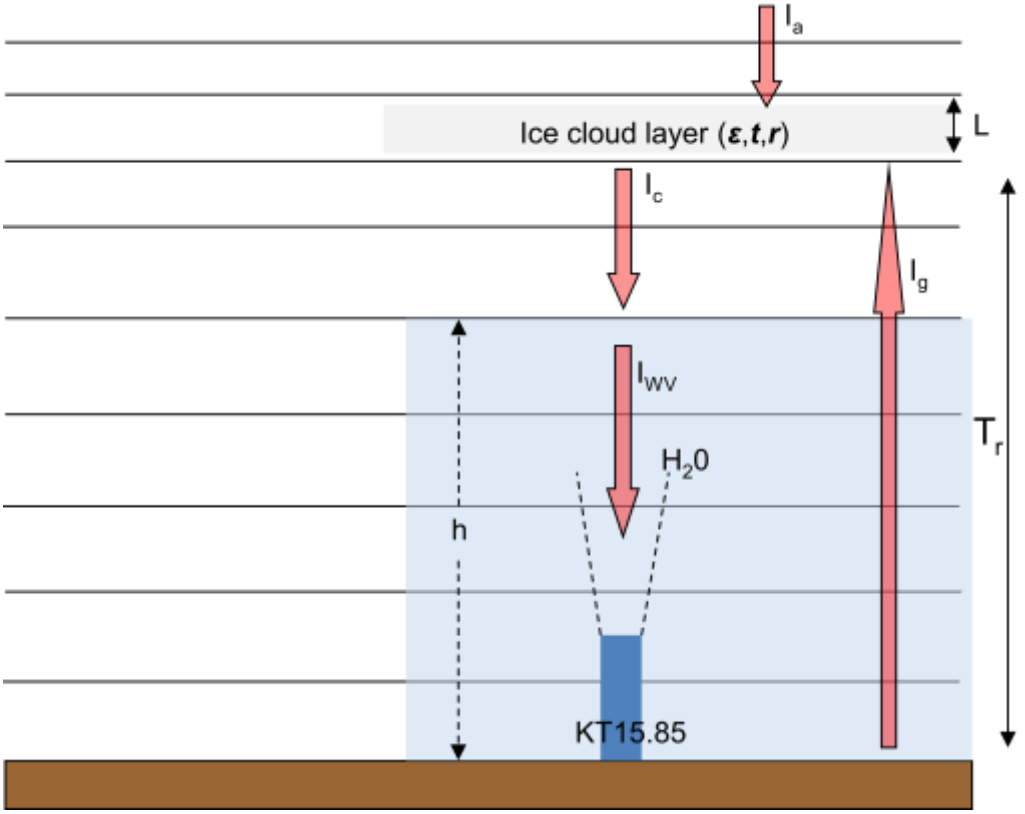

Figure 3-33: KT15.85 zenith pointing layout, in a plane parallel atmosphere consisting of a slant of WV confined in the lower atmospheric layers and a thin cirrus layer above it.

The irradiance *I* impinging on the radiometer detector, which is an integral of the spectral radiance *P* over the instrument sensitivity spectrum and the solid angle subtended by the instrument, can be expressed as:

$$I(BT) = I_{WV} + I_c T_r + I_a t T_r + I_g T_r r T_r + I_s \qquad (3.10)$$

Where:

1. **$I(BT)$ is the irradiance measured**
2. **I_{WV} is the down-welling irradiance originating from the atmospheric layers below the cloud (from cloud base height (CBH) to ground, this is the contribution coming from the slab of WV as we have assumed that it is the only atmospheric gas present)**
3. **I_c is the irradiance emitted by the cloud**
4. **T_r is the atmospheric transmittance (from CBH to ground)**
5. **I_a is the irradiance originating from the atmospheric layers above the cloud**
6. **t is the cloud transmittance**
7. **I_g is the up-welling irradiance coming from ground**
8. **r is the cloud reflectance**
9. **ε is the cloud emissivity**
10. **h is the depth of the WV slab**
11. **I_s is the solar irradiance**

The first term on the right hand side of Eq. 3.10 is the contribution originating from the WV slab. The second term is the fraction of the direct contribution from the cloud transmitted down to ground. The third term accounts for the radiant flux coming from above the cloud which is first transmitted through the cloud and then through the atmospheric layers below. The fourth term is the fraction of the radiation coming from ground transmitted through the atmosphere below the cloud, back reflected by the cloud and then retransmitted down into the instrument. In the coming paragraphs the first and second terms of the right hand side of Eq. 3.10 will be discussed. The left hand side of Eq. 3.10 that is the total irradiance observed can be thought of as the double integration of the Planck's distribution $P(\omega,T)$ for the brightness temperatures observed multiplied by the instrument emissivity setting ε_I (which has been set to 1) and the instrument response function $S(\omega)$ over the instrument spectral sensitivity range and over the solid angle ($\Delta\Omega$) subtended by the instrument field of view (FOV). The integrands are assumed to have no angular dependence so that the solid angle $\Delta\Omega$ can be taken out of the integration as a multiplying factor. The most straightforward method for integrating the Planck's distribution consists of assuming $S(\omega)$ as being sufficiently narrow to be approximated with a delta function which is always zero with the exception of the centre of the spectral band λ_c (approximately 10.6 μm) expressed in terms of the circular frequency ω_c:

$$\omega_c = \frac{2\pi c}{\lambda_c} \tag{3.11}$$

Under this assumption I becomes:

$$I = \frac{\Delta\Omega \int_{\omega_1}^{\omega_2} \varepsilon_I P(\omega, BT_{obs})\, S(\omega) d\omega}{\int_{\omega_1}^{\omega_2} S(\omega) d\omega} \approx \Delta\Omega\ P(\omega_c, BT_{obs}) \tag{3.12}$$

An alternative method (170) leading to the integration of the Planck's distribution is proposed in section 6.3 of the appendix. The Planck's distribution will be at first expanded in the sum of an infinite number of terms. Then it will be truncated to the order of accuracy wanted.

3.6.2 Downwelling radiation from the atmosphere below the cloud (I_{WV})

Let us assume that the main atmospheric component acting as absorber and emitter of radiation in our range of interest, below the cloud, be WV. Let us also assume that a slab of gas (H_2O) of thickness *h* confined in the first few hundred meters of the planetary boundary layer be the only gas species contributing in terms of thermal emission. We assume that no molecule overlaps (or shadows) another in the direction of the beam, that all the molecules are identical, all orientations are equally likely and that the contribution due to interference is negligible. For randomly oriented molecules the absorption coefficient is independent from light polarization. For a uniform layer of moist air of thickness *h* the zenith emissivity can be written as (86):

$$\varepsilon_{moistair} = 1 - \exp\left(-3.3\ 10^{28}\ IWV\ \sigma_a \right) \tag{3.13}$$

1. ***IWV* is the depth of liquid water that would result if all the water vapour molecules in the moist air layer were condensed to liquid (it is obtained from the IWV measured by the GPS station)**
2. **σ_a is the water molecule absorption cross section (it changes significantly over our instrument sensitivity spectrum, but it will be fitted as a single "effective" parameter in the clear sky model)**

Eq. 3.13, derived in paragraph 1.4.1 (see Eq. 1.24), has been obtained by assuming that scattering and therefore reflectivity are negligible compared to absorption, for the wavelength of observation, and that the emissivity (equal to the absorptivity) is given by 1 minus the transmissivity. The latter is given in Eq. 3.14.

$$T_r = \exp\left(-3.3\ 10^{28}\ \ IWV\ \ \sigma_a\right) \tag{3.14}$$

The irradiance I_{WV} can be expressed as:

$$I_{WV} = \frac{\Delta\Omega \int_{\omega_1}^{\omega_2} \varepsilon_{moistair}\ S(\omega)\ P(CGT) d\omega}{\int_{\omega_1}^{\omega_2} S(\omega) d\omega} \tag{3.15}$$

where

1. **$\Delta\Omega$ is the solid angle subtended by the radiometer**
2. ***S(ω)* is the radiometer response function**
3. ***P*(CGT) is the Planck's distribution calculated at CGT temperature**

The integration is over the instrument sensitivity spectrum, this time expressed in terms of angular frequency ω. The integrands are assumed having no angle dependence so that the solid angle $\Delta\Omega$ can be taken out of the integration as a multiplying factor. If substituted with their explicit expressions and by using the impulse response Eq. 3.15 becomes:

$$I_{WV} = \Delta\Omega\left(1-\exp\left(-3.3\ 10^{28}\ IWV\ \sigma_a\right)\right)\frac{\hbar\,\omega_c^3}{4\pi^2 c^2}\frac{1}{\exp\left(\frac{\hbar\omega_c}{k_B\ CGT}\right)-1} \tag{3.16}$$

The normalization factor at the denominator of Eq. 3.15 will be omitted in the following equations for the sake of brevity. However it should be considered as implicitly present.

3.6.3 Direct emission from ice cloud corrected for transmission (I_{ci})

The irradiance originating directly from the cloud, corrected for the transmission of the atmosphere below the cloud, can be quantified as follows:

$$I_{ci} = \Delta\Omega\int_{\omega_1}^{\omega_2}\varepsilon\ S(\omega)P(T_c)T_r d\omega =$$

$$= \Delta\Omega\int_{\omega_1}^{\omega_2}\varepsilon\ S(\omega)\left(\exp\left(-3.3\cdot10^{28}\cdot IWV\cdot\sigma_a\right)\right)\frac{\hbar\omega^3}{4\pi^2\ c^2}\frac{1}{\exp\left(\frac{\hbar\omega}{k_B T_c}\right)-1}d\omega \tag{3.17}$$

Where:

1. ***ΔΩ* is the solid angle subtended by the radiometer**
2. ***ε* is the cloud emissivity**
3. ***S(ω)* is the radiometer spectral sensitivity**
4. ***P*(T_c) is the Planck's distribution calculated at cloud temperature T_c**
5. **T_r is the atmospheric transmission from CBH to ground**
6. **T_c is the cloud temperature**

Having assumed that below the cloud there is nothing but a slab of WV, T_r is determined solely by its transmissive properties. It is the fraction of the radiation originating from the cloud and transmitted through the water vapour slab down to ground.

Analogously to above I_{ci} reduces to Eq. 3.18:

$$I_{ci} = \Delta\Omega\varepsilon(\omega_c)\left(\exp\left(-3.3\ 10^{28}\ IWV\ \sigma_a\right)\right)\frac{\hbar\omega_c^3}{4\pi^2\ c^2}\frac{1}{\exp\left(\frac{\hbar\omega_c}{k_B T_c}\right)-1} \tag{3.18}$$

3.6.4 Ice cloud transmittance and reflectance (*t*,*r*)

With respect to Eq. 3.10, while it is assumed that the fraction of infrared radiation coming from the layers above the cirrus I_a and transmitted down to ground is negligible, the fraction of thermal radiation coming from ground and reflected by the cirrus is not. Direct solar contribution is also considered negligible as not falling within the instrument FOV. It implies retaining only the first, second and fourth terms of Eq. 3.10. In other words we assume that the irradiance seen from

ground is the sum of the radiant flux emitted by the atmosphere below the cloud, the direct cloud emission and the fraction of radiation coming from ground and reflected back into the instrument.

3.6.5 I_{ci} for spherical ice particles

In this paragraph Eq. 3.18 will be rewritten in Eq. 3.21 by modelling cirrus emissivity under the assumption of spherical ice particles. However, it should be stated that with respect to the determination of the cirrus detection threshold discussed in paragraph 3.8 only Eq. 3.18 will be used. Scattering of radiation is assumed to be negligible in comparison to absorption and emission. This is a reasonable assumption over the instrument sensitivity spectrum. If we assume a cirrus layer composed of spherical ice particles (which is of course a gross simplification) of radius *a*, the optical depth of a cirrus layer of thickness *L* can be written as:

$$\tau_a = \pi a^2 Q_a n L \tag{3.19}$$

Where:

1. ***Q_a is the absorption extinction efficiency calculated by Twomey to be 1.04 for 50 µm radius ice spheres in the 8-13 µm region*** **(171) (172)**
2. ***n is the number concentration, $5*10^5$ m^{-3} of ice particles for "typical cirrus" or $5*10^4$ m^{-3} for "cirrus haze"*** **(172)**
3. ***L is the geometric cloud depth which could be assumed to be typically 200m according to Freeman's definition*** **(172)**

If cirrus is assumed to be in thermodynamic equilibrium, its emissivity is (172)

$$\varepsilon = \left(1 - \exp\left(-\tau_a\right)\right)\left(1 - r\right) \tag{3.20}$$

and the contribution of the cloud to the irradiance observed would then be:

$$I_{ci} = \Delta\Omega\left(1 - \exp\left(-\tau_a\right)\right)\left(1 - r\right)\exp\left(-3.3\,10^{28}\ IWV\ \sigma_a\right)\frac{\hbar\omega_c^3}{4\pi c^2}\frac{1}{\exp\left(\dfrac{\hbar\omega_c}{k_B T_c}\right) - 1} \tag{3.21}$$

3.6.6 Total Irradiance

Under the assumptions set out in paragraph 3.6.4, the irradiance observed is the sum of the contribution coming from WV, direct cloud emission and fraction of radiation coming from ground and reflected (scattered) by the cloud back to ground respectively:

$$I = \Delta\Omega\left(1-\exp\left(-3.3\ 10^{28}\ IWV\ \sigma_a\right)\right)\frac{\hbar\omega_c^3}{4\pi^2c^2}\frac{1}{\exp\left(\frac{\hbar\omega_c}{k_B\ CGT}\right)-1}+$$
$$+\Delta\Omega\left(1-\exp\left(-\tau_a\right)\right)\left(1-r\right)\left(\exp\left(-3.3\ 10^{28}\ IWV\ \sigma_a\right)\right)\frac{\hbar\omega_c^3}{4\pi^2c^2}\frac{1}{\exp\left(\frac{\hbar\omega_c}{k_B T_c}\right)-1}+I_g T_r r T_r \quad (3.22)$$

By combining Eq. 3.12 and 3.22 we obtain:

$$\Delta\Omega\ P\left(\omega_c, BT_{obs}\right)=\Delta\Omega\left(1-\exp\left(-3.3\ 10^{28}\ IWV\ \sigma_a\right)\right)\frac{\hbar\omega_c^3}{4\pi^2c^2}\frac{1}{\exp\left(\frac{\hbar\omega_c}{k_B\ CGT}\right)-1}+$$
$$+\Delta\Omega\left(1-\exp\left(-\tau_a\right)\right)\left(1-r\right)\exp\left(-3.3\ 10^{28}\ IWV\ \sigma_a\right)\frac{\hbar\omega_c^3}{4\pi^2c^2}\frac{1}{\exp\left(\frac{\hbar\omega_c}{k_B T_c}\right)-1}+I_g T_r r T_r \quad (3.23)$$

3.6.7 Clear sky total irradiance

If no clouds are in the FOV of the instrument, the observed irradiance is only due to the WV thermal emission and Eq. 3.23 reduces to Eq. 3.24:

$$P\left(\omega_c, BT_{obs}\right)=\left(1-\exp\left(-3.3\cdot10^{28}\cdot IWV\cdot\sigma_a\right)\right)\frac{\hbar\cdot\omega_c^{\ 3}}{4\pi^2c^2}\frac{1}{\exp\left(\frac{\hbar\omega_c}{k_B\cdot CGT}\right)-1} \quad (3.24)$$

3.6.8 Water vapour absorption cross section fit

Eq. 3.24 can now be used to fit the only unknown parameter σ_a which is the effective molecular water vapour absorption cross section. All the other relevant quantities BT_{obs} (brightness temperature measured by the radiometer), IWV_{obs} (precipitable water vapour is derived from the IWV measured by the GPS station installed in Bayfordbury), CGT_{obs} (the screen level air temperature is measured by the available weather station) are measured. It should be noticed that approximate equality symbols have been replaced with equalities for simplicity. Strictly speaking the following equations should be considered as approximate equalities. Eq. 3.24 can be rewritten as in Eq. 3.25, Eq. 3.26 and ultimately as in Eq. 3.27.

$$P\left(\omega_c, BT_{obs}\right)\frac{4\pi^2c^2}{\hbar\cdot\omega_c^{\ 3}}\left(\exp\left(\frac{\hbar\omega_c}{k_B\ CGT_{obs}}\right)-1\right)=\left(1-\exp\left(-3.3\ 10^{28}\ IWV_{obs}\ \sigma_a\right)\right) \quad (3.25)$$

$$\exp\left(-3.3\,10^{28}\ IWV_{obs}\ \sigma_a\right)=1-P\left(\omega_c,BT_{obs}\right)\frac{4\pi^2c^2}{\hbar\,\omega_c{}^3}\left(\exp\left(\frac{\hbar\omega_c}{k_B\ CGT_{obs}}\right)-1\right) \tag{3.26}$$

$$-3.3\,10^{28}\ IWV_{obs}\ \sigma_a=\ln\left(1-P\left(\omega_c,BT_{obs}\right)\frac{4\pi^2c^2}{\hbar\,\omega_c{}^3}\left(\exp\left(\frac{\hbar\omega_c}{k_B\ CGT_{obs}}\right)-1\right)\right) \tag{3.27}$$

σ_a (Eq. 3.28) is obtained from least square regression:

$$\sigma_a=\frac{\sum_{j=1}^{N}X_jY_j}{\sum_{j=1}^{N}X_j^2} \tag{3.28}$$

where X_j and Y_j are expressed in Eq. 3.29 and 3.30:

$$X_j=-3.3\cdot10^{28}\cdot IWV_j \tag{3.29}$$

$$Y_j=\ln\left(1-P\left(\omega_c,BT_j\right)\frac{4\pi^2c^2}{\hbar\cdot\omega_c{}^3}\left(\exp\left(\frac{\hbar\omega_c}{k_B\cdot CGT_j}\right)-1\right)\right) \tag{3.30}$$

σ_a has m^2 units, and represents the effective area of the WV molecule which is responsible for the attenuation of the incident beam energy. The sum is done over all the clear sky data points found at night. By doing this calculation with respect to the case shown in Figure 3-34, σ_a obtained is:

$$\sigma_a=6.20\cdot10^{-28}\mathrm{m}^2$$

It should be noted that the value so found is broadly consistent with the water vapour absorption cross section shown in Figure 1-27 for the central wavelength of our measuring instrument. The modelled clear sky radiance (MP) can now be expressed as in Eq. 3.31

$$MP\left(\omega_c,CGT,IWV,\sigma_a\right)=\left(1-\exp\left(-3.3\,10^{28}\ IWV\ \sigma_a\right)\right)\frac{\hbar\,\omega_c{}^3}{4\pi^2c^2}\frac{1}{\exp\left(\frac{\hbar\omega_c}{k_B\ CGT}\right)-1} \tag{3.31}$$

By inverting Eq. 1.40 the corresponding modelled brightness temperature MT is obtained (see Eq. 3.32).

$$MT(\omega_c, CGT) = \frac{\hbar \cdot \omega_c}{k_B} \frac{1}{\ln\left(\frac{\hbar \omega_c^{\,3}}{4\,\pi\, c^2 MP} + 1\right)} \tag{3.32}$$

If we now compare MT to the corresponding BT time series, both shown in Figure 3-34, MT seems to follow the BT trend fairly well apart from large discrepancies observed between the 8th and 9th of July or occurring when clouds are in the FOV. MT data gaps like the one observed around the 8th of July are due to gaps in the water vapour soundings.

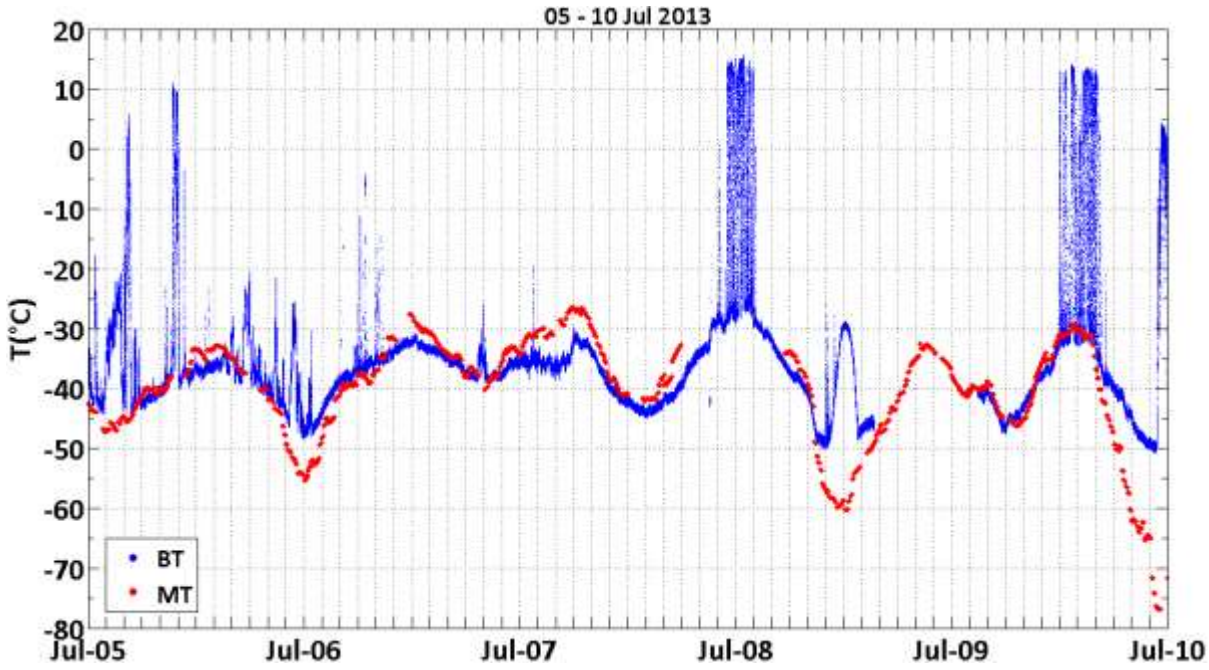

Figure 3-34: Time series of the observed BT from July the 5th to July the 10th 2013 and corresponding MT.

The same has been done to model the observed BT between the 27th of April and the 5th of May 2013 as Figure 3-35 shows. This time the WV data have been smoothed to reduce the noise occurring in the WV soundings from reflecting in the modelled temperature MT.

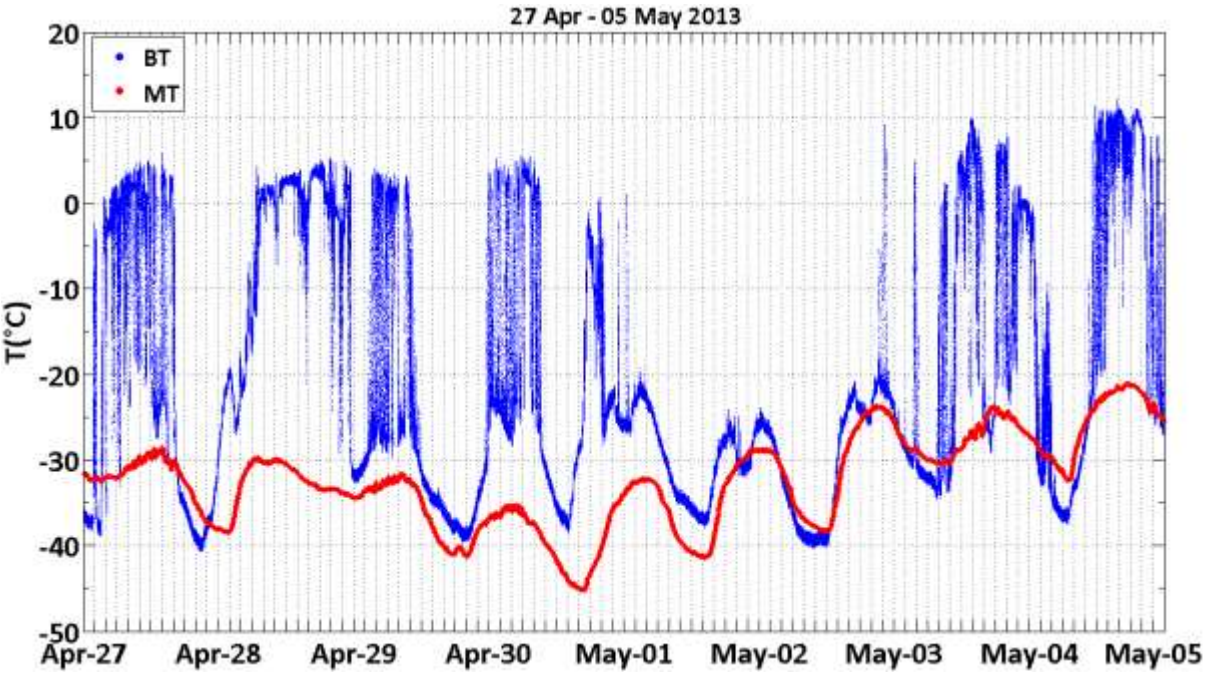

Figure 3-35: Time series of the observed BT from April the 25th to May the 5th 2013 and corresponding MT.

By repeating the same procedure for every patch of clear sky detected through DFA at night over nearly two years from November 2013 to August 2015 it is possible to obtain long-term time series of σ_a as the top plot of Figure 3-36 shows. The corresponding WV, CGT and BT time series are shown in the bottom plot.

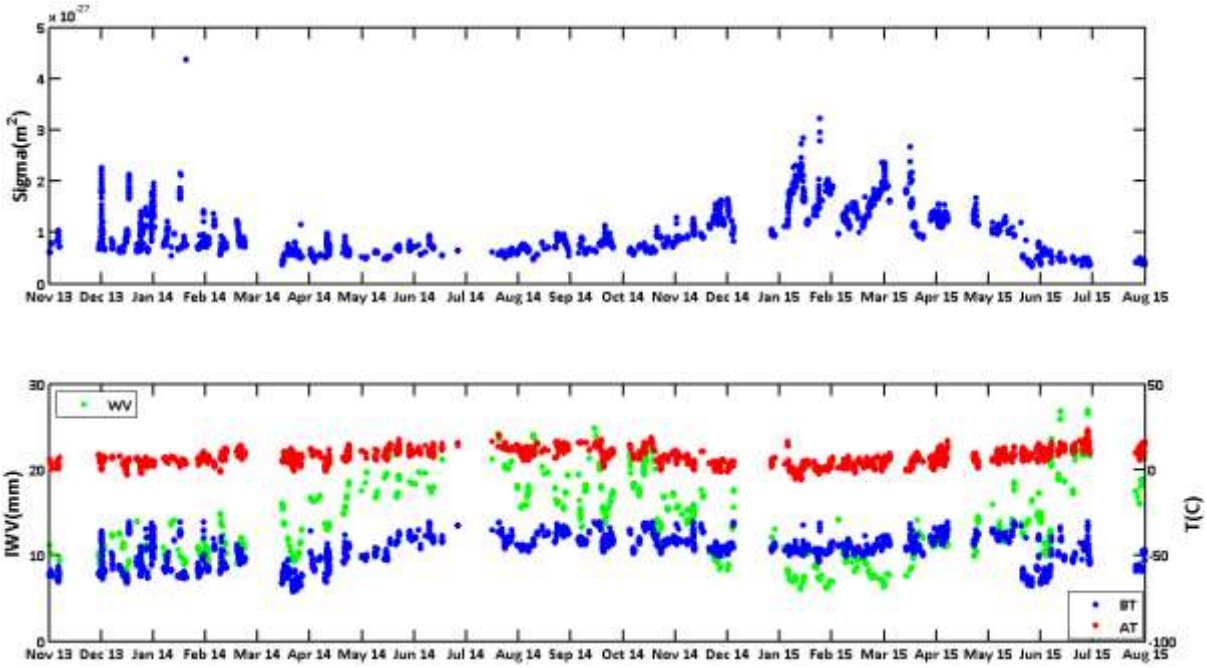

Figure 3-36: σ_a calculation over clear sky patches occurring from Nov 2013 to Aug 2015.

Given the more relatively stable values that σ_a takes on in summer, it has been decided that a reasonable value for σ_a is given by its mean value calculated during this period. It is:

$$\sigma_a = 6.6 \cdot 10^{-28} \mathrm{m}^2$$

In addition to the calculation of σ_a, BT, CGT and IWV have been recorded under clear skies. By visually inspecting the same dataset, from now on referred to as dataset 1, it has been found that it is significantly cloud contaminated. This was caused by the fact that the DFA function was found to be noisy over the time scale chosen. A new DFA algorithm has been implemented in Matlab to obtain a further cloud screened dataset, from now on referred to as data set 2, ranging from Nov 2013 to Mar 2016. The new algorithm is faster and provides a more stable DFA function. This is achieved by dividing the time interval (of the BT time series) of length L into $N_\tau = L/\tau$ non-overlapping segments of equal length τ. Given that L need not be a multiple of the considered time scale τ, and in order not to disregard the short part at the end of the time interval which remains in most cases, the same procedure is repeated starting from the other end of the time interval. In this way $2N_\tau$ segments are obtained and a least-square fit of the data is calculated for each of them. Then the DFA function for the segment duration τ is calculated as the difference of the original time series and the fits. Details of this procedure are provided in literature (173). The main limitation of the old DFA algorithm consisted in constraining τ to take on values such that L were multiple of τ.
Fewer clear sky data points are obtained compared to dataset 1, consistently with the enhanced sensitivity of the new DFA algorithm.

3.7 Model deviation from observations

In this section the deviation of the model from the observed BT is calculated, using as input parameter the summer-time averaged σ_a calculated above. The deviation is expressed as the modelled temperature minus the observed one (see Eq. 3.33) for both data set 1 and data set 2.

$$\mathrm{DT} = \mathrm{MT} - \mathrm{BT} \tag{3.33}$$

With respect to data set 1, MT, BT, CGT, WV, z and corresponding time have been recorded for all the clear sky periods found through DFA. Figure 3-37 is a scatter plot of DT vs z. Dot size is proportional to CGT and the colour accounts for the WV amount - high IWV data points are red, low IWV ones are blue. Analogously Figure 3-38 shows the same data set but this time the dot size is proportional to the amount of WV and the colour is showing the temperature. Red dots are warmer, blue dots are colder.

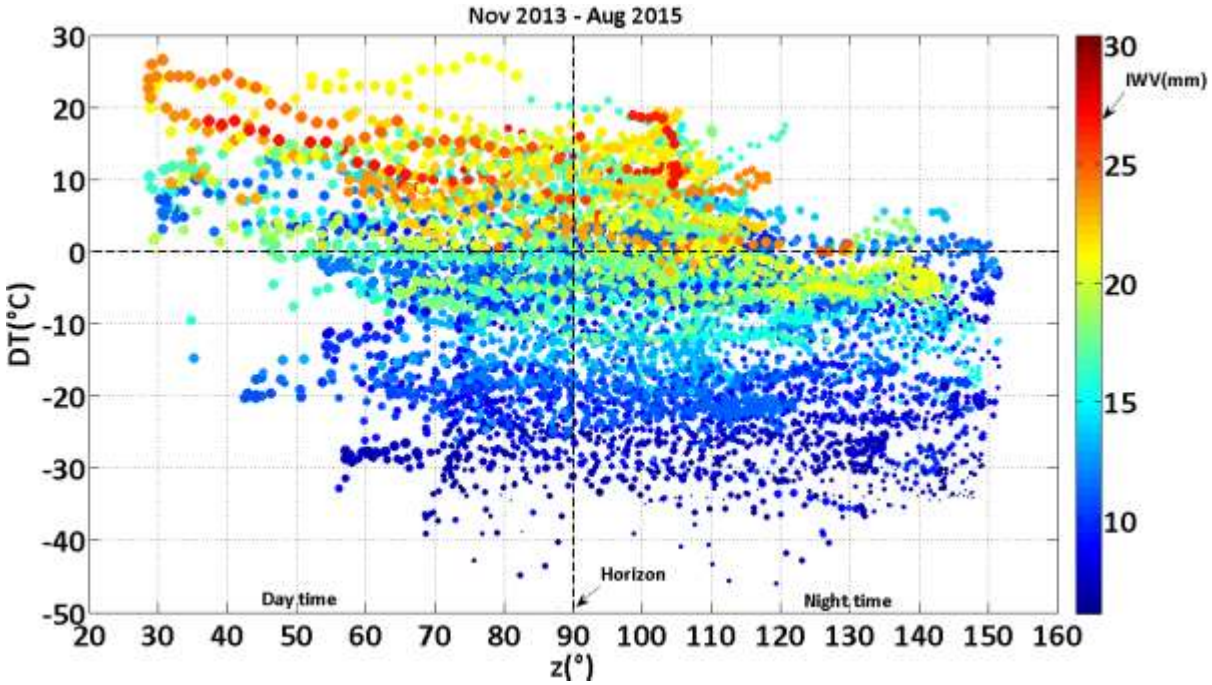

Figure 3-37: DT vs ZD scatter plot corresponding to the time period ranging from Nov the 16th 2013 to Aug the 31st 2015; the black dashed horizontal line represent zero deviation, the black dashed vertical line is the horizon. Notice that the point colour specifies the amount of WV while the point size is proportional to CGT.

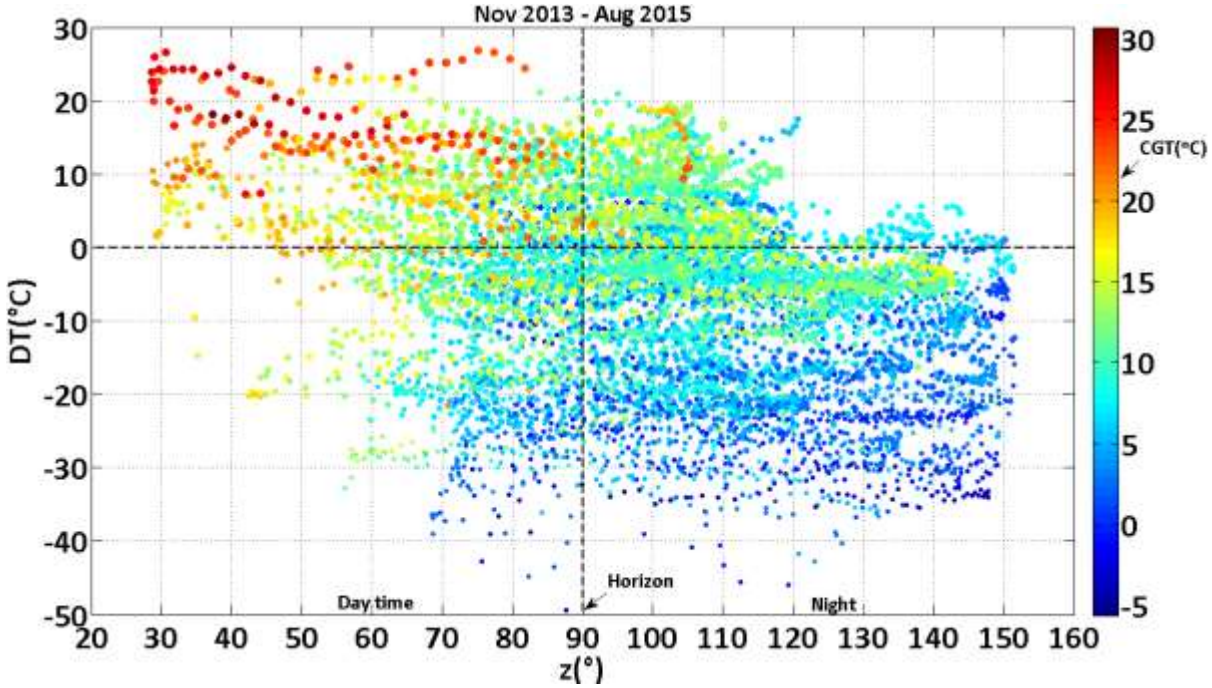

Figure 3-38: DT vs ZD scatter plot corresponding to the time period ranging from Nov the 16th 2013 to Aug the 31st 2015; the black dashed horizontal line represent zero deviation, the black dashed vertical line is the horizon. Notice that the point colour specifies CGT while the point size is proportional to the IWV.

When CGT is above 10°C and WV between 20 and 25 mm the model tends to overestimate the actual BT irrespectively of night or day, whereas underestimation occurs mostly when WV decreases below 15 mm and CGT drops below 10°C. When IWV and CGT drop below 10 mm and 5°C respectively deviations can be as large as 15%. This could indicate that CGT is causing an overestimate of the actual radiative T of the slab of WV when the sun gets close to zenith and the other way around at night. This could be related to the PBL (Planetary Boundary Layer) temperature lapse rate which during day time is expected to be larger than at night, when temperature inversions are more likely to occur. When the same analysis is done on data set 2 something similar is observed (see Figure 3-39). Interestingly, the majority of data points cluster between -10 K and 20 K as if the remaining points were possibly non cloud-free outliers.

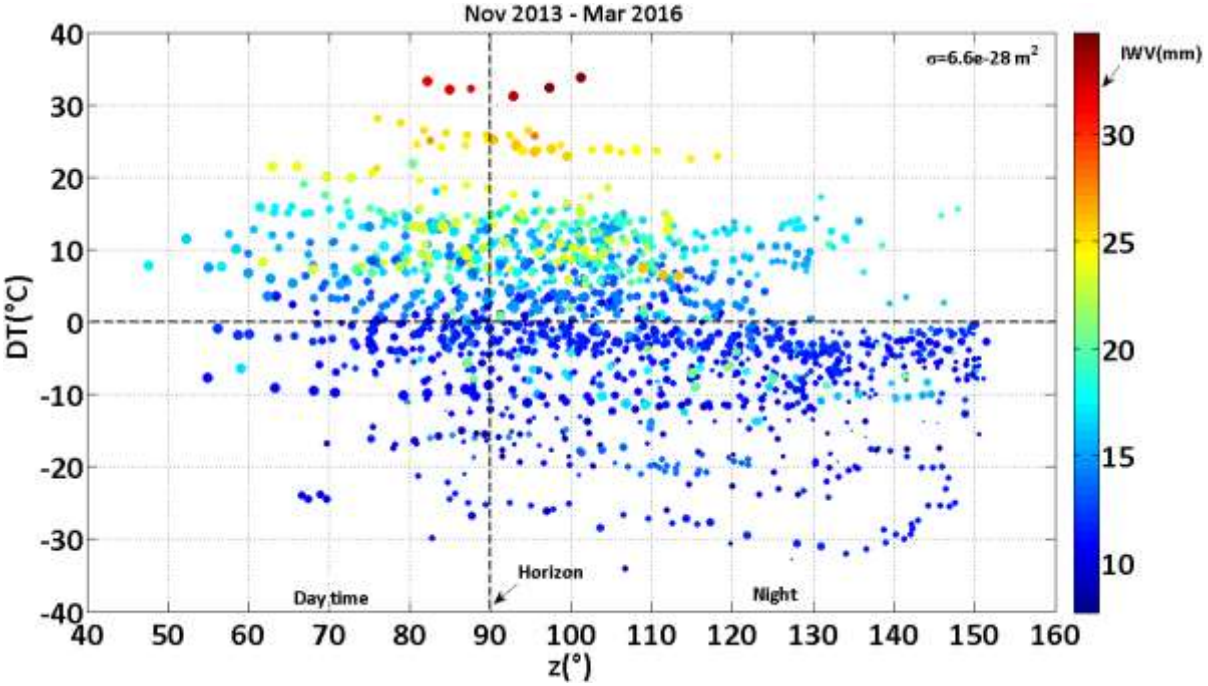

Figure 3-39: DT vs ZD scatter plot corresponding to the time period ranging from Nov the 16th 2013 to Aug the 31st 2015; the black dashed horizontal line represent zero deviation, the black dashed vertical line is the horizon. Notice that the point colour specifies the amount of WV while the point size is proportional to CGT.

In order to see if the PBL lapse rate hypothesis is true, MET office modelled temperatures (MET_T) have been used as input in place of CGT. Hourly MET_T and MET specific humidity (SH) profiles have been taken into account to determine at which altitude along the profile most of the WV is concentrated and what temperature it is at. The outcome will be shown after a brief comparison between data set 1 and 2.

To see if the modelled temperature deviation follows any diurnal pattern, DT has been plotted against the time of the day. This has been done for the four seasons (Dec,/ Jan,/ Feb, - Mar,/ Apr,/ May, - June,/ July,/ Aug, - Sep,/ Oct,/ Nov) in order to separate possible seasonal trends, only for data set 1. Figure 3-40 for instance is the plot for the winter season (Dec 2013 to Feb 2014). The data point size is proportional to the data point density or in other words to the number of neighbour points. This has been done to highlight the time of the day when data points cluster the most. The dashed line indicates zero deviation. Thus in winter the model mostly underestimates the observed BT, except in the afternoon from 3 pm to 7 pm. In spring (Mar 2014 to May 2014) DT varies mostly between +5% to -5% with overestimation and underestimation equally likely (see Figure 3-41). From June 2014 to August 2014 overestimation is dominant from 7 am till 7 pm as Figure 3-42 shows. Again DT is contained mostly between +5% and -5%. Between September 2014 and November 2014

the trend changes as underestimation becomes dominant despite of the time of the day (see Figure 3-43) and DT mostly varies between 0 and -5%. From December 2014 up to May 2015 enhanced underestimation occurs as DT varies mostly between -5 and -15% (see Figure 3-44 and Figure 3-45). With summer-time (June 2015 to August 2015) DT becomes again positively biased varying from 0 to 10% (see Figure 3-46). However, the presence of a diurnal pattern is not evident.

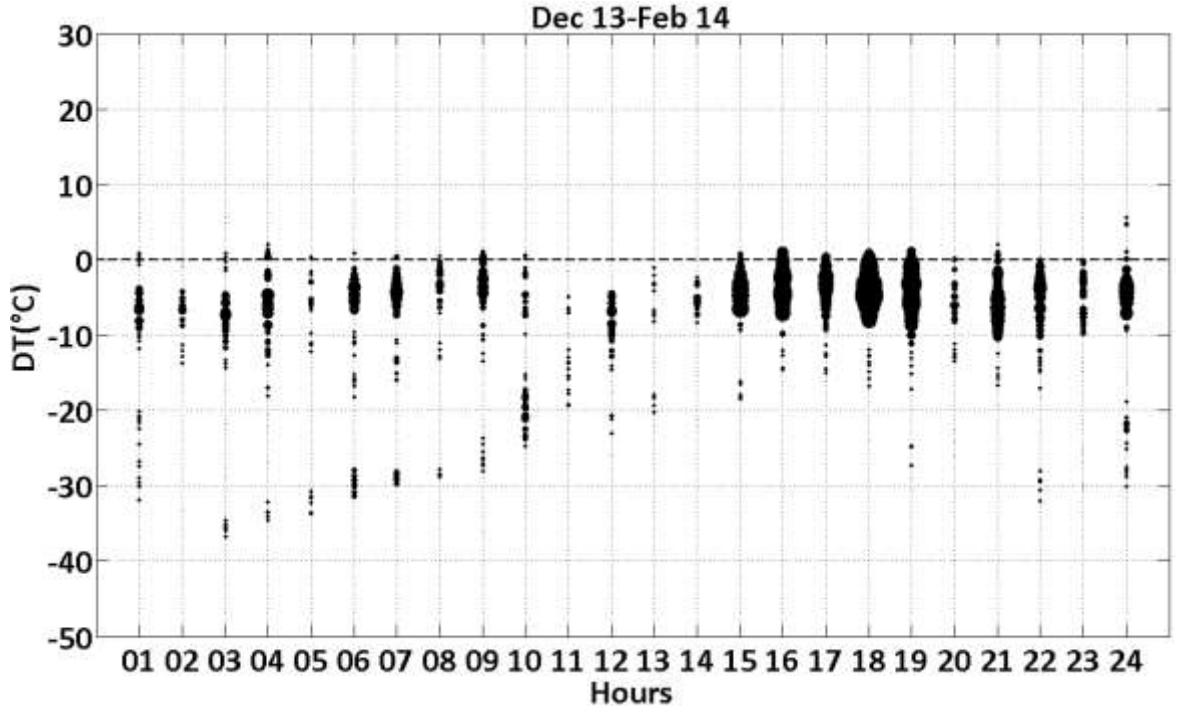

Figure 3-40: DT vs time of the day - from Dec 2013 to Feb 2014.

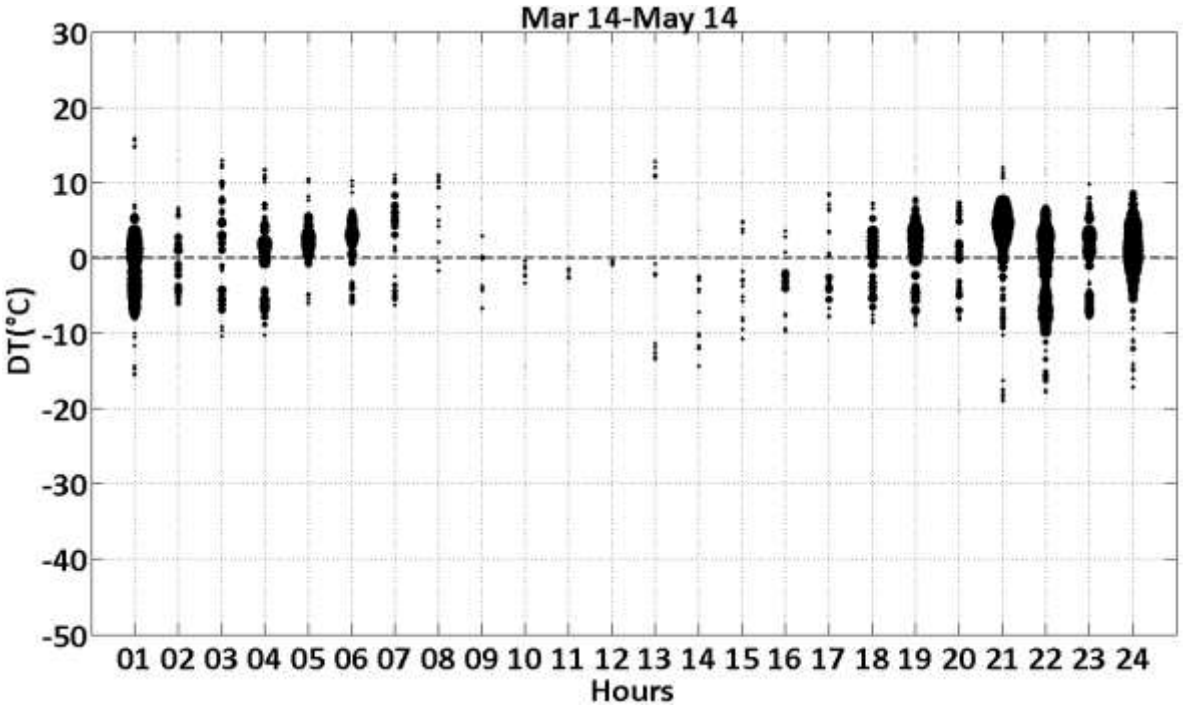

Figure 3-41: DT vs time of the day - from Mar to May 2014.

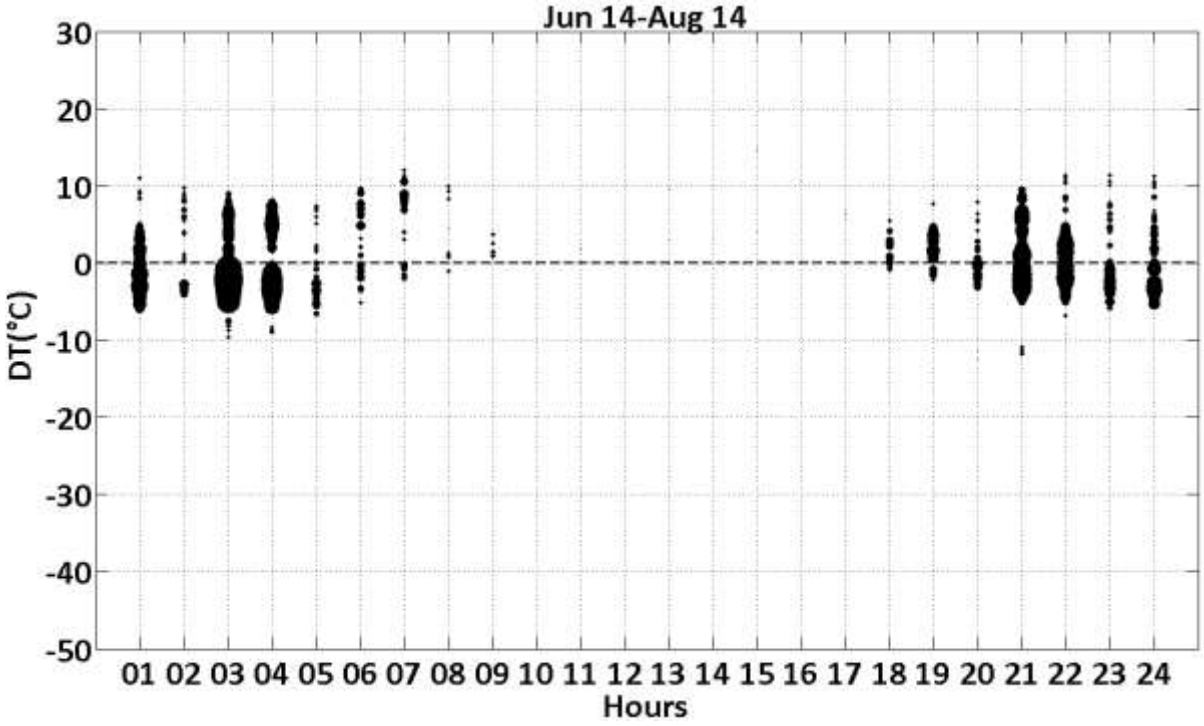

Figure 3-42: DT vs time of the day - from Jun to Aug 2014.

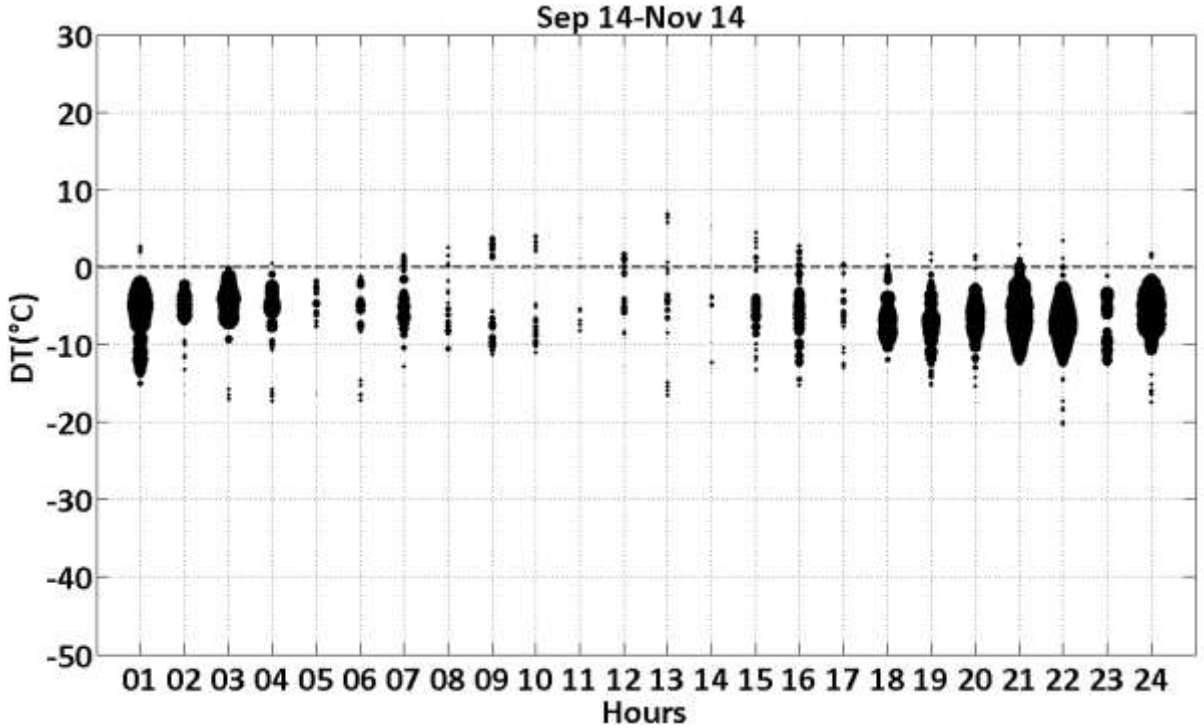

Figure 3-43: DT vs time of the day - from Sep to Nov 2014.

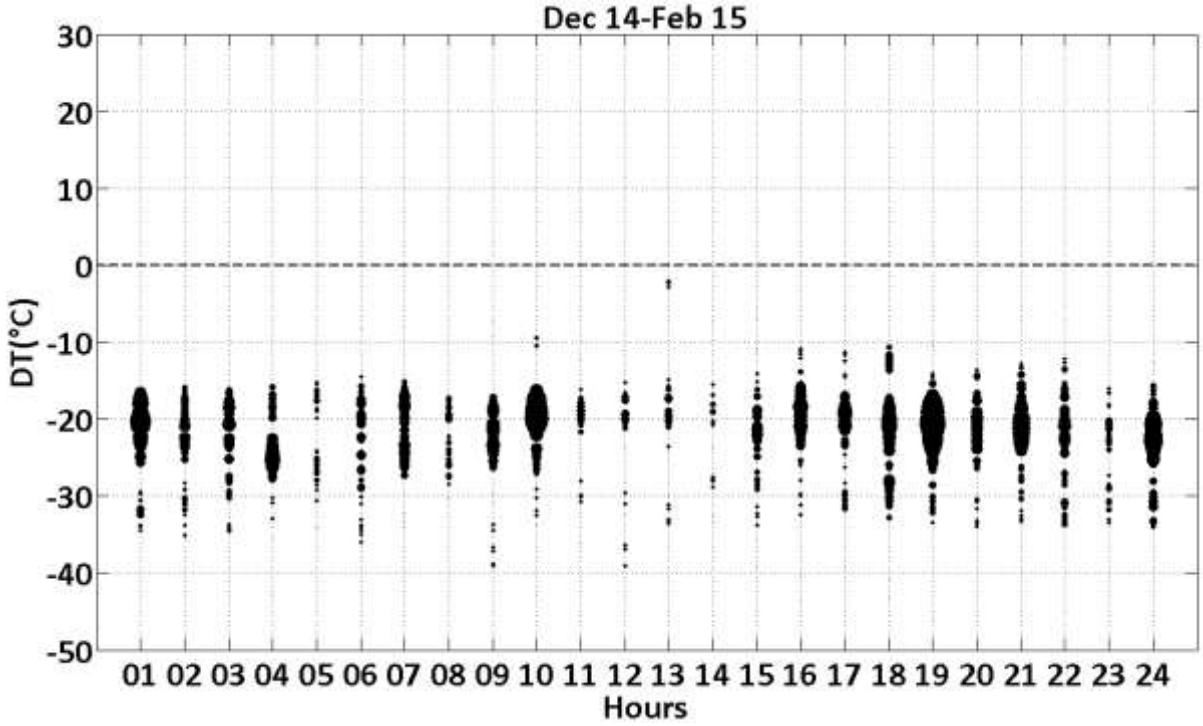

Figure 3-44: DT vs time of the day - from Dec 2014 to Feb 2015.

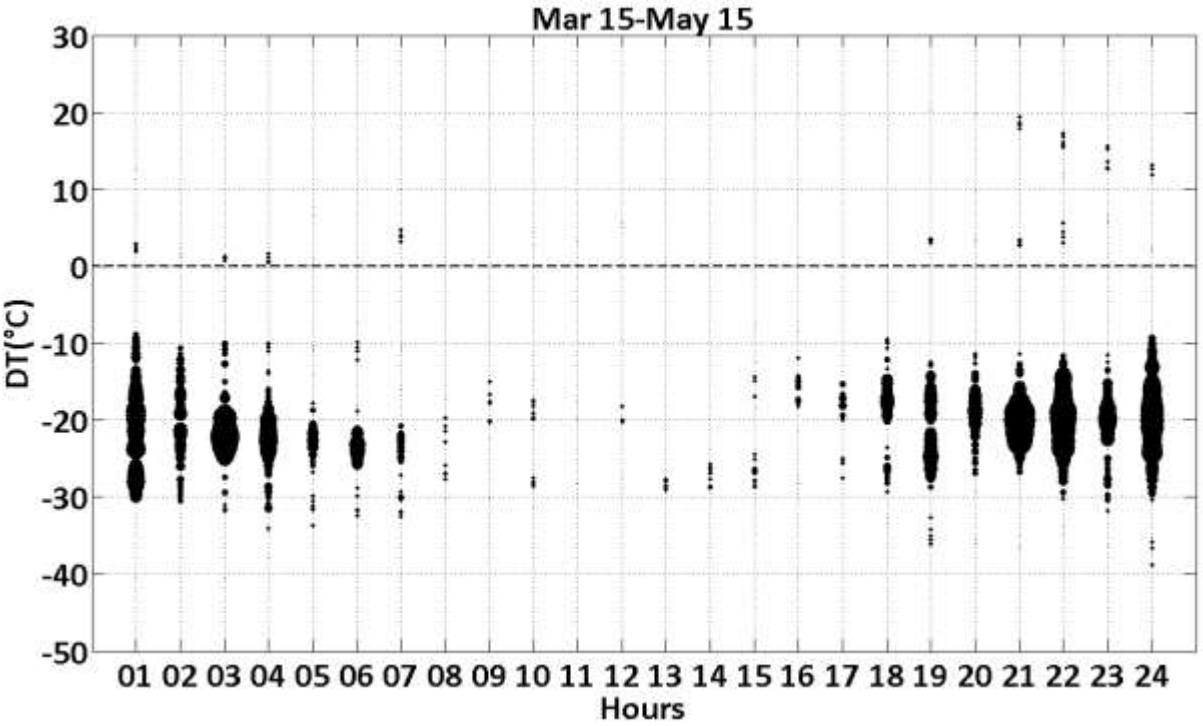

Figure 3-45: DT vs time of the day - from Mar to May 2015.

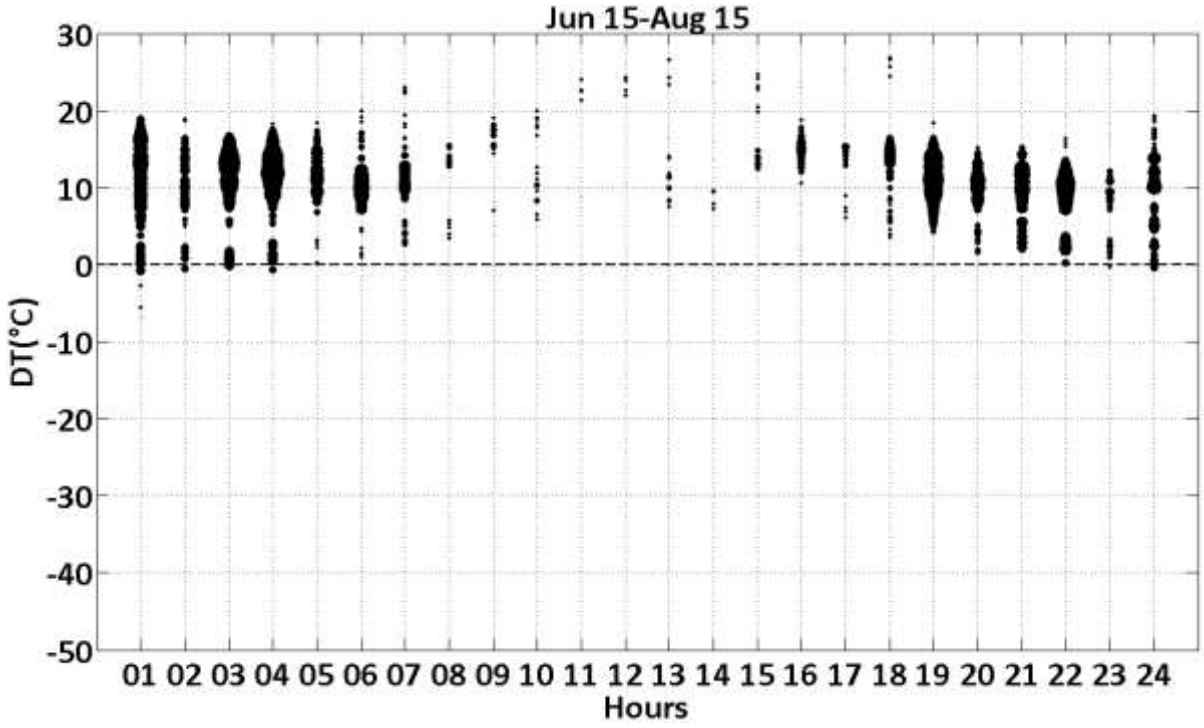

Figure 3-46: DT vs time of the day - from Jun to Aug 2015.

DT has also been plotted against CGT and IWV, with the respective regression line (red dashed line), for each of the four seasons, setting the data point size proportional to IWV or CGT. Blue and black dots have been used to distinguish day and night time, respectively. Given that no observable pattern has arisen from each individual season, the entire data set is used. This is what Figure 3-47 and Figure 3-48 show for the data set 1. When CGT and IWV are less than 5^{o}C and 10 mm, respectively, underestimation is dominant. When CGT is above 15^{o}C and IWV is larger than 20 mm the model mostly overestimates BT. Overestimation and underestimation are equally likely when CGT and IWV are between 5^{o}C and 15^{o}C and 10 mm and 20 mm, respectively. This happens irrespectively of night or day time. The correlation coefficients are 0.62 for DT vs CGT and 0.73 for DT vs IWV. This is similar to what is found by using data set 2. Figure 3-49 and Figure 3-50 are the scatter plots showing DT against CGT and DT against IWV, respectively, with the respective regression line (red dashed line). This time the correlation coefficients are 0.50 (DT vs CGT) and 0.71 (DT vs IWV), respectively.

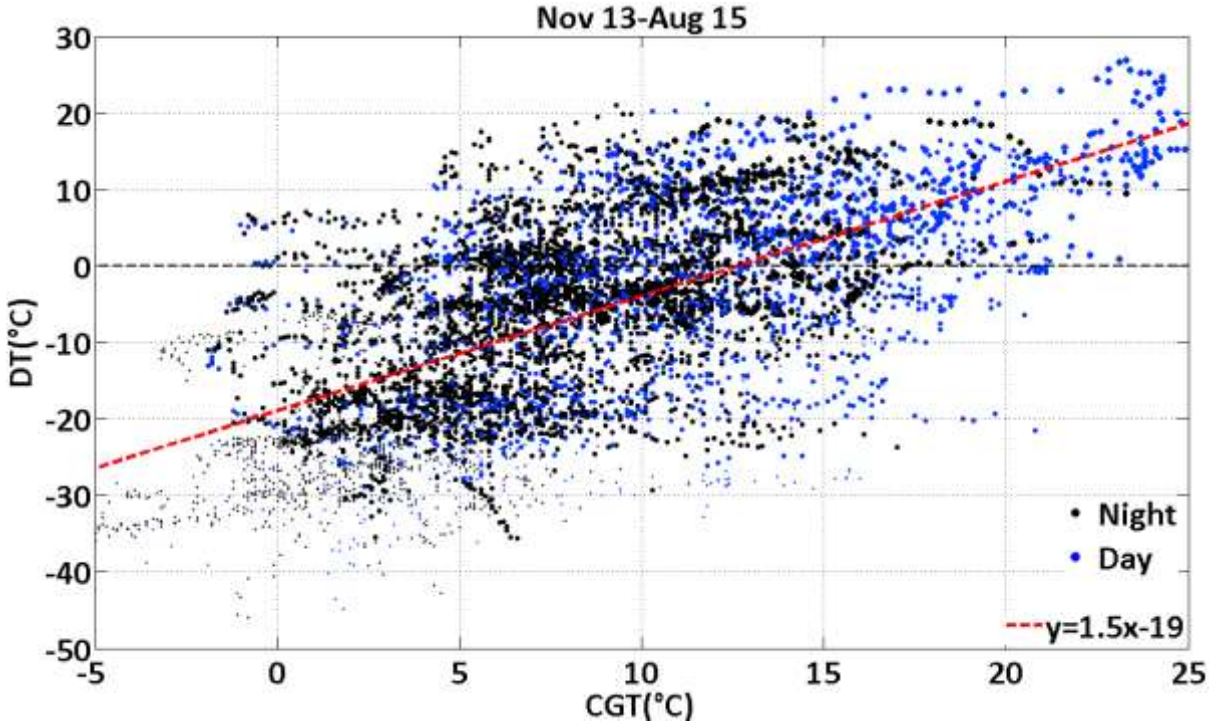

Figure 3-47: DT vs CGT - from Nov 2013 to Aug 2015 - dot size is proportional to IWV.

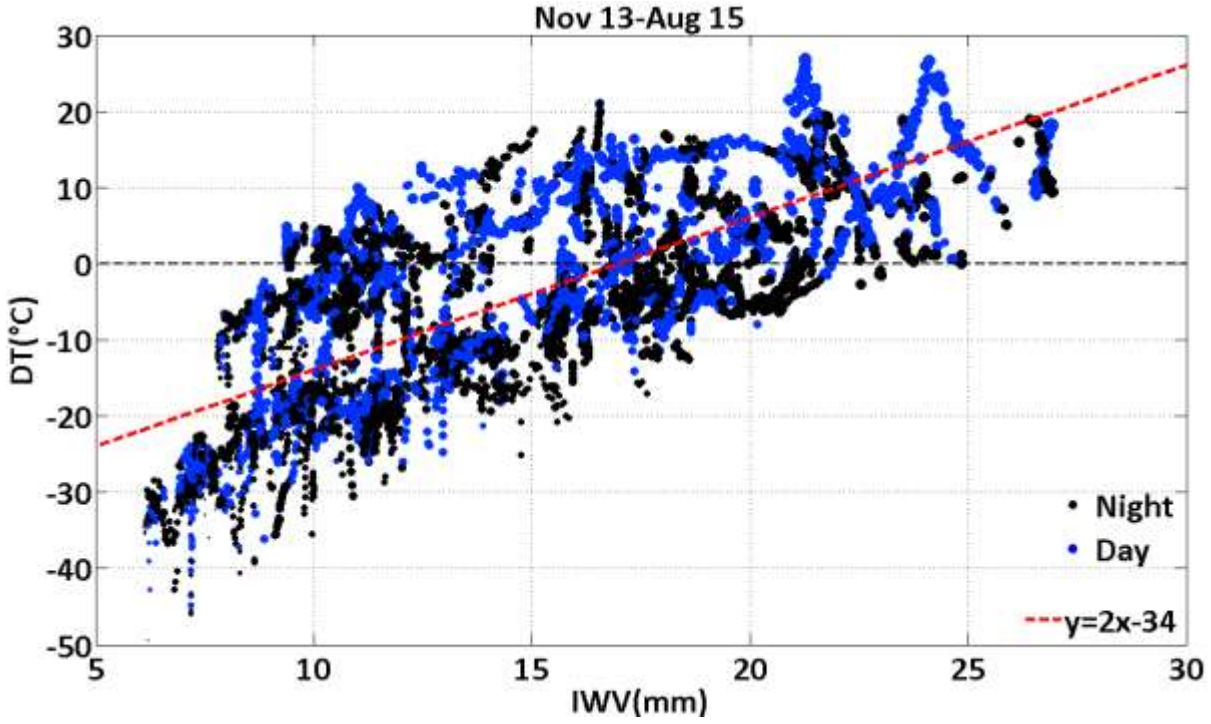

Figure 3-48: DT vs IWV - from Nov 2013 to Aug 2015 - dot size is proportional to CGT.

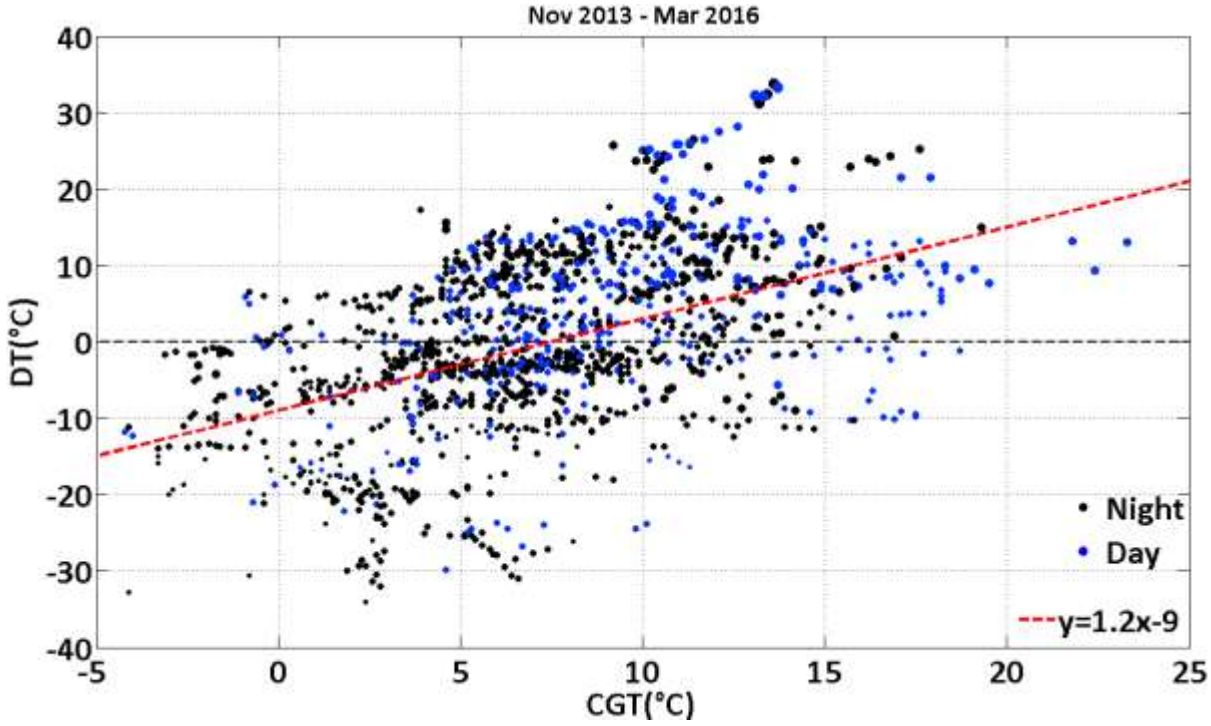

Figure 3-49: DT vs CGT - from Nov 2013 to Mar 2016 - dot size is proportional to IWV.

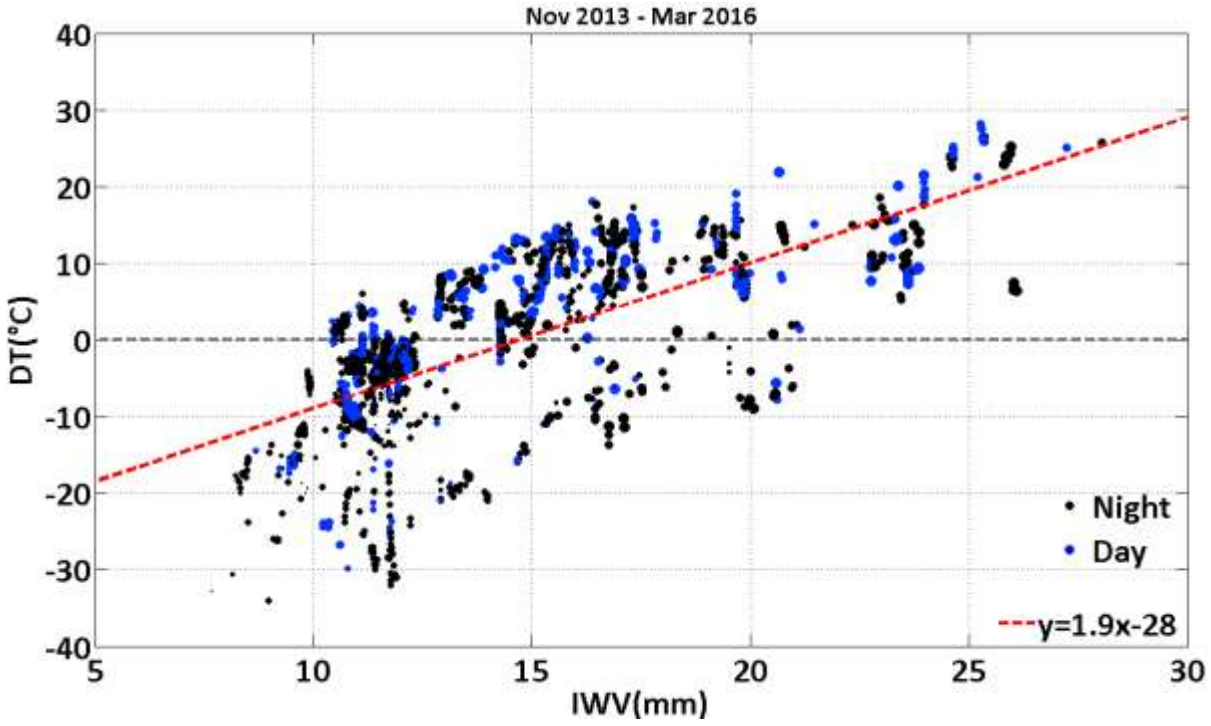

Figure 3-50: DT vs IWV - from Nov 2013 to Mar 2016 - dot size is proportional to CGT.

Figure 3-47 and Figure 3-49 suggest that the influence of CGT on BT is overestimated, and so is the influence of IWV on BT according to Figure 3-48 and Figure 3-50. In this respect, possible corrections such as the modification of the analytical form of Eq. 3.31 through the introduction of additional parameters will be explored in what follows.

Figure 3-51 shows DT (MT-BT) corresponding to data set 2 and the corresponding root-mean-square deviation (RMSD) in the top left corner. This is 11.03°C. The largest deviations occur between Dec 2013 and March 2014 and between November 2014 and May 2015 when the model can underestimate BT up to about 30°C.

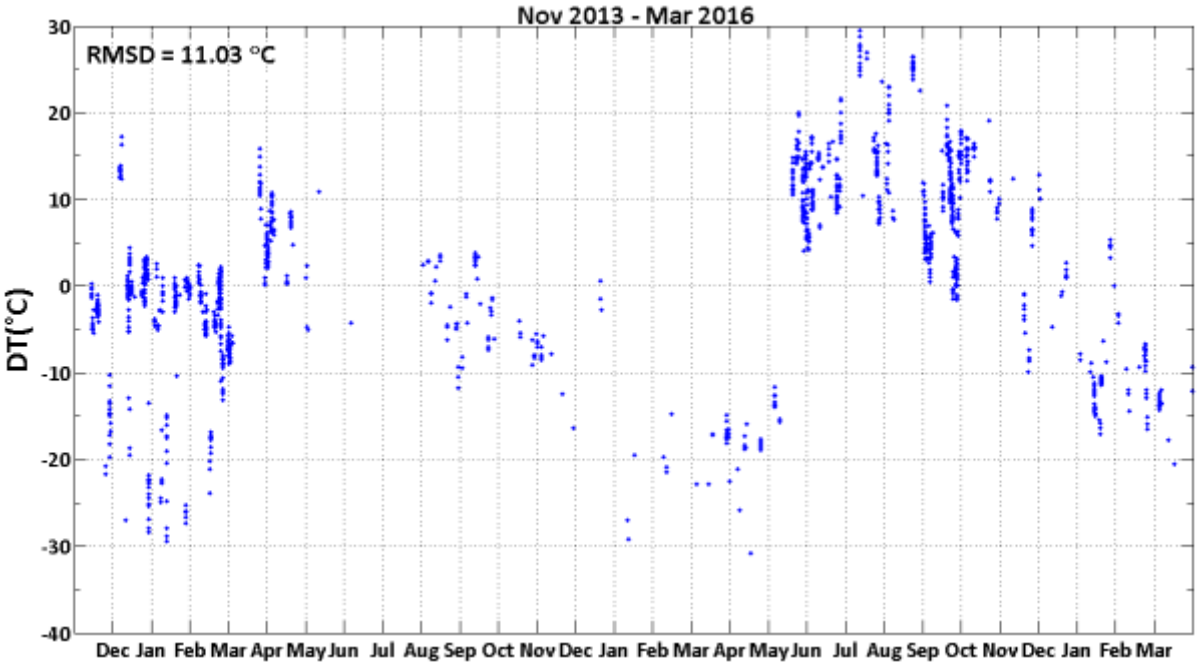

Figure 3-51: DT corresponding to data set 2.

Some of the All-sky cameras images associated with the largest deviations observed between December and March 2014 and January and April 2015 have been randomly picked and shown below (see Figure 3-52 to Figure 3-59). While on the one hand it is not possible to establish definitively the origin of such large deviations by looking at the All-sky cameras images, on the other hand it must be said that in some of these cases the stars look fuzzy, as to suggest that the sky may have not been actually clear (see Figure 3-52, Figure 3-57, Figure 3-58 and Figure 3-59). It seems reasonable to assume that the measurement was not at fault as periodic checks of the radiometer window are carried out and replacement takes place in case it looks degraded. To see how DT correlates with the relative humidity (RH), DT has been plotted against RH and shown in Figure 3-60. Interestingly the largest underestimations of BT occur when RH is higher than 70%. When RH gets so large aerosol particles can take on water and grow into haze droplets, and at even larger humidities fog can form. This would be consistent with what at least Figure 3-57, Figure 3-58 and Figure 3-59 seemingly suggest.

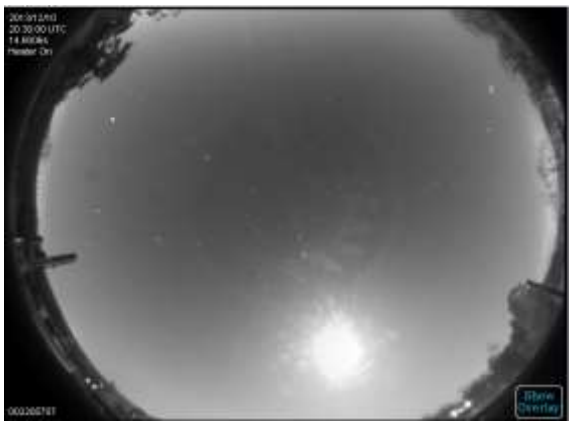

Figure 3-52: 10 Dec 2013 8:30 pm.

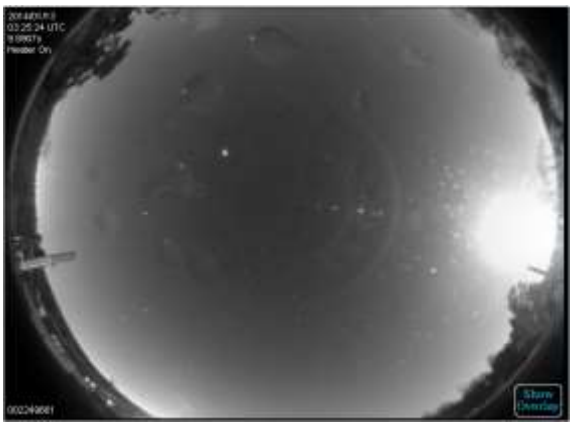

Figure 3-53: 13 Jan 2014 03:25 am.

Figure 3-54: 13 Jan 2014 08:07 am.

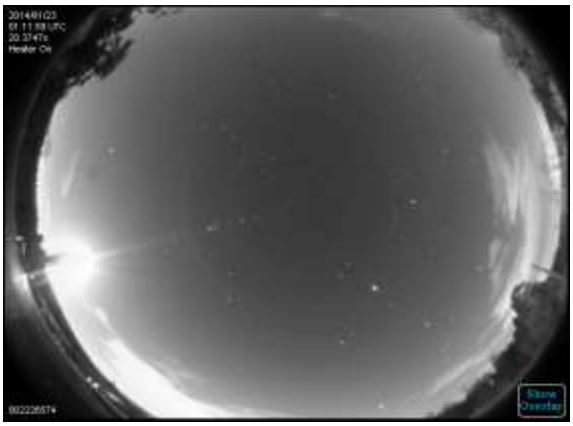

Figure 3-55: 23 Jan 2014 01:12 am.

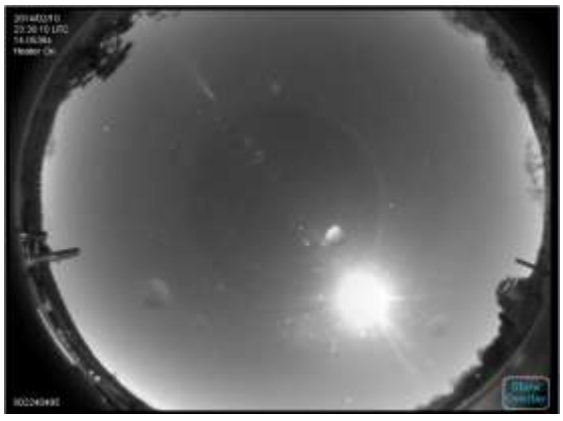

Figure 3-56: 10 Feb 2014 11:30 pm.

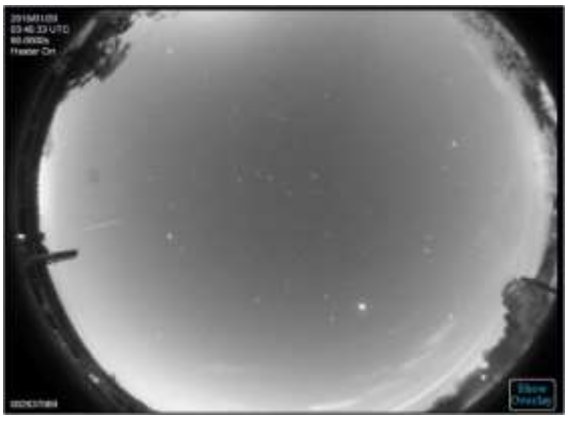

Figure 3-57: 20 Jan 2015 3:45 am.

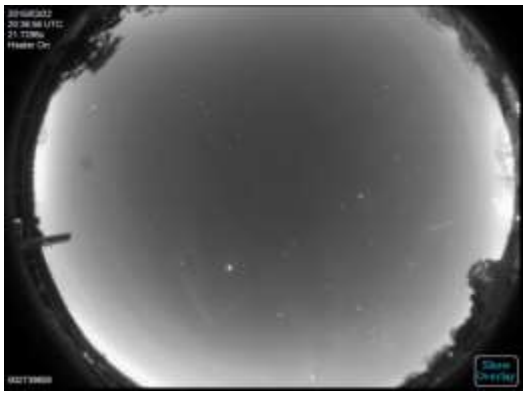

Figure 3-58: 05 Apr 2015 08:00 pm.

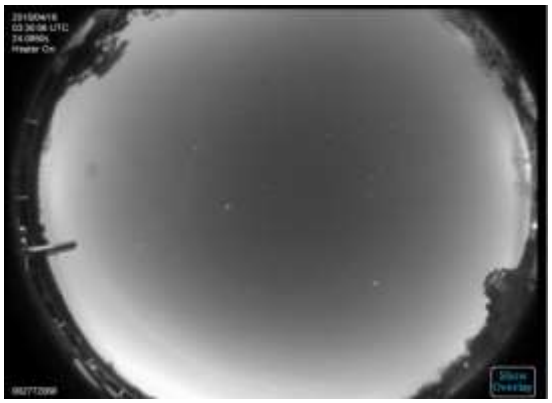

Figure 3-59: 16 Apr 2015 03:30 am.

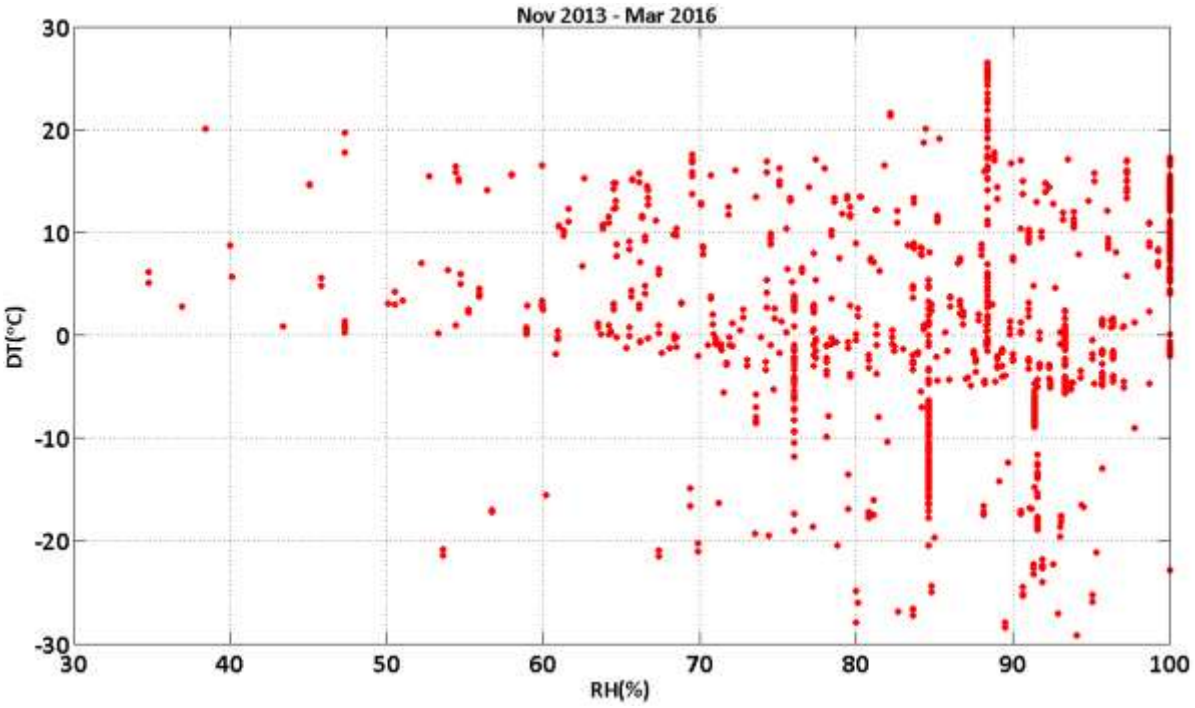

Figure 3-60: DT vs RH (data set 2).

A further attempt to improve the model has been done by using the Met Office modelled temperatures MET_T in place of CGT. With the purpose of giving a better estimate of the actual radiative temperature of the water vapour column, Dr. R. North, Research Scientist at Met Office, has provided us with modelled temperature and specific humidity profiles from January 2014 to October 2015 obtained through the operational 1.5 km configuration of the Met Office Unified Model (MetUM). The specific humidity (SH), which in this case is expressed in kg/kg units, is the mass of WV in a unit mass of air (WV plus dry air) and is used to derive the water vapour pressure (WVP) which in turn allows establishing at which altitude most of WV is concentrated. SH is linked to the mixing ratio by mass MR which is the mass of WV to the mass of dry air through the following equation:

$$MR = \frac{SH}{1 - SH} \tag{3.34}$$

MR in turn is related to the water vapour pressure (WVP) through Eq. 3.35 where *p* is the atmospheric pressure:

$$WVP = \frac{p}{\left(\frac{0.622}{MR} + 1\right)} \tag{3.35}$$

Eq. 3.35 is obtained from the definition of MR by assuming the ideal gas law for both humid and dry air and solving for the partial pressure of water vapour. To give an estimate of the altitude at which most of WV is found, *p* has been weight-averaged over the WVP profile as specified in Eq. 3.36

$$\langle p \rangle = \frac{\sum_{j=1}^{N} WVP_j \, p_j}{\sum_{j-1}^{N} WVP_j} \tag{3.36}$$

From <*p*> the corresponding modelled temperatures MET_T have been extracted from the temperature profiles. From MET_T the modelled brightness temperatures MET_MT are obtained. Figure 3-61 shows DT (MET_MT - BT) as obtained by replacing CGT with the modelled temperatures MET_T. The RMSD (top left corner) is slightly smaller than the RMSD calculated when CGT is used. Although such a correction might not significantly reduce the observed discrepancies, the lower RMSD so found suggests that the use of modelled temperatures MET_T is preferable.

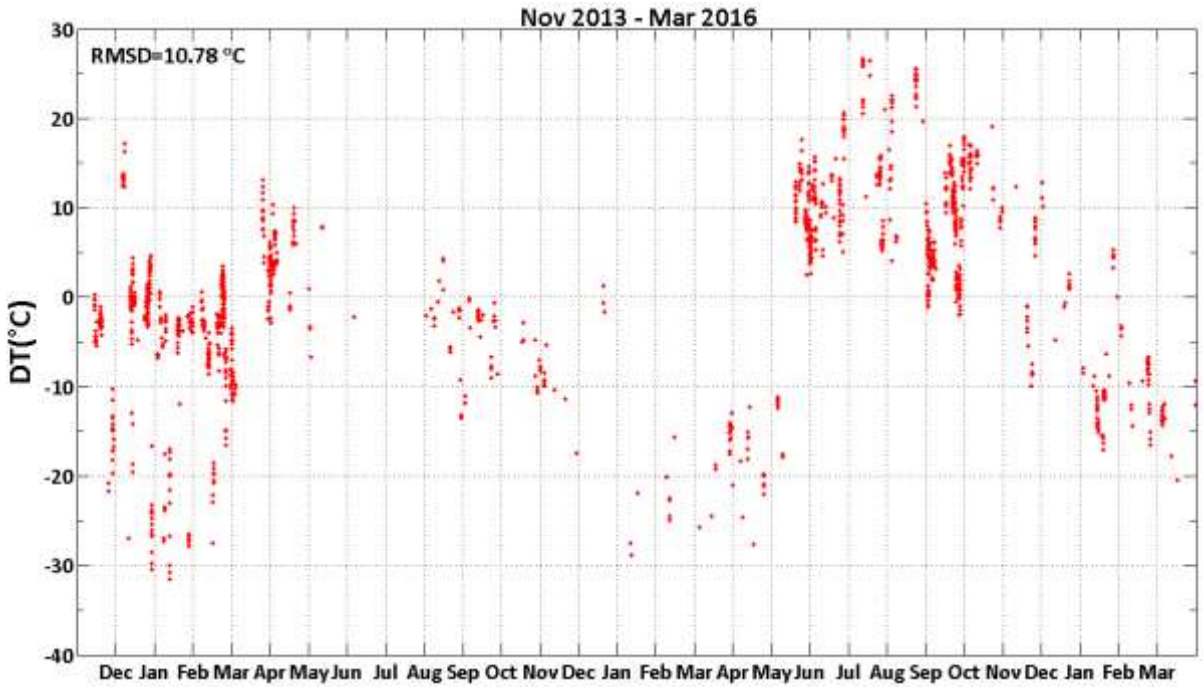

Figure 3-61: DT corresponding to data set 2 obtained by replacing CGD with the modelled MET-T.

In order to see if the amount of aerosol is correlated to DT, a scatter plot of DT (MET_MT - BT) against cloud free AOD (1.64 μm), measured through the multiband Cimel sun-photometer CE318-N (see section 2.8), has been obtained (see Figure 3-62). DT has then been averaged (blue dots) over 0.01 AOD size bins. A regression line of the averages has then been calculated (black dashed line) and used to correct the modelled brightness temperature MET_MT. The corresponding RMSD so found is slightly larger than the one obtained without correction and is 11.49°C. This suggests that also such a correction may be small. However it should be noted that AOD data are not always available and therefore it would be recommended to repeat what was done over a larger AOD data set.

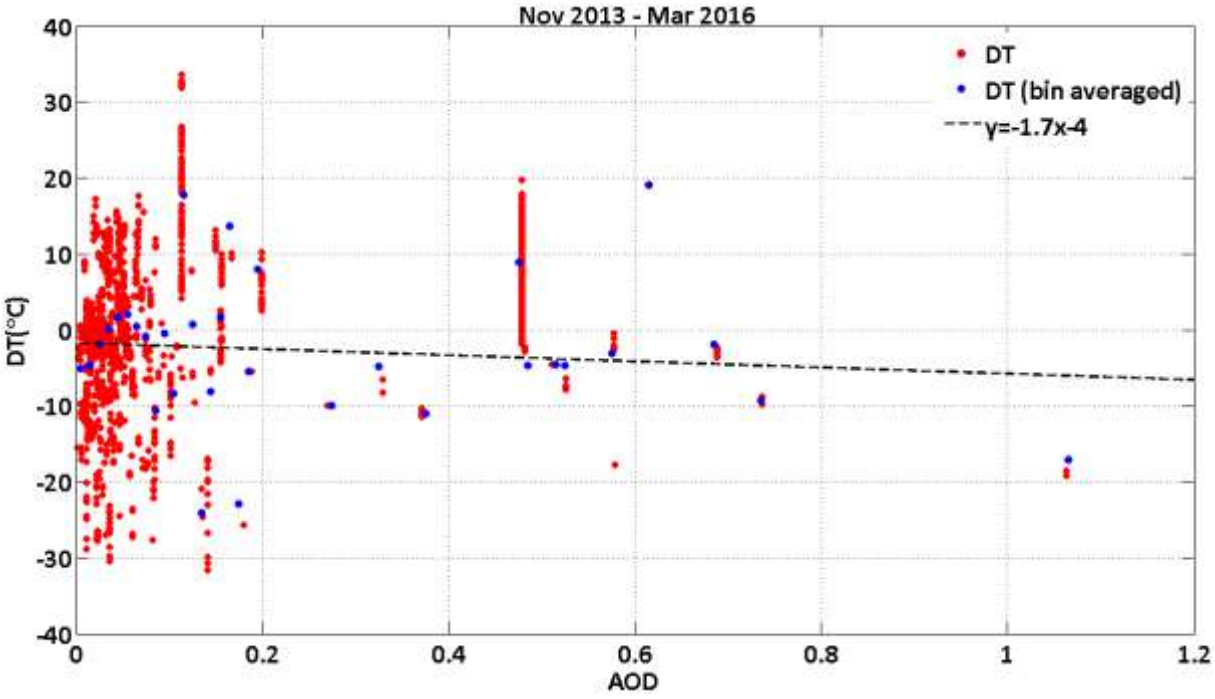

Figure 3-62: DT (MET-T corrected) vs AOD, bin averaged DT and regression line.

Given that the analytical form of Eq. 3.31 leads to an overestimation of the influence of CGT and IWV on BT, an additional reduction of the departure of MT from the actual BT can be obtained by modifying Eq. 3.31 in such a way to reduce the influence of the above mentioned parameters. If Eq. 3.31 is modified by the inclusion of three additional parameters p_1, p_2, p_3 (see Eq. 3.37) an optimization of the model based on mathematical grounds can be performed. The parameter p_1 which appears in the WV emissivity term is expected to compensate for the fact that the instrument is also sensitive to those wavelengths on either sides of the central one. The other two, p_2 and p_3, are intended to account for possible changes in the radiative temperature of the WV column due to the PBL lapse rate.

$$MP(\omega_c, CGT, IWV, \sigma_a) = \left(1 - p_1 \exp\left(-3.3\,10^{28}\ IWV\ \sigma_a\right)\right) \frac{\hbar\ \omega_c^{\ 3}}{4\pi^2 c^2} \frac{1}{\exp\left(\dfrac{\hbar\omega_c}{k_B\left(p_2 + p_3\ CGT\right)}\right) - 1} \qquad (3.37)$$

Figure 3-63 shows DT corresponding to data set 2 after the optimization of the MT and the corresponding RMSD (see top left corner). This becomes 7.53°C suggesting that a significant improvement of the modelled brightness temperature MT can be achieved through this method. The coefficient p_1, p_2 and p_3 so found are 0.44, 147.6°K and 0.30 respectively. A comparable though slightly larger RMSD value of 7.56°C is obtained if the optimization procedure is done using

MET_MT. Figure 3-64 shows a comparison of the RMSDs associated with MT (no corrections), MET_MT, aerosol corrected MET_MT, optimized MET_MT and optimized MT respectively. The latter which provides the lowest RMSD is the one which so far gives the minimum departure from the observed BT.

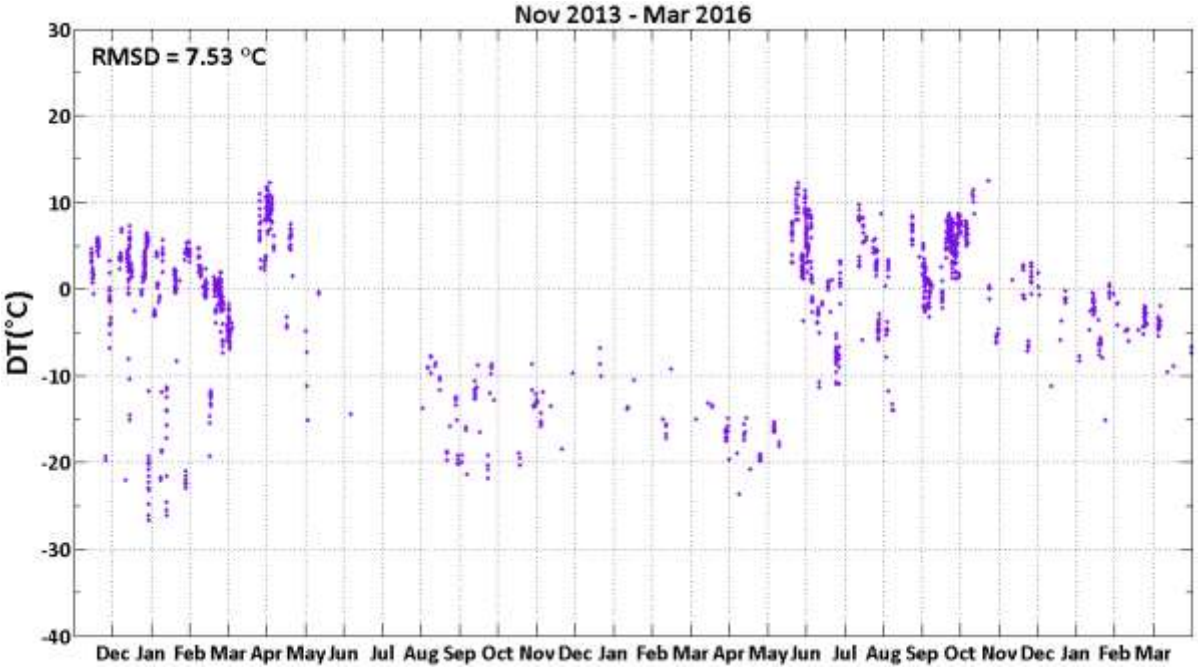

Figure 3-63: DT corresponding to data set 2 after optimization of MT with no additional corrections.

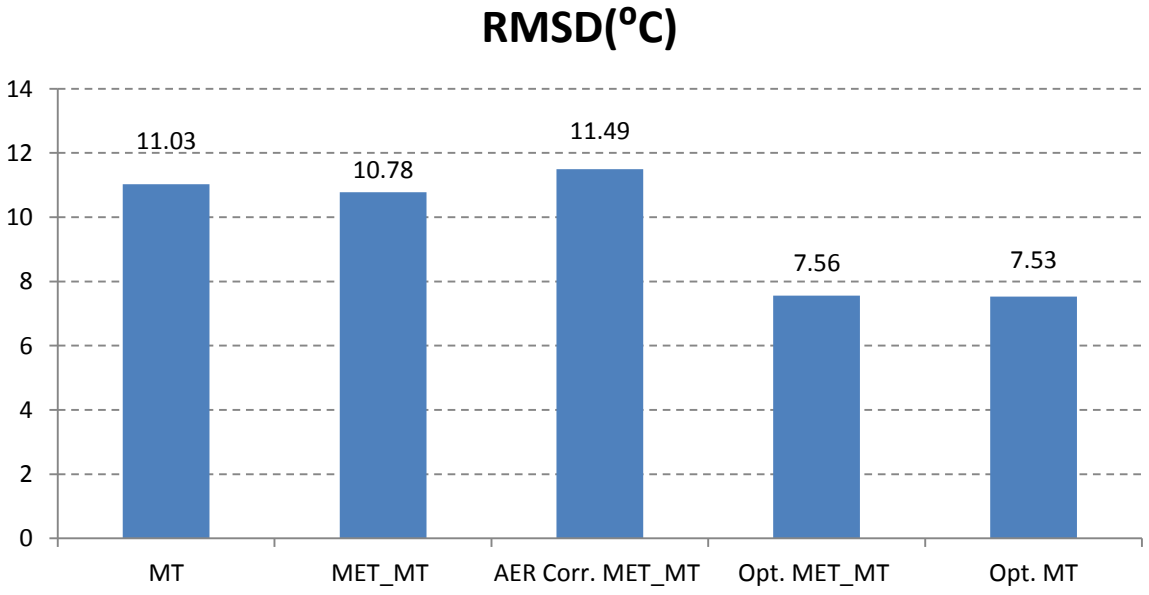

Figure 3-64: RMSD obtained without corrections, after Met Office MET-T correction, MET-T plus aerosol correction, MET-T correction plus optimization, just optimization of MT respectively.

In the following section it will be shown how to discriminate between warm and cold clouds, with the working approximation of clear sky BT now available. A threshold separating warm and cold thermodynamic phases will be set by estimating the departure from clear sky BT that an optically thick and relatively warm cirrus would give rise to.

3.8 Cirrus detection threshold

By examining a time period of a few days when BT measured is available it is possible to appreciate the variations, as large as 70°C, that BT undergoes when clouds entering the field of view of the radiometer KT15.85 alternate with clear sky periods (see Figure 3-65, blue dot). The clear sky modelled brightness temperature MT (see Figure 3-65, red dot) is obtained by following the procedure explained in section 3.6. In order to establish via BT whether warm or cold clouds are present in the field of view of our instrument, an estimate of the departure of BT from the clear sky MT due to cirrus can be calculated. More precisely we want to set the maximum possible departure from clear sky MT ascribable to cirrus which will occur when the cloud is warmest and optically thick. Warm liquid clouds would certainly determine a departure from MT larger than the one due to such cirrus and hence would lend themselves to be discriminated. By assuming an optically thick cirrus (ε = 1) at a temperature of -38°C, representative of the upper temperature limit of ice clouds (174), an estimate of the irradiance due to the direct emission of cirrus corrected for the atmospheric attenuation, as derived in Eq. 3.18, can be obtained (see Figure 3-65 green dot). Above the green curve we would have optically thick clouds warmer than -38°C, i.e. technically not cirrus. Although ice clouds can be found at temperature warmer than -38°C the rationale of the derivation of the threshold would be the same.

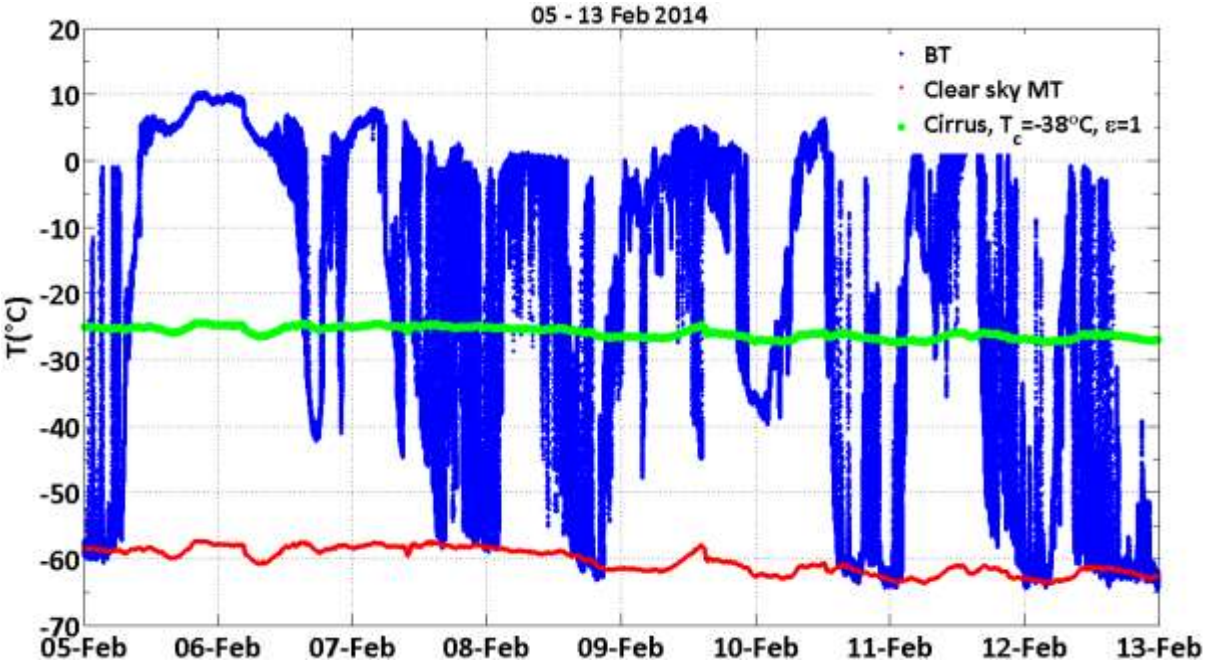

Figure 3-65: BT (blue dot), clear sky MT (red dot) and cirrus (T_c = -38°C, ε = 1).

To establish what type of clouds we could find between the green and red curves assumptions on cloud emissivity ε, cloud transmissivity t, and temperature should be made. Let us assume to have a relatively "cold" mixed phase or water cloud characterized by an emissivity ε of 0.3. Let us also assume a conventional temperature lapse rate of 2.2°C/300 m and a ground temperature GT equal to 10°C representative of its annual mean value at our observation site. With such a lapse rate at an altitude of 3 km, an estimate of cloud temperature would be T_{wc} = -12°C. Let us also assume a ground emissivity of 0.98 and a cloud reflectivity given in Eq. 3.38.

$$r = 1 - \varepsilon - t \tag{3.38}$$

For such a low emissivity cloud a reasonable assumption of its optical depth τ could be 1. This is an intermediate value between 0.1 (thin cloud) and 10 (thick cloud). Cloud transmissivity t would then be given by Eq. 3.39.

$$t = e^{-\tau} \tag{3.39}$$

Cloud reflectivity r would be about 0.33 as a consequence of Eq. 3.38. Under the above assumptions, Figure 3-66 shows what the departure from clear sky MT would be, by virtue of the presence of a warm cloud in the field of view of the instrument, if only the cloud direct emission (magenta curve) and cloud emission plus reflection of radiation coming from ground (brown curve) were taken into account, respectively. The cloud reflectivity value so estimated leads to a departure from clear sky MT which is about twice as much as the one obtained when only cloud direct emission is accounted for.

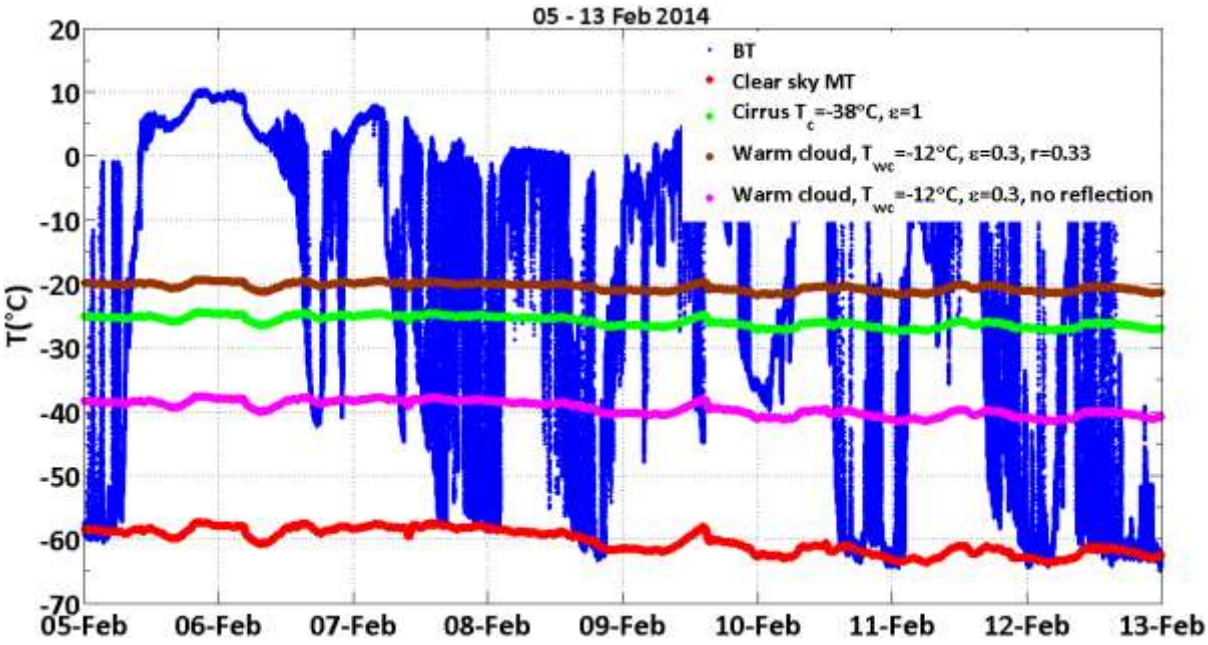

Figure 3-66: BT (blue dot), clear sky MT (red dot), cirrus (T_c = -38°C, ε = 1, green dot), warm cloud direct emission (magenta dot), warm cloud direct emission plus reflection of thermal radiation from ground (brown dot).

However, radiative transfer calculations in water clouds in the 10 µm window region (175) and additional works (176) (177) show that cloud reflectivity is never larger than 0.03. By assuming a value of 0.03 for cloud reflectivity while keeping all the other parameters the same, Figure 3-67 shows the corresponding outcome. If we were to replace the generic warm cloud with an altocumulus - whose base temperature would be T_{Alto} = -26.6°C for a cloud base height of 5 km and the same temperature lapse rate as assumed above - Figure 3-68 is obtained. It should be noted that the assumption of a cloud emissivity value of 0.3 has been made according to J. Allen's measurements of cloud emissivity in the 8-13 µm waveband (178). Low clouds exhibit an emissivity of 1±0.03, altocumulus have on average an emissivity of 0.79 although values ranging from 0.25 to 0.3 were observed, while cirrus emissivity can vary from 0.05 to 1. The position of the brown curves in Figure 3-67 and Figure 3-68 suggests that a relatively "cold" and optically thin mixed-phase or water cloud could not be detected using the "thick cirrus" threshold method.

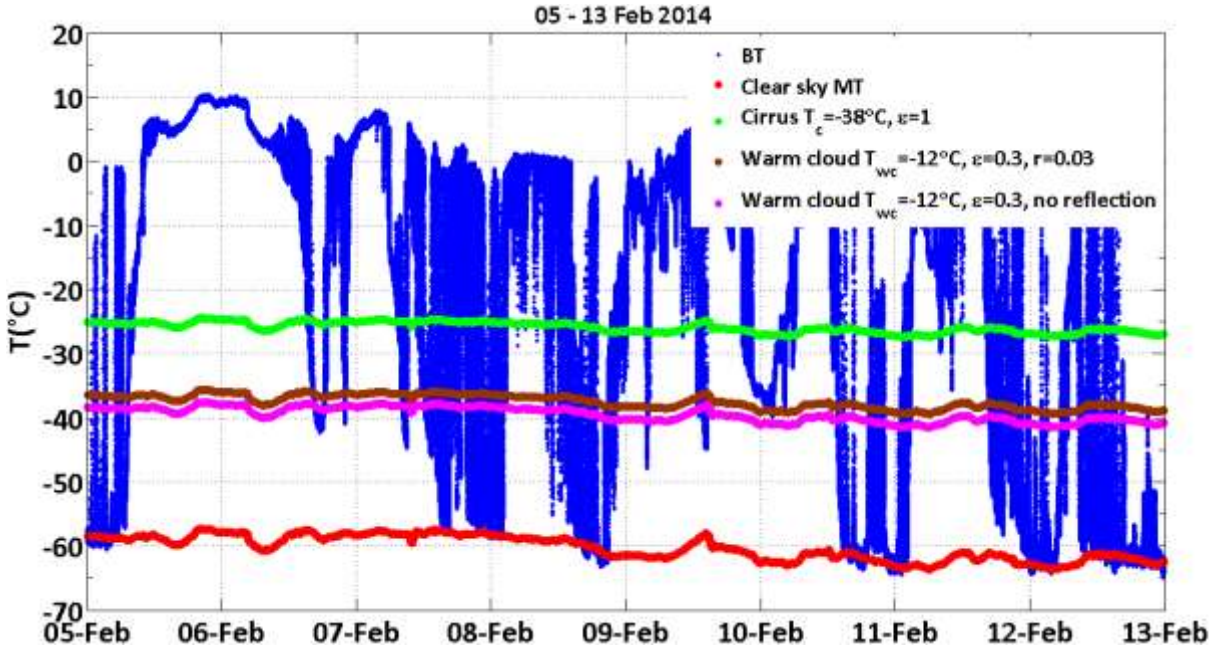

Figure 3-67: BT (blue dot), clear sky MT (red dot), cirrus (T_c = -38°C, ε = 1, green dot), warm cloud (ε = 0.3) direct emission (magenta dot), warm cloud direct emission plus reflection (r = 0.03) of thermal radiation from ground (brown dot).

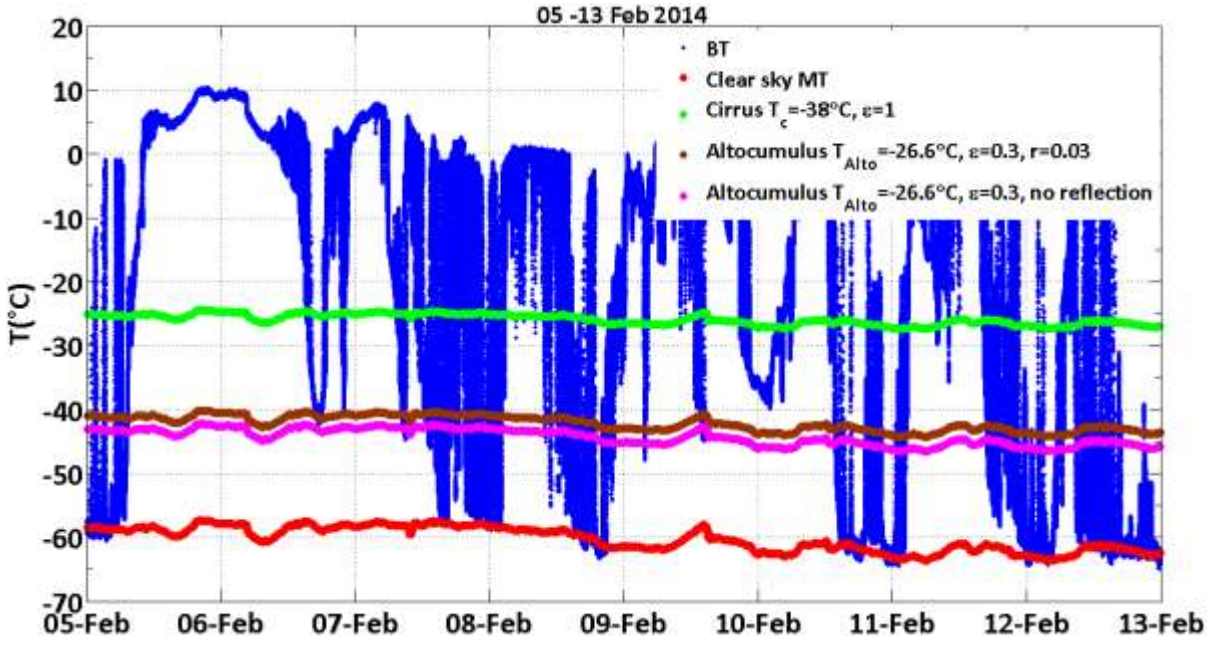

Figure 3-68: BT (blue dot), clear sky MT (red dot), cirrus (T_c = -38°C, ε = 1, green dot), Altocumulus (ε = 0.3) direct emission (magenta dot), Altocumulus (ε = 0.3) direct emission plus reflection (r = 0.03) of thermal radiation from ground (brown dot).

We now want to characterize clouds found between the red and green curves in terms of their optical depth τ. More precisely we want to estimate the minimum τ needed, for a potentially mixed phase cloud at its lowest possible temperature, to give rise to a departure from clear sky MT as large as the one due to thick cirrus. This will allow us to set the lower τ limit below which the method may fail in discriminating cirrus from mixed phase clouds. Notice that the most difficult case to

discriminate, for a given τ, is set by choosing the minimum temperature that the cloud can be at. If scattering by cloud particles in the infrared region is neglected, cloud emissivity can be expressed as:

$$\varepsilon = 1 - e^{-k_a h} \tag{3.40}$$

where k_a is the absorption coefficient and h is the geometric thickness of the cloud. Here it is assumed that k_a is constant over the geometric depth of the cloud. According to our estimate, under the assumption of an altocumulus whose cloud base temperature is T_{Alto} = -26.6°C, the cloud optical depth τ necessary to give rise to a departure from clear sky MT slightly larger than the one due to the "thick" cirrus (see Figure 3-69) is 1.5. This means that relatively "cold" and optically thick (τ > 1.5) warm clouds are potentially detectable using the cirrus threshold (Ci threshold).

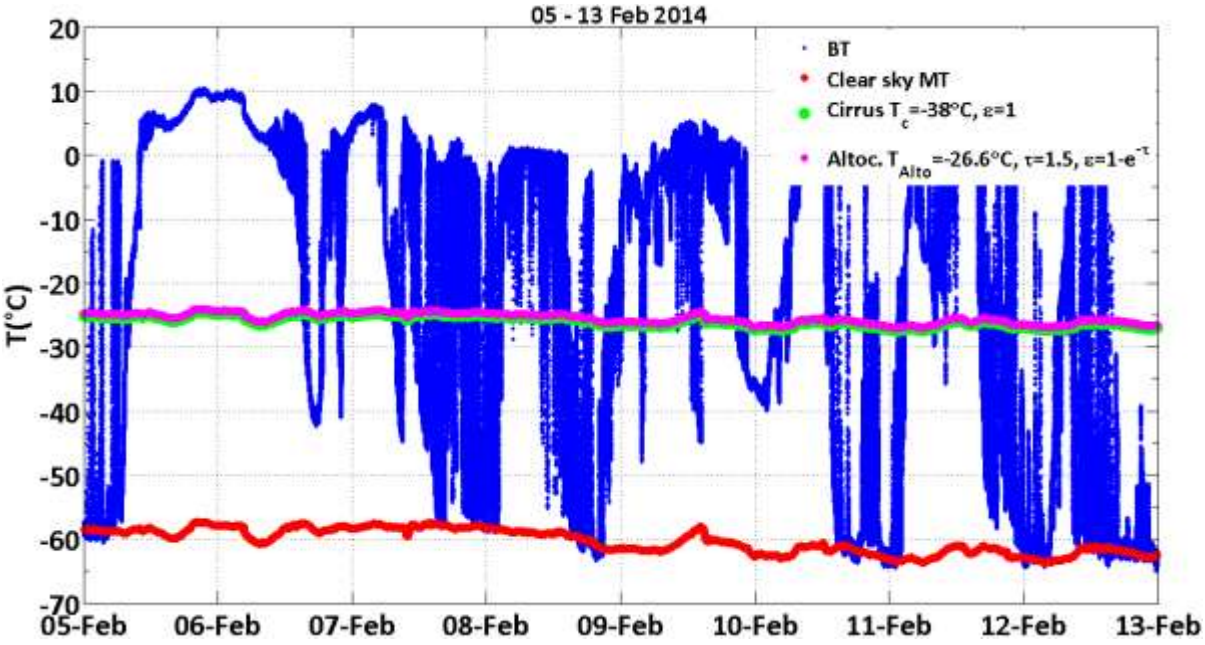

Figure 3-69: BT (blue dot), clear sky MT (red dot), cirrus (T_c = -38 °C, ε = 1, green dot), Altocumulus (T_{Alto} = -26.6°C, τ = 1.5, ε = 1-e$^{-\tau}$) direct emission (magenta dot).

3.9 Conclusions to radiometry

A two-steps cirrus detection algorithm has been proposed. The first step consists in the calculation of the brightness temperature fluctuations through De-trended Fluctuation Analysis (DFA) which allows the discrimination of clouds (except when very optically thin) from clear sky. As the second step, a model of down-welling thermal radiation under clear skies has been proposed to discriminate between warm and cold clouds. A narrow band infrared radiation pyrometer (KT15.85 II) whose response function is centred at 10.6 µm has been employed to observe down-welling irradiance represented as brightness temperature (BT). The model attempts to reproduce the observed BT. De-trended fluctuation analysis (DFA) of the BT data has been used to cloud-screen the data points later on used to test the model. Only those observations such that BT < -30°C have been taken into account. Based only on first principles of black-body radiation, the model's fundamental assumption is that WV is the only one among the atmospheric gas species to act as absorber and emitter of thermal radiation. No other radiative contribution has been taken into account. Furthermore the model has been derived by using only the central wavelength of the instrument response function S(λ) assumed to be sufficiently narrow to be replaced with an impulse function. Close to ground temperature (CGT) and integrated water vapour (IWV) are two of the three parameters used. The

third one is the water vapour absorption cross section (σ_a), and this one has been fitted using observational data. CGT and IWV are measured on site by means of a weather and a GPS station, respectively. The main issue faced when testing the model is that DFA may fail in discriminating clear sky. Therefore the model has been tested over a data set which could have been partly cloud-contaminated. Further cloud screening is necessary if a more accurate estimate of clear sky BT is needed. However, the model deviation from the observed BT has been obtained for a period covering more than two years. The extreme error value can be as large as 30^{o}C. On average the RMSD is of the order of 10^{o}C for the basic version of the model. At present, it is not possible to associate the largest deviations to obvious external factors. In this respect several attempts have been done. All-sky cameras images have been visually inspected to spot the presence of clouds or thick aerosol. Met Office modelled temperatures have been used to compensate either for possible temperature inversions occurring at night, or for possible increase in the PBL lapse rate taking place in the warmer hours of the day. DT and AOD have been scatter-plotted to see if a correlation exists; suggestions of the presence of a weak negative correlation seem plausible but need to be confirmed, possibly by having recourse to further cloud-free AOD data. The analytical form of the model has also been modified through the inclusion of three additional coefficients (see Eq. 3.37) which have been determined by optimizing the performance of the model in reproducing the observed BT. RMSD reduces to 7.5^{o}C when the optimized model is used. The discrimination of ice clouds proposed here consists in estimating the departure of BT from modelled clear sky BT (MT) due to the presence of a relatively "warm" and optically thick cirrus. This allows setting a threshold which represents an estimate of the maximum departure from clear sky BT associated with "thick" cirrus. This threshold is not fixed but accounts for the atmospheric transmission associated with the atmosphere below the cloud. According to our estimate it turns out that warm clouds characterized by an optical depth τ larger than 1.5 would determine a departure of BT from clear sky BT larger than the one due to the above "thick" cirrus, and would therefore lend themselves to be discriminated. According to this estimate, for values of τ lower than 1.5 discrimination might fail. However this method has not been validated yet. This will be discussed in the coming section together with suggestions on how to decrease the uncertainty in the estimate of down welling thermal radiation under clear skies.

3.9.1 Recommendations for further work

Testing the "thick" cirrus threshold method for discriminating warm and cold clouds should be done if an assessment of the reliability of the method is to be carried out. It could be tested by means of either microwave radiometry, which can be used to measure integrated liquid water, or through LIDAR which allows the retrieval of cloud height, and indirectly cloud temperature if assumptions on temperature lapse rate are made. On the other hand improving our ability to model atmospheric radiation under clear skies would lead to a better estimate of cloud temperature in particular when cloud emissivity is known (i.e. optically thick clouds). In order to improve the model performance in simulating BT some potential solutions are proposed. Alternative analytical expressions to the impulse function used to simulate the radiometer response function could be considered. A narrow rectangular window function for instance centred around the nominal central wavelength 10.5 μm could be used together with the integration method (170) suggested at the end of section 3.6.1. The integration could be done to the level of accuracy needed as demonstrated in the appendix. It is reasonable to think that accounting for a set of wavelengths in addition to the central one and doing the corresponding integration of Eq. 3.15 could lead to a further reduction of the modelled temperature errors, but this is just an hypothesis which has to be verified.
Further cloud-screened AOD data could be used to establish whether the existence of negative correlation between DT and AOD as suggested by Figure 3-62 is genuine. Higher resolution modelled air temperatures could be used in place of CGT. These could be provided by the Met Office and obtained through their operational 1.5 km configuration Unified Model (MetUM).
With the necessary corrections for the All-sky cameras (discussed in paragraphs 2.5, 2.6, 2.7, 2.9, 2.10 respectively) at hand, the measure of the HR is now possible.

In the coming chapter 4 time series of HR, BT, Ci threshold, DFA and irradiance corresponding to specific test cases will be analysed bearing in mind the measure of the HR will be limited to images such that $z < 65^{o}$ and $z > 75^{o}$ for the reasons explained in paragraph 2.10.

4 Halo ratio - test cases

In this chapter we will be measuring the HR under different atmospheric conditions: at first under clear skies, subsequently under cloudy skies, in particular under halo and non-halo cirrus, mixed phase and liquid clouds. We will be assessing whether clear sky HR takes on some characteristic value that could be referred to as "typical" clear sky HR (CSHR); also we will see how the HR varies under cirrus and if in particular our measure is sensitive to the halo-non halo nature of ice clouds. More in general this will allow us to have a glimpse of the potential of the HR measure to characterize cirrus.

4.1 Clear sky HR

The time series of the HR, BT, DFA, Ci threshold and irradiance have been plotted for a day of relatively clear sky, the first of November 2015 between 2 pm and 4 pm (see Figure 4-1). The respective All-sky camera quick-looks are shown in Figure 4-3. Despite not always below the DFA threshold (0.02), the relatively low values of the FC in combination with the pyranometer measurements (bottom plot) which can be used to retrieve cloud optical depth (179) (180) (181) suggest that the assumption of clear sky is plausible. This is also backed by the LIDAR plot of logarithmic range-corrected backscatter signal (LRCBS) shown in Figure 4-2 (see footnote*). If data such that FC > 0.02 are excluded from the average, the HR mean value, from now on referred to as the clear sky halo ratio (CSHR), is 0.92.

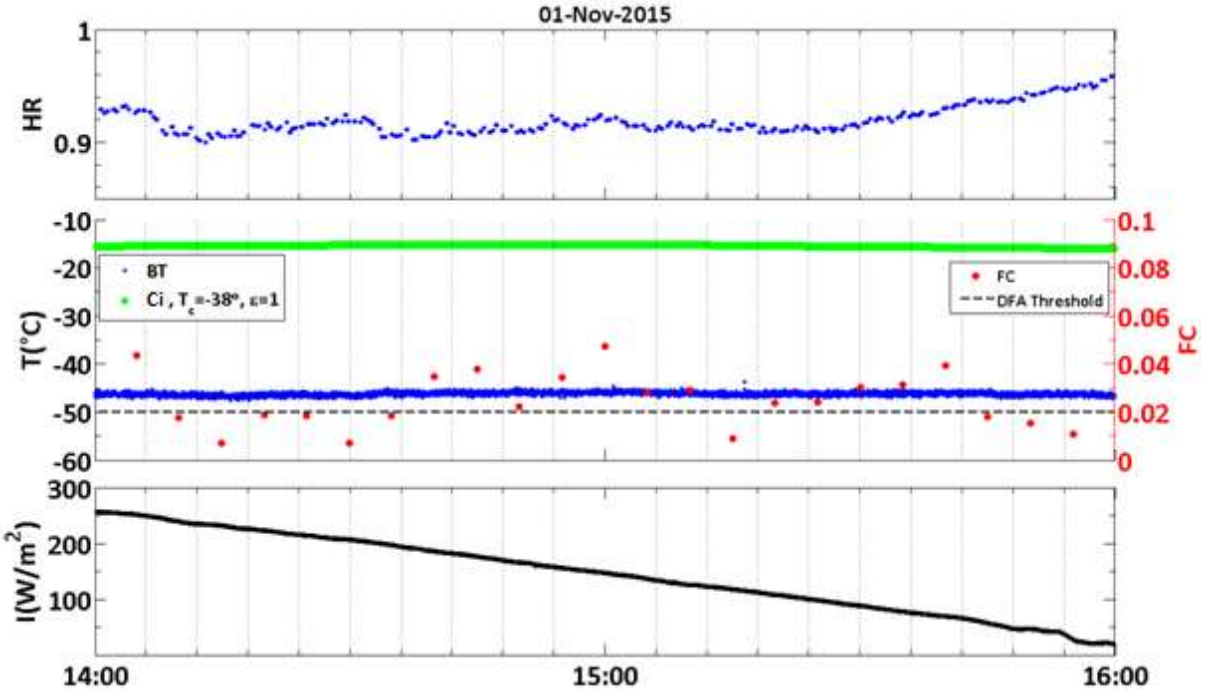

Figure 4-1: Top plot: HR time series - Middle plot: BT (blue dot), DFA(red dot), DFA threshold (dashed black line), cirrus threshold (green dot) time series - Bottom plot: solar irradiance time series. Data from 1st November 2015 between 2 pm and 4 pm.

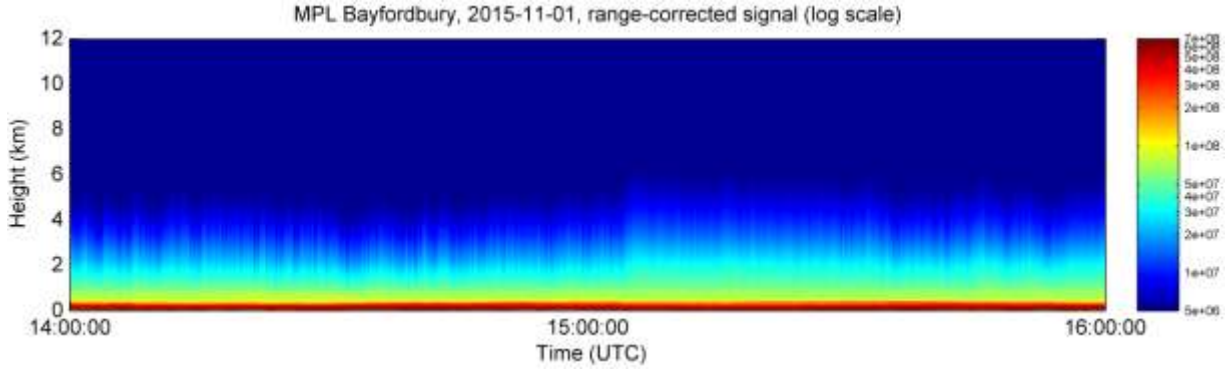

Figure 4-2: LIDAR range-corrected backscatter signal shown on log scale (*). Data from 1st November 2015.

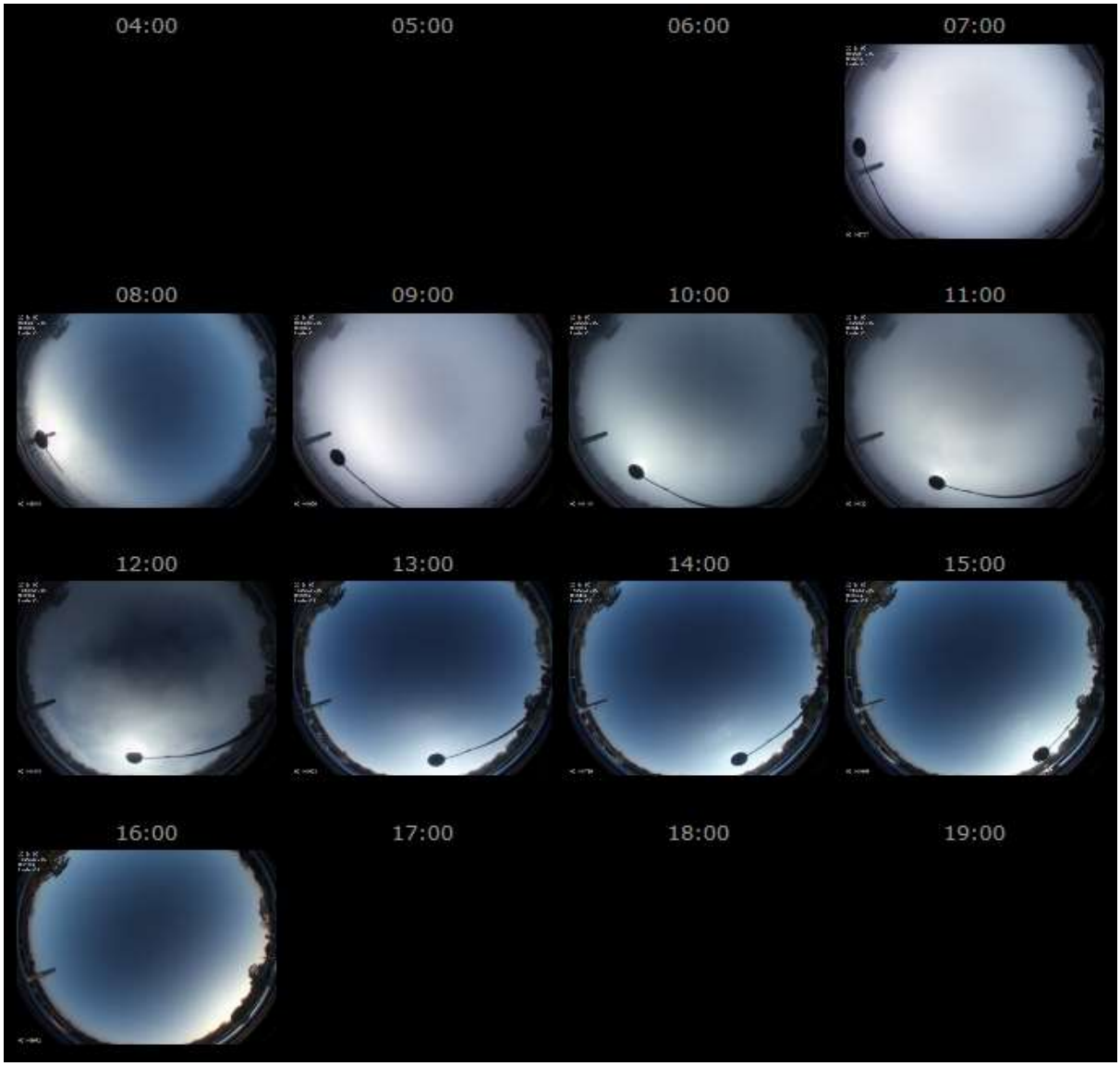

Figure 4-3: All-sky camera quick looks - 1st November 2015 between 7 am and 4 pm.

* Data processing by Dr. M. Tesche, Lecturer at University of Hertfordshire - School of Physics Astronomy and Mathematics

In the next three paragraphs, analogously to what done under clear skies, four test cases, showing mostly cloudy skies will be examined.

4.2 HR test case: 18th-Jul-2015

The first case to consider is the 18th of July 2015 between 7 am and 5 pm (see Figure 4-4). To have an idea of what the sky looks like over this period, LRCBS and All-sky camera quick looks are given in Figure 4-5 and Figure 4-6 respectively. An initial phase of relatively clear sky is observed between 7 am and 10 am (see Figure 4-6), with the exception of a low level cloud visible from the All-sky images at about 8:20 am (see Figure 4-7). Scattered warm clouds below a fairly clear sky are apparent from 10 am until 11:30 am when a layer of high altitude clouds moves into the field of view of the radiometer. The Ci threshold (see Figure 4-4, green line) would suggest this to be cirrus. Presence of both high and low level clouds lasts until about 1:15 pm, while cirrus, with varying optical depth, persist until the end of the observation period. From 7 am until about 10 am, the HR is fairly stable around 0.9 apart from some relatively large fluctuations due to the low altitude cloud at 8:20 am. From 10 am on when both high and low altitude clouds co-occur the HR fluctuates between 0.87 and about 1.05. However, while the large HR values observed at 10:24 am, 11 am and 11:48 am do not correspond to halo occurrences, those ones at 12:30 am, 1 pm and 1:24 pm do, as the All-sky images confirm (see Figure 4-8, Figure 4-9, Figure 4-10). This is consistent with the time cirrus starts thickening (roughly around 12 am). When only cirrus occurs (from 1:30 pm on) HR fluctuations attenuate: from 0.87 to 0.97, between 2 pm and 3 pm, when halo cirrus seems dominant while it slightly drops from 3:30 pm to 4:30 pm, when colder non-halo cirrus becomes prevalent, to rise again from 4:30 pm to 5 pm correspondingly to cloud optical depth. This example shows that if on the one hand a relatively large HR (HR > CSHR) can be indication of presence of halo-producing cirrus, on the other hand this might not be the case. If data points above the Ci threshold, for sake of brevity approximated with its mean value, are screened out and BT is scatter plotted against HR (see Figure 4-11), there is suggestion that the HR might be increasing with COD.

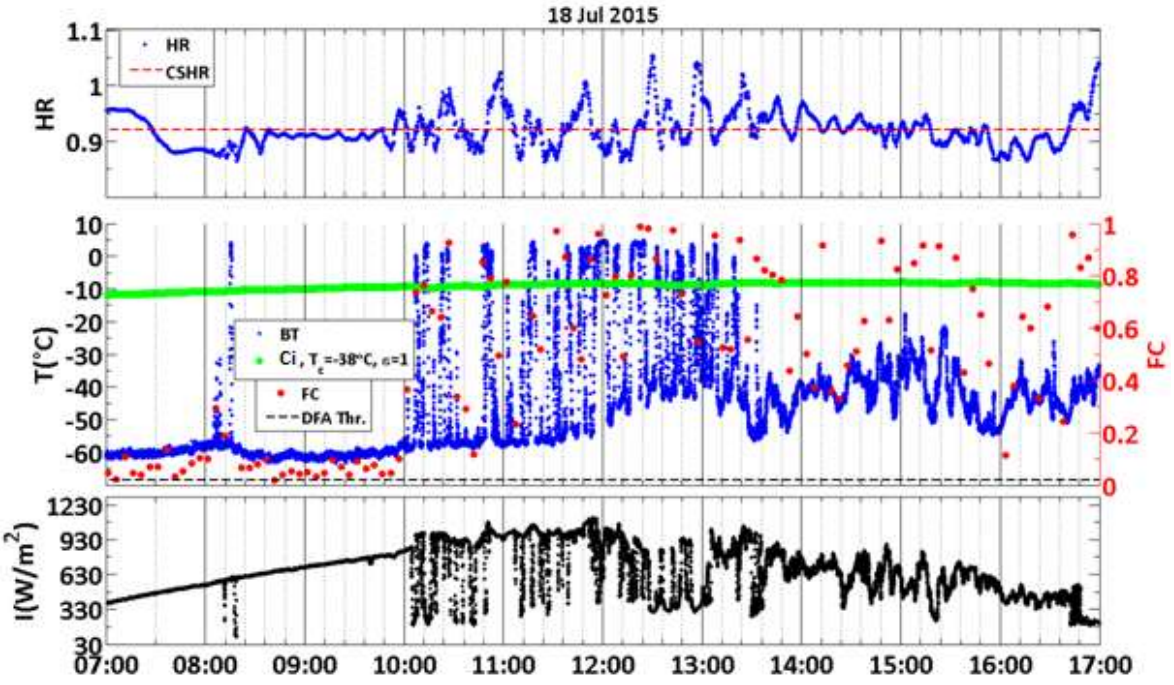

Figure 4-4: Top plot: HR and clear sky HR (CSHR) time series - Middle plot: BT (blue dot), FC time series (red dot), DFA threshold (dashed black line), Ci threshold (green dot) - Bottom plot: solar irradiance time series. Data from 18th of July 2015 between 7 am and 5 pm.

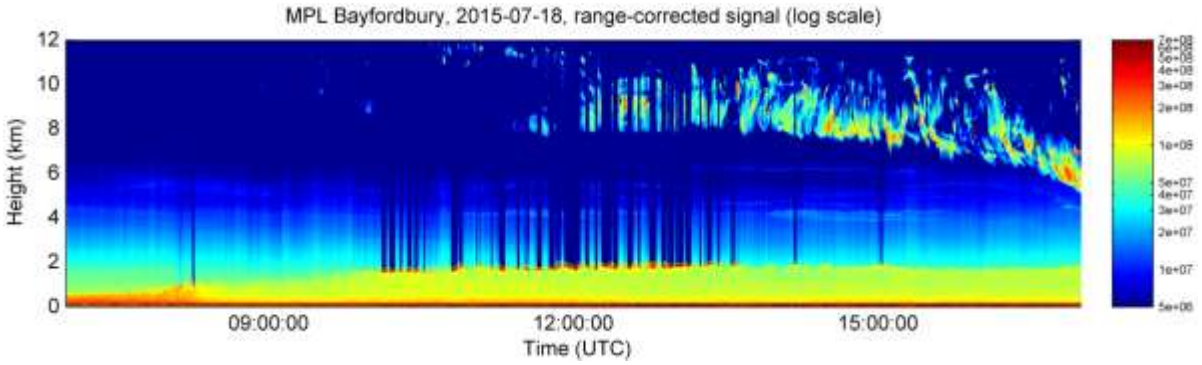

Figure 4-5: LIDAR range-corrected backscatter signal shown on log scale (*). Data from 18th of July 2015 between 7 am and 5 pm.

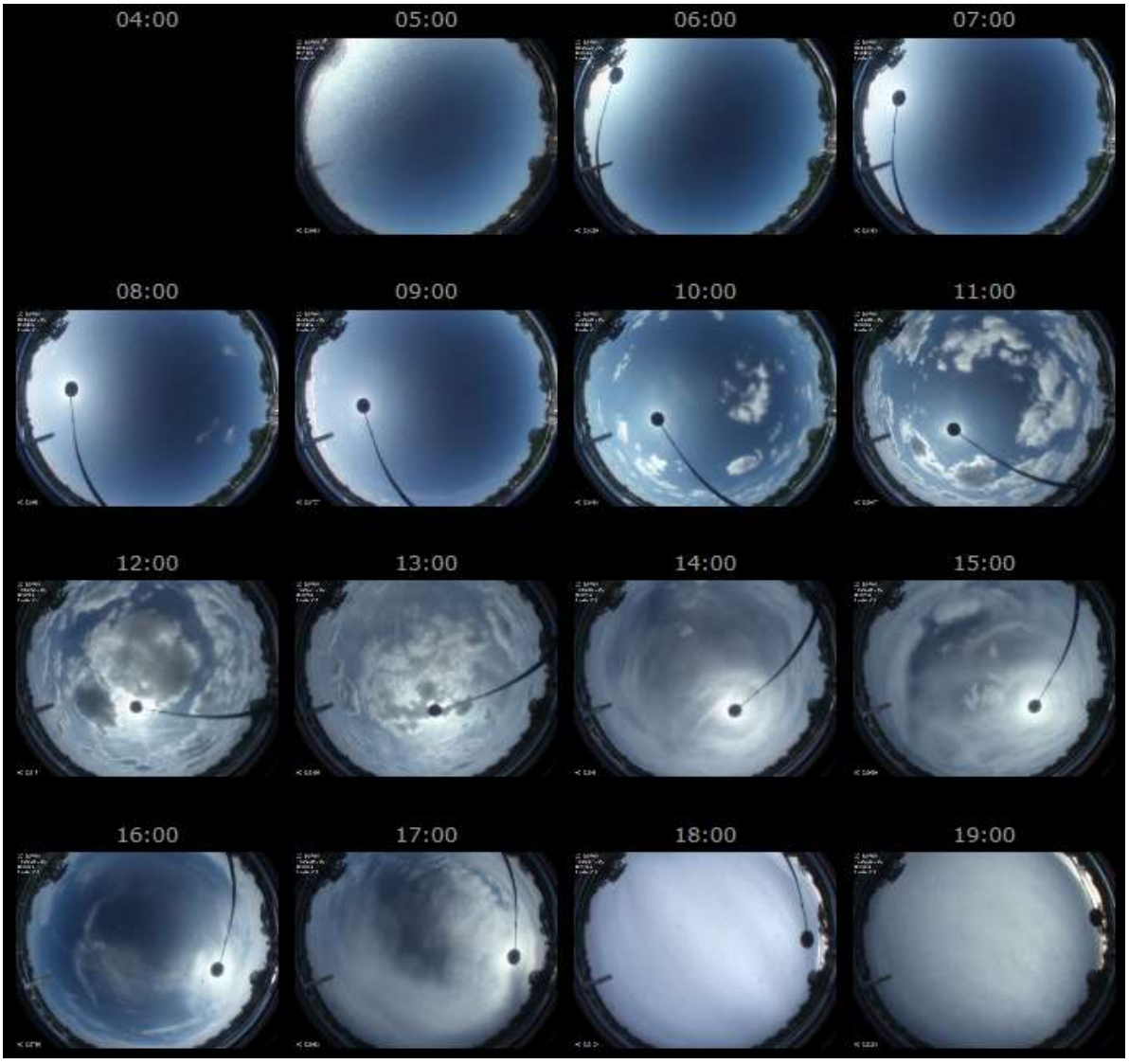

Figure 4-6: All-sky camera quick looks - 18th of July 2015 between 5 am and 7 pm.

Figure 4-7: 18 July 2015 08:15 am.

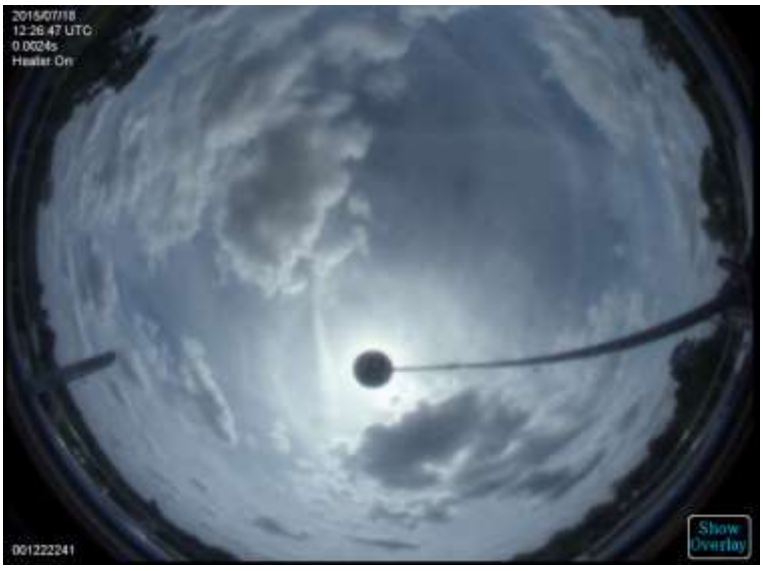

Figure 4-8: 18 July 2015 12:26 pm.

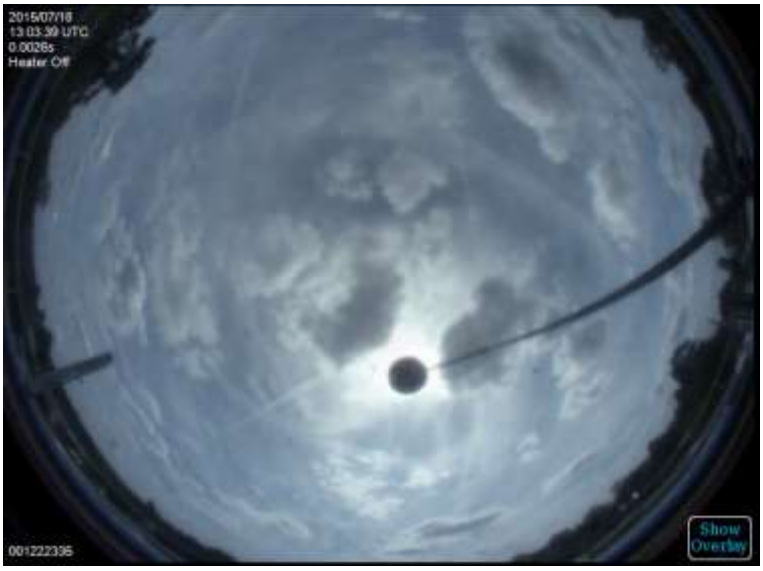

Figure 4-9: 18 July 2015 1:03 pm.

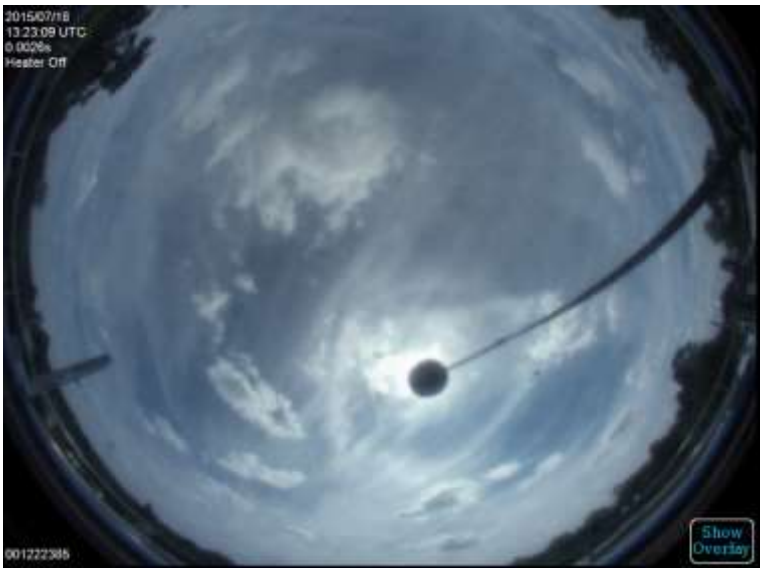

Figure 4-10: 18 July 2015 1:23 pm.

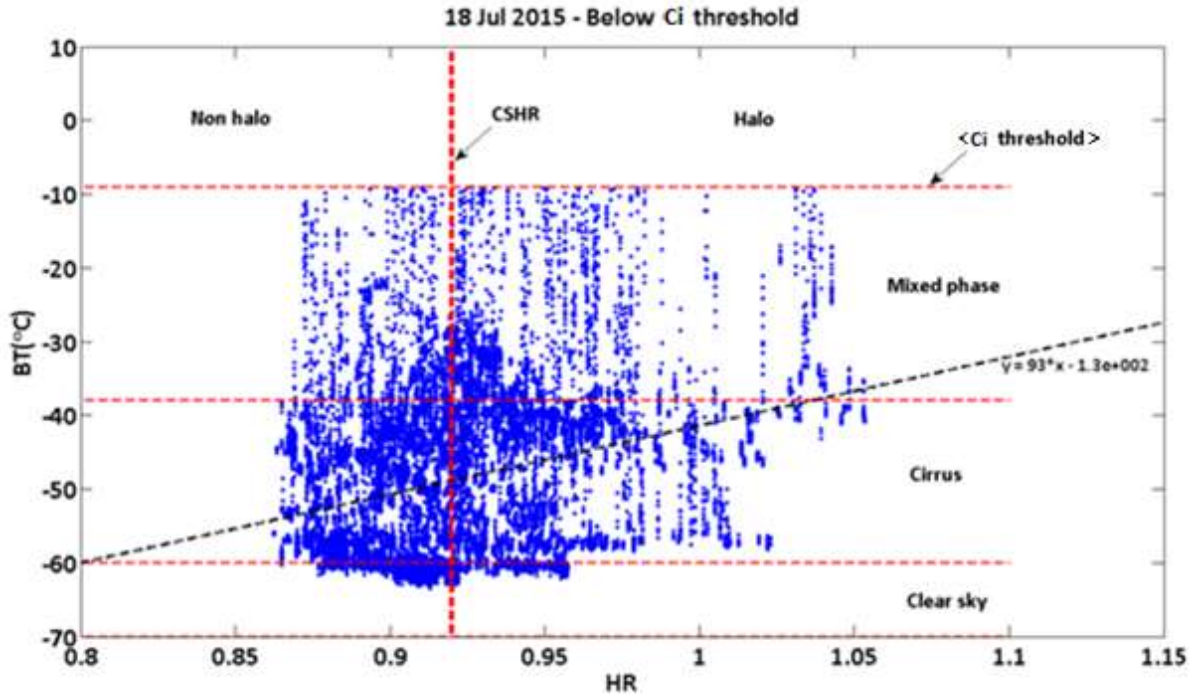

Figure 4-11: BT (warm cloud-screened) vs HR scatter plot corresponding to the 18th of July 2015. For the sake of completeness the horizontal red dashed lines delimiting clear sky, cirrus and mixed phase cloud regions are based on the assumption that -38°C is the transition zone from ice to mixed-phase clouds.

4.3 HR test case: 1st-Aug-2015

Another example to discuss is the 1st of August 2015 from 7 am to 5 pm (see Figure 4-12). Cirrus is visible throughout the early morning until about 10:30 am (see Figure 4-13 and Figure 4-14); from 7:15 am halo-cirrus becomes prevalent, when linear contrails are replaced by more continuous cloud. From about 10:36 am warm clouds occur and persist throughout the afternoon until around 4:20 pm except from 11:12 am to 12:12 pm, from 1:48 pm to 2:15 pm, and from 2:48 pm to 3 pm as the decreased BT indicates. In this regard while around midday the LIDAR too senses presence of thin cirrus at about 10 km (see Figure 4-13), this is not the case under the other two circumstances (from 1:48 pm to 2:15 pm, and from 2:48 pm to 3 pm) probably because of liquid clouds preventing the LIDAR from reaching to higher altitudes. Cold clouds, mostly non-halo cirrus become again dominant until 7 pm (see Figure 4-14). The HR is relatively large under halo cirrus (see Figure 4-12 from 7:30 am to after 10 am), reaching a maximum of 1.1 at about 7:30 am, while it drops to roughly 0.87, between 10:30 am and 12:00 noon, when a layer of mid-level clouds is observed (see Figure 4-13) before fluctuating significantly under warm clouds (roughly from 12:12 pm to 4:12 pm). The HR spikes observed in the latter case are often artefacts caused by the image becoming brighter at larger scattering angles, possibly due to bright cloud edges. Non-halo-producing cold clouds, associated to relatively lower HRs, such as those ones observed around 12 noon, 2pm and 3pm could be cirrocumulus (see Figure 4-14). Figure 4-15 shows data points below the Ci threshold plotted against the HR. Data points with HR > 0.97 (vertical red dashed line) mostly cluster in the transition zone from ice to slightly warmer, hypothetical mixed-phase clouds.

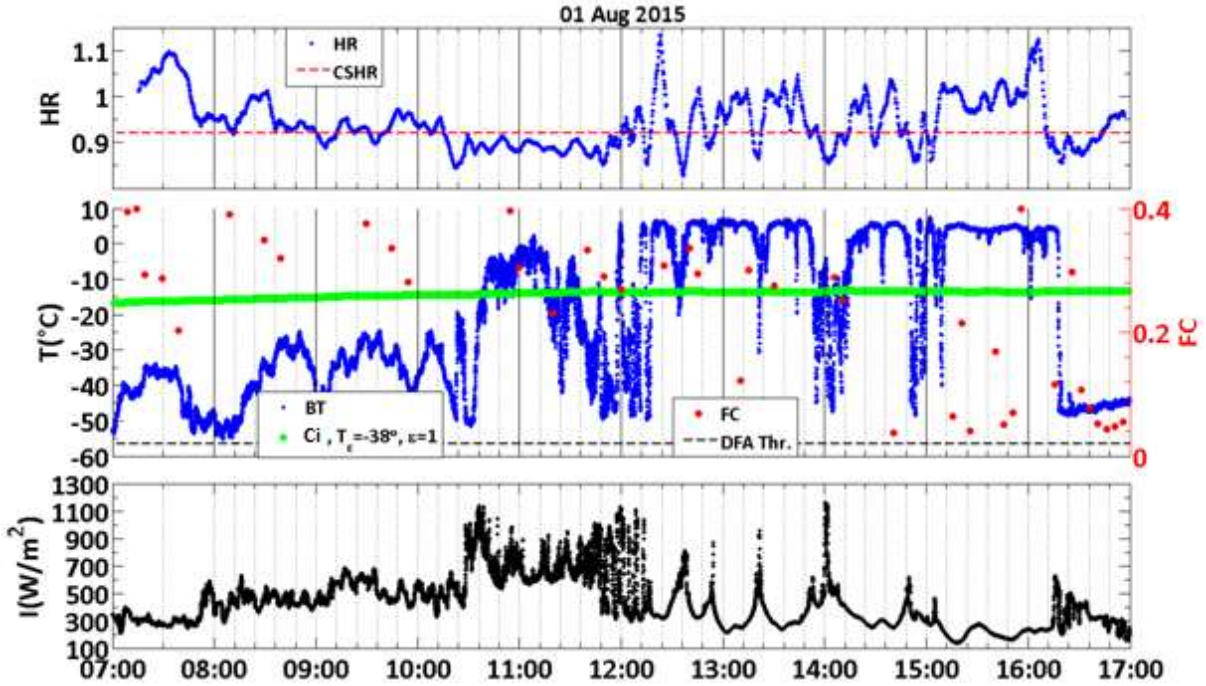

Figure 4-12: Top plot: HR time series - Middle plot: BT (blue dot), FC (red dot), DFA threshold (dashed black line), Ci threshold (green dot) time series - Bottom plot: solar irradiance time series. Data from 1th August 2015 between 7 am and 5 pm.

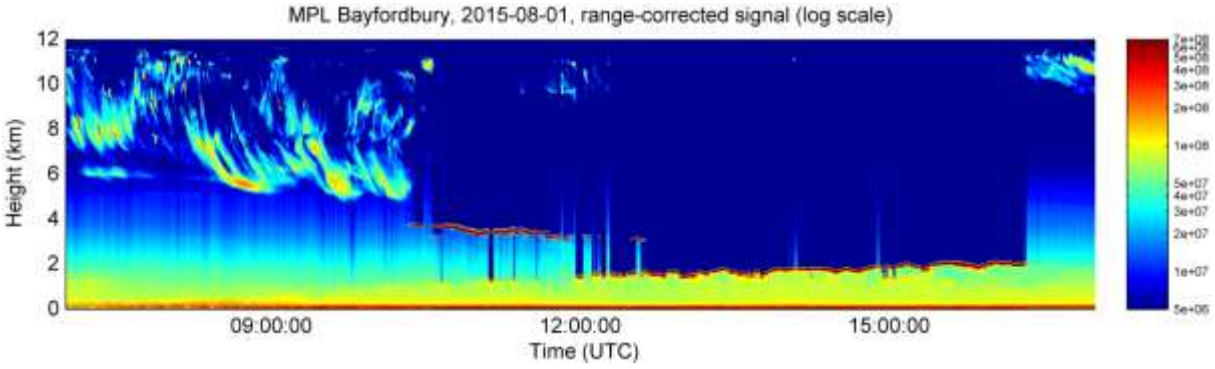

Figure 4-13: LIDAR range-corrected backscatter signal shown on log scale (*). Data from 1th August 2015 between 7 am and 5 pm.

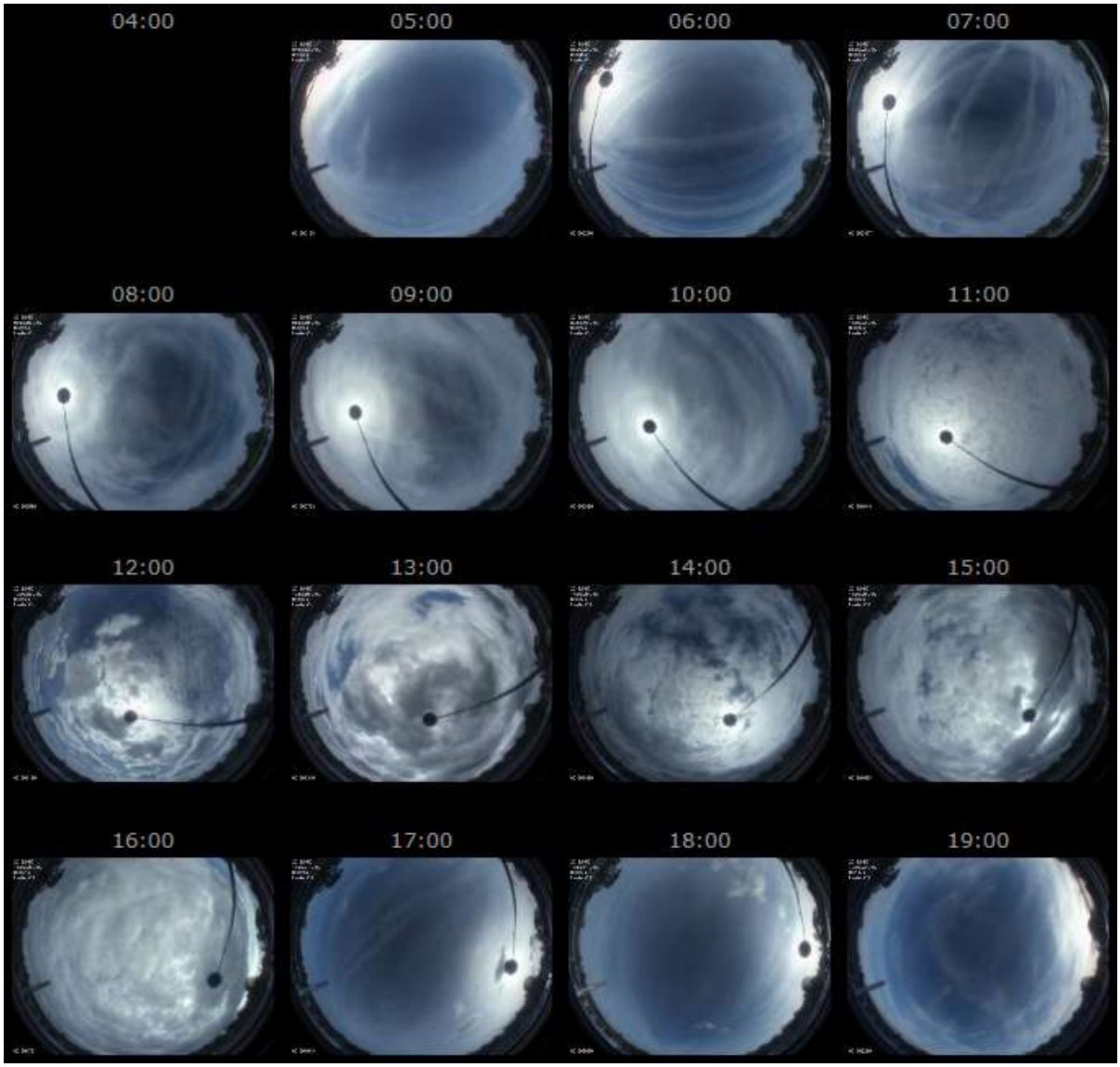

Figure 4-14: All-sky camera quick looks - 1st August 2015 between 5 am and 7 pm.

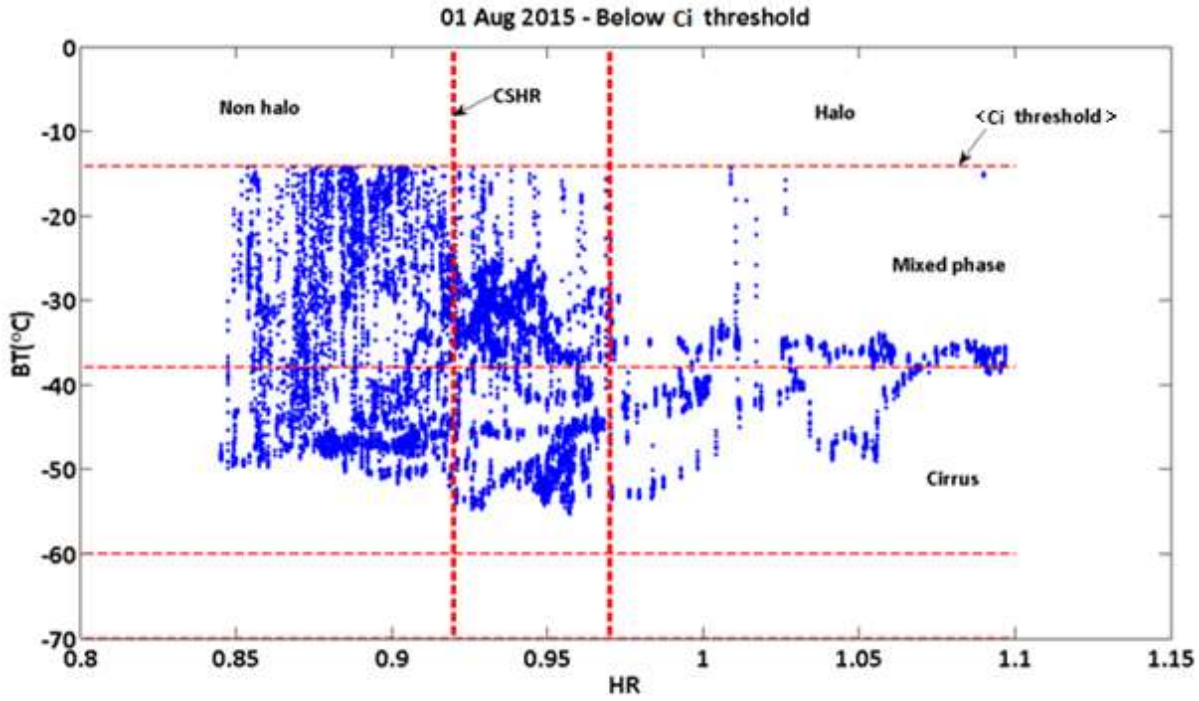

Figure 4-15: BT (warm cloud screened) vs HR scatter plot corresponding to the 1st August 2015 between 7 am and 5 pm. For the sake of completeness the horizontal red dashed lines delimiting, cirrus and mixed-phase cloud regions are based on the assumption that -38°C is the transition zone from ice to mixed-phase clouds.

4.4 HR test case: 10th-Apr-2016

On the 10th of April 2016 after an early morning of relatively clear sky (between 5 am and 7 am), cirrus occurs and persists until 5 pm (see Figure 4-16). However, this appears to be in contradiction with what both the Ci threshold method and the LIDAR quick looks suggest (see Figure 4-17 and Figure 4-18). From 1 to 5 pm in fact, BT is above the Ci threshold except between roughly 2 pm and 2:30 pm and around 3:06 pm and 3:30 pm respectively. Similarly from about 11 am till the end of the observation period the LRCBS shows presence of mid level clouds extending from 4 km to 6 km. Nevertheless the relatively large FC, which can be regarded as a measure of the spatial structure of the cloud, shows cirrus-like, fibrous structure which is likely to indicate presence of cirrus. The HR, which fluctuates mostly between 0.9 and 1 throughout the day, reaches its maximum of 1.15 at about 3:45 pm when an optically thick and relatively warm halo-producing cloud occurs (see Figure 4-19). Analogously HR relative maxima at about 3.18 pm and 1:42 pm show presence of halo producing clouds as confirmed by the All-sky images (see Figure 4-20 and Figure 4-21). This example shows that ice clouds can occur at mixed-phase temperatures, as correctly indicated by the Ci threshold method and the corresponding relatively large HR, which in fact, testifies to the presence of cloud dominated by ice.

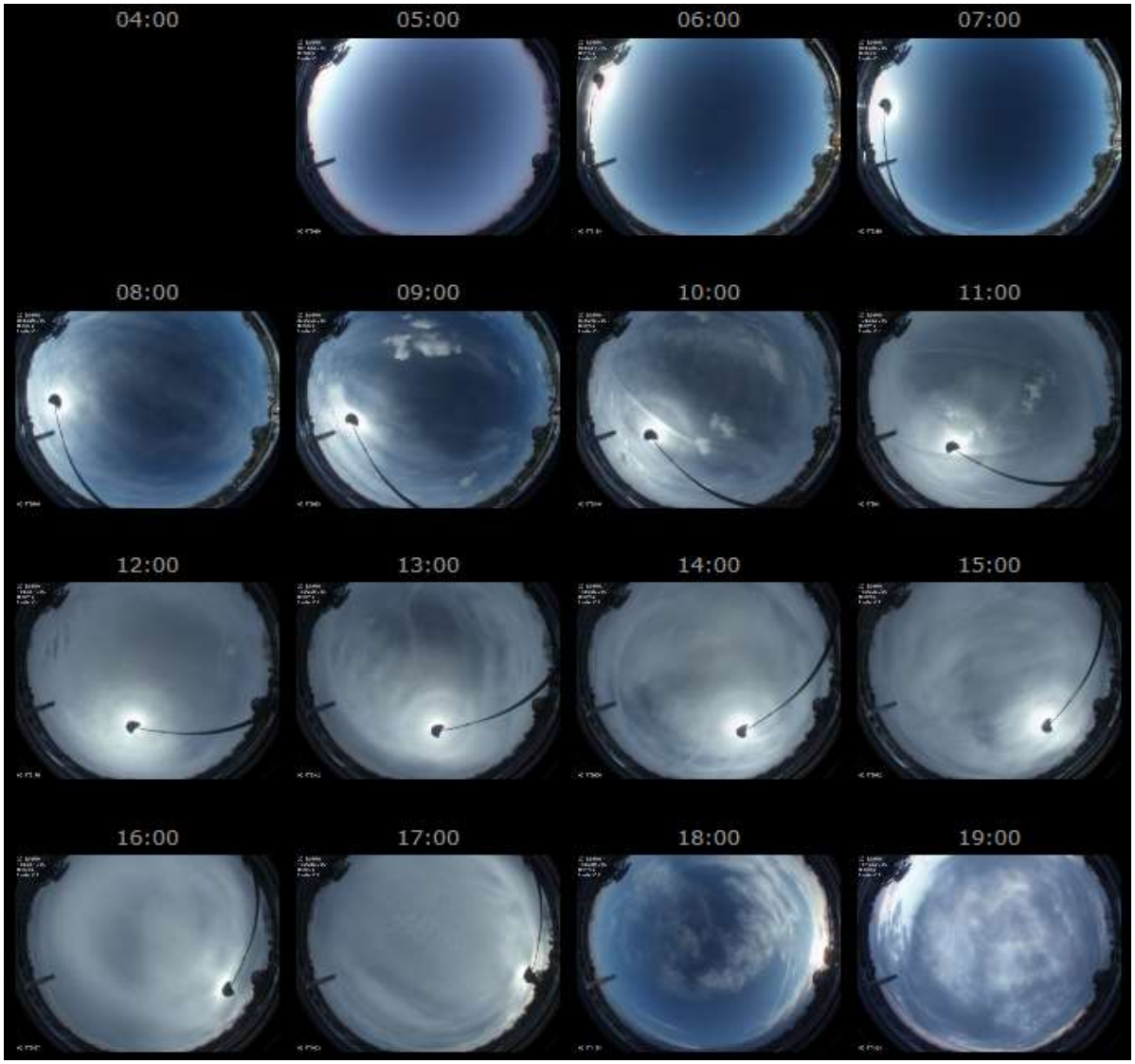

Figure 4-16: All-sky camera quick looks - 10th of April 2016 between 8 am and 4 pm.

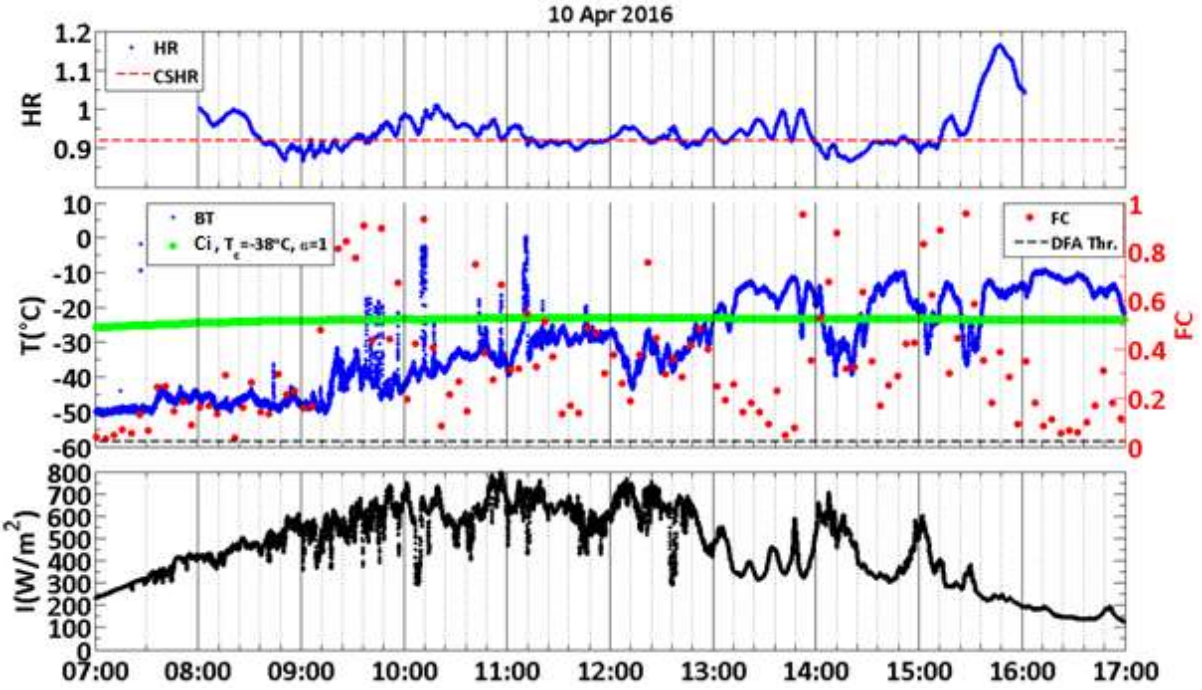

Figure 4-17: Top plot: HR time series - Middle plot: BT (blue dot), FC (red dot), DFA threshold (dashed black line), Ci threshold (green dot) time series - Bottom plot: solar irradiance time series. Data from 10th of April 2016 between 7 am and 5 pm.

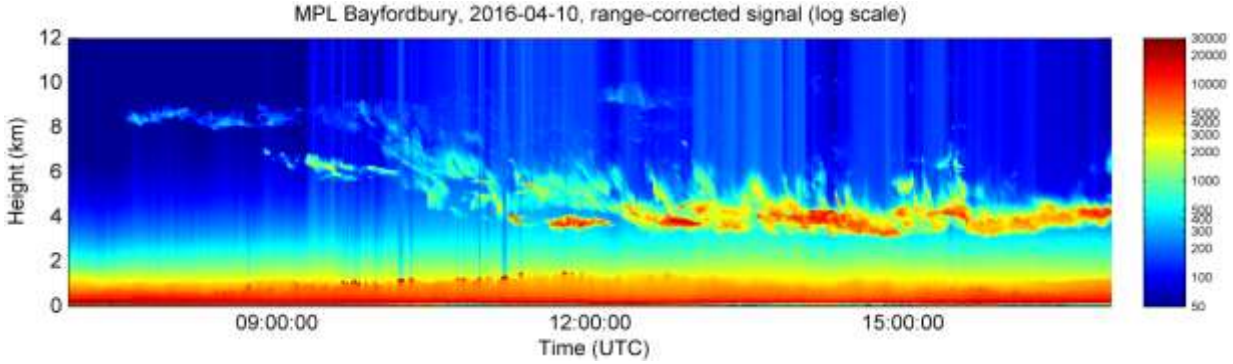

Figure 4-18: LIDAR range-corrected backscatter signal shown on log scale (*). Data from 10th of April 2015 between 7 am and 5 pm.

Figure 4-19: 10 April 2016 3:47 pm.

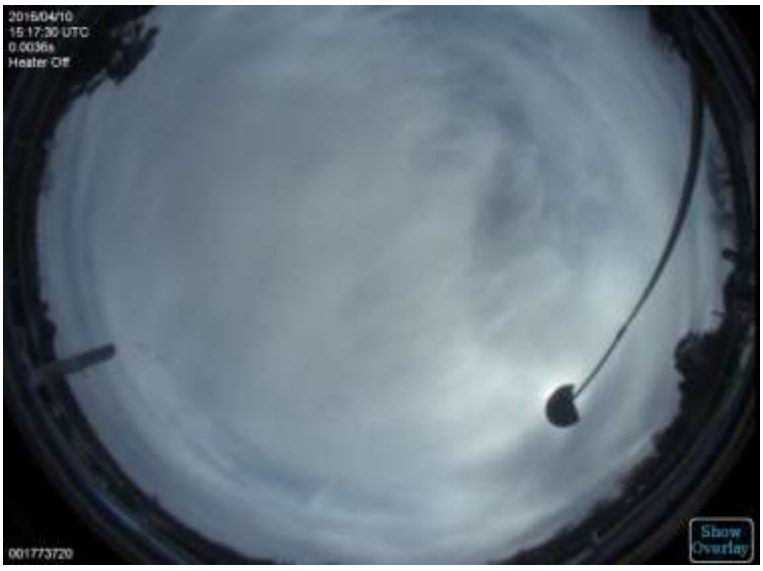

Figure 4-20: 10 April 2016 3:17 pm.

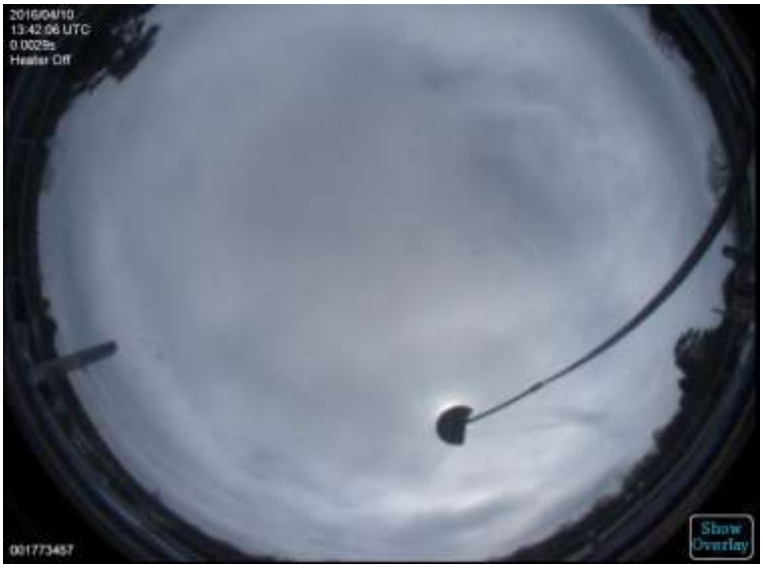

Figure 4-21: 10 April 2016 1:42 pm.

4.5 HR test case: 20th-Apr-2016

The last test case to discuss is on 20th of April 2016, a day when mostly optically thin non-halo cirrus occurs throughout the afternoon (see Figure 4-22 and Figure 4-24). After an initial phase of apparent clear sky lasting from 5 am to 7 am low level clouds occur and persist from roughly 8 am to 9 am. The latter are visible from the day time All-sky camera and from the corresponding increase in BT. Analogously the LIDAR quick look shows relatively strong LRCBS mostly originating from below 1 km. From approximately 10 am onwards thin cirrus with variable optical depth occurs and lasts till the end of the observational period. This seems to be confirmed from the All-sky images and the FC which is above the DFA threshold throughout the observation period. The gaps observed in the LRCBS between successive cirrus occurrences, which might be mistaken for clear sky, are probably ascribable to the low sensitivity of LIDAR to very thin cirrus. The HR (see Figure 4-23), quite unstable under low level clouds, shows significant fluctuations between 11 am and 12 noon and between 2 pm and 3 pm respectively, probably associated with the corresponding increase of cirrus optical depth. The HR stays mostly below CSHR throughout the duration of the observation except after 3:30 pm when relatively high values are observed. These ones are likely to be artefacts associated to the relative vicinity of the sun to the edge of the mask which, for the reasons stated in paragraph 2.10, can give rise to an unwanted plateau in the SPF located near the region from which the HR is calculated. This suggests that the current limitation to images such that that $z < 65^{o}$ and $z > 75^{o}$ might not be sufficiently stringent and should be rethought. However, if measures after 3:30 pm and between 6 am and 10 am are not accounted for, the HR spans between 0.84 and 0.94. This example and the observed range of variation of HR under halo-cirrus (from 1.1 to 0.87) and non-halo cirrus (from 1 to 0.84) suggests that CSHR cannot be taken as a simple reference threshold to establish the transition from halo to non-halo regions.

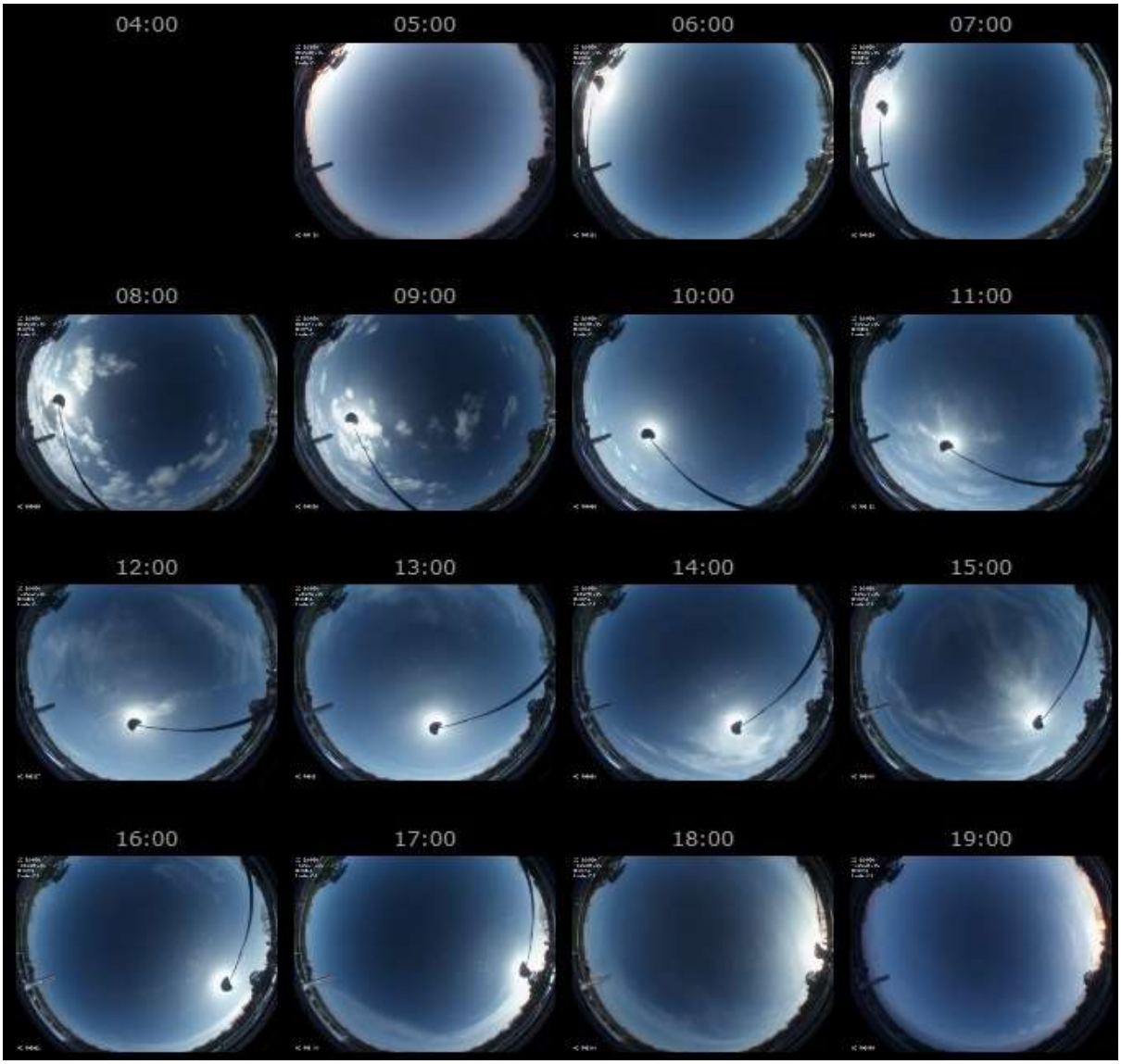

Figure 4-22: All-sky camera quick looks - 20th of April 2016 between 5 am and 7 pm.

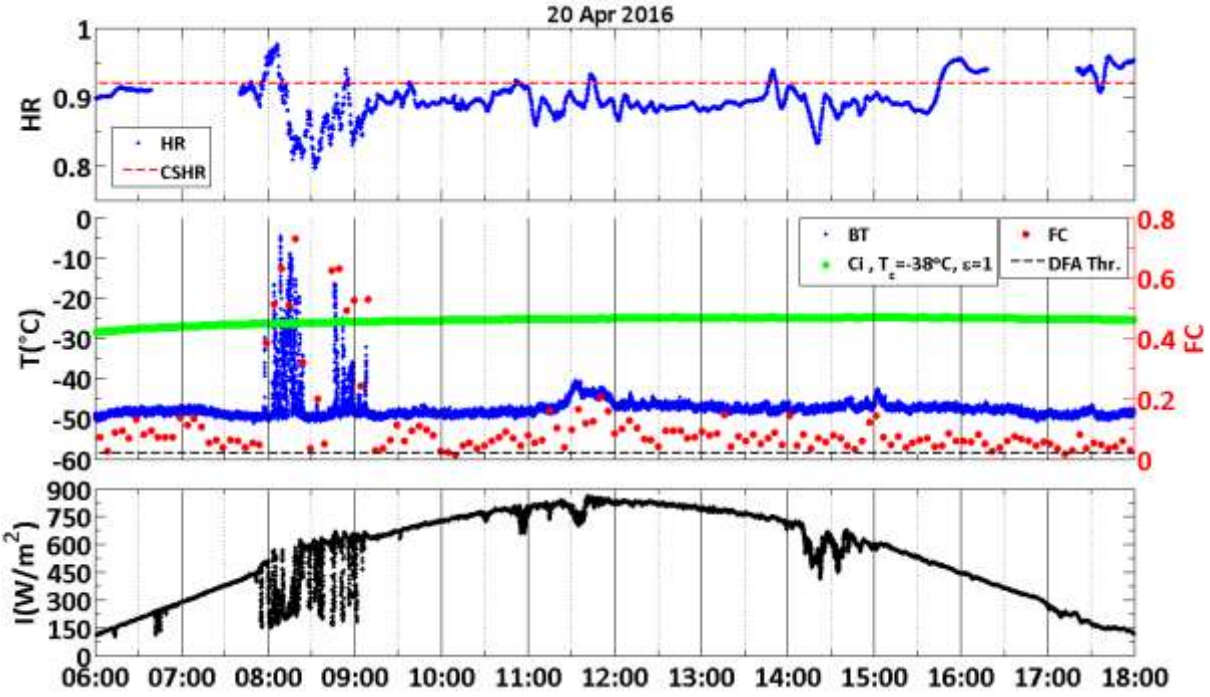

Figure 4-23: Top plot: HR time series - Middle plot: BT (blue dot), FC (red dot), DFA threshold (dashed black line), Ci threshold (green dot) time series - Bottom plot: solar irradiance time series. Data from 20th of April 2016 between 06 am and 06 pm.

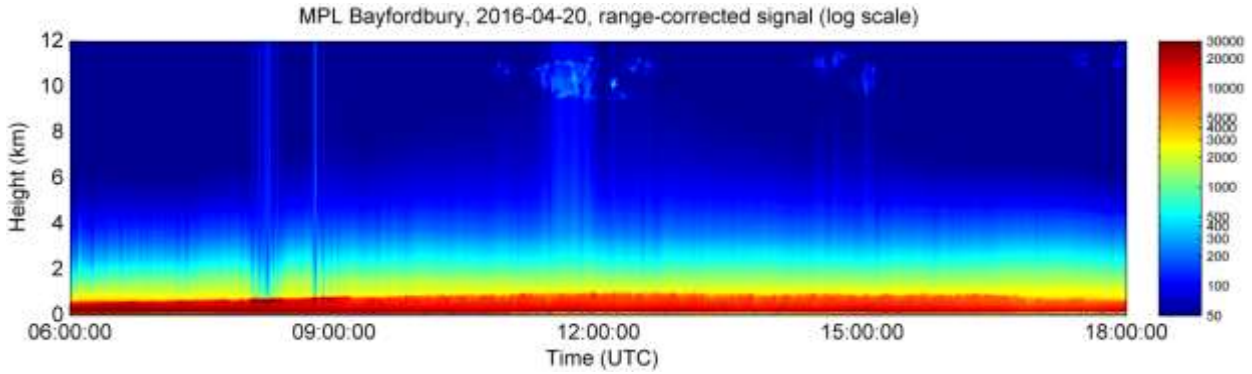

Figure 4-24: LIDAR range-corrected backscatter signal shown on log scale (*). Data from 20th of April 2015 between 6 am and 6 pm.

What we have learned from these case studies is that if on the one hand a relatively large HR (HR > CSHR) can be an indication of the presence of halo-producing cirrus, on the other hand this might not be the case as the observed artefacts, caused by the image becoming brighter at larger scattering angles, possibly associated to bright cloud edges, demonstrate. Artefacts can also be ascribable to the relative vicinity of the sun to the edge of the mask. This suggests that the current limitation to images such that that $z < 65^o$ and $z > 75^o$ might not be sufficiently stringent and should be rethought. We have also seen that ice clouds can occur at mixed-phase temperatures, as correctly indicated by the Ci threshold method and the corresponding relatively large HR, which in fact, testifies to the presence of cloud dominated by ice. The observed range of variation of HR under halo-cirrus (from 1.1 to 0.87) and non-halo cirrus (from 1 to 0.84) suggests that CSHR cannot be taken as a simple reference threshold to establish the transition from halo to non-halo regions.

However it is reasonable to expect that, the HR being an ice cloud characteristic, the screening of artefacts and non-ice cloud occurrences through the cirrus detection algorithm would lead to a better estimation of the range of variation of HR under cirrus and to reliable HR statistics.
A cirrus characterization flow chart based on the two-steps cirrus detection algorithm covered in chapter 3 and on the measure of the HR, is now proposed. The DFA algorithm is at first applied to the BT time series to detect presence of clouds, then BT is compared to the Ci threshold and lastly the HR measure is assessed. This is done for the sake of discussion and by supposing that the detection algorithm has already been tested. It should also be clear that the HR is merely meant for characterizing cirrus and is not part of the detection algorithm. Assuming that the FC > DFA threshold (0.02) and BT < Ci threshold are sufficient conditions for the occurrence of cirrus and that a reference measure to assess the halo - non halo nature of cirrus exists, two possible scenarios present themselves:

1 HR is relatively large (> HR reference threshold)

2 HR is relatively small (< HR reference threshold)

A relatively large HR suggests that halo cirrus presence is fairly likely in the first scenario while in the second one occurrence of non-halo cirrus is very probable.

4.6 Cirrus characterization flow chart

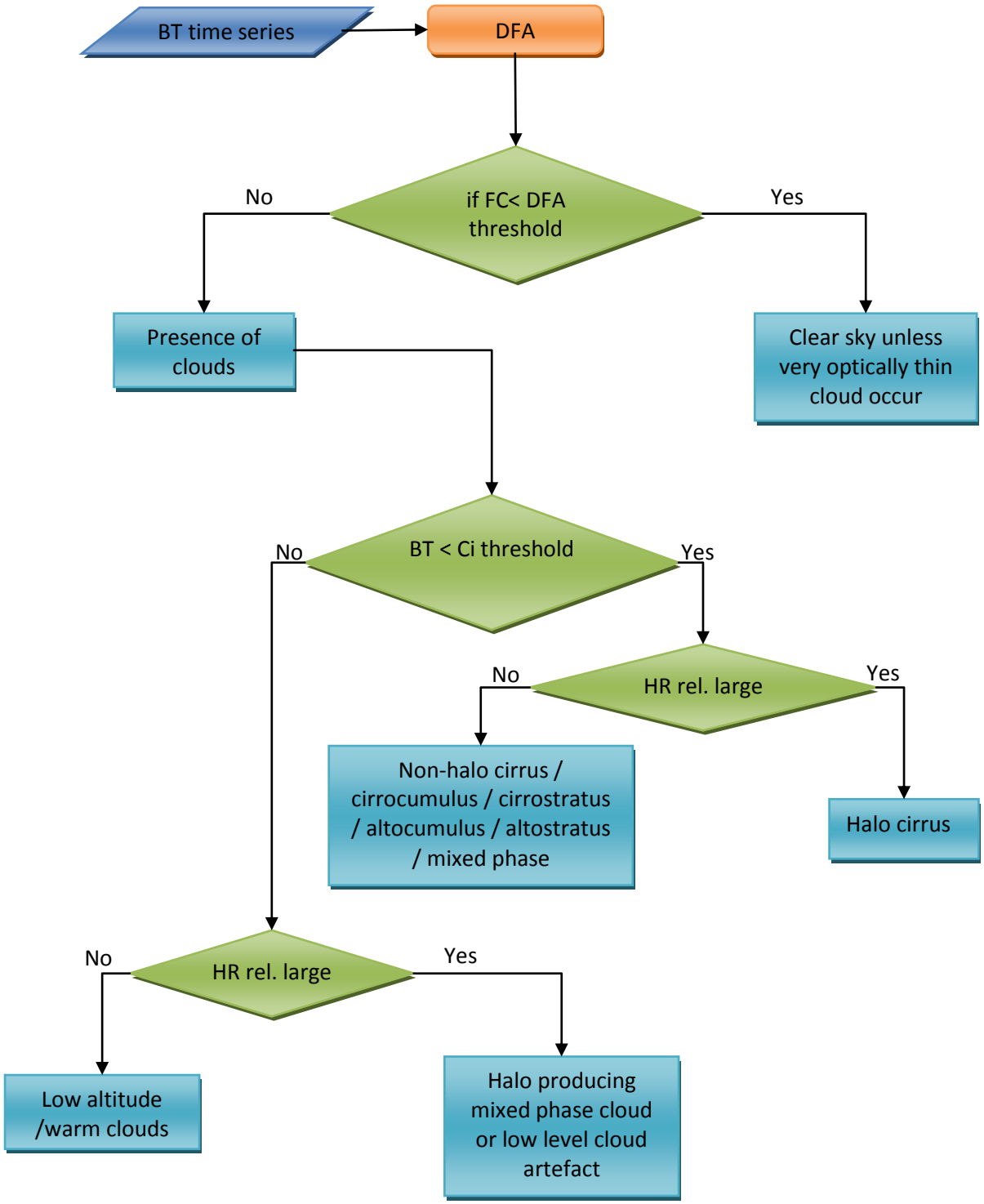

5 Conclusions

In this chapter we will first recapitulate what has been achieved through the all sky imaging and how this allows us to measure the HR. Then we will summarize the two step cirrus detection algorithm giving particular focus to the modelling of downwelling clear sky radiance, novel in the field of cloud detection to the best of my knowledge. Subsequently, suggestions for further work and where the results achieved in this investigation could lead with respect to future investigation will be given.

5.1 All sky imaging

All-sky night and day time cameras have been used for characterizing cirrus clouds. The halo ratio (HR), which is a quantitative criterion to characterize the occurrence of the 22^o halo, can be obtained from the measure of the forward scattering phase function (SPF - see paragraph 1.3) associated to ice clouds. This can be measured through All-sky imaging by averaging the image brightness over the azimuth angle in the light-source-centred system of coordinates. Here the steps which lead to obtain the forward SPF have been implemented through image processing. The initial step consists in reconstructing the image over a new system of coordinates such that the light source centre and zenith coincide. To do so, the original linear projection of the fish-eye lens, radially symmetric with respect to zenith, has to be remapped onto spherical coordinates before implementing the rotation which centres the light source at zenith. In doing so, two alternative methods, interpolation and remapping have been applied. As the corresponding performances are similar, interpolation seems to be the preferable one as it is easier to implement. Correction for the air mass contribution (which causes increased brightness towards the horizon) has also been taken into consideration. Two models have been assumed for the quantification of the air mass: the plane parallel and the radially symmetric atmosphere. The corresponding results have been compared. If on the one hand the two models match fairly well from zenith up to one degree above the horizon, on the other hand the radially symmetric atmosphere is found to be the preferable choice as it provides more realistic results for the air mass near the horizon. The last correction to have been taken into account is vignetting which affects wide field of view lenses in particular. This has been measured by comparing the sky brightness as observed through imaging and sun-photometry. A working approximation for correcting for vignetting has then been obtained and used to measure the HR whose time series have been plotted at least for a few test cases. These ones include HR time series under clear skies, low, mid and high level clouds in particular under halo and non-halo cirrus. An average HR of 0.92 has been measured over two hours of relatively clear sky when the HR is fairly stable. This fluctuates quite significantly under low level clouds exhibiting HR maxima that are mostly artefacts due to the image being brighter at larger scattering angles, possibly due to bright cloud edges. While on that, cases of scattered cumulus have not been accounted for the time being though it would be desirable to see how the HR varies in such a scenario too. HR fluctuations do attenuate under cirrus skies when the HR can span from 0.87 to 1.1 under halo cirrus and from 0.84 to 1 under non-halo cirrus. In this regard a similar spectrum of HR values has been observed under a case of mid level clouds when the HR can be as large as 1.17 if halo producing. While the HR seems to be fairly sensitive to the halo-non halo nature of cirrus an actual threshold for the transition from halo to non-halo cirrus could not be determined. However in the perspective of analysing a larger dataset, it seems plausible that a more accurate range of variation for both the halo and non-halo cirrus HR can be found. The utilization of the all sky cameras for measuring the SPF from which the HR is retrieved is a particularly novel aspect of this investigation, this has not been done previously to the best of my knowledge.

5.2 Cirrus detection algorithm

In the meantime though, a frequency distribution of HRs cannot be achieved until the performance of the two-steps cirrus detection algorithm covered in Chapter 3 is tested. The first step consists in the quantification of the brightness temperature temporal fluctuations through De-trended Fluctuation Analysis (DFA) which allows the discrimination of clouds (except when very optically thin) from clear sky. In this regard, the improvement of the initial version of the DFA algorithm has led to faster performance, a more stable DFA function and additional cloud-screening. As the second step, a simple analytical model of down-welling thermal radiation under clear skies is used to discriminate between warm and cold clouds. The method proposed here consists in estimating the departure of BT from modelled clear sky BT due to the presence of a relatively "warm" and optically thick cirrus. This allows setting a threshold which represents an estimate of the maximum departure from clear sky BT associated with "thick" cirrus. This threshold is not fixed but accounts for the atmospheric transmission associated with the atmosphere below the cloud and sets the transition BT to the liquid phase. According to our estimate it turns out that warm clouds characterized by an optical depth τ larger than 1.5 would determine a departure of BT from clear sky BT larger than the one due to the above "thick" cirrus, and would therefore lend themselves to be discriminated. Conversely, for values of τ lower than 1.5 discrimination might fail. The cirrus detection algorithm here proposed is original in that with respect to previous works (102) does not require any additional technique, such as microwave radiometry or LIDAR, to distinguish cloud phase and makes uses of a BT threshold which is not fixed but accounts for the attenuating properties of the medium below the cloud.

5.2.1 Clear sky modelling

A narrow band infrared radiation pyrometer (KT15.85 II) sensitive to a spectral band centred at about 10.6 μm, where atmospheric transmission is high, has been employed to observe down-welling irradiance represented as brightness temperature (BT). The model attempts to reproduce the observed BT. De-trended fluctuation analysis (DFA) and standard deviation (STD) of the BT data have been used to cloud-screen the data points later on used to test the model. Only those observations such that BT < -30^{o}C have been taken into account. Based only on first principles of black-body radiation, the model's fundamental assumption is that WV is the only one among the atmospheric gas species to act as absorber and emitter of thermal radiation. No other radiative contribution has been taken into consideration. Furthermore the model has been derived by using only the central wavelength of the instrument response function, assumed to be sufficiently narrow to be replaced with an impulse function. Close to ground temperature (CGT) and integrated water vapour (IWV) are two of the three parameters used. The third one is an effective water vapour absorption cross section, and this one has been fitted using observational data. CGT and IWV are measured on site by means of a weather and a GPS station, respectively. The main issue faced when testing the model is that DFA may fail in discriminating clear sky. Therefore the model has been tested over a data set which could have been partly cloud-contaminated. Further cloud screening is necessary if a more accurate estimate of the deviation of the model from clear sky BT is needed. However, the model deviation from the observed BT has been obtained for a period covering more than two years. The extreme error value can be as large as 30^{o}C. On average the RMSD is of the order of 10 ^{o}C for the basic version of the model. At present, it is not possible to associate the largest deviations to obvious external factors though several attempts have been done. All-sky cameras images have been visually inspected to spot the presence of clouds, thick aerosol or fog. Interestingly the largest underestimations of BT occur when RH is higher than 70%. When RH gets so large aerosol particles can take on water and grow into haze droplets. Met Office hourly modelled temperatures have been used to compensate either for possible temperature inversions occurring at night, or for possible increase in the PBL lapse rate taking place in the warmer hours of the day. DT and AOD have been scatter-plotted to see if a correlation exists; suggestions of the presence of a

weak negative correlation seem plausible but need to be confirmed, possibly by having recourse to further cloud-free AOD data. The overestimated influence of CGT and IWV on BT justify the modification of the analytical form of the model through the inclusion of three additional coefficients (see Eq. 3.37) which have been determined by optimizing the performance of the model in reproducing the observed BT. RMSD reduces to 7.5 ^{o}C when the optimized model is used. Ultimately a working approximation for modelling clear sky downwelling thermal radiation under clear skies has been obtained. This aspect of the work is also original in that no one, to the best of my knowledge, has ever attempted to model clear sky radiance as here proposed. Most of the attempts done in the past rely on empirical models (94) (95) (88) (96) (97) (98) meant to reproduce the down-welling long-wave irradiance under clear and cloudy skies typically by making use of temperature and or vapour pressure close to ground and by fitting the parametric coefficients appearing in the analytical form over clear sky data. The downwelling thermal radiation is then estimated through the Stephan-Boltzmann law by expressing the clear-sky apparent emissivity as function of either one screen level parameter such as water vapour density, vapour pressure, dew point temperature, air temperature or a combination of the latter and vapour pressure for instance. However, the use of such broad spectral range (1 μm < λ < 40 μm) models has the main disadvantage of being limited to the specific location. Similarly, a cloud detection algorithm (103), that uses the downwelling infrared radiance measured by a narrow-band infrared pyrometer, relies on a predicted clear-sky BT, obtained by an empirical formula as a function of surface air temperature and water vapour pressure, and on radiative transfer calculations which use temperature and humidity profiles as input. The novelty of our method lies in the fact that the model is not location dependent, does not require detailed knowledge of the atmosphere, like temperature and water vapour mixing ratio profiles, and does not rely on full radiative transfer simulations.

5.3 Further work

5.3.1 Suggestions for clear sky modelling improvement

Improving our ability to model atmospheric radiation under clear skies would lead to a better estimate of cloud temperature in particular when cloud emissivity is known (i.e. in practice optically thick clouds) and to a better estimate of the cirrus threshold. In order to improve the model performance in simulating BT some potential solutions can be proposed. Alternative analytical expressions to the impulse function used to simulate the radiometer response function could be considered. A window function for instance centred around the nominal central wavelength 10.6 μm could be used together with the integration method (170) suggested at the end of section 3.6.1. The integration could be done to the level of accuracy needed as demonstrated in section 6.3 of the appendix. It is reasonable to think that accounting for a set of wavelengths in addition to the central one and doing the corresponding integration of Eq. 3.15 could lead to a further reduction of the modelled temperature errors, but this is just a hypothesis which has to be verified. Further cloud-screened AOD data could be used to establish whether the existence of negative correlation between DT and AOD as suggested by the data (see Figure 3-62) is genuine. Higher resolution modelled air temperatures could be used in place of CGT. These could be provided by the Met Office and obtained through their operational 1.5 km configuration Unified Model. Also, possible corrections for RH which have not been taken into account for the time being should be further investigated.

5.3.2 Cirrus detection validation

The cirrus detection method has not been validated yet. We propose the validation of the "thick" cirrus threshold method by means of either microwave radiometry, which can be used to measure integrated liquid water, or through LIDAR which allows the retrieval of cloud height, and indirectly

cloud temperature if assumptions of the lapse rate are made. The testing of the detection algorithm could be carried out simultaneously to the measurement of the HR over an extended observational period. Once cirrus occurrences are available the corresponding cirrus HR time series will be selected.

5.4 Application and further prospects

The combined use of the cirrus detection algorithm and the HR retrieval from all sky imaging will allow us to obtain HR statistics. This could be combined with simultaneous and independent measures of ice crystal size, shape, roughness and *g*. Microphysical and optical parameters can be retrieved from in-situ or remote sensing observations: cloud probes of the SID type can be used to retrieve 2D scattering patterns containing information about crystal size, shape and roughness (82); LIDAR linear depolarization ratios are sensitive to particle shape (8); the asymmetry parameter can be retrieved by looking for the closest fit of simulated cirrus reflectance to satellite observations of cirrus polarized reflectance (182); it can also be inferred from Polar Nephelometer measurements (80) or with radiative transfer models from measured cirrus microphysics and shortwave radiative flux profiles (183). The automatic method discussed in this work for the retrieval of a HR statistics could lead, in the context of the current research about cirrus, to further constrain the optical and microphysical properties of ice clouds which are still poorly understood.

6 Appendix

6.1 Radiance

Let us consider a monochromatic, mono-directional, uniform beam of light. To measure the amount of radiant energy transported by the beam, let us imagine a surface *A* placed in the beam with the normal to it parallel to the beam (see Figure 6-1).

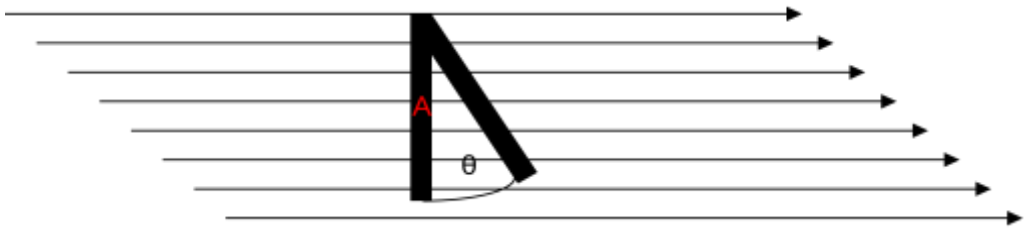

Figure 6-1: The rate at which radiant energy is transported across an area A in a mono-directional radiation field depends on the orientation of A (86).

If N_0 is the number of photons traversing *A* per unit time, by multiplying it by the photon energy and dividing by *A* we get the total radiant energy traversing *A* per unit time and surface. This quantity would not only be a property of the radiation field but also of the orientation of *A*. Let us tilt *A* so that its normal makes an angle ϑ with the beam. Let *N* be the number of photons crossing *A* per unit time under this new orientation.
It results that:

$$N_0 \cos\vartheta = N \tag{6.1}$$

From which it follows:

$$\frac{N_0}{A} = \frac{N}{A\cos\theta} \tag{6.2}$$

The right hand side of Eq. 6.2 is a property solely of the radiation field.
Let *A* be the planar and sensitive surface of our radiation detector hit by radiant flux *R* coming from direction *Ω* (see Figure 6-2)

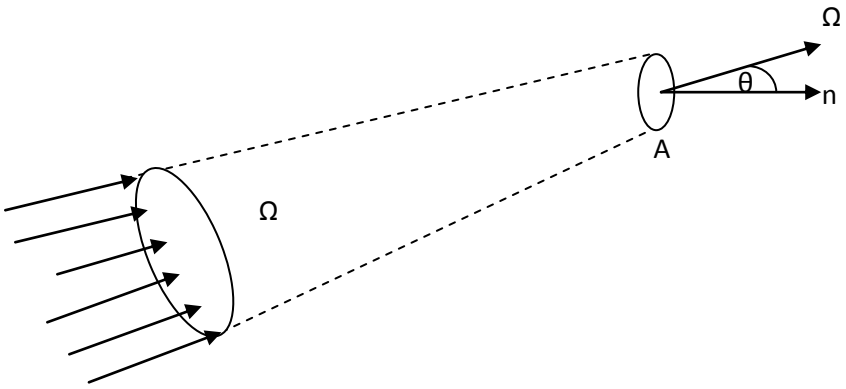

Figure 6-2: Radiant energy *R(A,Ω,Δω,Δt)*, confined to a solid angle *Ω* around the direction *Ω*, is incident on a detector with area *A*. The unit vector n is normal to *A* (86).

R is defined by its integral properties, and in general depends on position, direction, frequency, and time, so we sometimes write it as *R(x,Ω, ω, t)* to explicitly indicate these dependencies. Consider *A* at any point in space be planar, a set of directions with solid angle *Ω*, a set of frequencies between ω_1 and ω_2, and a time interval between t_1 and t_2. The total amount of radiant energy confined to this set of frequencies and directions, and crossing this surface in the specified time interval is given by Eq. 6.3

$$\int_{t_1}^{t_2}\int_{\omega_1}^{\omega_2}\int_{A}\int_{\Omega} R(x,\Omega,\omega,t)\cos\theta\cdot d\Omega\cdot dA\cdot d\omega\cdot dt \tag{6.3}$$

With respect to the zenith pointing layout of KT15.85 the term "cosϑ" is 1. The down-welling radiant flux observed by KT15.85 is the result of an integration over the instrument sensitivity spectrum, over the solid angle *Ω* subtended by its field of view and over the area *A* of its sensitive detector. The dimensions of *R* as defined in Eq. 1.41 is power per unit area, solid angle, frequency. This is generally referred to as spectral radiance and found in literature as R_λ, R_ω, R_ν. The total radiance is the integration of the spectral radiance over a finite spectral range. From the mean value theorem applied to multiple integrals it is possible to rewrite Eq. 6.3 as

$$\underline{R}\cdot\underline{\cos\vartheta}\cdot\Omega\cdot A\cdot\Delta\omega\cdot\Delta t \tag{6.4}$$

where $\underline{R}$ and $\underline{\cos\vartheta}$ indicate some value of *R* and cosϑ over the domain of integration, $\Delta\omega = \omega_2 - \omega_1$, and $\Delta t = t_2 - t_1$. Equation 6.4 provides a means by which we can (in principle) measure the radiance at a point and in a particular direction. Let us assume to have a detector with area *A* at the point where *R* is to be measured (see Figure 6-2). The detector is collimated in that it receives radiation only over a set of directions with solid angle *Ω*, around some direction *Ω*, and is equipped with a filter that passes only radiation in some frequency interval *Δω*. If we measure the total radiant energy *E(A,Ω,Δω,Δt)* received by this detector over some time interval *Δt* and then divide this energy by *A* cosϑ *Ω Δω Δt* estimate for *R* is obtained (*A* can be oriented relative to *Ω* so that cosϑ has the limiting value 1 as *Ω* shrinks.). If we now consider the quotient

$$\frac{E(A,\Omega,\Delta\omega,\Delta t)}{A\cdot\cos\theta\cdot\Omega\cdot\Delta\omega\cdot\Delta t} \tag{6.5}$$

and decrease the values of *A*, *Ω*, *Δω*, and *Δt* until it no longer changes, as any fractional change in either *A*, *Ω*, *Δω*, or *Δt* leads to the same fractional change in *E(A,Ω,Δω,Δt)*, we obtain a radiation field uniform over the geometric quantities *A* and *Ω* and the intervals *Δt* and *Δω*. The quotient so obtained is *R* at space point *x*, in the direction *Ω*, for frequency *ω*, at time *t* (86).

6.2 Scattering by molecules

Charges in matter are acted on by electromagnetic fields. When radiation acts on molecules the charges which constitute the molecules oscillate changing the field they are acted on by. This change is transmitted outwards in the form of secondary waves. In the dipole approximation of a molecule, if the *radiative reaction* which is another dissipative term accounting for the loss of energy by radiating is taken into account, it can be shown that the time-averaged rate at which work is done on the dipole by the incident field is the contribution due to absorption plus scattering.

$$\langle P\rangle = \langle P_a\rangle + \langle P_s\rangle \tag{6.6}$$

where:

$$\langle P_a \rangle = \frac{e^2}{2m} E_0^2 \frac{\omega^2 \gamma_a}{\left(\omega_0^2 - \omega^2\right)^2 + \gamma^2 \omega^2} \tag{6.7}$$

$$\langle P_s \rangle = \frac{e^2}{2m} \frac{E_0^2}{\omega_0^2} \frac{\omega^4 \gamma_s}{\left(\omega_0^2 - \omega^2\right)^2 + \gamma^2 \omega^2} \tag{6.8}$$

$$\gamma = \gamma_a + \gamma_s \frac{\omega^2}{\omega_0^2} \tag{6.9}$$

and where:

1. **γ_a is the dissipation term**
2. **γ_s is the radiative reaction**

Unlike absorption scattering does not imply a transformation of radiant energy into other forms. Scattering is a redistribution of the incident radiation into different directions. Energy is conserved. Because molecules are in motion there is not pure elastic scattering in nature. The radiation reemitted is always Doppler-shifted. When the resonant frequency ω_0 is much larger than the frequency ω of the emitted field Eq. 6.8 reduces to the Rayleigh's scattering regime:

$$\langle P_s \rangle \approx \frac{e^2}{2m} \frac{E_0^2}{\omega_0^6} \gamma_s^2 \omega^4 \tag{6.10}$$

This is only an approximation and is only valid when the frequency of the incident radiation is far from the resonant frequency. Also Eq. 6.7 and 6.8 show that absorption and scattering are related to each other in fact if the dissipative factor changes so does the reaction term and the other way around. Analogously to what done for the absorption cross section the scattering cross section of a molecule is defined as:

$$\langle P_s \rangle = W_s = \sigma_s I \tag{6.11}$$

Where W_s is the power scattered over all directions by the molecule and I is the incident irradiance.
It should be pointed out that unlike the absorption the scattering cross section depends on the direction and given the scatterer size relative to the wavelength it can be highly asymmetric.

6.3 Integration of Plack's distribution

6.3.1 Integration step1: the change of variable (from *ω* to *x=h ω/2πk T*)

$$\int_{\omega_1}^{\omega_2} \frac{\hbar \cdot \omega^3}{4\pi^2 c^2} \frac{1}{\exp\left(\frac{\hbar\omega}{k_B \cdot T}\right) - 1} d\omega$$

$$\frac{\hbar\omega}{k_B \cdot T} = x \Rightarrow \quad dx = \frac{\hbar}{k_B \cdot T} d\omega \tag{6.12}$$

$$\int_{x_1}^{x_2} \frac{\hbar \cdot \frac{x^3 (k_B \cdot T)^3}{\hbar^3}}{4\pi^2 c^2} \frac{1}{\exp(x) - 1} \frac{k_B \cdot T}{\hbar} dx =$$

$$= \frac{(k_B \cdot T)^4}{4\pi^2 c^2 \hbar^3} \int_{x_1}^{x_2} \frac{x^3}{\exp(x) - 1} dx$$

6.3.2 Integration step2: expanding the integrand as a series of functions

$$\int_{x_1}^{x_2} \frac{x^3}{\exp(x)-1}\,dx$$

$$\frac{1}{\exp(x)-1} = \frac{\exp(-x)}{1-\exp(-x)} = \exp(-x)\cdot\frac{1}{1-\exp(-x)} =$$

$$= \exp(-x)\cdot\sum_{n=0}^{\infty}\exp(-nx) = \sum_{n=1}^{\infty}\exp(-nx) \Rightarrow \tag{6.13}$$

$$\Rightarrow \int_{x_1}^{x_2} \frac{x^3}{\exp(x)-1}\,dx = \int_{x_1}^{x_2} x^3\sum_{n=1}^{\infty}\exp(-nx)dx =$$

$$= \sum_{n=1}^{\infty}\int_{x_1}^{x_2} x^3\exp(-nx)dx$$

6.3.3 Integration step3: Integration by parts

$$\int_{x_1}^{x_2} x^3\exp(-nx)dx = x^3\left(\frac{-\exp(-nx)}{n}\right) - \frac{1}{n}\int_{x_1}^{x_2} 3x^2\left(-\exp(-nx)\right)dx =$$

$$= x^3\left(\frac{-\exp(-nx)}{n}\right)_{x_1}^{x_2} - \frac{1}{n^2}\left[3x^2\exp(-nx)_{x_1}^{x_2} - \int_{x_1}^{x_2} 6x\exp(-nx)dx\right] =$$

$$= x^3\left(\frac{-\exp(-nx)}{n}\right)_{x_1}^{x_2} - 3x^2\left(\frac{\exp(-nx)}{n^2}\right)_{x_1}^{x_2} + \frac{1}{n^3}\left[-6x\exp(-nx)_{x_1}^{x_2} + \int_{x_1}^{x_2} 6\exp(-nx)dx\right] = \tag{6.14}$$

$$= x^3\left(\frac{-\exp(-nx)}{n}\right)_{x_1}^{x_2} - 3x^2\left(\frac{\exp(-nx)}{n^2}\right)_{x_1}^{x_2} - 6x\left(\frac{\exp(-nx)}{n^3}\right)_{x_1}^{x_2} + \frac{1}{n^3}\int_{x_1}^{x_2} 6\exp(-nx)dx =$$

$$= \left[x^3\left(\frac{-\exp(-nx)}{n}\right) - 3x^2\left(\frac{\exp(-nx)}{n^2}\right) - 6x\left(\frac{\exp(-nx)}{n^3}\right) - \frac{6}{n^4}\exp(-nx)\right]_{x_1}^{x_2}$$

6.3.4 Integration step4

From the integration step 1 follows:

$$\frac{(k_B \cdot T)^4}{4\pi^2 c^2 \hbar^3} \sum_{n=1}^{\infty} \int_{x_1}^{x_2} x^3 \exp(-nx) dx =$$
$$= \frac{(k_B \cdot T)^4}{4\pi^2 c^2 \hbar^3} \sum_{n=1}^{\infty} \left(\exp(-nx_1) \left(\frac{x_1^3}{n} + \frac{3x_1^2}{n^2} + \frac{6x_1}{n^3} + \frac{6}{n^4} \right) - \exp(-nx_2) \left(\frac{x_2^3}{n} + \frac{3x_2^2}{n^2} + \frac{6x_2}{n^3} + \frac{6}{n^4} \right) \right) \quad (6.15)$$

6.3.5 Integration steps: the total irradiance

Based on the above calculations, and on the assumption that cloud emission and HO_2 absorption cross section might be considered for the moment independent from the wavelength (which is a gross simplification), Eq. 3.22 reduces to Eq. 6.16 if reflected ground radiation is neglected for the time being:

$$I = \left(1 - \exp\left(-3.3 \cdot 10^{22} \cdot d \cdot \sigma_a\right)\right) \frac{(k_B \cdot T_A)^4}{4\pi^2 c^2 \hbar^3} \cdot$$
$$\cdot \sum_{n=1}^{\infty} \left(\exp(-nx_{A1}) \left(\frac{x_{A1}^3}{n} + \frac{3x_{A1}^2}{n^2} + \frac{6x_{A1}}{n^3} + \frac{6}{n^4} \right) - \exp(-nx_{A2}) \left(\frac{x_{A2}^3}{n} + \frac{3x_{A2}^2}{n^2} + \frac{6x_{A2}}{n^3} + \frac{6}{n^4} \right) \right) +$$
$$+ \left(1 - \exp(-\tau_a)\right) \cdot (1 - r) \cdot \exp\left(-3.3 \cdot 10^{22} \cdot d \cdot \sigma_a\right) \frac{(k_B \cdot T_{IC})^4}{4\pi^2 c^2 \hbar^3} \cdot \quad (6.16)$$
$$\cdot \sum_{n=1}^{\infty} \left(\exp(-nx_{IC1}) \left(\frac{x_{IC1}^3}{n} + \frac{3x_{IC1}^2}{n^2} + \frac{6x_{IC1}}{n^3} + \frac{6}{n^4} \right) - \exp(-nx_{IC2}) \left(\frac{x_{IC2}^3}{n} + \frac{3x_{IC2}^2}{n^2} + \frac{6x_{IC2}}{n^3} + \frac{6}{n^4} \right) \right)$$

Where

$$x_{A1} = \frac{\hbar\omega_1}{kT_A} \quad x_{A2} = \frac{\hbar\omega_2}{kT_A} \quad T_A = AirT$$
$$x_{IC1} = \frac{\hbar\omega_1}{kT_{Ic}} \quad x_{IC2} = \frac{\hbar\omega_2}{kT_{Ic}} \quad T_{IC} = IcecloudT \quad (6.17)$$

Despite the fact that the summation is over an infinite number of terms, these series of functions quickly converge if the parameter $x=h\omega/2\pi kT$ is greater than 4 (170).
Fortunately, over the range of meteorological temperatures (200 K < T <300 K) and over the atmospheric window (8 μm < λ < 12 μm) x ranges from 4 to 9 (see Figure 6-3).

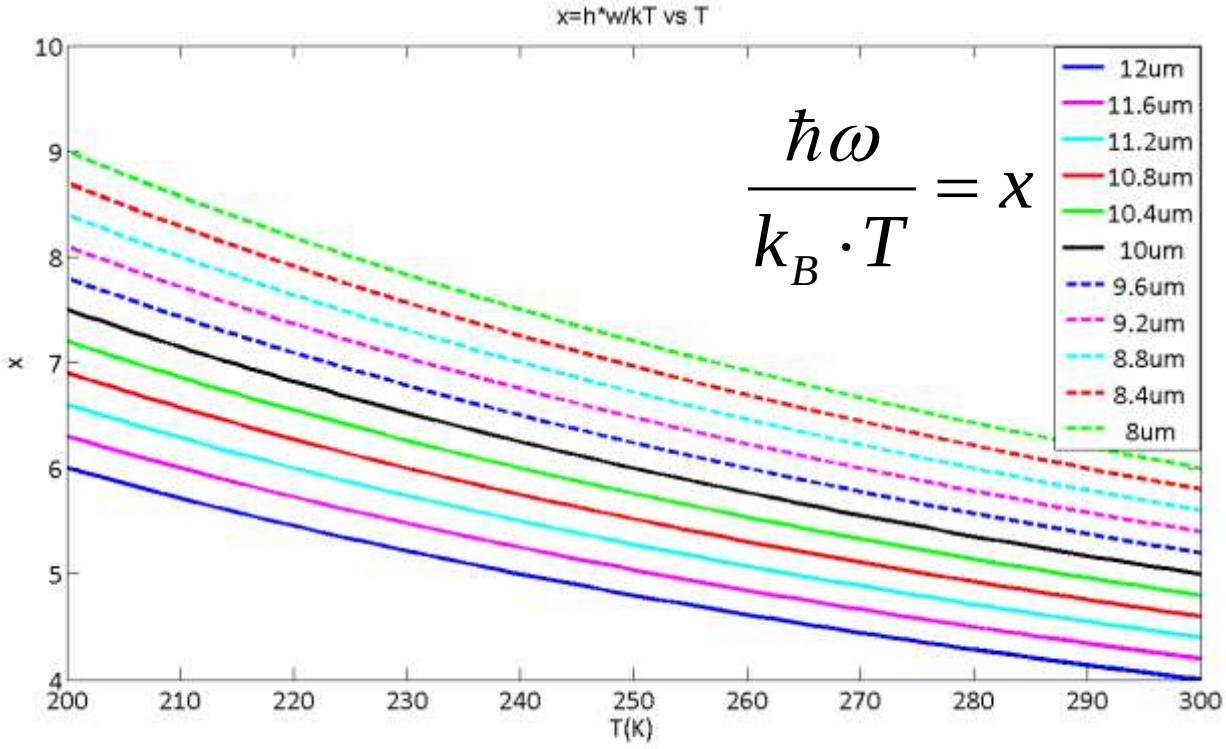

Figure 6-3: X parameter as function of meteorological temperatures and wavelength.

Eq. 6.16, apart from multiplicative factors, is the sum of the series S_1, S_2, S_3 , S_4 which are defined as follows:

$$\begin{aligned} S_1 &= \sum_{n=1}^{\infty}\left(\frac{\exp(-nx)}{n}\right) \\ S_2 &= \sum_{n=1}^{\infty}\left(\frac{\exp(-nx)}{n^2}\right) \\ S_3 &= \sum_{n=1}^{\infty}\left(\frac{\exp(-nx)}{n^3}\right) \\ S_4 &= \sum_{n=1}^{\infty}\left(\frac{\exp(-nx)}{n^4}\right) \end{aligned} \qquad (6.18)$$

Let us see the behaviour of S_j(j=1:4) with respect to the parameter *x*: the first thing to notice is that among the S_j the one whose terms tend to zero slowest is S_1 as it is the one which has the denominator with the lowest power of *n*. This implies that if S_1 converges within the first *N* terms so certainly S_j (for j=2:4) will do.

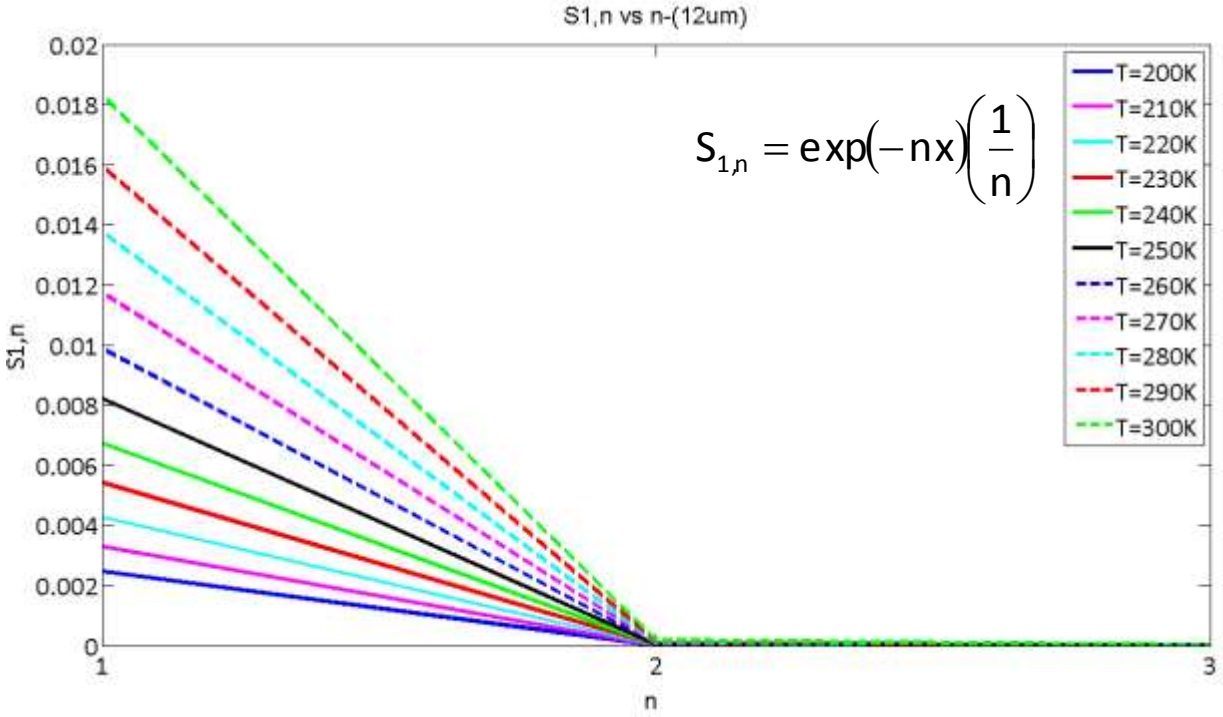

Figure 6-4: $S_{1,n}$ vs n (λ=12µm).

Notice how for higher T the *x* parameter decreases and this slows down the convergence of the series. In analogous way, the higher the wavelength *λ* the lower the parameter *x* is, and again, the convergence rate of the terms $S_{1,n}$ gets slower (see Figure 6-4 and Figure 6-5 for comparison).

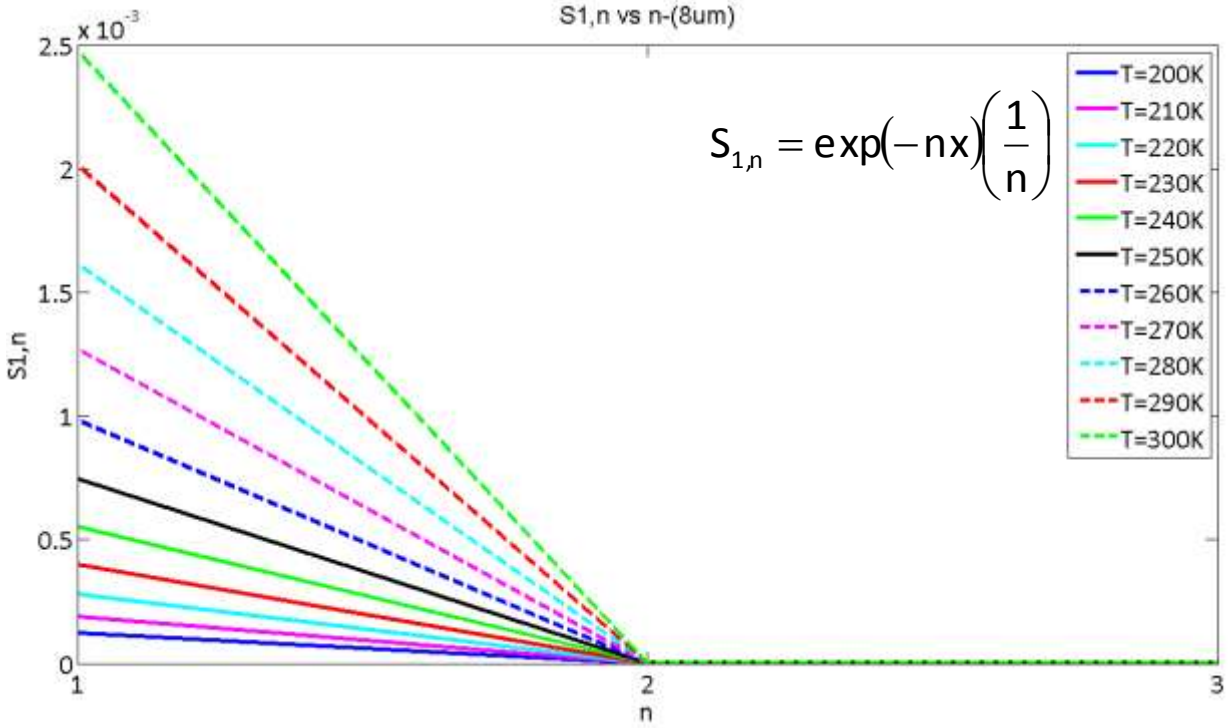

Figure 6-5: $S_{1,n}$ vs n (λ=8µm).

6.3.6 To what term do we truncate the series?

To establish to which term to truncate S_1 we should first set the accuracy that we want to achieve. Let us assume for the moment that we want to truncate our series when the $S_{1,n}$ term becomes zero to the tenth significant digit.
When the parameter *x* is minimum (for T=300K and λ=12µm), S_1 converges to zero more slowly than $S_{j,n}$ for j=2,3,4.

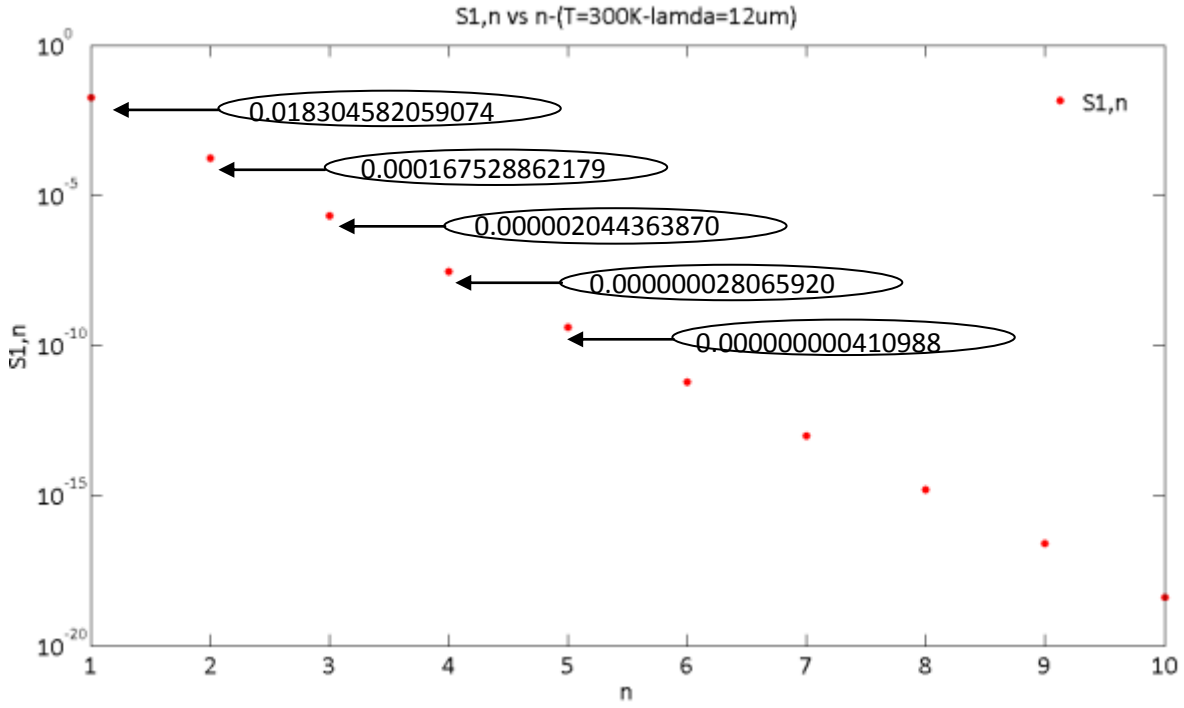

Figure 6-6: $S_{1,n}$ vs n (T=300K, λ=12µm)

Eq. 6.16 could then be truncated to *N*=5 to get to the accuracy of the tenth significant digit, being sure that $S_{j,n}$ for j=2,3,4 will necessarily be smaller than $S_{1,n}$ (zero for digits higher than 10). Eq. 6.16 would reduce to Eq. 6.19 shown as follows.

$$
\begin{aligned}
I = {} & \left(1-\exp\left(-3.3\cdot 10^{22}\cdot d\cdot \sigma_a\right)\right)\frac{\left(k_B\cdot T_A\right)^4}{4\pi^2 c^2 \hbar^3}\cdot \\
& \cdot\sum_{n=1}^{N}\left(\exp\left(-n x_{A1}\right)\left(\frac{x_{A1}^{\ 3}}{n}+\frac{3x_{A1}^{\ 2}}{n^2}+\frac{6x_{A1}}{n^3}+\frac{6}{n^4}\right)-\exp\left(-n x_{A2}\right)\left(\frac{x_{A2}^{\ 3}}{n}+\frac{3x_{A2}^{\ 2}}{n^2}+\frac{6x_{A2}}{n^3}+\frac{6}{n^4}\right)\right)+ \\
& +\left(1-\exp\left(-\tau_a\right)\right)\cdot(1-r)\cdot\exp\left(-3.3\cdot 10^{22}\cdot d\cdot \sigma_a\right)\frac{\left(k_B\cdot T_{IC}\right)^4}{4\pi^2 c^2 \hbar^3}\cdot \\
& \cdot\sum_{n=1}^{N}\left(\exp\left(-n x_{IC1}\right)\left(\frac{x_{IC1}^{\ 3}}{n}+\frac{3x_{IC1}^{\ 2}}{n^2}+\frac{6x_{IC1}}{n^3}+\frac{6}{n^4}\right)-\exp\left(-n x_{IC2}\right)\left(\frac{x_{IC2}^{\ 3}}{n}+\frac{3x_{IC2}^{\ 2}}{n^2}+\frac{6x_{IC2}}{n^3}+\frac{6}{n^4}\right)\right)
\end{aligned}
\tag{6.19}
$$

6.4 Matlab scripts - flow diagrams

6.4.1 Geometric correction - Remapping

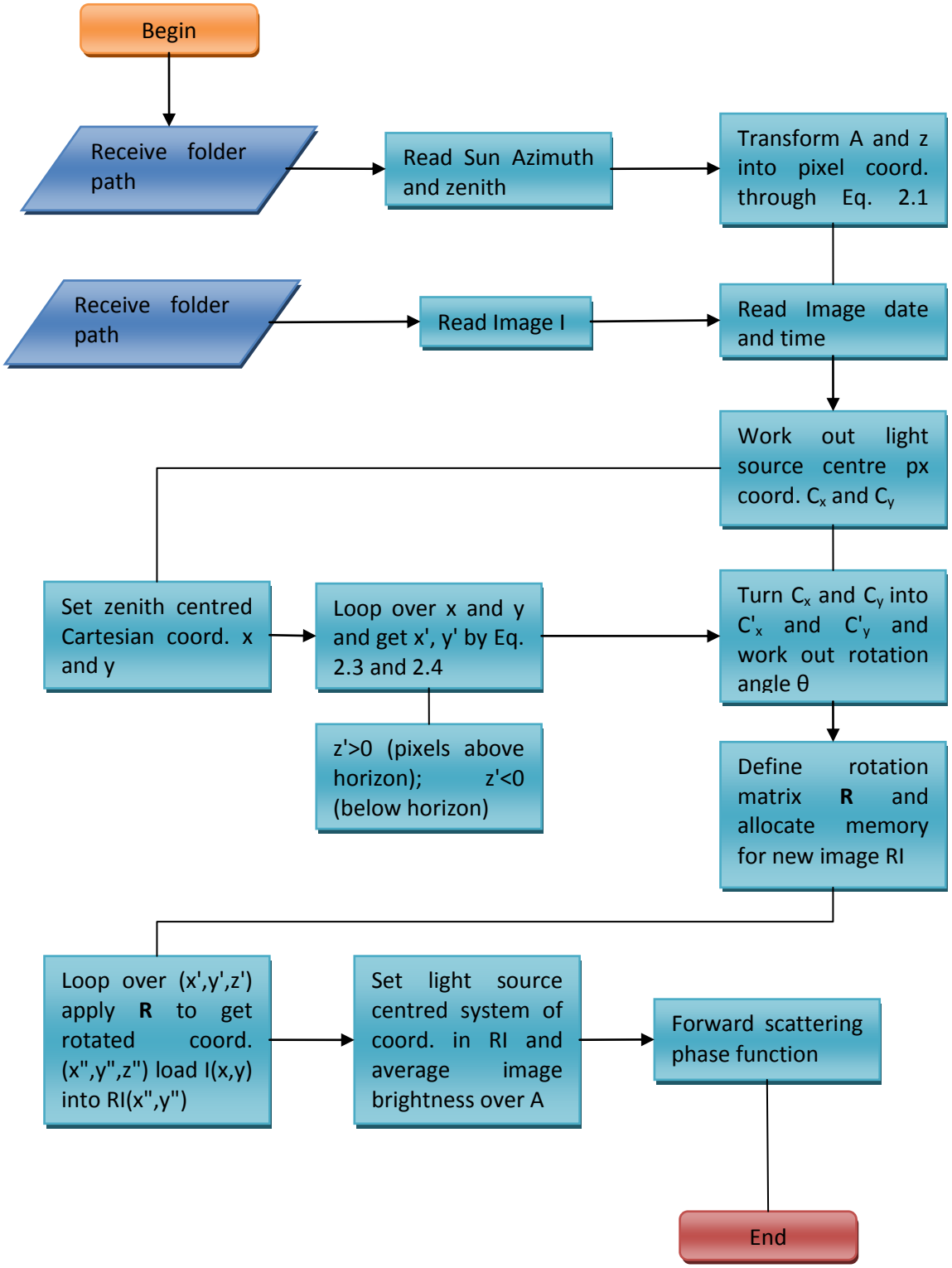

6.4.2 Geometric correction - Interpolation

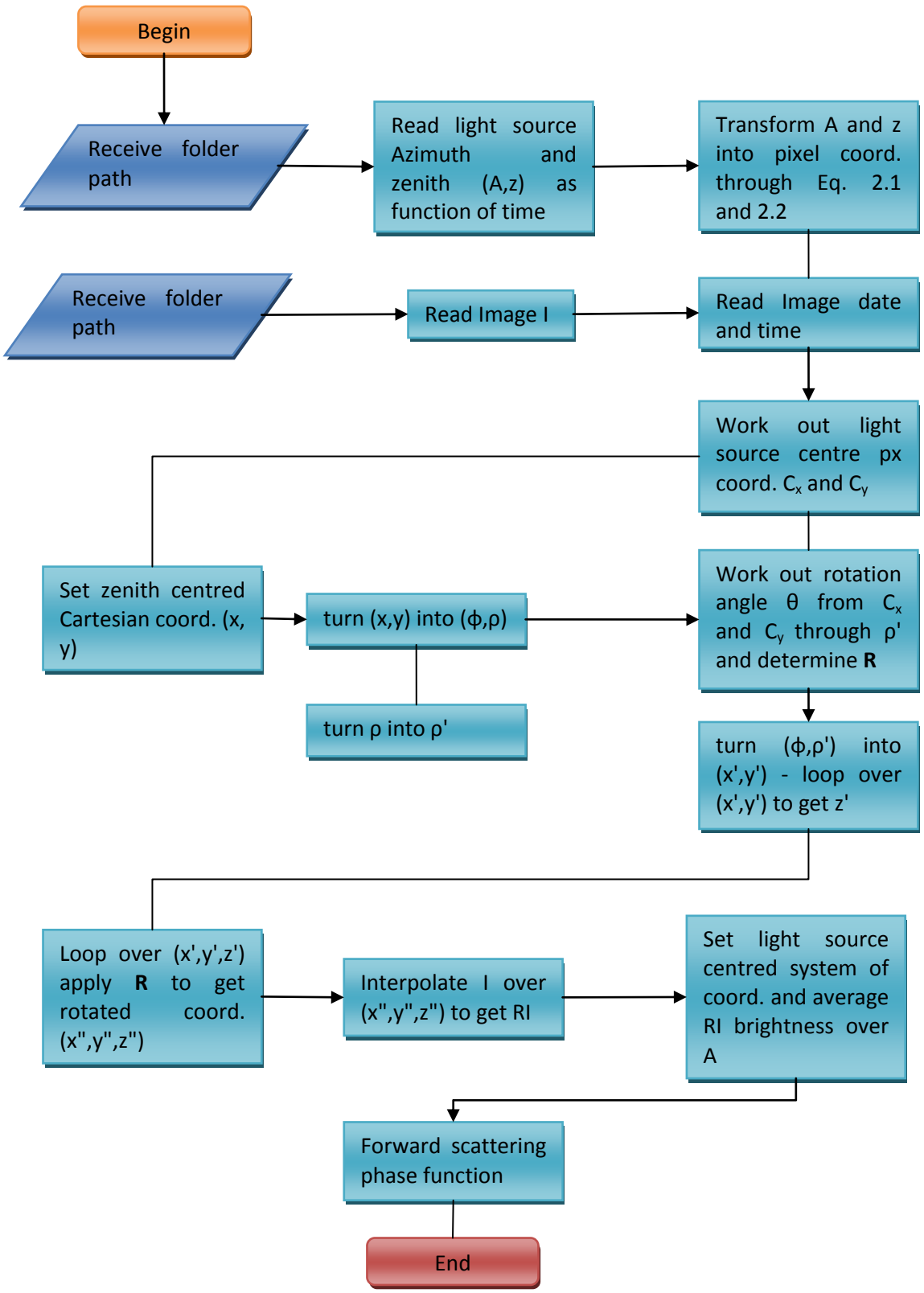

6.4.3 AM Correction

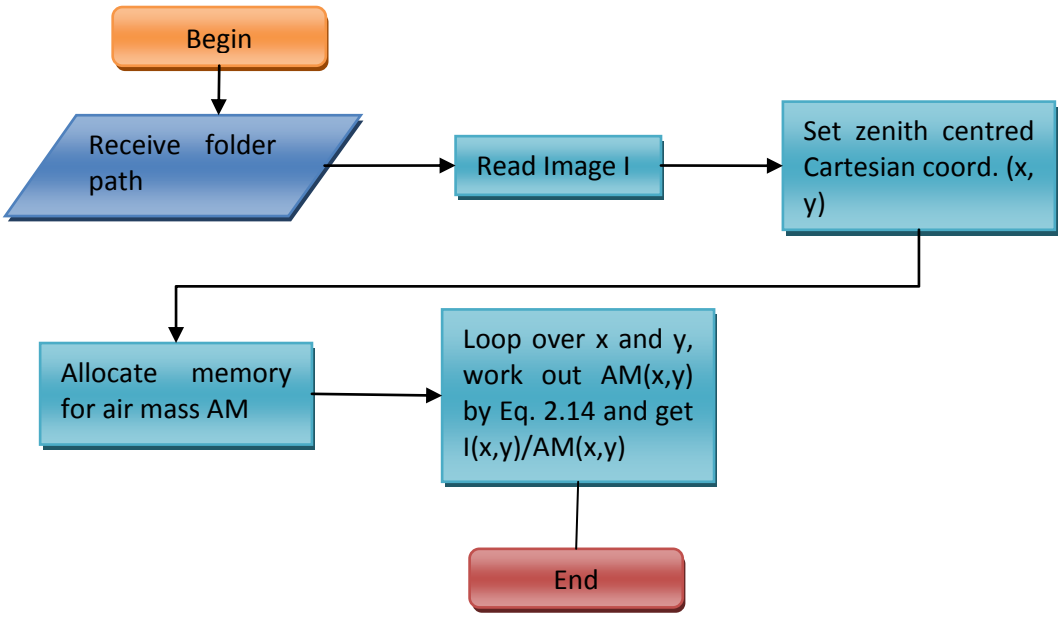

6.4.4 Vignetting correction

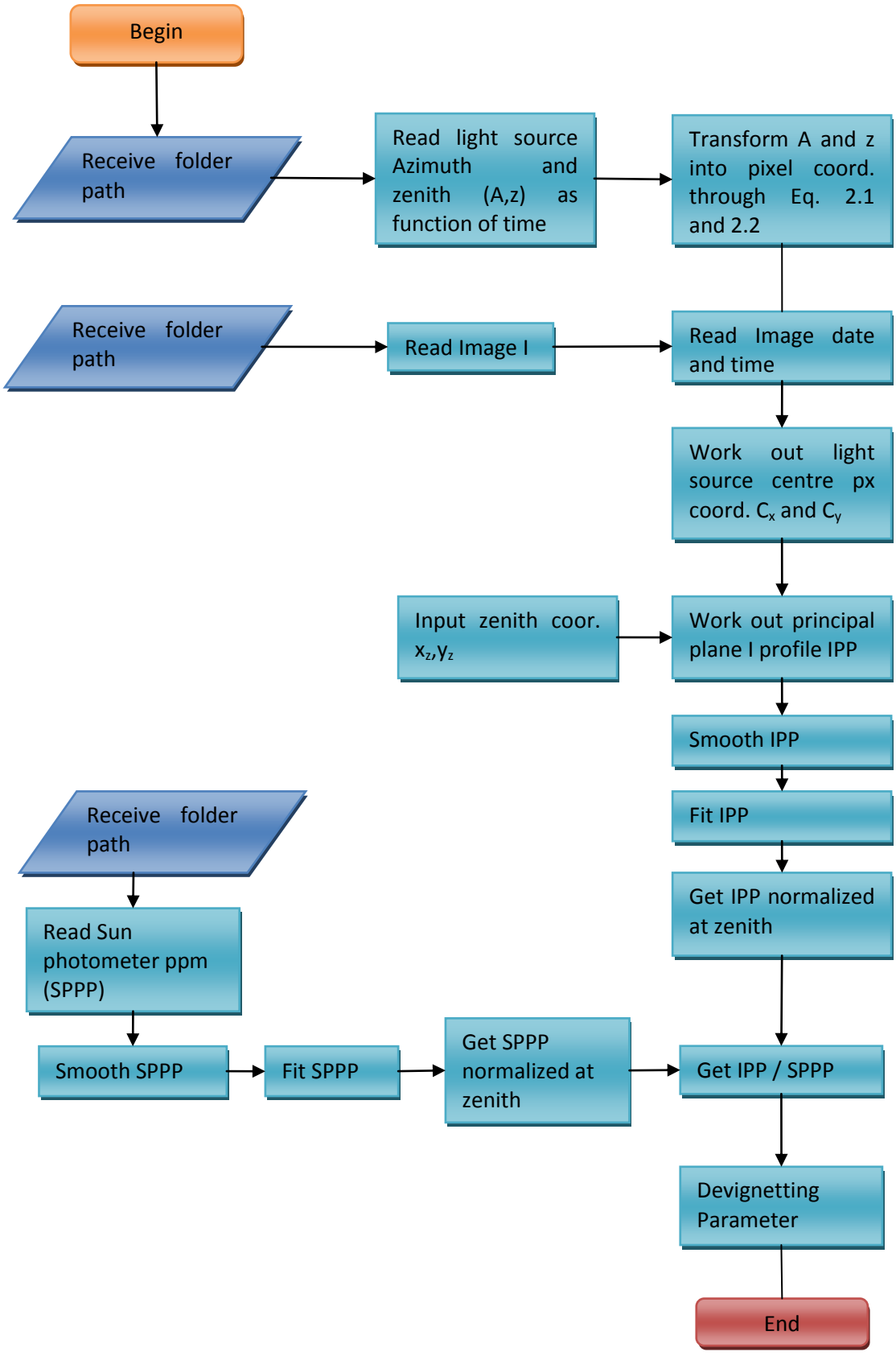

6.4.5 Occulting disk mask

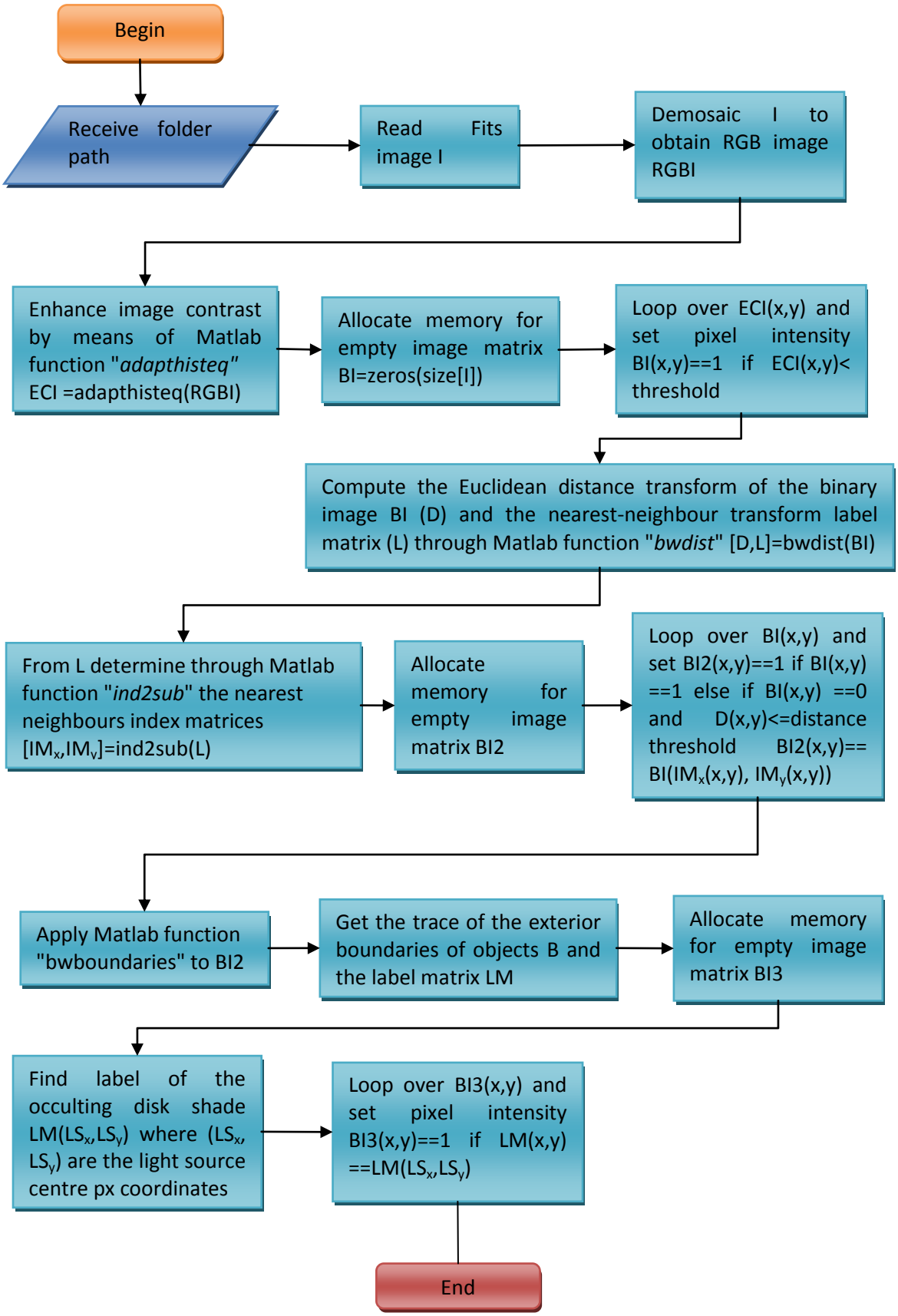

6.4.6 HR algorithm

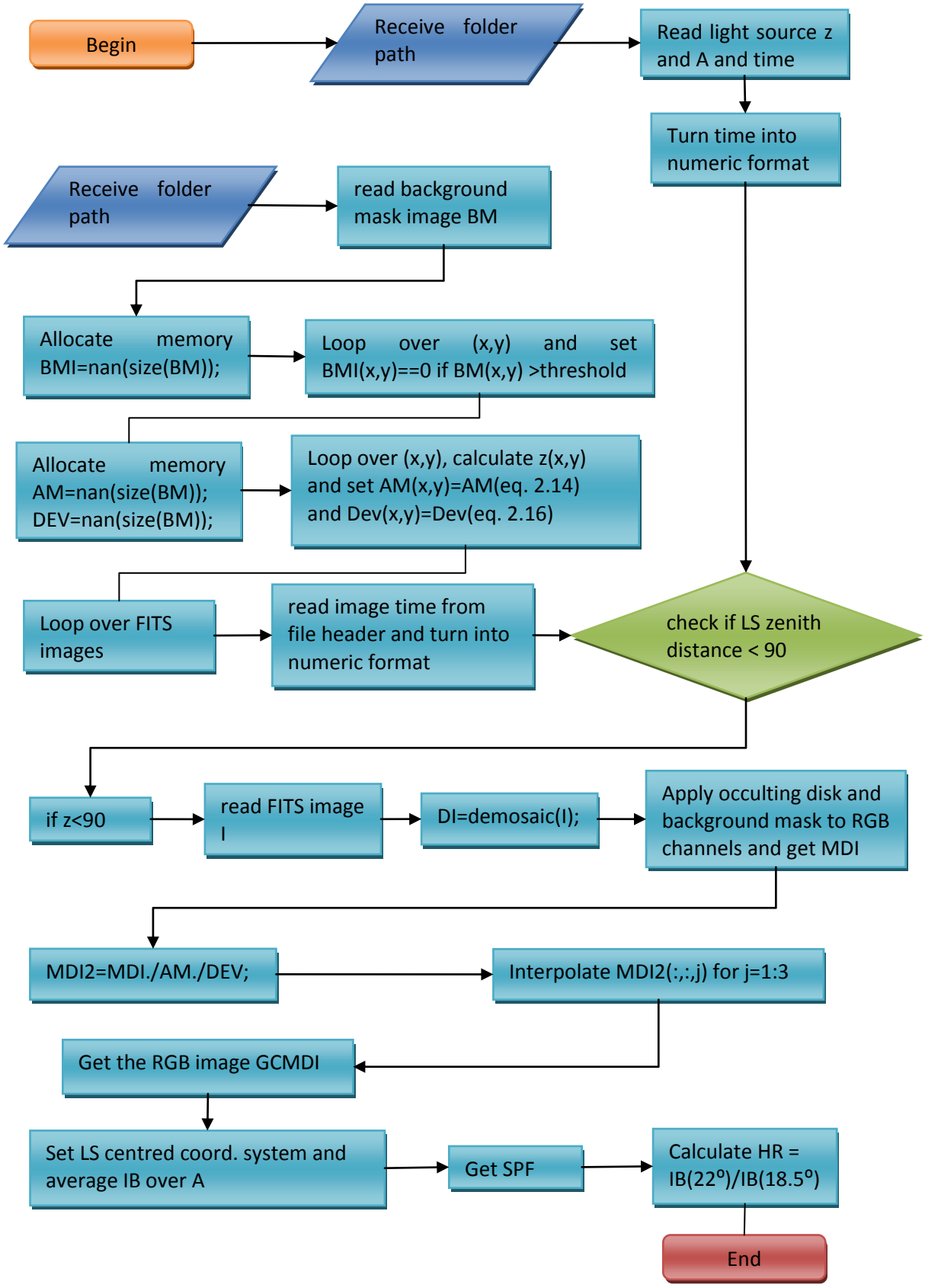

6.4.7 DFA

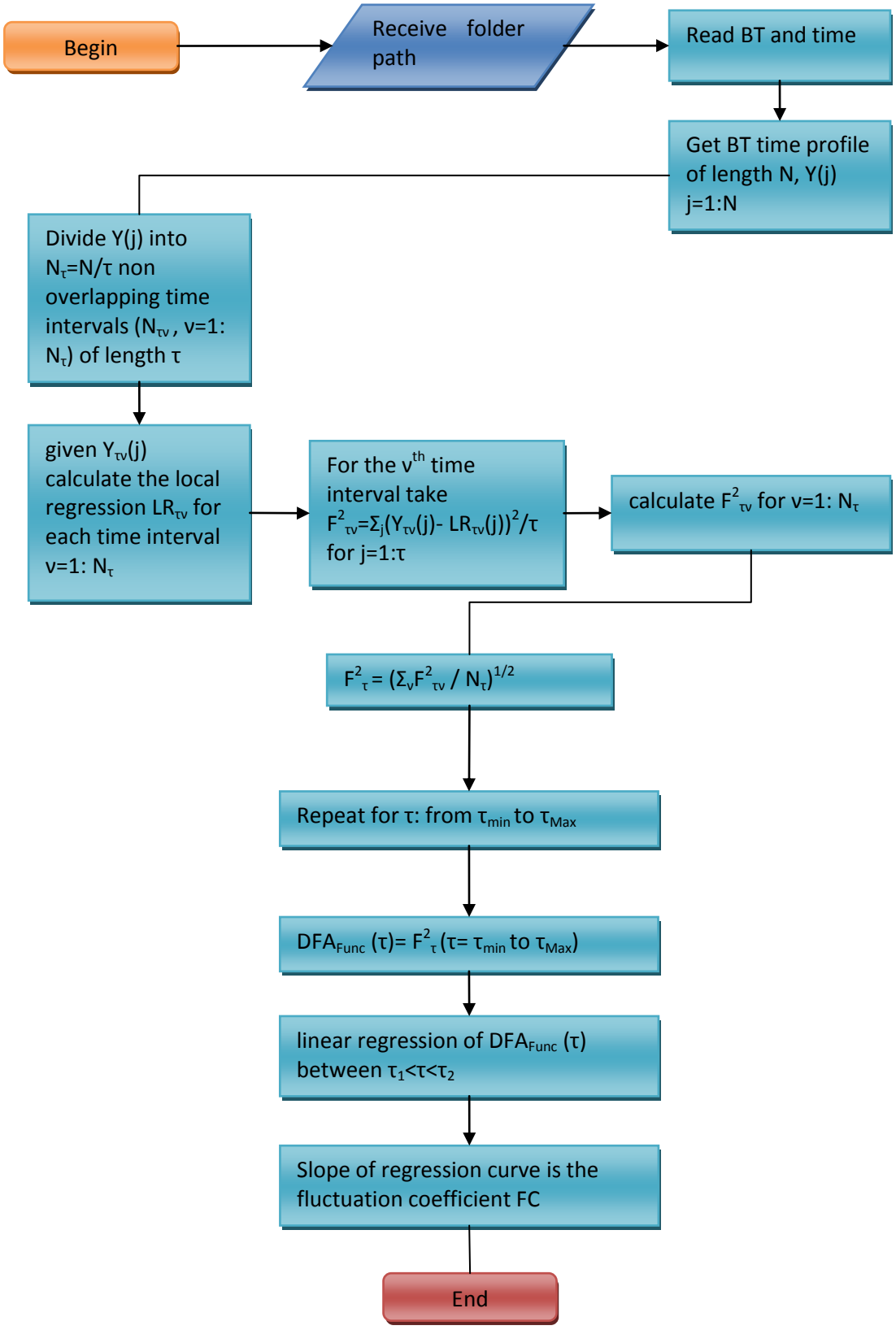
Begin
Receive folder path
Read BT and time
Get BT time profile of length N, Y(j) j=1:N
Divide Y(j) into $N_\tau=N/\tau$ non overlapping time intervals ($N_{\tau v}$, v=1: N_τ) of length τ
given $Y_{\tau v}(j)$ calculate the local regression $LR_{\tau v}$ for each time interval v=1: N_τ
For the v^{th} time interval take $F^2_{\tau v}=\Sigma_j(Y_{\tau v}(j)- LR_{\tau v}(j))^2/\tau$ for j=1:τ
calculate $F^2_{\tau v}$ for v=1: N_τ
$F^2_\tau = (\Sigma_v F^2_{\tau v} / N_\tau)^{1/2}$
Repeat for τ: from τ_{min} to τ_{Max}
$DFA_{Func}(\tau)= F^2_\tau(\tau= \tau_{min}$ to $\tau_{Max})$
linear regression of $DFA_{Func}(\tau)$ between $\tau_1<\tau<\tau_2$
Slope of regression curve is the fluctuation coefficient FC
End

6.4.8 BT-DFA-STD time series: text file generator

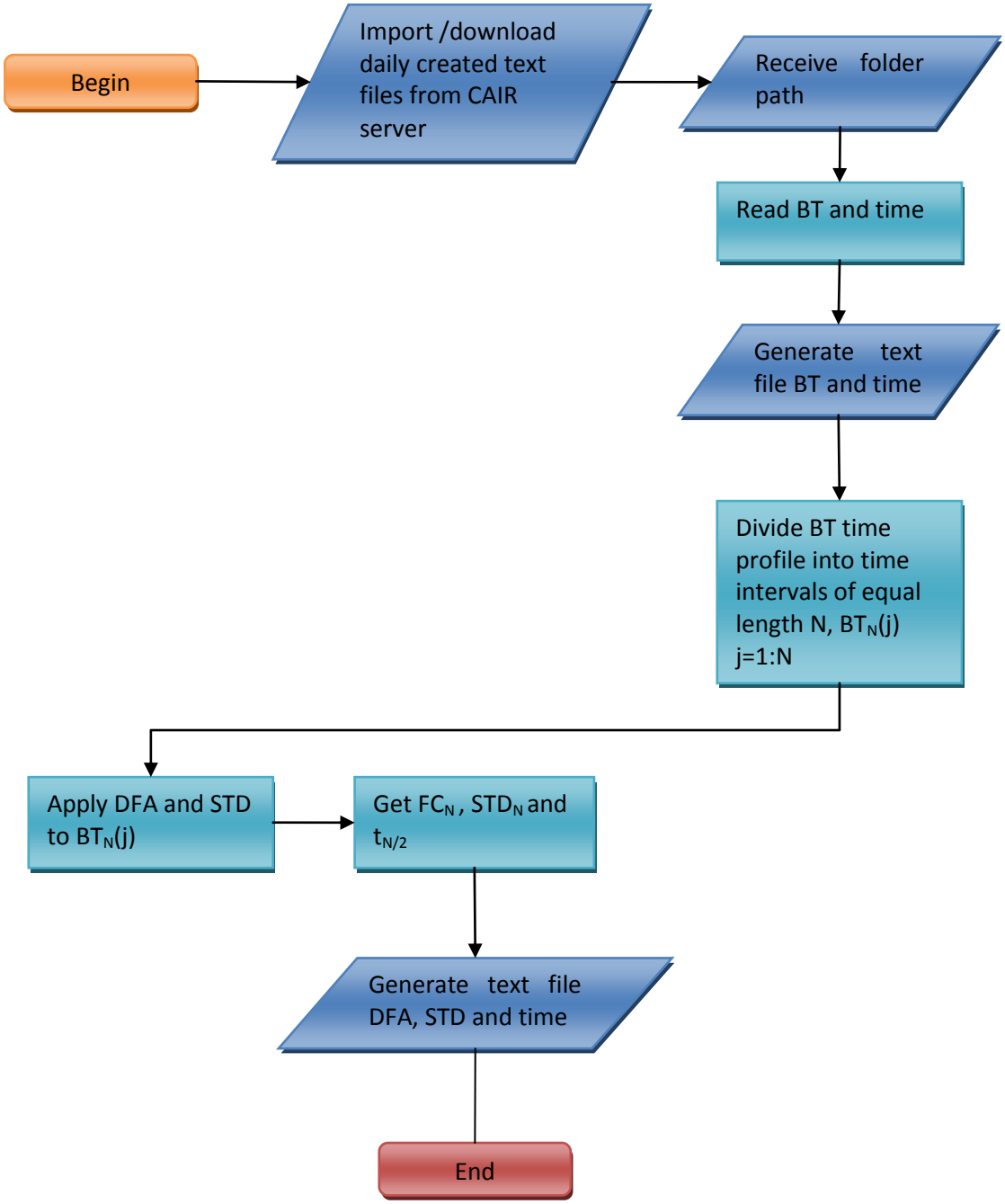

6.4.9 IWV smoothing and time series: text file generator

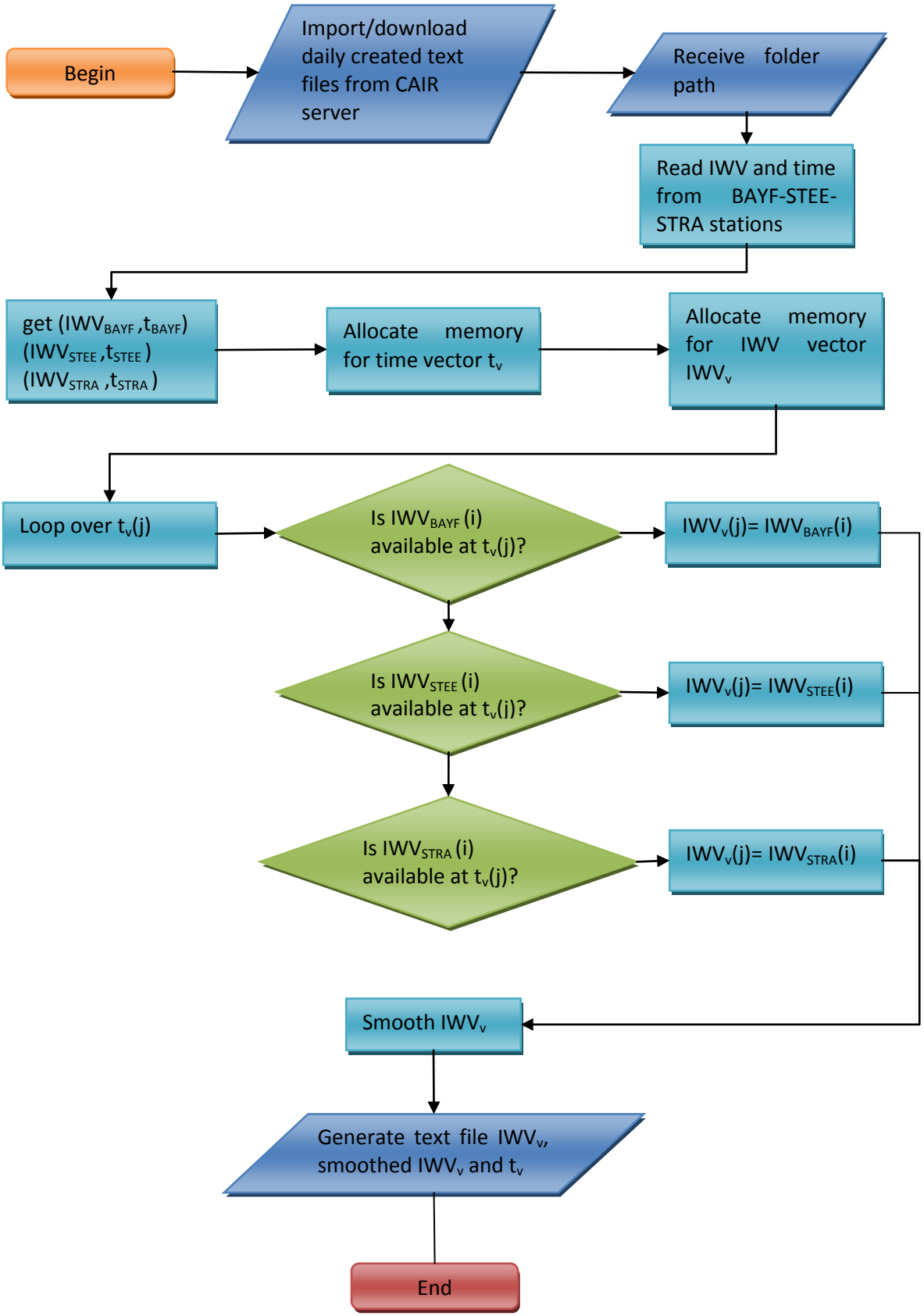

6.4.10 CGT time series: text file generator

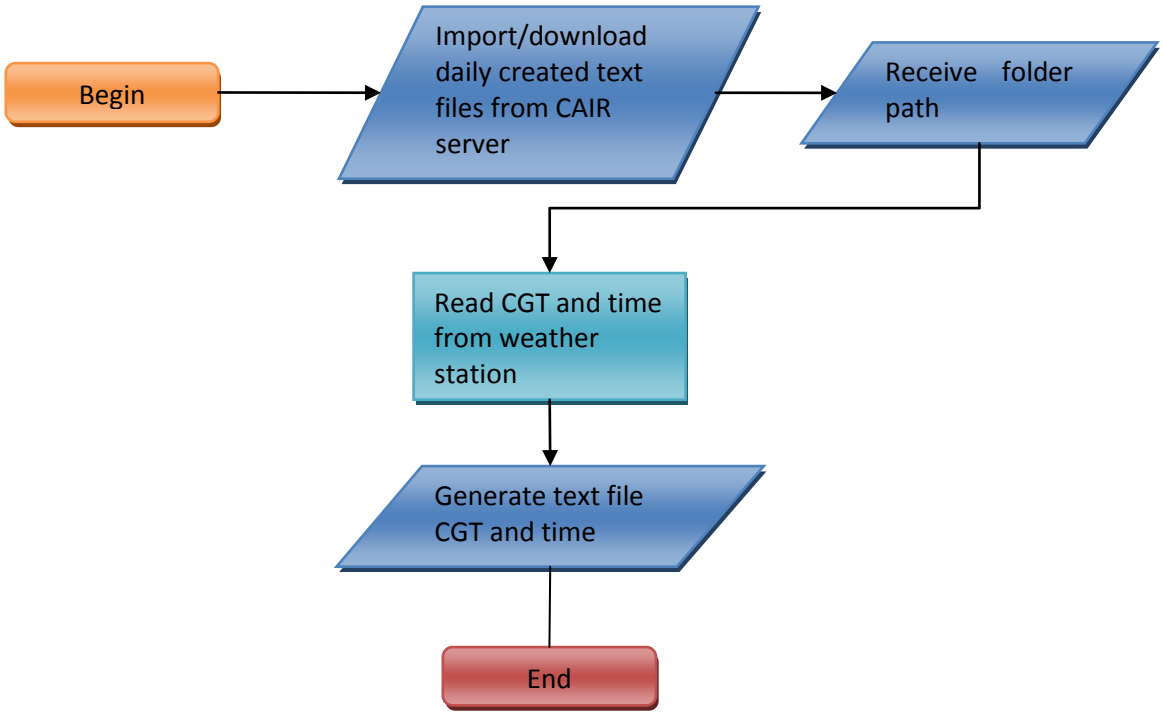

7 Bibliography

1. **R. Tapakis, A. Charalambides,** 2012, *Equipment and methodologies for cloud detection and classification: A review,* Solar Energy, Elsevier, 95, 392-430.
2. **W.R. Cotton, G.H. Bryan, S. C. Van de Heever,** 2011, *Storm and cloud dynamics*, Contemporary Physics, 52, 610-611.
3. **D.P. Duda, P. Minnis, K. Khlopenkov, T. L. Che, R. Boeke,** 2013, *Estimation of 2006 Northern Hemisphere contrail coverage using MODIS data,* Geo. Res. Let., 40, 612-617.
4. **A. J.Baran,** 2012, *From the single-scattering properties of ice crystals to climate prediction: A way forward,* Atm. Res., 112, 45-69.
5. **C. F. Bohren, D. R. Huffman,** Published Online: 29 DEC 2007, *Absorption and Scattering of Light by Small Particles,* John Wiley online Library, Online ISBN: 9783527618156, DOI 10.1002/9783527618156.
6. **A. Kokhanovsky,** 2004, Optical properties of terrestrial clouds, Earth-Science Rev., 64, 189-241, DOI:10.1016/S0012-8252(03)00042-4.
7. **Les Cowley,** 1998, *Atmospheric optics*, last access Jan 2016, http://www.atoptics.co.uk.
8. **K. Sassen, N. C. Knight, Y. Takano, A. J. Heymsfield,** 1994, *Effects of ice-crystal structure on halo formation: cirrus cloud experimental and ray-tracing modeling studies,* App. Opt., 33, 4590-4601, DOI: 10.1364/AO.33.004590.
9. **D. Deirmendjian,** 1969, *Electromagnetic scattering on spherical polydispersions*, New York : American Elsevier Pub. Co., Science, 290 pp.
10. **R. McGraw, S. Nemesure, S. E. Schwartz,** 1998, *Properties and evolution of aerosols with size distributions having identical moments,* J. Aer. Sci., 29, 761-772.
11. **H. Qingyuan,** 1994, *Near-Global Survey of Effective Droplet Radii in Liquid Water Clouds Using ISCCP Data,* J. Clim., 7, 465-497.
12. **O.A. Volkovitsky, L.N. Pavlova, A.G. Petrushin,** 1984, *Optical Properties of the Ice Clouds* (Gidrometeoizdat Leningrad), (in Russian).
13. **Y. Takano, K. N. Liou,** 1989, *Solar radiative transfer in cirrus clouds: 1. Single scattering and optical properties of hexagonal ice crystals,* J. Atmos. Sci., 46, 3-19.
14. **P. Yang et al.,** 2001, *Sensitivity of cirrus bidirectional reflectance to vertical inhomogenity of ice crystal habits and size distributions for two moderate-resolution imaging spectroradiometer (MODIS) bands,* J. Geophys. Res., 106, 17267-17291, DOI: 10.1029/2000JD900618.
15. **C. Magono, C.W. Lee,** 1966, *Meteorological classification of natural snow crystals,* J. Fac. Sci. Hokkaido Univ. Japan, Ser. 7, Vol. II, no. 4, http://hdl.handle.net/2115/8672.
16. **Landolt-Bornstein,** 1988, *Numerical data and functional relationships in science and technology In: Fischer, G. (Ed.), Group V: Geophysics and Space Research. V.5: Meteorology. Subvolume b. Physical and Chemical Properties of the Air,* Springer-Verlag.
17. **P. Yang, K.N. Liou, K. Wyser, D. Mitchell,** 2000, *Parameterization of the scattering and absorption parameters of individual ice crystals,* J. Geophys. Res., 105, 4699-4718.
18. **P.R. Field, A.J. Heymsfield, A. Bansemer**, 2008, *Determination of the combined ventilation factor and capacitance for ice crystal aggregates from airborne observations in a tropical anvil cloud,* J. Atmos. Sci., 65, 376-391.
19. **P.R. Field, A.J. Heymsfield, A. Bansemer,** 2007, *Snow size distribution parameterization for midlatitude and tropical ice cloud,* J. Atmos. Sci., 64, 4346-4365.
20. **A.H. Auer, D.L. Veal,** 1970, *The dimension of ice crystals in natural clouds,* J. Atmos. Sci., 27, 919-926.
21. **A. Macke, J. Mueller, E. Raschke,** 1996, *Scattering properties of atmospheric ice crystals,* J. Atmos. Sci., 53 no.19, 2813-2825.
22. **A. A. Kokhanovsky,** 2003, *Optical properties of irregularly shaped particles,* J. Phys. D App. Phys., 36, 915-923.

23. **A. J. Heymsfield, S. Lewis, A. Bansemer, J. Iaquinta, L. M. Miloshevich, M. Kajikawa, C. Twohy, M. R. Poellot,** 2002, *A general approach for deriving the properties of cirrus and stratiform ice cloud particles,* J. Atmos. Sci., 59, 3-29.
24. **P. R. Field, R. J. Hogan, P. R. A. Brown, A. J. Illingworth, T. W. Choularton, R. J. Cotton,** 2005, *Parameterization of ice-particle size distribution functions for mid-latitude stratiform cloud, Q.* J.R. Meteorol. Soc., 131, 1997-2017, DOI: 10.1256/qj.04.134.
25. **A. J. Baran, P. J. Connolly, A. J. Heymsfield, A. Bansemer,**. 2011, *Using in-situ estimate of ice water content, volume extinction coefficient, and the total solar optical depth obtained during the tropical ACTIVE campaign to test an ensemble model of cirrus ice crystals,* Q.J.R. Meteorol. Soc., 137, 199-218, Part A.
26. **K. N. Liou,** 2002, *An introduction to Atmospheric Radiation,* 2nd ed., Academic press, p. 583.
27. **R. P. Lawson, D. O'Connor, P. Zmarzly, K. Weaver, B. Baker, Q.X. Mo, H. Jonsson,** 2006, *The 2D-Stereo probe: Design and preliminary tests of a new airborne, high-speed, high resolution imaging probe,* J. Atmos. Ocenic tech., 23, 1462-1477.
28. **A. Macke, M.I. Mishchenko, B. Cairns,** 1996, *The influence of inclusions on light scattering by large ice particles,* J. Geophys. Res., 101, 23311–23316, DOI: 10.1029/96JD02364.
29. **P. Yang, K.N. Liou,** 1998, *Single-scattering properties of complex ice crystals in terrestrial atmosphere,* Contr. Atmos. Phys., 71(2), 223-248.
30. **L. C. Labonnote, G. Brogniez, J.C. Buriez, M. Doutriaux-Boucher, J.F. Gayet, A. Macke,** *Polarized light scattering by inhomogeneous hexagonal monocrystals: validation with ADEOSPOLDER measurements,* J. Geophys. Res., 2001, 106, 12139–12153, DOI: 10.1029/2000JD900642.
31. **Y. Xie, P. Yang, G.W. Kattawar, B.A. Baum, Y. Hu,** 2011, *Simulation of the optical properties of plate aggregates for application to the remote sensing of cirrus clouds,* Appl. Opt., 50(8), 1065-1081.
32. **J. Um, G.M. McFarquhar,** 2007, *Single-scattering properties of aggregates of bullet rosettes in cirrus,* J. Appl. Met. Clim., 46, 757-774.
33. **A.J. Baran, L.C. Labonnote,** 2006, *On the reflection and polarization properties of ice cloud,* J. Quant. Spect. Rad. Tran., 100, 41-54, DOI: 10.1016/j.jqsrt.2005.11.062.
34. **G.M. McFarquhar, P. Yang, A. Macke, A.J. Baran,** 2002, *A new parameterization of single scattering solar radiative properties for tropical anvils using observed ice crystal size and shape distributions,* J. Atm. Sci., 59, 2458-2478.
35. **P. Yang, B.A. Baum, A.J. Heymsfield, Y.X. Hu, H.L. Huang, S.C. Tsay, S. Ackerman,** 2003, *Single-scattering properties of droxtals,* J. Quant. Spec. Rad. Transf., 79-80, 1159-1169.
36. **T. Nousiainen, G.M. McFarquhar,** 2004, *Light scattering by small quasispherical ice crystals,* J. Atm. Sci., 61(18), 2229-2248.
37. **J. Um, G.M. McFarquhar,** 2011, *Dependence of the single-scattering properties of small ice crystals on idealized shape models,* J. Atm. Chem. Phys., 11, 3159-3171, DOI: 10.5194/acp-11-3159-2011.
38. **B. A. Baum, P. Yang, A.J. Heymsfield, C.G. Schmitt, Y. Xie, A. Bansemer, Y.X. Hu, Z. Zhang,** 2011, *Improvements in shortwave bulk scattering and absorption models for the remote sensing of ice clouds,* J. App. Met. Clim., 50, 1037-1056.
39. **A. J. Baran, L. C. Labonnote,** 2007, *A self-consistent scattering model for cirrus. 1: the solar region,* Q. J. R. Met. Soc., 133, 1899-1912.
40. **A. J. Baran, A. Bodas-Salcedo, R. Cotton, C. Lee,** 2011, *Simulating the equivalent radar reflectivity of cirrus at 94 GHz using an ensemble model of cirrus ice crystals: a test of the Met office global numerical weather prediction model,* Q. J. R. Met. Soc., 137, 1547-1560, DOI: 10.1002/qj.870.
41. **G. Hong, P. Yang, B.A. Baum, A.J. Heymsfield,** 2008, *Relationship between ice water content and equivalent radar reflectivity for clouds consisting of nonspherical ice particles,* J. Geoph. Res., 113, D20205, DOI: 10.1029/2008JD009890.
42. **Z. Ulanowski, E. Hesse, P. Kaye and A. J. Baran,** 2006, *Light scattering by complex ice-analogue crystals,* J. Quantit. Spectr. Rad. Transf.,100, 382–392.

43. **P. R. Field, A. J. Heymsfield, A. Bansemer,** 2006, *Shattering and particle interarrival times measured by optical array probes in ice clouds,* J. Atm. Oc. Tech., 23, 1357-1371, DOI: http://dx.doi.org/10.1175/JTECH1922.1.
44. **P. kaye, E. Hirst, R. Greenway, Z. Ulanowski, E. Hesse,** 2008, *Classifying atmospheric ice crystals by spatial light scattering,* Opt. Lett., 33(13), 1545-1547.
45. **Z. Ulanowski, P. Kaye, E. Hirst, R. Greenway,** 2012, *Retrieving the size of particles with rough surfaces from 2D scattering patterns,* J. Quant. Spec. Rad. Tran., 113, 2457-2464.
46. **R. Cotton, S. Osborne, Z. Ulanowski, E. Hirst, P. H. Kaye and R. S. Greenaway,** 2009, *The Ability of the Small Ice Detector (SID-2) to Characterize Cloud Particle and Aerosol Morphologies Obtained during Flights of the FAAM BAe-146 Research Aircraft,* J. Atm. Oc. Tech., 27, 290-303.
47. **Z. Ulanowski, C. Stopford , E. Hesse, P.H. Kaye, E. Hirst, R. Greenaway and M. Schnaiter,** 2008, *Small Ice Detector 2: Characterization of Ice Crystals Using Analysis of Azimuthal Scattering Patterns,* Geoph. Res. Abs., 10, DOI: EGU2008-A-11262.
48. **H. Jacobowitz,** 1971, *A method for computing the transfer of solar radiation through clouds of hexagonal ice crystals,* J. Quant. Spec. Rad. Tran., 11, 691-695.
49. **P. Wendling, R. Wendling and H. K. Weickmann,** 1979, *Scattering of solar radiation by hexagonal ice crystals,* Appl. Opt., 18(15), 2663-2671.
50. **P. Yang, K. N. Liou, L. Bi, C. Liu, B. Yi, and B. A. Baum,** 2015, *On the Radiative Properties of Ice Clouds: Light Scattering, Remote Sensing, and Radiation Parameterization,* Adv. Atm. Sci., 32, 32-63.
51. **E. Hesse, D. S. McCall, Z. Ulanowski, C. Stopford and P. H. Kaye,** 2009, *Application of RTDF to particles with curved surfaces,* J. Quant. Spect. Rad. Tran., 110, 1599-1603.
52. **E. Hesse, Z. Ulanowski,** 2003, *Scattering from long prisms computed using ray tracing combined with diffraction on facets,* J. Quant. Spect. Rad. Trans., 79-80, 721-732.
53. **A.J.M. Clarke, E. Hesse, Z. Ulanowski, P.H. Kaye,** 2006, *A 3D implementation of ray-tracing with diffraction on facets: verification and a potential application,* J. Quant. Spect. Rad. Trans., 100, 103-114.
54. **E. Hesse,** 2008, *Modelling diffraction during ray-tracing using the concept of energy flow lines,* J. Quant. Spect. Rad. Trans., 109, 1374-1383.
55. **S. K. Yee,** 1966, *Numerical solution of initial boundary value problems involving Maxwell's equations in isotropic media,* IEEE Tran. Ant. Prop., 14, 302-307, DOI: 10.1109/TAP.1966.1138693.
56. **P. Yang and K. N. Liou,** 1995, *Light scattering by hexagonal ice crystals: Comparison of finite-difference time domain and geometric optics method,* J. Opt. Soc. Amer. A., 12, 162-176, DOI: 10.1364/JOSAA.12.000162.
57. **P. Yang and K. N. Liou,** 1996, *Finite-difference time domain method for light scattering by small ice crystals in three dimensional space,* J. Opt. Soc. Amer. A., 13, 2072-2085, DOI: 10.1364/JOSAA.13.002072.
58. **G. Chen, P. Yang and G. W. Kattawar,** 2008, *Application of the pseudospectral time-domain method to the scattering of light by nonspherical particles,* J. Opt. Soc. Am. A, 25, 785-790.
59. **Q. H. Liu,** 1997, *The PSTD algorithm: A time-domain method requiring only two cells per wavelength,* Mic. Opt. Tech. Lett., 15, 158-165, DOI: 10.1002/(SICI)1098-2760(19970620).
60. **C. Liu, R. L. Panetta and P. Yang**, 2012, Application of the pseudo-spectral time domain method to compute particle single-scattering properties for size parameters up to 200, J. Quant. Spec. Rad. Tran., 113, 1728-1740, doi:10.1016/j.jqsrt.2012.04.021.
61. **E. M. Purcell and C. R. Pennypacker,** 1973, *Scattering and absorption of light by nonspherical dielectric grains,* Astroph. J., 186, 705-714.
62. **M. A. Yurkin, A. G. Hoekstra, R. S. Brock and J. Q. Lu,** 2007, *Systematic comparison of the discrete dipole approximation and the finite difference time domain method for large dielectric scatterers,* Opt. Express, 15, 17902-17911, DOI: 10.1364/OE.15.017902.
63. **C. Liu, L. Bi, R. L. Panetta, P. Yang and M. A. Yurkin,** 2012, *Comparison between the pseudo-spectral time domain method and the discrete dipole approximation for light scattering simulations,* Opt. Express, 20, 16763-16776, DOI:10.1364/OE.20.016763.

64. **D. I. Podowitz, C. Liu, P. Yang and M. A. Yurkin,** 2014, *Comparison of the pseudo-spectral time domain method and the discrete dipole approximation for light scattering by ice spheres,* J. Quant. Spec. Rad. Tran., 146, 402-409, DOI: 10.1016/j.jqsrt.2014.02.032.
65. **P. C. Waterman,** 1965, *Matrix formulation of electromagnetic scattering,* Proc. IEEE, 53, 805-812.
66. **M. I. Mishchenko, L. D. Travis and D. W. Mackowski,** 1996**,** *Tmatrix computations of light scattering by nonspherical particles: a review,* J. Quant. Spec. Rad. Tran., 55, 535-575, DOI: 10.1016/0022-4073(96)00002-7.
67. **A. J. Baran, P. Yang and S. Havemann,** 2001, *Calculation of the single-scattering properties of randomly oriented hexagonal ice columns: A comparison of the T-matrix and the finite-difference time-domain methods,* Appl. Opt., 40, 4376-4386.
68. **B. A. Baum, P. Yang, A. J. Heymsfield, C. Schmitt, Y. Xie, A. Bansemer, Y. X. Hu and Z. Zhang,** 2011, *Improvements in shortwave bulk scattering and absorption models for the remote sensing of ice clouds,* J. App. Met. Climatol., 50, 1037-1056.
69. **Y. X. Hu, D. Winker, M. Vaughan, B. Ling, A. Omar, C. Trepte, D. Flittner, P. Yang, S. L. Nasiri, B. baum, W. Sun, Z. Liu, Z. Wang, S. Young, K. Stamnes, J. Huang, R. Kuehn and R. Holz,** 2009, *CALIPSO/CALIOP cloud phase discrimination algorithm,* J. Atm. Oce. Tech., 26, 2293-2309, DOI: 10.1175/2009JTECHA1280.1.
70. **H. Chepfer, G. Brogniez and Y. Fouquart,** 1998, *Cirrus clouds' microphysical properties deduced from POLDER observations,* J. Quant. Spec. Rad. Tran., 60, 375-390.
71. **L. C. Labonnote, G. Brogniez, J. C. Buriez and M. Doutriaux-Boucher,** 2001, *Polarized light scattering by inhomogeneous hexagonal monocrystals: Validation with ADEOS-POLDER measurements,* J. Geoph. Res., 106, 12139–12153, DOI: 10.1029/2000JD900642.
72. **B. H. Cole, P. Yang, B. A. Baum, J. Riedi and L. C. Labonnote,** 2014, *Ice particle habit and surface roughness derived from PARASOL polarization measurements,* Atm. Chem. Phys., 14, 186-196.
73. **A. J. Baran, P. Hill, K. Furtado, P. Field and J. Manners,** 2014, *A coupled cloud Physics-Radiation parameterization of the bulk optical properties of cirrus and its impact on the met office unified model global atmosphere 5.0 configuration,* J.Climate, 27, 7725-7752, DOI: 10.1175/JCLI-D-13-00700.1.
74. **V. Shcherbakov, J. F. Gayet, O. Jourdan, J. Strom, A. Minikin,** 2006, *Light scattering by single ice crystals of cirrus clouds,* Geophys. Res. Lett., 33, DOI: 10.1029/2006GL026055.
75. **A. J. Baran, P. N. Francis, L. C. Labonnote and M. Doutriaux Boucher,** *A scattering phase function for ice cloud: tests of applicability using aircraft and satellite multi-angle multiwavelength radiance measurements of cirrus,* Q. J. Roy. Met. Soc., 2001, 127, 2395–2416, DOI: 10.1002/qj.49712757711 .
76. **P. R. Field, A. J. Baran, P. H. Kaye, E. Hirst and R. Greenaway,** 2003, *A test of cirrus ice crystal scattering phase functions,* Geoph. Res. Lett., 30(14), DOI: 10.1029/2003GL017482.
77. **A. Korolev, G. A. Isaac, and J. Hallett,** 2000, *Ice particle habits in stratiform clouds,* Q. J. Roy. Meteor. Soc., 126, 2873–2902.
78. **B. H. Cole, P. Yang, B. A. Baum, J. Riedi, L. C. Labonnote, F. Thieuleux, and S. Platnick,** 2013, *Comparison of PARASOL observations with polarized reflectances simulated using different ice habit mixtures,* J. Appl. Meterol. Clim., 52, 186-196.
79. **A. Lampert, A. Ehrlich, A. Dörnbrack, O. Jourdan, J. F. Gayet, G. Mioche, V. Shcherbakov, C. Ritter and M. Wendisch,** 2009, *Microphysical and radiative characterization of a subvisible midlevel Arctic ice cloud by airborne observations – a case study,* Atm. Chem. Phys., 9, 2647-2661, DOI: 10.5194/acp-9-2647-2009.
80. **T. J. Garrett, P. V. Hobbs and H. Gerber,** 2001, *Shortwave, single scattering properties of arctic ice clouds,* J. Geophys. Res., 106, 15155–15172.
81. **E. Hesse, A. Macke, S. Havemann, A. J. Baran, Z. Ulanowski and P. H. Kaye,** 2012, *Modelling diffraction by facetted particles,* J. Quant. Spec. Rad. Tran., 113, 342–347, DOI: 10.1016/j.jqsrt.2011.11.017.

82. **Z. Ulanowski, P. H. Kaye, E. Hirst, R. S. Greenaway, R. J. Cotton, E. Hesse, C. T. Collier,** 2014, *Incidence of rough and irregular atmospheric ice particles from Small Ice Detector 3 measurements*, Atmos. Chem. Phys., 13, 1649–1662.
83. **F. Auriol, J. F. Gayet, G. Febvre, O. Jourdan, L. Labonnote and G. Brogniez,** 1998, *In situ observations of cirrus cloud scattering phase function with 22 and 46 halos: cloud field study on 19 February,* J. Atm. Sci., 58, 3376-3390.
84. **J. F. Gayet, G. Mioche, V. Shcherbakov, C. Gourbeyre, R. Busen, and A. Minikin,** 2011, *Optical properties of pristine ice crystals in mid-latitude cirrus clouds: a case study during CIRCLE-2 experiment,* Atmos. Chem. Phys., 11, 2537-2544.
85. **P. Spichtinger and K. M. Gierens,** 2009, *Modelling of cirrus clouds – Part 2: Competition of different nucleation mechanisms,* Atm. Chem. Phys., 9, 2319-2334, DOI: 10.5194/acp-9-2319-2009.
86. **C. F. Bohren, E. E. Clothiaux,** 2006, *Fundamentals of Atmospheric Radiation,* Weinheim: Wiley-VCH.
87. **R. SLoan, J. H. Shaw and D. Williams,** 1955, *Infrared Emission Spectrum of the Atmosphere,* J. Opt. Soc. Am., 45(6), 455-460.
88. **D. Brunt,** 1932, *Notes on radiation in the atmosphere,* Quart. J. R. Met. Soc., 58, 389-420 .
89. **J. A. Shaw. and L. S. Fedor,** 1993, *Improved calibration of infrared radiometers for cloud temperature remote sensing,* Opt. Eng., 32, 1002-1010, DOI: 10.1117/12.133232.
90. **E. E. Ebert and J. A.Curry,** 1992, *A parameterization of ice cloud optical properties for climate models,* J. Geo. Res., 97, 3831–3836, DOI: 10.1029/91JD02472.
91. **J. Shaw and P. Nugent,** 2013, *Physics principles in radiometric infrared imaging of clouds in the atmosphere,* Eur. J. Phys., 34, DOI: 10.1088/0143-0807/34/6/S111.
92. **D. G. Murcray, J. N. Brooks, F. H. Murcray, W. J. Williams,** 1974, *10 to 12 um Spectral Emissivity of a Cirrus Cloud,* J. Atm. Sci., 31, 1940-1942.
93. **W. Zhang et. al.,** 2007, *A Feasibility study of cloud base height remote sensing by simulating ground-based thermal infrared brightness temperature measurements,* Chinese J. of Geo., 50, 339–350, DOI: 10.1002/cjg2.1041.
94. **J. C. Dupont, M. Haeffelin, P. Drobinski and T. Besnard,** 2008, *Parametric model to estimate clear-sky longwave irradiance at the surface on the basis of vertical distribution of humidity and temperature,* J. Geo. Res., 113, DOI: 10.1029/2007JD009046.
95. **W. Brutsaert,** 1975, *On a derivable formula for long-wave radiation from clear skies,* Wat. Res. Res., 11, 742–744, DOI: 10.1029/WR011i005p00742.
96. **S.B. Idso, R.D. Jackson,** 1969, *Thermal radiation from the atmosphere,* J. Geo. Res., 74, 5397–5403, DOI: 10.1029/JC074i023p05397.
97. **M. Unsworth, J. Monteith,** 1974, *Long wave radiation at ground,* J.R. Met. Soc., 101, 13-24, DOI: 10.1002/qj.49710142703.
98. **W.C. Swinbank,** 1963, *Long-wave radiation from clear skies,* Quart. J. R. Met. Soc., 89, 339-348.
99. **M. Sugita, W. Brutsaert,** 1993, *Cloud effect in the estimation of instantaneous downward longwave radiation,* Water Res. Res, 29, 599–605, DOI: 10.1029/92WR02352.
100. **J.R. Key, A.J. Schweiger,** 1998, *Tools for atmospheric radiative transfer: STREAMER and FLUXNET,* Comput Geosci, 24, 443–451, DOI: 10.1016/S0098-3004(97)00130-1.
101. **A. Berk, L. S. Bernstein, D. C. Robertson,** 1989, *MODTRAN: a moderate resolution model for LOWTRAN7,* Geophysics Laboratory, 89, Issue 122 of Geophysics Laboratory technical report.
102. **E. Brocard, M. Schneebeli, C. Mätzler,** 2011, *Detection of Cirrus Clouds Using Infrared Radiometry,* IEEE Trans. on Geosc. and Rem. Sens., 49, 595-602.
103. **M. H. Ahn, D. Han, H. Y. Won, V. Morris,** 2015, *A cloud detection algorithm using the downwelling infrared radiance measured by an infrared pyrometer of the ground-based microwave radiometer,* Atmos. Meas. Tech., 8, 553-566.
104. **O. L. Fassig,** 1915, *A revolving cloud camera,* Mon. Wea. Rev., 43, 274-275.
105. **H. Sellers and A. K. McGuffie,** 1989, *Almost a century of imaging clouds over the whole-sky dome.* Bull. Am. Meteorol. Soc., 70(10), 1243-1253.

106. **L. Georgi,** 1933, *The photographic sky mirror,* Weather, 12, 149-153.
107. **R. G. Mallmann and A.G.Greenler** 1972, *Circumscribed halos,* Science, 176, 128-131.
108. **W. P. Winn, T. V. aldridge and C.B. Moore,** 1973, *Video tape recordings of lightning flashes,* J. Geo. Res., 78, 4515-4519.
109. **R. Hill,** 1924, *A lens for whole sky photographs,* Quart. J. roy. Met. Soc., 50, 227-235.
110. **C. E. Deppermann,** 1949, *An improved mirror for photography of the whole sky,* Bull. Amer. Met. Soc., 30, 282-285.
111. **W.S. Von Arx,** 1958, *Synoptic photograph,* Weather, 13, 179-197.
112. **R. W. Wood,** 1911, *Physical Optics,* New York: Macmillan, p. 768.
113. **I. A. Shaklin and M. D. Lund,** 1972, *Photogrammetrically determined cloud-free lines-of-sight through the atmosphere,* J. App. Met., 11, 773-782.
114. **I. A. Shaklin and M. D. Lund** 1973, *Universal methods for estimating cloud-free lines-of-sight through the atmosphere,* J. App. Met., 12, 28-35.
115. **I. A. Lund,** 1973, *Joint probabilities of cloud-free lines of sight through the atmosphere at Grand Forks, Fargo, and Minot, North Dakota. AFCR1-TR-73-0178.* Air Forces Surveys in Geophys., no. 262, AFGL.
116. **I. A. Lund, D. D. Grantham and R.E. Davis,** 1980, *Estimating probabilities of cloud-free field of view from the Earth through the atmosphere,* J. App. Met., 19, 452-463.
117. **L. O. Pochop and M. D. Shaklin,** 1966, *Sky cover photograms: a new technique,* Weatherwise, 19, 198-203.
118. **R. L. Holle and S. A.Mackay,** 1975, *Tropical cloudiness from all-sky cameras on Barbados and adjacent Atlantic Ocean,* J. App. Met., 14, 1437-1450.
119. **R. L. Holle, J. Simpson and S. W. Leavitt,** *Gate B-scale cloudiness from whole-sky cameras on four U.S. ships.* 1979, Mon. Weath. Rev., 107, 874-895.
120. **R. W. Johnson and W. S. Hering,** 1987, *Automated cloud cover measurements with a solid-state imaging system, Proceedings of the Cloud Impacts on DOD Operations and Systems, Workshop* (Atmospheric Science Division, Air Force Geophysics Laboratory, Air Force Systems Command, Hanscom Air Force Base,1987), 59-69.
121. **R. W. Johnson, T. L. Koehler and J. E. Shields,** 1988, *A multistation set of whole sky imagers and a preliminary assessment of the emerging data base,* in Proceedings of the Cloud Impact on DOD Operations and Systems, 1988 Workshop, (Science and Technology Corporation, 1988), 159-162.
122. **J. E. Shields, R. W. Johnson and M. E. Karr,** 1994, *Upgrading the day/night whole sky imager from manual/interactive to full automatic control,* Final Report to the Office of Naval Research Contract N00014-89-D-0142 (DO #18), Marine Physical Laboratory, Scripps Institution of Oceanography, University of California, San Diego, MPL-U-140/94, NTIS N. ADA292296.
123. **J. E. Shields, R. W. Johnson, M. E. Karr and R.A. Weymouth,** 1997, *Delivery and development of a day/night whole sky imager with enhanced angular alignment for full 24 hour cloud distribution assessment,* Final Report to the Office of Naval research Contract N00014-93-D-0141-DO#11, Marine Physical Laboratory, Scripps Institution of Oceanography, University of California, San Diego, MPL-U-8/97, NTIS N. ADA333269.
124. **S. B. Mende and R. H. Eather,** 1976, *Monochromatic all-sky observations and auroral precipitation patterns,* J. Geo. Res., 81, 3771-3780, DOI: 10.1029/JA081i022p03771.
125. **R. D. Lyons,** 1971, *Computation of height and velocity of clouds over Barbados from a whole-sky camera network*, Sat. and Mesomet. Res. Project, Res. Pap. no. 95, University of Chicago, Illinois.
126. **J.E. Hay and L. B. McArthur,** 1979, *On the anisotropy of diffuse solar radiation,* Bull. Amer. Met. Soc., 59, 1442-1443.
127. **G. T. Johnson and I. D. Watson,** 1986, *Estimating view factor using video imagery,* Computational Mechanics Pubs., Proc. Int. Conf. on Dev. and App. of Comp. Tech. to Env. Studies, 627-638.
128. **T. J. Herbert,** 1987, *Area projections of fish-eye photographic lenses,* Agric. Forest. Met., 39, 215-223.

129. **G. Pfister, R. L. Mckenzie, J. B. Liley, W. Thomas, B. W. Forgan and C. N. Long.,** 2003, *Cloud coverage based on all-sky imaging and its impact on surface solar irradiance,* J. Appl. Met., 42, 1421-1434.
130. **J. E. Shields, M. E. Karr, R. W. Johnson and A. R. Burden,** 2013, *Day/night whole sky imagers for 24-h cloud and sky assessment: history and overview,* App. Opt., 52, 1605-1616.
131. **J. Kleissl,** 2013, *Solar Resource Assessment and Forecasting,* Academic Press, Elsevier. The reading continues for pp. 177-182 of Chapter 8: "Overview of Solar-Forecasting Methods and a Metric for Accuracy Evaluation," by Coimbra, Kleissl, and Marquez [found on ANGEL].
132. **C. W. Chow, B. Urquhart, M. Lave, A. Domingues, J. Kleissl, J. E. Shield and B. Washom,** 2011, *Intra-hour forecasting with a total sky imager at the UC San Diego sola test bed,* Sol. Energy, 85, 2881-2893.
133. **J. J. DeLuisi and C. N. Long,** 1998, *Development of an automated hemispheric sky imager for cloud fraction retrievals,* Tenth Symposium on Meteorological Observations and Instrumentation, Amer. Met. Soc., 171-174.
134. **R. W. Johnson and W.S. Hering,** 1987, *Automated cloud cover measurements with a solid state imaging system,* Proceedings of the Cloud Impacts on DOD Operations and Systems, Workshop (Atmospheric Sciences Division, Air Force Geophysics Laboratory, Air Force Systems Command, Hanscom Air Force Base) 59-69.
135. **R. W. Johnson, T. L. Koehler and J. E. Shields,** 1988, *A multistation set of whole sky imagers and a preliminary assessment of the emerging data base,* Proceedings of the Cloud Impacts on DOD Operations and Systems, Workshop (Science and Technology Corporation), 159-162.
136. **J. E. Shield, T. L. Koelher and R. W. Johnson,** 1990, *Whole sky imager,* Proceeding of the Cloud Impact on DOD Operations and Systems, 1989/90 Conference (Science and technology Corporation, Meetings Division, 101 Research Drive, 1990), 123-128.
137. **A. Heinle, A. Macke and A. Srivastav,** 2010, *Automatic cloud classification of whole sky images,* Atm. Meas. Tech., 3, 557-567.
138. **C. Hughes, M. Glavin and E. Jones,** 2011, *Simple fish-eye calibration method with accuracy evaluation,* Elec. Lett. Comp. Vis. Im. Analys., 10, 54-62.
139. **C. Hughes, P. Denny, E. Jones, M. Glavin,** 2010, *Accuracy of fish-eye lens models,* App. Opt., 49, 3338-3347.
140. **F. Yue, B. Li, M. Yu.** 2013, *Direct fitting of center collinear circles for equidistant fish-eye camera calibration,* J. Elec. Imag., 22. , DOI: 10.1117/1.JEI.22.1.013004.
141. **M. Bauer, D. Griebach, A. Hermerschmidt, S. Kruger, M. Sheele and A. Shischmanow.** 2008, *Geometrical camera calibration with diffractive optical elements,* Opt. Expr., 16, 20241-20248.
142. **A. Arfaoui, and S. Thibault,** 2013, *Fisheye lens calibration using virtual grid,* App. Opt., 52, 2577-2583, DOI: 10.1364/AO.52.002577.
143. **E. Schwalbe,** 2005, *Geometric modelling and calibration of fisheye lens camera systemss,* Proceedings 2nd Panoramic Photogrammetry Workshop, Int. Archives of Photogrammetry and Remote Sensing, 5-8.
144. **J. Kannala and S. S. Brandt,** 2004, *A generic camera calibration method for fish-eye lenses,* Pattern Recognition, 2004. ICPR 2004. Proceedings of the 17th International Conference on, 1, 10-13, DOI: 10.1109/ICPR.2004.1333993.
145. **J. Kannala and S. S. Brandt,** 2006, *A generic camera model and calibration method for conventional, wide angle, and fish-eye lenses,* IEEE Trans. Pattern Anal. Mach. Intell., 28, 1335-1340.
146. **D. Scaramuzza, A. Martinelli, R. Siegwart,** 2006, *A Toolbox for Easily Calibrating Omnidirectional Cameras,* Intelligent Robots and Systems (IROS), IEEE/RSJ Intern Conf., 5695-5701.
147. **S. Dev, F. M. Savoy, Y. H. Lee, S. Winkler,** 2016, *WAHRSIS: A low cost, High-resolution Whole Ski Imager With Near-Infrared Capabilities,* Bib. code: 2016arXiv160506595D, Proc. IS&T/SPIE Infrared Imaging Systems, 2014.

148. **K. Tohsing, M. Schrempf, S. Riechelmann, H. Schilke and G. Seckmeyer,** 2013, *Measuring high-resolution sky luminance distributions with a CCD camera,* App. Opt., 52, 1564-1573, 10.1364/AO.52.001564.
149. **University of Hertfordshire,** 2014, *Bayfordbury All-sky cameras*, last access 07-2016, http://star.herts.ac.uk/allsky/.
150. **D. Campbell,** 2010, *Widefield Imaging at Bayfordbury Observatory,* University of Hertfordshire, p. 47.
151. **SBIG astronomical instruments***,* 2010, *Operating manual All-sky 340 and 340C CCD cameras,* www.sbig.com.
152. **A. Lukin, D. Kubasov,** 2004, *An Improved Demosaicing Algorithm,* Graphicon 2004 Conference Proceedings.
153. **TRUESENSE imaging,** *KAI-0340 Image Sensor 640 (H) x 480 (V) Interline CCD Image Sensor*, 2012, Rev. 1.0 PS-0024.
154. **A. Arfaoui, S. Thibault,** 2013, *Fisheye lens calibration using virtual grid,* App. Opt., 52, 2577-2583, DOI: 10.1364/AO.52.002577.
155. **C. Hughes, P. Denny, E. Jones, M. Glavin,** 2010, *Accuracy of fisheye lens models,* Appl. Opt., 49, 3338-3347.
156. **U.S. Naval Observatory,** 2011, *Topocentric Positions of Major Solar System Objects and Bright Stars,* http://aa.usno.navy.mil/data/docs/topocentric.php, last acc. Jul 2016.
157. **Ígor Rapp-Arrarás and J. M. Domingo-Santos,** 2011, *Functional forms for approximating the relative optical air mass,* J. Geo. Res., 116, DOI: 10.1029/2011JD016706.
158. **A. Bemporad,** 1906, *Die extinktion des lichtes in der erdatmosphäre,* 6, 538‑557.
159. **A. Jacobs, M. Wilson,** 2007, *Determining lens vignetting with HDR techniques,* XII National Conference on Lightning, Light 2007.
160. **D. B. Goldman,** 2010, *Vignette and Exposure Calibration and Compensation,* IEEE Trans. on Pattern Analysis and Machine Intelligence, 32, 2276 - 2288, DOI: 10.1109/TPAMI.2010.55.
161. **Cimel Electonique,** 2015, *Multiband photometer CE318-N - User's manual.*
162. **B. Holben,** 1993, **AERONET Aerosol Robotic Network,** last access Jul 2016, URL: http://aeronet.gsfc.nasa.gov/.
163. **Wikipedia contributors**, (2016, April 18). In *Wikipedia, The Free Encyclopedia*. Retrieved 15:09, July 7, 2016, from https://en.wikipedia.org/w/index.php?title=Local_regression&oldid=715865047.
164. **HEITRONICS Infrarot Messtechnik GmbH, 1996 - 2016,** *Infrared radiation pyrometer KT15*.
165. **V. R. Morris,** *Infrared Thermometer (IRT) Handbook,* 2006, ARM TR-015, U.S. Department of Energy, 14 pp., available at: http://www.arm.gov/publications/tech_reports/handbooks/irt_ handbook.pdf?id=36, last access: 11 Jul 2016.
166. **M. Bevis, S. Businger, T. A. Herring, C. Rocken, R. A. Anthes and R. H. Ware,** 1992, *GPS Meteorology: Remote Sensing of Atmospheric Water Vapor Using the Global Positioning System,* J. Geo. Res., 97, 15787–15801, DOI: 10.1029/92JD01517.
167. **J. Saastamoinen,** 1972, *Atmospheric correction for the troposphere and stratosphere in radio ranging of satellites, in The Use of Artificial Satellites for Geodesy,* Geo. Mono. Ser., 15, 272.
168. **EUMETNET - The Network of European Meteorological Services,** 2005, E-GVAP. *The EUMETNET EIG GNSS water vapour programme,* last access Jul 2016, URL: http://egvap.dmi.dk/.
169. **NERC Natural Environment Research Council,** 2011, *NERC British Isles continuous GNSS Facility*, last access Jul 2016, URL: http://www.bigf.ac.uk/.
170. **W. K. Widger,** 1976, *Integration of the black body radiation function,* Bull. Am. Met. Soc., 57(10), 1217-1219.
171. **S. Twomey,** 1963, *Tables of Scattering and Extinction Efficiencies,* U. S. Weather Bureau, Physical Science Laboratory. Unpublished.
172. **F. F. Hall,** 1968, *A Physical Model of Cirrus 8-13 micron Infrared Radiance,* App. Op., 7, 2264-2269, DOI: 10.1364/AO.7.002264.

173. **J. W. Kantelhardt, E. Koscielny-Bunde, H. H. A. Rego, S. Havlin and A. Bunde,** 2001, *Detecting Long-range Correlations with Detrended Fluctuation Analysis,* arXiv: cond-mat/0102214v1 [cond-mat.stat-mech].
174. **A. Heymsfield, M. Krämer, P. Brown, D. Cziczo, C. Franklin, P. Lawson, U. Lohmann, A. Luebke, G. M. McFarquhar, Z. Ulanowski,** (In preparation)*, Cirrus. In: Ice Formation and Evolution in Clouds and Precipitation: Measurement and Modeling Challenges,* Chapter 2, Met. Monographs, AMS Boston.
175. **G. Yamamoto, M. Tanaka, K. Kamitani,** 1966, *Radiative Transfer in Water Clouds in the 10 um Window Region,* 23, 305-313.
176. **W. G. Zdunkowski and W. K. Crandall,** 1971, *Radiative transfer of infrared radiation in model clouds*, Tellus, 23, 517-527, DOI: 10.1111/j.2153-3490.1971.tb00600.x.
177. **G. E. Hunt,** 1973, *Radiative properties of terrestrial clouds at visible and infrared thermal window wavelengths,* Quart. J. R. Met. Soc., 99(420), 346-369, DOI: 10.1002/qj.49709942013.
178. **J. R. Allen,** 1970, *Measurements of cloud emissivity in the 8-13 um waveband,* J. Appl. Met., 10, 200-265.
179. **M.F. Warren and S.G.Fitzpatrick,** 2005, *Transmission of solar radiation by clouds over snow and ice surfaces. Part II: Cloud optical depth and shortwave radiative forcing from pyranometer measurements in the Southern Ocean.,* J. Clim., Vol. 18, pp. 4637-4648.
180. **J. Qiu,** 2006, *Cloud optical thickness retrievals from ground-based pyranometer measurements.* J. Geophys. Res., Vol. 111, p. D22206.
181. **R. Boers, A. V. Lammeren and A. Feijt,** 2000, *Accuracy of cloud optical depth retrievals from ground-based pyranometers,* J. Atm. Oce. Tech., Vol. 17, pp. 916-927.
182. **B. V. Diedenhoven, B. Cairns, I. V. Geogdzhayev, A. M. Fridlind, A. S. Ackerman, P. Yang, B. A. Baum,** 2012, *Remote sensing of ice crystal asymmetry parameter using multi-directional polarization measurements – Part 1: Methodology and evaluation with simulated measurements,* Atmos. Meas. Tech., 5, 2361–2374, DOI: 10.5194/amt-5-2361-2012.
183. **J. D. Spinhirne, W. D. Hart, D. L. Hlavka,** 1996, *Cirrus Infrared Parameters and Shortwave Reflectance Relations from Observations.,* J. Atm. Sci., 53, 1438-1458.
184. **Matlab R2007b,** 1984-2007**,** *Flexible Image Transport System (FITS) Files: working with scientific data formats (Matlab Programming),* The MathWorks, Inc., Natick, Massachusetts, United States.